Very high-resolution polarimetric SAR image characterization through Blind Sources Separation techniques

Nikola Besic

Nikola Besic. Very high-resolution polarimetric SAR image characterization through Blind Sources Separation techniques. Signal and Image Processing. Université de Grenoble; Université du Monténégro, 2014. English. NNT : . tel-01118690v1

HAL Id: tel-01118690

https://hal.univ-grenoble-alpes.fr/tel-01118690v1

Submitted on 19 Feb 2015 (v1), last revised 18 May 2016 (v2)

UNIVERSITÉ DE GRENOBLE

THÈSE

Pour obtenir le grade de

DOCTEUR DE L'UNIVERSITÉ DE GRENOBLE

Spécialité : **Signal, Image, Parole, Télécoms**

Arrêté ministériel : 7 août 2006

Et de

DOCTEUR DE L'UNIVERSITÉ DU MONTÉNÉGRO

Spécialité : **Traitement du signal**

Présentée par

Nikola BESIC

Thèse dirigée par **Gabriel VASILE, Jocelyn CHANUSSOT** et **Srdjan STANKOVIC**

préparée au sein des **Grenoble Image Parole Signal Automatique laboratoire (GIPSA-lab)** et **Faculté d'électrotechnique (ETF)**, dans **EEATS** et **ETF**

Séparation aveugle des sources polarimétriques en télédétection RSO satellitaire à très haute résolution spatiale

Thèse soutenue publiquement le **21 novembre 2014**,
devant le jury composé de :

Mme Marie CHABERT
Professeur, INP Toulouse, Présidente
M. Laurent FERRO-FAMIL
Professeur, Université de Rennes I, Rapporteur
M. Philippe RÉFRÉGIER
Professeur, École Centrale de Marseille, Rapporteur
M. Predrag MIRANOVIC
Professeur, Université du Monténégro, Examinateur
M. Antonio PLAZA
Professeur, Université d'Estrémadure, Examinateur
M. Guy D'URSO
Ingénier de recherche, R&D EDF, Membre invité
M. Gabriel VASILE
Chargé de recherche, CNRS, Encadrant
M. Jocelyn CHANUSSOT
Professeur, Grenoble INP, Directeur de thèse
M. Srdjan STANKOVIC
Professeur, Université du Monténégro, Co-Directeur de thèse

THESIS

VERY HIGH-RESOLUTION POLARIMETRIC SAR IMAGE CHARACTERIZATION THROUGH BLIND SOURCES SEPARATION TECHNIQUES

Presented and defended by

Nikola BESIC

for jointly obtaining the

DOCTORATE DEGREE

of University of Grenoble
Doctoral School for Electronics, Power Systems, Automatic Control and Signal Processing
Specialization: Signal, Image, Speech, Telecommunications

and the

PHD DEGREE IN TECHNICAL SCIENCES

of University of Montenegro
Faculty of Electrical Engineering
Specialization: Signal Processing

Thesis supervised by Gabriel VASILE,
directed by Jocelyn CHANUSSOT and Srdjan STANKOVIC.

Prepared in the Grenoble Image Parole Signal Automatique laboratory (GIPSA-lab) and partly, at the Faculty of Electrical Engineering.

Defended in Grenoble, on 21th November 2014, in front of the jury:

President:	Marie CHABERT	- Professor, INP Toulouse
Opponents:	Laurent FERRO-FAMIL	- Professor, University of Rennes I
	Philippe RÉFRÉGIER	- Professor, École Centrale de Marseille
Examiners:	Predrag MIRANOVIC	- Professor, University of Montenegro
	Antonio PLAZA	- Professor, University of Extremadura
Guest member:	Guy D'URSO	- Research Engineer, R&D EDF
Supervisor:	Gabriel VASILE	- Research Scientist, CNRS
Director:	Jocelyn CHANUSSOT	- Professor, Grenoble INP
Co-Director:	Srdjan STANKOVIC	- Professor, University of Montenegro

Acknowledgements

Ce sera plutôt les remerciements... Ne pas dire thanks, mais merci, c'est mon devoir et mon désir.

J'aimerais d'abord remercier Messieurs Philippe Réfrégier et Laurent Ferro-Famil, les rapporteurs de ma thèse, pour leurs analyses très appréciées des travaux effectués pendant ma thèse et présentés dans ce manuscrit. Merci à Madame Marie Chabert d'avoir accepté le rôle de la présidente du jury, ainsi qu'aux examinateurs, Messieurs Antonio Plaza et Predrag Miranovic, pour leurs questions et remarques très intéressantes. C'est un grand honneur pour moi que tous ces scientifiques extraordinaires aient accepté de faire partie de cette histoire, mon histoire.

Sans aucun dilemme, le plus grand merci va à Gabriel. Si cette thèse pouvait avoir un coauteur, ce serait lui. Si on pouvait dire que, après cette thèse, on a quelqu'un qui ressemble à un scientifique, ce serait lui qui l'a créé. Si rien d'autre, il a gagné un ami fidèle.

Je suis très reconnaissant à mes directeurs de thèse, pour leur soutien sans réserve et leurs conseils qui m'ont aidé à rester sur le bon chemin. Merci à Jocelyn d'avoir eu toujours de la patience pour m'écouter, malgré le fait qu'il était toujours très occupé et moi, assez souvent, un vrai casse-pied. Merci à Srdjan pour toutes nos discussions et surtout, d'avoir été quelqu'un, dont l'opus scientifique considérable, avait ouvert la porte vers ma vie en France.

J'ai très envie de mentionner ici l'équipe des ingénieurs-chercheurs du R&D EDF. Un grand merci à M. Guy d'Urso, qui a également fait partie du jury, ainsi qu'à Messieurs Alexandre Girard et Didier Boldo, d'être toujours là pour me conseiller mais aussi pour juger le qualité de mon travail, dans un contexte un peu plus pragmatique. Un aussi grand merci va à Monsieur Jean-Pierre Dedieu, pour une collaboration qui m'a beaucoup plu et qui va, j'espère, continuer.

Merci à mes parents et à mon frère, d'être toujours de mon coté. Sans eux, tout ce que j'ai fait et tout ce que je vais faire, auraient aucun sens.

Merci à toutes et à tous qui ont fait (partie de) ma vie pendant ces trois ans, de manier (le) plus ou un peu moins intime. On m'avait dit qu'il fallait ajouter au moins quelques prénoms ici, mais à moi vous semblez être trop importants pour être catalogués. Vous allez vous reconnaître de toute façon, j'en suis sûr. Et moi, je vous porterai dans mon cœur, partout et toujours... Pas comme les souvenirs d'une période merveilleuse de ma vie, mais comme la partie de l'essence, de ce qu'elle est ma vie.

Pour finir, je veux évoquer un aspect novateur de ma soutenance, qui a sans doute apporté pas mal d'émotions à la discussion. Notamment, au plein milieu de cette dernière j'ai eu un coup de mou et je suis tombé dans les pommes devant mon jury et quelques amis qui sont restés dans la salle après ma présentation. Leurs réactions formidables m'ont permis de me remettre en forme assez vite et d'ensuite continuer la discussion, mais elles m'ont surtout

beaucoup touché... Jocelyn et Guy qui me réveillent, Gildas qui panique et qui court pour chercher de l'aide, Lucia qui vient pour tous nous calmer, Gabriel avec de l'eau, Fakhri avec du chocolat... Ce sont des images qui vont sûrement rester gravées pour toujours dans ma mémoire. Pas comme des mauvais souvenirs, mais plutôt comme une autre preuve (bien qu'elle n'était pas forcement nécessaire) que j'ai gagné beaucoup plus que quelques diplômes... ici, dans la capitale des Alpes.

À mes parents et leurs parents,

pour tout l'amour et tout ce que je suis.

"L'homme n'est pas une idée..."

Albert Camus, *La peste*

Contents

Abbreviations and acronyms

AML	Approximate Maximum Likelihood
BSS	Blind Source Separation
DEM	Digital Elevation Model
DERD	Double bounce Eigenvalue Relative Difference
DMRT	Dense Media Radiative Transfer
ECD	Elliptically Contoured Distributions
EDF	*Eléctricité de France*
EM	ElectroMagnetic
GLRT	Generalized Likelihood Ratio Test
IC	Independent Components
ICA	Independent Component Analysis
ICTD	Incoherent Target Decomposition
IEM-B	Integral Equation Model-B
InSAR	Interferometric SAR
LRT	Likelihood Ratio Test
MI	Mutual Information
ML	Maximum-Likelihood
MLC	Multi-Look Complex
MLE	Maximum Likelihood Estimation
MODIS	Moderate-Resolution Imaging Spectroradiometer
MORDOR	*MOdèle à Réservoirs de Détermination Objective du Ruissellement*
NC FastICA	Non-Circular FastICA
PC	Principal Components
PCA	Principal Component Analysis
PDF	Probability Density Function

POLSAR	Polarimetric SAR
SAR	Synthetic Aperture Radar
SCM	Sample Covariance Matrix
SECM	Sample Extended Covariance Matrix
SERD	Single bounce Eigenvalue Relative Difference
SIRV	Spherically Invariant Random Vector
SIRP	Spherically Invariant Random Process
SLC	Single-Look Complex
SPM	Sample Pseudo-covariance Matrix
SSD	Spherical Symmetric Distributions
SWE	Snow Water Equivalent
SWEEP	Snow Water Equivalent Estimation at the Pixel scale
TD	Target Decomposition
TSVM	Target Scattering Vector Model
QCA	Quasi Crystalline Approximation
QCA-CP	Quasi Crystalline Approximation with Coherent Potentials

Mathematical notations and operators

Scalars are designated using italic formating, e.g.

f - frequency,

with the exception of multi-letter ones, e.g.

SWE - Snow Water Equivalent.

Vectors are designated using bold formating and lower case, e.g.

$\mathbf{k}$ - target vector.

Matrices are designated using bold formating and upper case, e.g.

$\mathbf{S}$ - scattering matrix.

Particular probability density functions are designated using calligraphic style, e.g.

$\mathcal{N}$ or p - PDF of the normal distribution,

with p being a general notation.

The operators:

$[\cdot]^T$ - transposed,
$[\cdot]^H$ - conjugated-transposed,
$[\cdot]^*$ - conjugated,
$[\cdot]^{-1}$ - inversed,
$\langle . \rangle$ or $\widehat{[\cdot]}$ - estimated,
$\tilde{[\cdot]}$ - whitened,
$\bar{[\cdot]}$ - mean value,
$|\cdot|$ - absolute value - ℓ_1 norm,
$||\cdot||_2$ - Euclidean norm - ℓ_2 norm,
$\mathbb{E}[\cdot]$ - mathematical expectation,
$\Re\{\cdot\}$ - real part of a complex value,
$\Im\{\cdot\}$ - imaginary part of a complex value,
$[\cdot] \otimes [\cdot]$ - Kronecker product,
$\neg[\cdot]$ - negation,
$[\cdot] \oplus [\cdot]$ - exclusive disjunction.

Preface

Remote Sensing is the science of acquiring information about the Earth's surface without an actual contact with it, by sensing and recording scattered, reflected or emitted electromagnetic energy and processing, interpreting and applying that information. It can be defined as an applied scientific discipline, comprising and relying on more fundamental domains, as signal and image processing, electromagnetics and virtually all Earth's sciences. Nowadays, it is impossible to envisage the latter ones deprived for a wide spatial coverage of, either objects present on our planet, or processes and phenomena occurring all over its surface. This makes remote sensing an indispensable tool in the Earth observation.

The importance of this science and the necessity for its further development are emphasized by some of the biggest challenges humanity is facing in the modern age: the observed climate changes, the rapid growth of the world population, the sustainable development etc.

The significant impact of the global warming on the environment, reflected primarily through the melting of ice on the poles and in the mountainous regions, imposes the surveillance of the cryosphere as one of our top priorities. Aside from this, glaciers and snow cover represent significant supply of both drinking and industrial water, whose quantity can be accurately estimated only by means of wide spatial assessment. The vegetation, particularly the forests, being the lungs of out planet, can be preserved only through careful and regular spatial evaluation of their state. The recognized need for food production upsurge, which ought to be done by optimizing the existing agricultural regions, requires their constant and accurate monitoring. Overseeing the oceans' surface, covering nearly 70% of the Earth, cannot be performed but by means of remote sensing.

These are just few of many examples, an effort to demonstrate the essentiality of remotely acquired information in the Earth observation. Generalizing, by saying that everything which could not be measured locally, by means of spatial sampling, depends upon remote sensing, should not be an exaggeration.

Depending on frequency of the electromagnetic (EM) waves carrying the information, we can distinguish between different types of active and passive sensors, which can be either spaceborne or airborne. Consequently, several remote sensing disciplines exist, among which, with respect to the current infrastructure, the passive optical remote sensing and the active Synthetic Aperture Radar (SAR) remote sensing could be considered as the pre-eminent ones.

Optical remote sensing operates in visible and infra-red parts of the electromagnetic spectrum. Depending on the spectral resolution i.e. how many different frequencies we use simultaneously, we can discriminate between monospectral (panchromatic), multispectral and hyperspectral optical images. Despite the fact that it can be acquired only during the day and the constraints concerning the presence of clouds, an optical image, being the "boosted" photography, represents a vital piece of information.

The SAR remote sensing, operating in the microwave part of the electromagnetic spectrum, remains to be particularly attractive due to its all-day and all-weather sensing capabilities. Aside from these, the advantage of SAR is the deeper penetration of microwaves with respect to the visible light, allowing us to deduce not just surface but volume properties as well. On the other side, there are also some disadvantages, among which the principal concerns the data interpretation. Namely, unlike it is the case with the optical images, due to the different geometry and peculiar interaction with a target, we can not entirely rely on our intuition, arising from our vision sense.

Analogously to the optical remote sensing where we simultaneously use several frequencies in order to get more information about the target, in the SAR remote sensing we rather use several polarizations of the EM waves at the transmission and at the reception. This subdiscipline is called Polarimetric SAR (POLSAR) and it results in a multichannel SAR image, with each channel corresponding to a different combination of the polarizations.

In this thesis we propose mostly the contributions to the analysis and the interpretation of the SAR images, but however, we do not neglect, but rather use and demonstrate the utility of multispectral optical images, as well.

The contributions presented in this thesis are divided in two principal parts. The first part deals with the theoretical advancements and as such, is related to the interpretation of polarimetric SAR data. More concrete, it concerns the implication of the Blind Source Separation (BSS) techniques, having an aim to enhance the interpretation quality by considering the particular characteristics of the recently acquired data. As the prelude, the methodological framework for the statistical assessment of these particularities is provided. The second part, dealing rather with the application - remote sensing of snow, concerns the role of SAR remote sensing in the snow mapping and finally, the Snow Water Equivalent (SWE) spatial modelling, performed by means of integrating the optical remote sensing datasets in the hydrological model, but still, considered in the context of POLSAR.

The particularities of the new data mostly regard the significant improvement of the spatial resolution i.e. the size of the smallest object which can be distinguished on the ground. This progress has an important influence on the SAR image statistics. Namely, the conventional assumption for the statistical model of the multichannel POLSAR image is multidimensional Gaussian distribution. However, the increase of the spatial resolution compromises this assumption, leading rather to the heterogeneous clutter, characterized by non-Gaussian statistics.

The dilemmas raising in the community *a propos* this issue could be summarized in two questions:

- Are the newly proposed statistical models truly appropriate for modelling POLSAR and other multi-dimensional SAR data sets?
- What are we exactly gaining by acknowledging the departure from the Gaussianity assumption, in terms of interpretation?

These two questions were a driving force for the research constituting the methodological context of this thesis.

After introducing the basics of SAR image statistics in the first chapter, in Chapter II we propose an elaborated statistical analysis, with the aim of quantitatively determining the necessity and the benefits of the altered statistical hypotheses. That is to say, we provide our answer to the first question.

The interpretation of POLSAR images principally assumes applying polarimetric decomposition, with the goal of expressing a total target backscattering as, either coherent or incoherent, sum of more elementary backscattering components. Among different decompositions, introduced along with the SAR polarimetry concept in the first chapter, the algebraic ones, happen to be the most widely utilized in the community nowadays. Being based on the eigenvalue analysis, they are intrinsically linked to the assumption of Gaussianity of the polarimetric SAR clutter. As it is discussed in the introduction of the methodology part, the shift from this assumption, leads to the derived eigenvector components not to be statistically independent, but rather only decorrelated. Therefore, by preferably employing the most prominent BSS technique - Independent Component Analysis (ICA), introduced in the first chapter, we propose a new approach in decomposing a polarimetric data in Chapter III. This decomposition would be our answer to the second question [1].

After introducing the basics of the snow remote sensing in Chapter IV, in the following chapter we come up with a new, stochastically based snow mapping method. Although applying the developed ICTD on the POLSAR images of snow regions resulted in interesting empirical conclusions, we have implicated a bit more electromagnetic properties of a snow in the context of single polarization SAR images. Namely, the snow dielectric properties depend significantly on the quantity of liquid water present in the snowpack. Consequently, the remote sensing techniques employed in extracting the snow pack parameters, which would be the ultimate goal of snow remote sensing, vary upon the type of snow: whether the snow is dry or wet. Therefore, in the very beginning, it is necessary to identify the type of the snow cover. In the proposed approach [2], aside from introducing a stochastic decision, we also derive a new variable backscattering threshold, discriminating the two types of snow, which is based on the backscattering simulator and the deduced backscattering mechanism, both introduced in Chapter IV.

Finally, we concentrate on the spatial derivation of SWE. Given the ill-posedness of the backscattering model inversion problem, which causes a single polarization SAR image not to be exactly useful in this context, we turn toward a conjunction of the hydrological model and the remote sensing data. As well, we briefly present the ongoing investigations of the potentials of SWE spatial modelling using POLSAR data, reinforced by implicating BSS (PCA) in the analysis of the derived parameters. However, the calibration method of the Snow Water Equivalent (SWE) hydrological model, based on the optical remote sensing data, remains the highlight of the last chapter [3]. The referent hydrological model, which required spatial calibration is introduced in Section IV.2. Chapter VI describes the proposed algorithm, and even more, serves as the demonstration of the eventual supremacy of remote sensing with respect to the local *in situ* measurements.

Part A

METHODOLOGICAL CONTEXT

CHAPTER I

POLSAR image and BSS

This chapter serves as an introduction to the state of the art methods which inspired us to carry out the research presented in the methodology part of the thesis. We contemplated this chapter to be their brief but systematic review. The fusion of one portion of these methods actually forms the basis of the presented theoretical contributions.

First of all, we introduce the concept of SAR polarimetry, with the particular emphasis on the most representative target decompositions. Further on, we discuss the basics of SAR and POLSAR image statistics. Finally, we introduce the family of Blind Source Separation techniques, by especially stressing the Principal Component Analysis (PCA) and the Independent Component Analysis.

I.1 SAR Polarimetry

The concept of radar polarimetry dates back to the early 1950s when George Sinclair, inspired by the work of Stokes and Poincaré in the XIX century, lay its cornerstone by introducing the famous scattering matrix [4]. Namely, George Stokes [4] and Henry Poincaré [5] independently defined an unified formalism for representing electromagnetic waves regardless their polarization state. Relying on this formalism, the Sinclair's scattering matrix provides information about the target "capacity" to change the polarization state of the incident polarization waves [6].

The forthcoming work by Kennaugh [7], Graves [8], Huynen [9] and the others, leaded to the establishment of radar polarimetry as a new remote sensing discipline. This was followed by an intensive technical progress, which meant the integration of the radar polarimetry into the activities of the aerospace agencies all around the world. In the beginning, mostly airborne polarimetric sensors were developed, as RAMSES (ONERA), ESAR (DLR), AIRSAR (JPL), PISAR (JAXA), CONVAIR (CCRS) etc. Soon, the space shuttle based instrument SIR-C/X-SAR (JPL) appeared as well [6]. Naturally, this huge amount of the acquired data induced significant further advancements in theory.

Further on, numerous contributions concerning the calibration techniques and particularly concerning the data analysis and interpretation have been introduced by the entire pléiaide of scientists, including Freeman, Yamaguchi, Cameron, Cloude, Pottier, Touzi etc. making POLSAR one of the most attractive research domains in the remote sensing community. New spaceborne instruments have been launched into the orbit, among which most recently: ALOS (JAXA), TerraSAR-X (DLR) and RADARSAT-2 (CCRS). The last two are still providing us valuable polarimetric data. The datasets acquired by all of these three "new" instruments, along with the RAMSES acquisitions, are being used in this thesis.

I.1.1 Basic principle

As already implied, the very purpose or radar polarimetry is to broaden the information about the target by considering its influence on the polarization of the incident EM waves.

The polarization of the EM wave refers to the spatio-temporal behaviour of the electrical field (**e**) i.e. to the projection of the vector's trajectory onto the plane perpendicular to the propagation direction $\mathbf{k}_{EM}$, defined by unit vectors **x** and **y** (Fig. I.1):

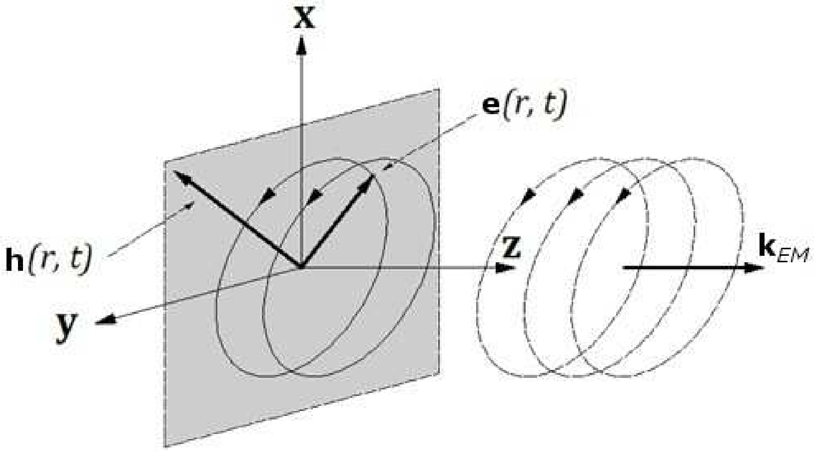

Figure I.1: EM field propagation

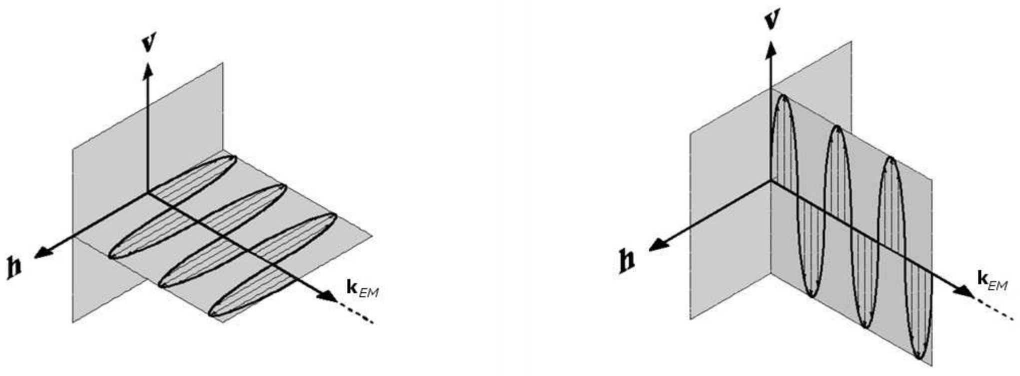

(a) (b)

Figure I.2: EM polarization: (a) horizontal, (b) vertical.

$$\begin{aligned}\mathbf{e}(x,y,z,t) &= \Re\left\{\mathbf{E_0}e^{j\left(2\pi ft-\frac{2\pi}{\lambda}z\right)}\right\} = e_x\mathbf{x}+e_y\mathbf{y} = \\ &= E_{0x}\cos\left(2\pi ft-\frac{2\pi}{\lambda}z+\delta_x\right)\mathbf{x}+E_{0y}\cos\left(2\pi ft-\frac{2\pi}{\lambda}z+\delta_y\right)\mathbf{y}\end{aligned} \tag{I.1}$$

with f being the frequency and λ the wavelength of the wave. It is actually the difference in phase between e_x and e_y ($\delta = \delta_x - \delta_y$), which determines the polarization state. For $\delta = \{0, \pi\}$ we have linear polarization, $\delta = \pi/2$ means circular one, while all the other values indicate the general case - eliptical polarization.

Therefore, in the most representative case (full POLSAR), we transmit linearly polarized waves: horizontal (H) and vertical (V) ones (Fig. I.2a and Fig. I.2b). At the reception, we collect the scattered signals using both horizontal and vertical antennas (Fig. C.1). The most rudimentary representation of the information acquired this way is the formerly mentioned scattering matrix:

$$\mathbf{S} = \begin{bmatrix} S_{hh} & S_{hv} \\ S_{vh} & S_{vv} \end{bmatrix} \tag{I.2}$$

with each of the elements being complex i.e. representing the impact of the target on the amplitude and the phase of the EM waves. It relates the incident and the scattered EM waves, represented by the Jones vector:

$$\mathbf{j} = [E_x \;\; E_y]^T = \left[E_{0x}e^{\delta_x} \;\; E_{0y}e^{\delta_y}\right]^T. \tag{I.3}$$

Depending on the choice of the coordinate system, it can take form of the Sinclair scattering

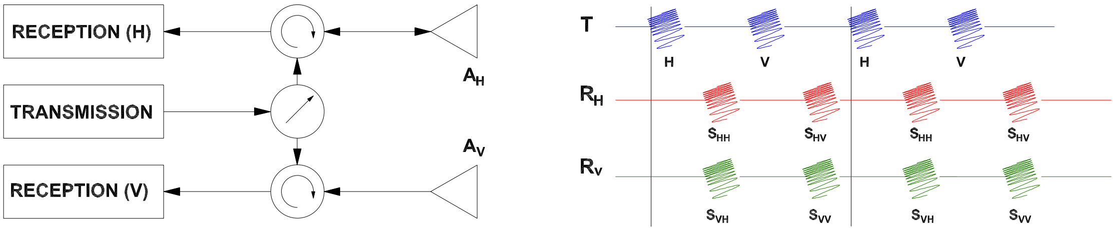

(a) (b)

Figure I.3: Polarimetry principal: (a) schema of the instrument, (b) the pulses at the transmission (T) and at the reception (R).

matrix or the Jones scattering matrix. Former is defined for the back scatterer alignment (BSA), while latter refers to the forward scatterer alignment (FSA). The difference between these two concerns the axis z. Namely, in the first case the direction of $\mathbf{z}$ stays the same for both incident and scattered wave, while in the second case $\mathbf{z}$ corresponds to $\mathbf{k}_{EM}$ (Fig. I.1).

In the case of monostatic configuration, when the same platform is used both for the transmission and the reception, we can assume reciprocity ($S_{hv} = S_{vh}$). Therefore, the scattering matrix is often replaced by the target vector, obtained by projecting the former onto the Pauli basis:

$$\mathbf{k} = \frac{1}{\sqrt{2}} \left[S_{hh} + S_{vv} \quad S_{hh} - S_{vv} \quad 2S_{hv} \right]^T \tag{I.4}$$

If the target does not depolarize the incident waves, we have coherent scattering, in which case either the scattering matrix or the target vector are indeed a suitable and sufficient representation. However, if we have a certain level of depolarization, we ought to rely on the estimated ($\langle\cdot\rangle$) spatial covariance of the target vector, expressed through the coherence matrix:

$$\begin{aligned} \mathbf{T} &= \mathbb{E}\left[\mathbf{k}\mathbf{k}^H\right] = \qquad\qquad (\mathrm{I.5}) \\ &= \frac{1}{2}\left\langle \begin{bmatrix} |S_{hh}|^2 + 2\Re(S_{hh}S_{vv}^*) + |S_{vv}|^2 & |S_{hh}|^2 - 2j\Im(S_{hh}S_{vv}^*) - |S_{vv}|^2 & 2S_{hh}S_{hv}^* + 2S_{vv}S_{hv}^* \\ |S_{hh}|^2 + 2j\Im(S_{hh}S_{vv}^*) - |S_{vv}|^2 & |S_{hh}|^2 - 2\Re(S_{hh}S_{vv}^*) + |S_{vv}|^2 & 2S_{hh}S_{hv}^* - 2S_{vv}S_{hv}^* \\ 2S_{hv}S_{hh}^* + 2S_{hv}S_{vv}^* & 2S_{hv}S_{hh}^* - 2S_{hv}S_{vv}^* & 4|S_{hv}|^2 \end{bmatrix} \right\rangle . \end{aligned}$$

Given that a partly polarized EM wave can be represented through the four elements Stokes Vector:

$$\mathbf{i} = \left\langle \left[|E_x|^2 + |E_y|^2 \quad |E_x|^2 - |E_y|^2 \quad 2\Re\{E_x E_y^*\} \quad -2\Im\{E_x E_y^*\} \right] \right\rangle^T \tag{I.6}$$

the incoherent scattering can be as well represented by 4 × 4 Kenaugh or Mueller matrix, depending on the backscattering coordinate system convention. E_x and E_y would be the complex "full" representations of e_x and e_y from Eq. I.2.

However, the proper exploitation and interpretation of the polarimetric information requires the appropriate decomposition of the backscattering process, represented either by the (projection of) scattering matrix or by the coherence matrix. The aim is to portray a target as a sum of more elementary backscatterers. Therefore, the polarimetric target decomposition (TD), due to its crucial role, undoubtedly represents the very essence of the SAR polarimetry.

I.1.2 Polarimetric decomposition

Target decomposition (TD), introduced in the first place in [9], aims to interpret polarimetric data by assessing and analysing the components involved in the scattering process [10]. Roughly speaking, the assessing assumes the derivation of the involved backscattering components, while the analysis dominantly concerns their parametrization. The former can be defined as:

$$\mathbf{X} = \sum_{i=1}^{N} k_i \mathbf{X}_i, \tag{I.7}$$

with $\mathbf{X}$ being the scattering matrix ($\mathbf{S}$) in case of a coherent target, or the coherence matrix ($\mathbf{T}$) in case of an incoherent one. Both the means of deriving the components ($\mathbf{X}_i$) and their parametrizations, differ for different types of decompositions. Here, we present the ones we found to be the most notable with respect to their historical and practical relevance. Afterwards, in the Chapter III, we will elaborate a new decomposition, the principal contribution of this thesis.

I.1.2.1 Coherent decompositions

The most elementary approach in decomposing a scattering matrix is based on a set of Pauli matrices, originally used by Wolfgang Pauli in his theory of quantum-mechanical spin. Due to their numerous interesting mathematical properties (e.g. hermitian, unitary and commutation properties), these matrices found their applications in many domains, among which, the SAR polarimetry. In case of monostatic configuration, the scattering matrix is decomposed into standard mechanisms as:

$$\begin{bmatrix} S_{hh} & S_{hv} \\ S_{vh} & S_{vv} \end{bmatrix} = \frac{\alpha_0}{\sqrt{2}} \begin{bmatrix} 1 & 0 \\ 0 & 1 \end{bmatrix} + \frac{\alpha_1}{\sqrt{2}} \begin{bmatrix} 1 & 0 \\ 0 & -1 \end{bmatrix} + \frac{\alpha_2}{\sqrt{2}} \begin{bmatrix} 0 & 1 \\ 1 & 0 \end{bmatrix}, \tag{I.8}$$

with the complex parameters:

$$\alpha_0 = \frac{S_{hh} + S_{vv}}{\sqrt{2}}, \ \alpha_1 = \frac{S_{hh} - S_{vv}}{\sqrt{2}}, \ \alpha_2 = \sqrt{2} S_{hv}, \tag{I.9}$$

making this approach a "model based" one. The first term in Eq. I.8 represent the odd-bounce scattering: flat surface, sphere, trihedral. The second one is related to the even-bounce scattering without polarization change - a dihedral with the axe of symmetry being parallel to the incident horizontally polarized wave. The third one represent the scatterer which favours the cross-polarized channel - a dihedral with the axe of symmetry rotated 45° with respect to the incident horizontally polarized wave [6].

A slightly different model based approach is proposed by Krogager in [11]. The second component in this case rather represents a dihedral with any orientation, while the third one represents a helix. The decomposition takes form of a:

$$\begin{bmatrix} S_{hh} & S_{hv} \\ S_{vh} & S_{vv} \end{bmatrix} = e^{j\phi} \left\{ e^{j_s^{\phi}} k_s \begin{bmatrix} 1 & 0 \\ 0 & 1 \end{bmatrix} + k_d \begin{bmatrix} \cos 2\theta & \sin 2\theta \\ \sin 2\theta & -\cos 2\theta \end{bmatrix} + e^{\mp 2\theta} k_h \begin{bmatrix} 1 & \pm j \\ \pm j & 1 \end{bmatrix} \right\}, \tag{I.10}$$

with the angles ϕ, ϕ_s, and θ being respectively the absolute phase, the single (odd) bounce component phase, the orientation of the dihedral. The real coefficients k_s, k_d, k_h are the contributions of single bounce, double bounce and helix scatterer. The latter one represents the non-symmetrical scattering i.e. the case when the target axe of symmetry doesn't lie in the plane perpendicular to the line of sight.

However, this decomposition is usually employed in the circular basis making this a suitable point for introducing the scattering matrix projected on the circular polarization basis. In the same way the projection onto the Pauli basis leads to the target vector, the projection onto the circular polarization ones, gives us the circular scattering matrix, which for the monostatic configuration takes the following form:

$$\mathbf{S}_C = \begin{bmatrix} S_{ll} & S_{lr} \\ S_{rl} & S_{rr} \end{bmatrix} = \frac{1}{2} \begin{bmatrix} S_{hh} + 2jS_{hv} + S_{vv} & j(S_{hh} + S_{vv}) \\ j(S_{hh} + S_{vv}) & -S_{hh} + 2jS_{hv} + S_{vv} \end{bmatrix}. \tag{I.11}$$

The lexicographic ordering of the these elements leads to the circular target vector:

$$\mathbf{k}_C = \begin{bmatrix} S_{ll} & \sqrt{2} S_{lr} & S_{rr} \end{bmatrix}^T. \tag{I.12}$$

The most representative algebraic coherent decomposition would be the Cameron decomposition [12]. In this approach we cannot actually assume reciprocity, meaning that we have to consider all four elements of the scattering matrix. The decomposing process can be roughly divided on two steps:

- The first step is related to the target geometrical properties. More precisely, we are initially trying to isolate the symmetric scattering from the non-symmetric one. By maximizing the former and consequently, minimizing the latter one, we can express the scattering matrix as:

$$\mathbf{S} = \mathbf{S}_{sym}^{max} + \mathbf{S}_{non-sym}^{min} \tag{I.13}$$

with:

$$\mathbf{S}_{sym}^{max} = \alpha_0 \begin{bmatrix} 1 & 0 \\ 0 & 1 \end{bmatrix} + (\alpha_1 \cos 2\psi + \alpha_2 \sin 2\psi) \begin{bmatrix} 1 & 0 \\ 0 & -1 \end{bmatrix}, \tag{I.14}$$

and

$$\mathbf{S}_{non-sym}^{min} = (\alpha_1 \sin 2\psi - \alpha_2 \cos 2\psi) \begin{bmatrix} 0 & 1 \\ 1 & 0 \end{bmatrix}. \tag{I.15}$$

The α parameters correspond to the ones introduced in Eq. I.9 and ψ is the rotation angle with respect to the reference basis.

- The second step would be algebraic, given that it represents one sort of the parametrisation of the symmetric part. Namely, if we express the matrix given in Eq. I.14 as:

$$\mathbf{S}_{sym}^{max} = \begin{bmatrix} 1 & 0 \\ 1 & z \end{bmatrix}. \tag{I.16}$$

we can define a vector:

$$\lambda(z) = \frac{1}{\sqrt{1+|z|^2}} \begin{bmatrix} 1 \\ z \end{bmatrix}. \tag{I.17}$$

Finally, if we define elementary reflectors in terms of z (e.g. $z = \{1, -1, \frac{1}{2}, -\frac{1}{2}\}$ correspond respectively to sphere, dihedral, cylinder, narrow dihedral), the symmetric target can be categorized by calculating the closeness to these elementary reflectors:

$$\lambda(z) = \frac{1}{\sqrt{1+|z|^2}} \frac{1}{\sqrt{1+|z_{ref}|^2}} |1 + z^* z_{ref}|. \tag{I.18}$$

I.1.2.2 Incoherent decompositions

Unlike it was the case with the coherent decompositions, here we are rather concentrated either on the already introduced coherence matrix, or on the covariance matrix, derived as the spatial covariance of the lexicographic target vector $\mathbf{k}_c$:

$$\begin{aligned} \mathbf{C} &= \mathbb{E}\left[\mathbf{k}_c \mathbf{k}_c^H\right] = \left\langle \begin{bmatrix} S_{hh} & \sqrt{2}S_{hv} & S_{vv} \end{bmatrix}^T \begin{bmatrix} S_{hh} & \sqrt{2}S_{hv} & S_{vv} \end{bmatrix}^* \right\rangle = \\ &= \left\langle \begin{bmatrix} |S_{hh}|^2 & \sqrt{2}S_{hh}S_{hv}^* & S_{hh}S_{vv}^* \\ \sqrt{2}S_{hv}S_{hh}^* & 2|S_{hv}|^2 & \sqrt{2}S_{hv}S_{vv}^* \\ S_{vv}S_{hh}^* & \sqrt{2}S_{vv}S_{hv}^* & |S_{vv}|^2 \end{bmatrix} \right\rangle \end{aligned} \tag{I.19}$$

The first incoherent decomposition was proposed by Huynen in [9], and it assumes decomposing the scattering as the incoherent sum of the fully polarized mechanisms and the fully unpolarized ones. Originally, the decomposition is based on Mueller matrix formalism:

$$\mathbf{M} = \mathbf{M}_{pol} + \mathbf{M}_{unpol} \tag{I.20}$$

but the same reasoning can be equally applied on either covariance or coherence matrix. The polarized matrix is then parametrized using nine parameters, among which only two are invariant with respect to the rotation around the line of sight.

The counterpart of formerly presented decompositions on standard mechanisms, in case of incoherent targets, are Freeman [13] and Yamaguchi [14] decompositions.

Freeman decomposition assumes decomposing the covariance matrix into the sum of first-order Bragg, double bounce and volume scattering:

$$\begin{aligned} \mathbf{C} &= \mathbf{C}_s + \mathbf{C}_d + \mathbf{C}_v = \qquad\qquad\qquad\qquad (\text{I.21}) \\ &= f_s \begin{bmatrix} \beta^2 & 0 & \beta \\ 0 & 0 & 0 \\ \beta & 0 & 1 \end{bmatrix} + f_d \begin{bmatrix} |\alpha|^2 & 0 & \alpha \\ 0 & 0 & 0 \\ \alpha^* & 0 & 1 \end{bmatrix} + f_v \begin{bmatrix} 1 & 0 & 1/3 \\ 0 & 2/3 & 0 \\ 1/3 & 0 & 1 \end{bmatrix}. \end{aligned}$$

Bragg scattering would be a more elaborated odd-bounce backscattering, which can provide us with some details about the surface dynamics. The real parameters β, f_s, f_d and f_v, and the complex parameter α, figuring in Eq. I.22 are supposed to be derived from a set of equations:

$$\begin{aligned} \langle |S_{hh}|^2 \rangle &= f_s\beta^2 + f_d|\alpha|^2 + f_v \qquad\qquad (\text{I.22}) \\ \langle |S_{vv}|^2 \rangle &= f_s + f_d + f_v \\ \langle S_{hh}S_{vv}^* \rangle &= f_s\beta + f_d\alpha + f_v/3 \\ \langle |S_{hv}|^2 \rangle &= f_v/3. \end{aligned}$$

However, there is one more unknown variable than there are equations. Therefore, in order to make this a well-posed problem, we need to consider the sign of $\langle S_{hh}S_{vv}^* \rangle - \langle |S_{hv}|^2 \rangle$. If it is negative, we take $\alpha = -1$, if not $\beta = 1$.

In case of Yamaguchi, there is an additional fourth component, representing non-symmetric, helix backscattering:

$$\mathbf{C}_h = \frac{f_x}{4} \begin{bmatrix} 1 & \pm j\sqrt{2} & -1 \\ \mp j\sqrt{2} & 2 & \pm j\sqrt{2} \\ -1 & \mp j\sqrt{2} & 1 \end{bmatrix}. \tag{I.23}$$

Another difference would be a complex β parameter, making $\mathbf{C}_{s_{31}}$ to be rather β^*. In this case, we have a system of five equations:

$$\begin{aligned}
\langle|S_{hh}|^2\rangle &= f_s|\beta|^2 + f_d|\alpha|^2 + \frac{8}{15}f_v + \frac{f_c}{4} \\
\langle|S_{hv}|^2\rangle &= \frac{2}{15}f_v + \frac{f_c}{4} \\
\langle|S_{vv}|^2\rangle &= f_s + f_d + \frac{3}{15}f_v + \frac{f_c}{4} \\
\langle S_{hh}S_{vv}^*\rangle &= f_s\beta + f_d\alpha + \frac{2}{15}f_v - \frac{f_c}{4} \\
\frac{1}{2}\Im\left\{\langle S_{hh}S_{hv}^*\rangle + \langle S_{hv}S_{vv}^*\rangle\right\} &= \frac{f_c}{4}.
\end{aligned} \tag{I.24}$$

Two parameters can be derived from the second and the last equation (Eq. I.25), while the rest of the system can be solved using the same hypothesis as in the case of Freeman decomposition.

The incoherent equivalents of the Cameron algebraic method would be the Cloude and Pottier [15] and the Touzi [16] decompositions. The particular emphasise will be put on introducing these two, given that the highlight of this thesis concern one incoherent target decomposition.

The first step in both of these two decompositions is the eigenvector decomposition of the target coherence matrix, allowing us to represent the total backscattering as a sum of three backscattering mechanism. Namely, given the Hermitian nature of positive semi-definite coherence matrix, the derived eigenvectors are mutually orthogonal and characterized by real eigenvalues. Each of the derived eigenvectors forms a coherence matrix with unity rank and therefore happens to be a fully polarized target vector. The corresponding eigenvalue (λ) represents its contribution to the total backscattering.

$$\mathbf{T} = \lambda_1\mathbf{k}_1\mathbf{k}_1^H + \lambda_2\mathbf{k}_2\mathbf{k}_2^H + \lambda_3\mathbf{k}_3\mathbf{k}_3^H \tag{I.25}$$

The principal difference between two decompositions would be, the second step - the parametrisation of the estimated target vectors i.e. backscattering mechanisms.

The Cloude and Pottier decomposition is based on the $\alpha - \beta - \gamma - \delta$ parametrisation of a target vector [15]:

$$\mathbf{k}_i = |\mathbf{k}_i| \exp j\theta \begin{bmatrix} 1 & 0 & 0 \\ 0 & \cos 2\psi_i & -\sin 2\psi_i \\ 0 & \sin 2\psi_i & \cos 2\psi_i \end{bmatrix} \begin{bmatrix} \cos\alpha_{pi} \\ \sin\alpha_{pi}\cos\beta_{pi}\exp j\delta_i \\ \sin\alpha_{pi}\sin\beta_{pi}\exp j\gamma_i \end{bmatrix}. \tag{I.26}$$

Among the obtained parameters, the very central place has the angle α_p, used in the

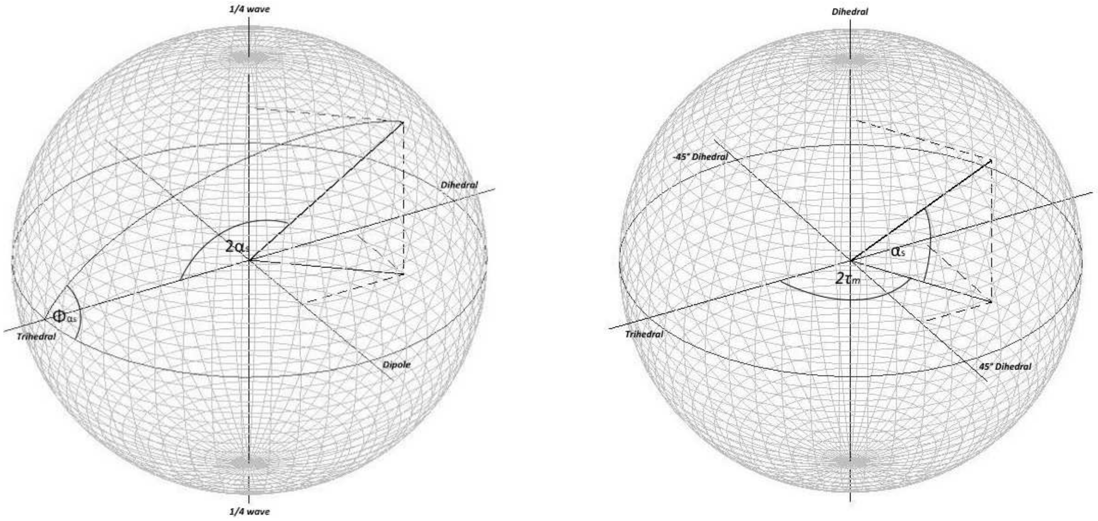

(a) (b)

Figure I.4: Poincaré sphere representation of TSVM parameters: (a) symmetric scattering ($\tau_m = 0$), (b) non-symmetric scattering ($\Phi_{\alpha_s} = 0$).

derivation of the mean backscattering mechanism ($\overline{\alpha}_p$), conditioned by the probabilities of α_{pi} to occur in the random sequence of parameters (P_i):

$$\overline{\alpha}_p = P_1\alpha_{p1} + P_2\alpha_{p2} + P_3\alpha_{p3} \tag{I.27}$$

Aside from this one, very important polarimetric descriptor would be the entropy, defining the appropriateness of using polarimetry [6]:

$$H = \sum_{i=1}^{3} -P_i \log_3 P_i, \quad P_i = \frac{\lambda_i}{\sum_{i=1}^{3} \lambda_i}. \tag{I.28}$$

The value zero indicates the absolute dominance of one fully polarized mechanism, while the value one points to the completely depolarizing target.

The third polarimetric descriptor we ought to mention would be the anisotropy:

$$A = \frac{\lambda_2 - \lambda_3}{\lambda_2 + \lambda_3} = \frac{P_2 - P_3}{P_2 + P_3}, \tag{I.29}$$

describing the relation of the second and the third estimated mechanisms.

The Touzi decomposition is rather based on the Target Scattering Vector Model (TSVM) [16].

Being based on Kennaugh-Huynen condiagonalization [7, 10] projected onto the Pauli basis, the TSVM [16] allows the parametrization of the target vector in terms of rotation angle (ψ), phase (Φ_s), maximum amplitude (m), target helicity (τ_m), symmetric scattering type magnitude (α_s) and symmetric scattering type phase (Φ_{α_s}), among which the last four are roll-invariant:

$$\mathbf{k} = m|\mathbf{k}|_m e^{j\Phi_s} \begin{bmatrix} 1 & 0 & 0 \\ 0 & \cos 2\psi & -\sin 2\psi \\ 0 & \sin 2\psi & \cos 2\psi \end{bmatrix} \begin{bmatrix} \cos\alpha_s \cos 2\tau_m \\ \sin\alpha_s e^{j\Phi_{\alpha_s}} \\ -j\cos\alpha_s \sin 2\tau_m \end{bmatrix}. \tag{I.30}$$

In order to avoid an ambiguity related to the Kennaugh-Huynen condiagonalization, the range of the orientation angle is reduced to the $[-\pi/4, \pi/4]$, by introducing the identity:

$$\mathbf{k}(\Phi_s, \psi, \tau_m, m, \alpha_s, \Phi_{\alpha_s}) = \mathbf{k}(-\Phi_s, \psi \pm \pi/2, -\tau_m, m, \alpha_s, -\Phi_{\alpha_s}). \tag{I.31}$$

Using TSVM parameters, it is eventually possible to represent the obtained target vectors on either symmetric or non-symmetric target Poincaré sphere [17, 18]. In the original decomposition, they necessarily form an orthogonal basis.

Being an integral part of the decomposition we propose in the Chapter III, the Touzi's TSVM has a very special place in this thesis.

I.2 SAR images statistics

The complex information characterizing one pixel of the SAR image represents totality of the backscattering in the corresponding spatial cell. It means that we cannot associate this value to one scatterer covering the area equivalent to one pixel, but rather to the ensemble of elementary scatterers distributed all over the same. The EM waves scattered by each of these elementary scatterers are summed coherently, which causes their either positive, or negative interference. This phenomena, due to its manifestation in the SAR image, in form of a granular noise, is called speckle effect, or speckle noise.

Using simplified mathematical formalism ($\mathbf{e} = Ae^{j\phi}\mathbf{i_e}$) we can illustrate this effect by representing the total received scattered EM wave as the vectorial sum of the individual scatterers in the complex space (Fig. I.5):

$$A_{tot}e^{j\phi_{tot}} = \sum_{i=1}^{n} A_i e^{j\phi_i} \tag{I.32}$$

Different random scattering amplitudes (A) and phases (ϕ) of the implicated elementary scatterers cause the formation of the SAR image to be rather a stochastic process. Therefore,

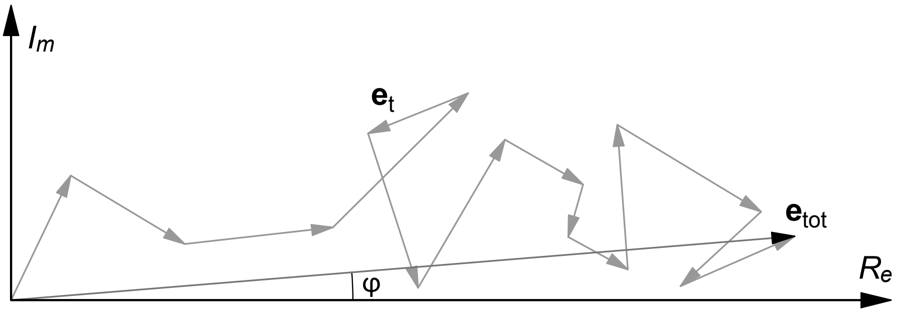

Figure I.5: Speckle noise.

in order to properly exploit the information contained in it, we ought to get acquainted with the statistics of the SAR image.

I.2.1 Single polarization image statistics

As it is the case with the POLSAR image, the elementary single-look (SLC) SAR image can provide complex information in each pixel, as well. This complex information can be presented in the form of amplitude and phase, but however, most commonly it is the single channel image providing intensity (I) information.

Goodman in [19] defined a fully developed speckle, characterized by the following hypotheses:

- the responses of each scatterer are independent,
- the amplitude and the phase are mutually independent,
- the amplitudes of each scatterer has the same probability density function (PDF),
- the phases are distributed uniformly.

By adopting $A_{tot}e^{j\phi_{tot}} = x+jy$, under these assumptions, both the real x and the imaginary part y of the pixel value, due to the central limit theorem, converge toward the centered Gaussian (normal) distribution:

$$\mathcal{N}(v|\mu_v = 0, \sigma_v) = \frac{1}{\sigma_v\sqrt{2\pi}} e^{\frac{v}{2\sigma_v^2}}, \quad v \in \{x, y\}, \tag{I.33}$$

with σ being the standard deviation (σ^2 - variance). The amplitude A_{tot} is distributed according to the Rayleigh distribution:

$$\mathcal{R}(A_{tot}|\sigma) = \frac{A_{tot}}{\sigma^2} e^{\frac{A_{tot}^2}{2\sigma^2}}. \tag{I.34}$$

In this case, the intensity i.e. the single-channel SAR image, expressed as $I = |A_{tot}e^{j\phi_{tot}}|^2 = x^2 + y^2$, follows the negative exponential distribution:

$$\mathcal{E}(I|\sigma) = \frac{1}{2\sigma^2} e^{-\frac{I}{2\sigma^2}}. \tag{I.35}$$

Having a multiplicative nature, speckle cannot be neutralized by increasing the intensity. Therefore, the most elementary approach in speckle reduction would be multi-looking, where on the expense of deteriorated spatial resolution, we obtain the decrease in speckle noise. Namely, we incoherently sum the intensities of a set of SLC images, by means of the operation which can be considered as a low-pass mean filtering (spatial averaging).

The amplitude of the multi-look (MLC) SAR image, obtained by summing N SLC images is distributed according to the generalized gamma distribution [20]:

$$\mathcal{G}_g(A_{tot}|\sigma, N) = \frac{2N^N}{2^N \sigma^{2N} (N-1)!} A_{tot}^{2N-1} e^{-\frac{NA_{tot}^2}{2\sigma^2}}, \tag{I.36}$$

while the intensity follows the gamma distribution:

$$\mathcal{G}(I|\sigma, N) = \frac{N^N I^{N-1}}{(N-1)! 2^N \sigma^{2N}} e^{-\frac{NI}{2\sigma^2}}. \tag{I.37}$$

The presented Rayleigh speckle model performs very well providing homogeneous nature of the considered POLSAR clutter. However, due to the amelioration of the spatial resolution, we ought to consider the clutter to be rather heterogeneous and thus, the SAR image to be textured. The texture model of the SAR image in terms of intensity (I) is given as:

$$I = \tau j, \tag{I.38}$$

with τ representing the texture variation, and j the normalized intensity ($j = \frac{i}{\sigma^2}$). Commonly, it is assumed for the texture to be a random gamma variable [21]:

$$\mathcal{G}(\tau|k, 1/k) = \frac{k^k \tau^{k-1}}{\Gamma(k)} e^{-k\tau}, \tag{I.39}$$

with k being the shape factor. Consequently, the intensity of the textured MLC SAR images, obtained by means of N looks, is distributed according to the K-distribution, using the modified Bessel function of the second kind ($K_n(.)$) [21]:

$$\mathcal{K}(I|k,\sigma,N) = \frac{2(Nk)^{(k+N)/2}}{(N-1)!\Gamma(k)} I^{\frac{(k+N)-1}{2}} K_{k-N}(2\sqrt{kNI}). \tag{I.40}$$

Analogously, the amplitude, being $A = \sqrt{I}$, follows [22]:

$$\mathcal{K}(A|k,\sigma,N) = \frac{4(Nk)^{(k+N)/2}}{(N-1)!\Gamma(k)} A^{(k+N)-1} K_{k-N}(2\sqrt{kN}A). \tag{I.41}$$

I.2.2 Polarimetric image statistics

In case of a POLSAR image, the statistical analysis gets a bit more sophisticated. Namely, we cannot stay concentrated exclusively on the amplitude or the intensity of separate channels. We ought to consider their relations, both in terms of phase and intensity, as well [21]. Therefore, the target vector of a reciprocal target **k** is supposed to follow multivariate complex Gaussian distribution [23]:

$$\mathcal{N}(\mathbf{k}|\mathbf{T}) = \frac{1}{\pi|\mathbf{T}|} e^{-\mathbf{k}^H \mathbf{T}^{-1} \mathbf{k}}. \tag{I.42}$$

Both real and imaginary part of each of the elements of **k** are assumed to have circular normal distribution [21], which was demonstrated in [24].

The coherence matrix of the multi-look POLSAR image (N looks) is estimated as a sample covariance matrix (SCM):

$$\widehat{\mathbf{T}}_m = \mathbb{E}\left[\mathbf{k}\mathbf{k}^H\right] = \frac{1}{N}\sum_{i=1}^{N} \mathbf{k}_i \mathbf{k}_i^H, \tag{I.43}$$

and it follows the complex Wishart distribution, which has a following PDF in case of non-reciprocal target:

$$\mathcal{W}(\widehat{\mathbf{T}}_m|\mathbf{T},N) = \frac{N^{3N}|\widehat{\mathbf{T}}_m|^{N-3} e^{-N\mathrm{Tr}(\mathbf{T}^{-1}\widehat{\mathbf{T}}_m)}}{K(N,3)|\mathbf{T}|^N}, \tag{I.44}$$

with Tr(.) being a trace operator and $K(N,3) = \pi^3\Gamma(N)\Gamma(N-1)\Gamma(N-2)$.

The previous formulas are equally valid for the covariance matrix (**C**), in case of considering the lexicographic target vector ($\mathbf{k}_c$) rather than the Pauli one (**k**).

The K-distribution of the intensity of textured MLC SAR image can be generalized to the POLSAR image [25]. Firstly, we rewrite Eq. I.38 in the vectorial form:

$$\mathbf{k} = \sqrt{\tau}\mathbf{z}, \tag{I.45}$$

with $\mathbf{z}$ being Gaussian multivariate random vector, and τ the texture defined by the distribution in Eq. I.39. Then, we estimate the multi-look SCM:

$$\widehat{\mathbf{T}}_m = \mathbb{E}\left[\mathbf{k}\mathbf{k}^H\right] = \frac{1}{N}\sum_{i=1}^{N} \tau_i \mathbf{z}_i \mathbf{z}_i^H. \tag{I.46}$$

Finally, we can represent the multivariate K-distribution of the textured MLC POLSAR data, or more concretely of the multi-look coherence matrix, as:

$$\mathcal{K}(\widehat{\mathbf{T}}_m|k, \mathbf{T}, N) = \frac{2|\widehat{\mathbf{T}}_m|^{N-3}(Nk)^{(k+3N)/2}}{K(N,3)|\mathbf{T}|^N\Gamma(k)} \frac{K_{k-3N}\left(2\sqrt{kN\mathrm{Tr}(\mathbf{T}^{-1}\widehat{\mathbf{T}}_m)}\right)}{\mathrm{Tr}(\mathbf{T}^{-1}\widehat{\mathbf{T}}_m)^{-(k-3N)/2}}, \tag{I.47}$$

where $K_n(.)$ and $K(N,3)$ have the same meaning as in the Eq. I.40 and Eq. I.44, respectively.

I.2.2.1 Spherically Invariant Random Vector

Spherically Invariant Random Process (SIRP) is the univariate stochastic model. Several special cases of univariate stochastic processes (K-compound, Weibull, etc.) have been extensively studied over the years (for example in coastal radar applications) before being reunited under the common umbrella of SIRP [26].

Spherically Invariant Random Vector (SIRV) is the multivariate generalization of SIRP. It is a multiplicative model:

$$\mathbf{y} = \sqrt{k}\mathbf{x}, \tag{I.48}$$

where $\mathbf{x}$ stands for multivariate Gaussian random vector, while random variable k can be distributed according to several distributions: Gamma, Inverse Gamma, Fisher, and even as a Dirac pulse. The random vector $\mathbf{y}$ is therefore distributed according to, respectively: K-distribution [27], G-distribution, [28], KummerU distribution [29] and finally, multivariate Gaussian distribution.

The covariance matrix of the Gaussian random vector is defined as a normalized coherency (covariance) matrix [30]:

$$\mathbf{M} = \mathbb{E}[\mathbf{x}\mathbf{x}^H] \tag{I.49}$$

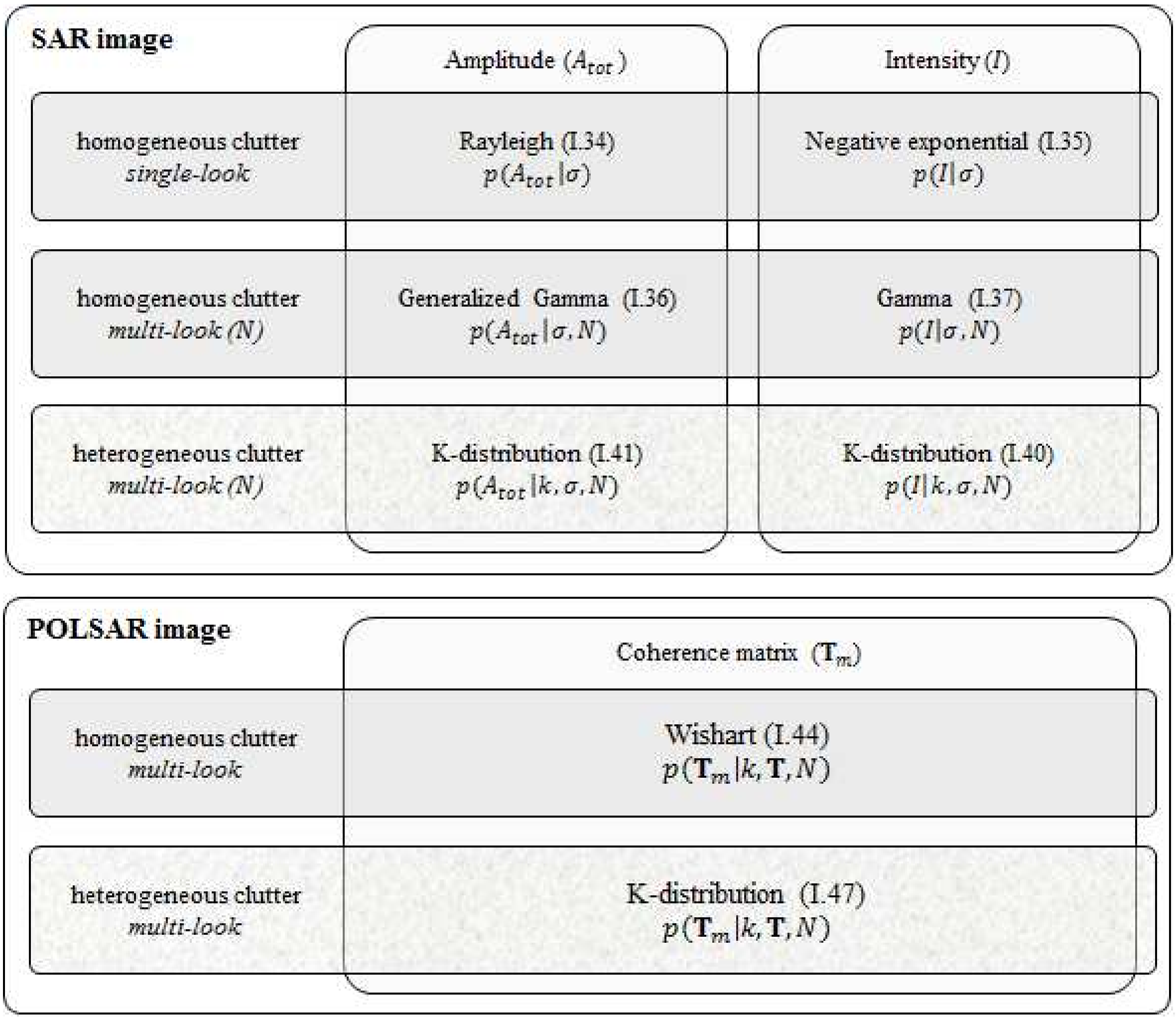

Figure I.6: Overview of presented SAR/POLSAR image statistical models.

The big advantage of SIRV in terms of generality with respect to the texture statistics [31], assures its privileged place in this thesis when dealing with the POLSAR image statistical modelling.

I.3 Blind Source Separation

Blind Source Separation (BSS) can be defined as a family of methods which aim to recover source signals from their mixture, without having any *a priori* knowledge of the mixing process [32]. Formally, BSS techniques use a set of observation vectors ($\mathbf{x}$) to retrieve the sources vector ($\mathbf{s}$) and the mixing matrix ($\mathbf{A}$), which gives the share of the sources in the observed process:

$$\mathbf{x}(t) = \begin{bmatrix} x_1(t) \\ x_2(t) \\ \vdots \\ x_n(t) \end{bmatrix} = \mathbf{As}(t) = \begin{bmatrix} A_{11} & A_{12} & \cdots & A_{1n} \\ A_{21} & A_{22} & \cdots & A_{2n} \\ \vdots & \vdots & \ddots & \vdots \\ A_{n1} & A_{n2} & \cdots & A_{nn} \end{bmatrix} \begin{bmatrix} s_1(t) \\ s_2(t) \\ \vdots \\ s_n(t) \end{bmatrix}, \tag{I.50}$$

where variable t can be related to time, space etc.

However, the criterion for separation varies upon the method being used. The pivotal classification is related to a degree of separation, in terms of statistics. That is, the sources are expected to be either mutually uncorrelated, or mutually independent. The most representative method of the former criterion would be Principal Component Analysis (PCA), introduced in this section. The latter criterion is represented by Independent Component Analysis (ICA). Given the essential role they have in this thesis, ICA methods are presented in more details.

I.3.1 Principal Component Analysis

The Principal Component Analysis, being a wide spread tool in data analysis [33], found its application in signal and image processing, as well.

The method itself is entirely based on the eigenvector decomposition of the sample covariance matrix of the observation data ($\mathbf{x}_{[n\times 1]} \in \mathbf{X}_{[n\times N]}$). Namely, the principal components (PC) can be represented as rows of matrix $\mathbf{Y}_{[n\times N]}$, derived as:

$$\mathbf{Y} = \mathbf{E}^T\mathbf{X}_c, \tag{I.51}$$

with the matrix $\mathbf{E}$ having as columns the eigenvectors of the covariance matrix, estimated using N samples of the observation data (centered with respect to the mean value μ - subscript c):

$$\mathbf{C} = \mathbb{E}[\mathbf{x}_c\mathbf{x}_c^T] = \frac{1}{N}\sum_{i=1}^{N}\mathbf{x}_{ci}\mathbf{x}_{ci}^T = \frac{1}{N}(\mathbf{X} - \mu_x)(\mathbf{X} - \mu_x)^T. \tag{I.52}$$

The same formalism can be applied in case of complex observations, by changing transposing (superscript T) with conjugate-transpose (H).

The derived principal components are mutually orthogonal and can be regarded as uncorrelated. In Fig. I.7 we demonstrate the derivation of PC, in the most simple case of two-dimensional data ($n = 2$). The notations of the axes are not random, but however imply that PC are in fact sources in the equation C.2 ($\mathbf{s} = \mathbf{y}$). Therefore, the columns of the mixing matrix are the eigenvectors of observation data's sample covariance matrix ($\mathbf{A} = \mathbf{E}$).

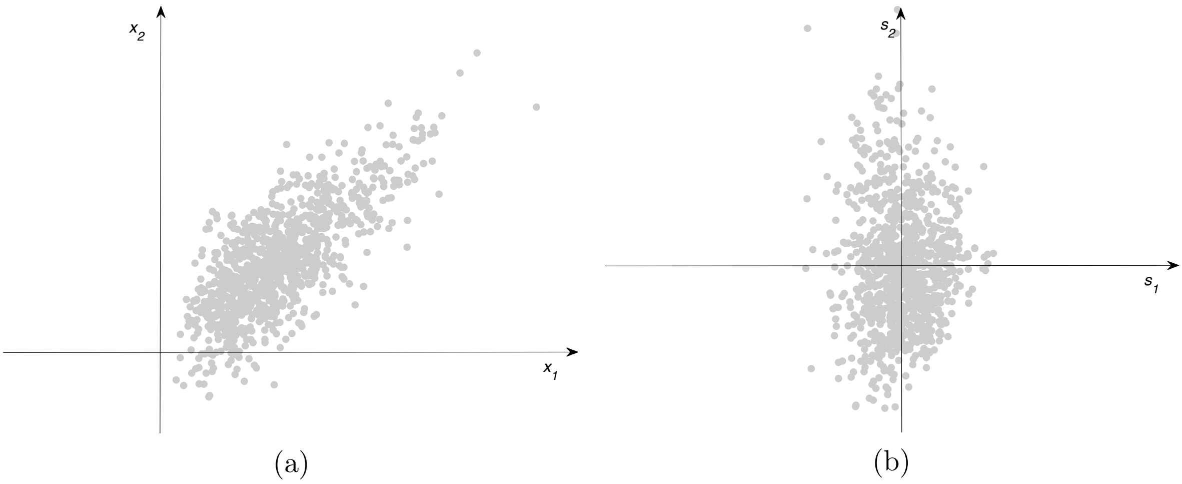

(a) (b)

Figure I.7: PCA: (a) observation data ($\mathbf{x}$), (b) uncorrelated sources ($\mathbf{s}$).

Effectively, as demonstrated, the eigenvector decomposition of the observations' covariance matrix, is the very simple, but efficient mean of sources separation.

I.3.2 Independent Component Analysis

In terms of statistics, uncorrelation does not necessarily imply independence. Namely, we say that two random variables are uncorrelated if their covariance equals zero:

$$c = \mathbb{E}[(s_1 - \mu_{s_1})(s_2 - \mu_{s_2})^T] = \mathbb{E}[s_1 s_2] - \mu_{s_1} - \mu_{s_2} = 0. \tag{I.53}$$

This way, we can claim that:

$$\mathbb{E}[s_1 s_2] = \mathbb{E}[s_1]\mathbb{E}[s_2] = \mu_{s_1}\mu_{s_2}, \tag{I.54}$$

which is not necessarily reflected on the relation of their PDFs (p):

$$p(s_1, s_2) = p(s_1)p(s_2), \tag{I.55}$$

being simultaneously the condition of statistical independence. Actually, the condition in Eq. I.54 needs to be satisfied for higher statistical moments, not just the second one (covariance) in order Eq. I.55 to be true. The exception are the Gaussian variables, where Eq. I.54 implies Eq. I.55, given that the second moment is the highest non-zero one.

Therefore, the common point for all ICA methods would be the estimation of independent components (IC), by relaying on the probability moments higher than two, where the estimation of IC in fact means, the estimation of the mixing matrix $\mathbf{A}$.

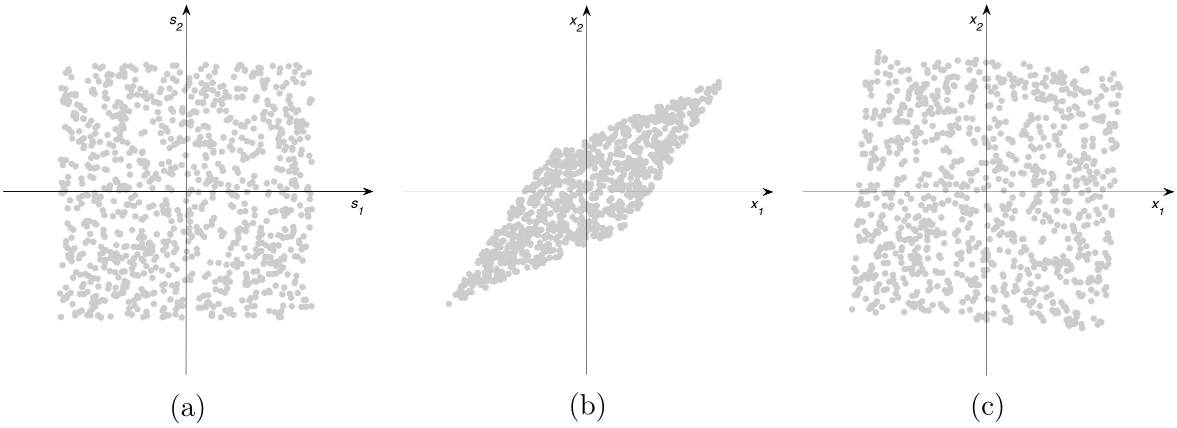

Figure I.8: ICA: (a) simulated uniformly distributed independent sources ($\mathbf{s}''$), (b) mixture ($\mathbf{x}$), (c) whitened mixture ($\tilde{\mathbf{x}}$).

Before proceeding with the detailed elaboration, by means of slightly complicated mathematical apparatus, we present a brief geometrical interpretation of the simplified two-dimensional scenario, given in Fig. I.8 [34]. At the same time, we present the two most important pre-processing steps: centering and whitening.

Namely, let us presume having two independent uniformly distributed sources $\mathbf{s}$, with a joint scatter plot as the one in Fig. I.8a. Multiplying them with a random, non-orthogonal mixing matrix $\mathbf{A}$, results in a mixture, presented in Fig. I.8b. We can consider this mixture to be the set of observation data $\mathbf{x}$, making thus the aim of the algorithm, simply, to transform the data from the space given in Fig. I.8b to the one given in Fig. I.8a. The first step would be centering i.e. subtracting the mean from each of the observations' channels, the operation which places the mixture in the centre of the "$\mathbf{x}$ space". Second, a bit more complex step, would be whitening i.e. the decorrelation of the observations' channels. This is achieved by multiplying the data by the whitening matrix $\mathbf{V}$:

$$\tilde{\mathbf{x}} = \mathbf{V}\mathbf{x} = \mathbf{E}\mathbf{D_e}^{-1/2}\mathbf{E}^T\mathbf{x}, \tag{I.56}$$

where the matrix $\mathbf{E}$ correspond to the one used in PCA (Eq. I.51), and the matrix $\mathbf{D}_e$ is the diagonal matrix of eigenvalues. This operation gives us the joint scatter plot, illustrated in the Fig. I.8c. As it can be intuitively inferred, the only remaining operation is the rotation. This operation is, in fact, ICA. In other words, the rotation we need is contained in the demixing matrix $\mathbf{D}$ (inverse of the mixing matrix - $\tilde{\mathbf{D}} = \tilde{\mathbf{A}}^{-1}$), and it is to be deduced from the higher order statistics. As we will demonstrate in this section, there are several means to achieve this, with most of them being based either on the iterative algorithms, or on the tensorial calculus.

The very important restriction of ICA methods, would be their unfitness in case of Gaussian observations. This constraint can be easily elucidated using the same intuitive geometrical approach. Namely, as it is seen in Fig. I.9, in case of a two-dimensional joint PDF space, Gaus-

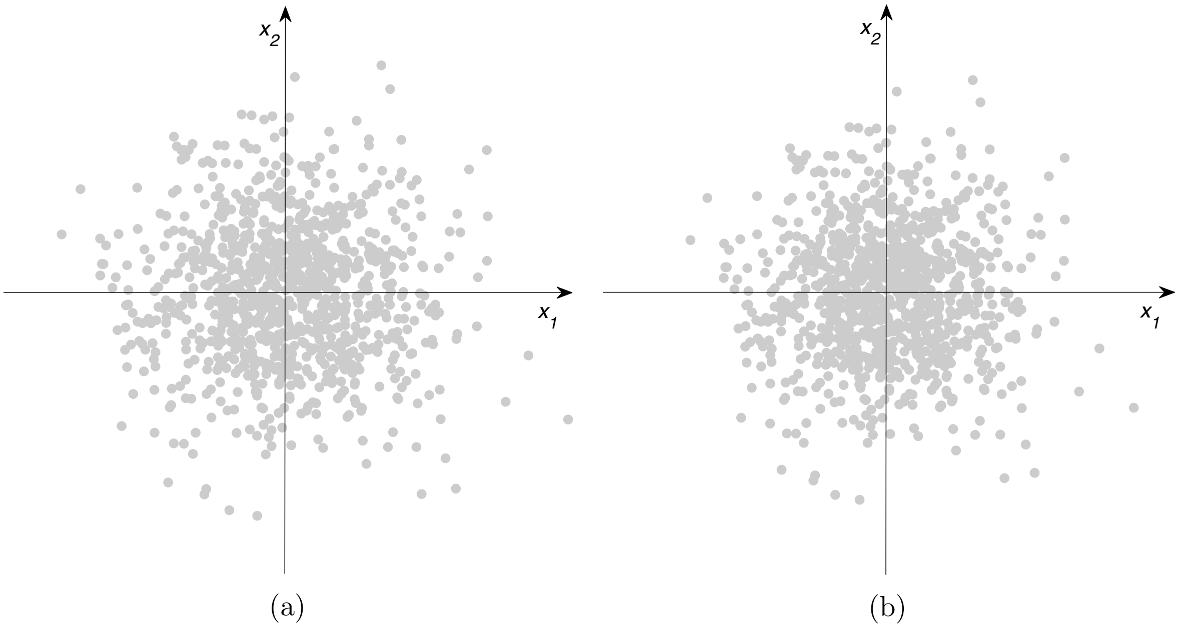

(a) (b)

Figure I.9: ICA: (a) Gaussian observation data ($\mathbf{x}$), (b) whitened Gaussian observation data ($\tilde{\mathbf{x}}$).

sian observations form a circle, the fact which does not change after centering and whitening. Therefore, estimating the appropriate rotation appears to be impossible.

Finally, in order to elaborate most representative, both iterative and tensorial, ICA methods, which are employed in this thesis, we ought to start from the common point - exploiting higher order statistics [35].

The statistical order k of a random variable is characterized by the k^{th} moment μ_k and the k^{th} cumulant κ_k, both derived from the characteristic function $\phi(\omega)$ of a random variable:

$$\begin{aligned} \sum_{k=0}^{\infty} \mu_k \frac{(j\omega)^k}{k!} &= = \phi(\omega) = \int_{-\infty}^{\infty} e^{j\omega s} p_s(s) ds \\ \sum_{k=0}^{\infty} \kappa_k \frac{(j\omega)^k}{k!} &= = \ln[\phi(\omega)] = \ln\left[\int_{-\infty}^{\infty} e^{j\omega s} p_s(s) ds\right]. \end{aligned} \tag{I.57}$$

Equivalent for the random vector, where we are particularly interested in the cumulant (cum_k), would be:

$$\sum_{k=0}^{\infty} \mathrm{cum}_k \frac{(j\omega)^k}{k!} = \ln\left[\int_{-\infty}^{\infty} e^{j\omega \mathbf{x}} p_{\mathbf{x}}(\mathbf{x}) d\mathbf{x}\right]. \tag{I.58}$$

On one side, the most widely spread iterative method, presented in the following subsection, is focused on the statistical properties of the source as a random variable. Therefore, in this case, the higher orders are exploited by means of parameters derived in Eq. I.58. On the other side, the tensorial methods are rather based on the higher order cumulants of the observation data. Them being a set of random vectors, this approach is rather relaying on the formalism emerging from Eq. I.58.

I.3.2.1 FastICA

The FastICA algorithm is a fast converging algorithm based on a fixed-point iteration scheme. Principally, the concept of FastICA is derived from the Central Limit Theorem. It states that the distribution of the sum of two independent random variables will always be closer to Gaussian than the original variables. Therefore, the independence of the components is ensured by maximizing the non-Gaussianity of the sources [36].

There are several criteria of Gaussianity measure (f_{ng}) and therefore several approaches, used in the FastICA algorithm:

- The **kurtosis** criterion: Being defined in its excess (normalized) form as the ratio of 4^{th} and 2^{nd} order cumulants, the kurtosis of a Gaussian variable equals zero:

  $$\text{kurt}(s) = \frac{\kappa_4}{\kappa_2} = \frac{\mu_4 - 3\mu_2^2}{\mu_2^2} \tag{I.59}$$

  Therefore by maximizing the kurtosis of each of the sources, we maximize as well their independence with respect to the other sources.

- The **negentropy** criterion: The Gaussian variable has the largest entropy among all the random variable with the same variance. The approximated negentropy [37], a quantity being different from zero in case of non-Gaussian variable (ν), is defined using any non-quadratic function $G(x)$ [34]:

  $$J(s) \propto (\mathbb{E}[G(s)] - \mathbb{E}[G(\nu)])^2 \tag{I.60}$$

  Using FastICA routine [34], we are ensuring the sources independence by maximizing the negentropy.

- **Mutual Information (MI)** is a natural measure of the dependence between random variables:

  $$I(s_1, s_2, ...s_n) = \sum_{i=1}^{n} H(s_i) - H(\mathbf{s}) = \int_{-\infty}^{\infty} \cdots \int_{-\infty}^{\infty} f(\mathbf{s}) \log \frac{f(\mathbf{s})}{f(s_1)f(s_2)\dots f(s_n)} d\mathbf{s} \tag{I.61}$$

  with $H(\mathbf{s})$ being the differential entropy derived from the joint PDF of the sources vector as: $-\int_{-\infty}^{\infty} \cdots \int_{-\infty}^{\infty} f(\mathbf{s}) \log f(\mathbf{s}) d\mathbf{s}$.

The aim in this case is to achieve zero value, which indicates independence between the sources.

- **Maximum Likelihood Estimation (MLE)** [38]: The log-likelihood function in the noise-free ICA model is given as [39]:

$$L = \sum_{t=1}^{T} \sum_{i=1}^{n} \log f_i(\mathbf{w}_i^T \tilde{\mathbf{x}}(t)) + T \log |\det \mathbf{W}| \tag{I.62}$$

After estimating the probability density function f_i of the sources $(s_1 ... s_n)$, the discrimination between independent sources is achieved through maximizing the log-likelihood function.

The columns of the mixing (de-mixing) matrix are estimated either separately or simultaneously by iteratively searching the maximum of non-Gaussianity of the source using centered and whitened observation data:

$$\max_{\mathbf{w}_i} J_{ng}(\mathbf{w}_i) = \max_{\mathbf{w}_i} \mathbb{E}\left[f_{ng}(\mathbf{w}_i^T \tilde{\mathbf{x}})\right], \tag{I.63}$$

with $\mathbf{w}_i$ being the column of the estimated mixing matrix, converging to the column of $\tilde{\mathbf{A}}$.

In case of complex observation data, the criteria of non-Gaussianity are defined analogously but however slightly differently, as it will be discussed in the Chapter III.

I.3.2.2 Tensorial methods

The most intuitive way to introduce tensor would be representing a matrix as a 2^{nd} order tensor. Therefore, a covariance matrix represents a second order cumulant tensor, composed of 2^{nd} order cumulants cum_2, while a 4^{th} order cumulant tensor ($\mathbf{F}$) consists of 4^{th} order cumulants cum_4. Presented tensorial decomposition could be regarded as the 4^{th} order algebraic equivalent of the 2^{nd} order eigenvector decomposition.

Forth-Order Blind Identification (FOBI) is one of the simplest tensorial ICA methods [40]. The independent backscattering mechanisms are derived as eigenvectors of the kurtosis matrix, estimated using a whitened set of observation vectors ($\tilde{\mathbf{x}}$), as the fourth order cumulant tensor of the identity matrix $\mathbf{I}$:

$$\mathcal{K}_{\mathbf{I}}(\tilde{\mathbf{x}}) = \mathbf{F}(\mathbf{I}) = \mathbb{E}\left[(\tilde{\mathbf{x}}^T \mathbf{I} \tilde{\mathbf{x}}) \tilde{\mathbf{x}} \tilde{\mathbf{x}}^T\right] - 2\mathbf{I} - \text{tr}(\mathbf{I})\mathbf{I} = \mathbb{E}\left[|\tilde{\mathbf{x}}|^2 \tilde{\mathbf{x}} \tilde{\mathbf{x}}^T\right] - (n+2)\mathbf{I}. \tag{I.64}$$

The most notable drawback of this method would be the condition that all the sources must have quite distant kurtosis values, implicating the failure in case of having several mechanisms characterized with the same distribution.

Joint Approximate Diagonalization of Eigenmatrices (JADE) is a generalization of FOBI [41]. Replacing the identity matrix with a set of tuning matrices (eigenmatrices of the cumulant tensor:$\{\mathbf{M_1}, ...\mathbf{M_p}\}$) results in a set of matrices: $\{\mathcal{K}_{\mathbf{M}_1}, ...\mathcal{K}_{\mathbf{M}_p}\}$. The whitened de-mixing matrix $\tilde{\mathbf{D}}$ is estimated by jointly diagonalizing these matrices, which reduces to the maximization problem:

$$\max_{\tilde{\mathbf{D}}} \mathcal{J}(\tilde{\mathbf{D}}) = \max_{\tilde{\mathbf{D}}} \sum_{i=1}^{p} ||\text{diag}\left(\tilde{\mathbf{D}}\mathcal{K}_{\mathbf{M}_i}\tilde{\mathbf{D}}^H\right)||_2^2 \tag{I.65}$$

where $||\text{diag}(.)||^2$ is the squared ℓ_2 norm of the diagonal. Given that the maximization of the diagonal elements is equivalent to the minimization of the off-diagonal ones, the resulting de-mixing matrix $\tilde{\mathbf{D}}$ jointly diagonalize the set of cumulants. This algorithm overcomes the mentioned drawback of FOBI, but stays limited to low-dimensional problems.

Second-Order Blind Identification (SOBI) is, sort of, infiltrated in this section, given that it does not explicitly rely on 4^{th} order statistics. It would be actually the counterpart of JADE in the 2^{nd} order statistics.

In this case, the observation data are divided into several series ($\tilde{\mathbf{X}}_i \in \tilde{\mathbf{X}}$) and each of them is represented by one covariance matrix ($\mathbf{C}_i$).

The mixing matrix is estimated by jointly diagonalizing a set of these sample covariance matrices of whitened observations [42]:

$$\max_{\tilde{\mathbf{A}}} \mathcal{S}(\tilde{\mathbf{A}}) = \max_{\tilde{\mathbf{A}}} \sum_{i=1}^{p} ||\text{diag}\left(\tilde{\mathbf{A}}\mathbf{C}_i\tilde{\mathbf{A}}^T\right)||_2^2 \tag{I.66}$$

For all presented tensorial methods, the provided formalism is entirely appropriate in case of complex observations, after changing the superscript T with H, as it was the case with PCA.

Chapter II

Statistical assessment of high-resolution POLSAR images

In this chapter we propose a methodological framework for the statistical evaluation of the particularities of high-resolution data. It assumes the analysis of three important statistical parameters: circularity, sphericity and spherical symmetry. All three of them are considered in the context of the SIRV statistical model. The conclusions drawn after applying this framework on the POLSAR datasets, are additionally reinforced by implicating high-resolution multi-pass InSAR data set, as well.

Firstly, we introduce classical circularity and sphericity tests along with their extensions to the SIRV stochastic model. Then, we present in detail the elaborated method of quantitative assessment of the conformity of the SIRV model, based on testing spherical symmetry. Finally, the results obtained using the proposed robust tests with synthetic, POLSAR and multi-pass InSAR datasets, are presented and appropriately analysed.

II.1 Introduction

As already implied in the preface of this thesis, we could ascertain that there is an ongoing debate in the SAR remote sensing community, which concerns the necessity to alter from the conventional multivariate Gaussian model, introduced in the previous chapter, in case of high and very high resolution POLSAR data. Namely, as indicated in Section I.2, the heterogeneous POLSAR clutter, emerging from the amelioration in spatial resolution, implies textured POLSAR images, characterized by the K-distribution. Furthermore, this statistical model has been generalized by rather suggesting the SIRV model, a family of distributions, comprising the K-distribution, as well. This has been done for POLSAR data [30, 29, 43, 44], but also for the InSAR data, being a multi-dimensional SAR dataset, as well [31, 45, 46].

This chapter has an aim to answer the first out of two questions portrayed in the preface as the driving force of this thesis. In fact, at this point, the form of the question is a bit more concise:

- Is the SIRV model appropriate for modelling POLSAR and other multi-dimensional SAR datasets (InSAR)?

This question motivated us to propose a general framework which allows a quantitative evaluation of the particularities of new generation datasets. More concretely, it is a framework which allows a quantitative evaluation of fitting of SIRV stochastic models, with respect to a given multi-channel SAR dataset. The illustrated multivariate high-resolution SAR datasets show that in this case, it can be worth challenging two specific and very important stochastic properties: the circularity and the sphericity.

Circularity concerns the statistics of a complex element of a target vector i.e. the relation of its real and imaginary part. Being often assumed in the case of Gaussian multivariate model, this parameter has been tested by extending the Gaussian circularity test to the SIRV one. The results indicate that in case of very-high resolution POLSAR dataset quite a bit non-circular target vectors occur, the phenomena which could be associated to the POLSAR data calibration performances. Sphericity rather concerns the relation between different target vector elements and, as it is demonstrated, complements the circularity test. However, its role becomes crucial when the introduced concept of spherical symmetry is considered. The last one, under certain constraints, serves to assess the appropriateness of the SIRV model in case of multivariate SAR datasets. It appears that the SIRV model fails to properly characterise target vectors in the regions with more explicit deterministic scattering.

The derived test are presented for the m-dimensional case. In case of POLSAR data, the observed sample is polarimetric target vector, (Eq I.4 or Eq. I.20), and therefore $m = 3$. In order to generalize the derived conclusion with respect to the type of multivariate SAR data, we include a multi-pass differential InSAR dataset, for which in the considered case, $m = 3$, as well.

II.1.1 SAR interferometry

Before proceeding to the very topic of this chapter, we will very briefly introduce the concept of SAR interferometry, in order to facilitate the interpretation of the results, reinforced using InSAR data.

SAR interferometry assumes exploiting the phase difference between m SAR images, acquired either from m different positions (across-track), or at m distinct time moments (along-track). In the case of conventional along-track two-pass InSAR system [47], we have two channels ($m = 2$). By denoting with $c = \rho \exp(j\phi)$ the complex correlation coefficient between the EM fields, the target relative displacement d_{12} between the two acquisitions can be retrieved from the exact knowledge of SAR antenna phase center positions, terrain height, acquisition geometry, and an estimate of the differential interferometric phase ϕ_{12}. ρ_{12} is called interferometric coherence and it describes both the local phase stability and the amplitude decorrelation of the InSAR pair. The phase information ϕ_{12} allows phase differences (interferograms) to be computed in order to measure topography or target displacements between repeated pass acquisitions. In the general case, the two-dimensional interferometric target vector $\mathbf{k}$ will contain information about the relative displacements between each combination of two passes.

The correlation coefficient (c) is derived from the covariance matrix, whose estimation strongly depends on the employed statistical model. This fact motivated us to reinforce the analysis of the considered statistical parameters by implicating InSAR data, as well.

II.2 Circularity and sphericity

In the context of multivariate SAR data, we introduce two stochastic properties, often taken as granted in case of a Gaussian model: circularity and sphericity. After adequately defining the properties, we present the classical tests (Gaussian model) and propose the ones extended to the SIRV stochastic model.

II.2.1 Circularity

A complex-valued random variable ($s = x + iy$) is circular if the joint PDF of real and imaginary part exhibits circular symmetry. This kind of joint PDF remains invariant to multiplication with complex numbers on the unity circle, which implies that the real random vector $\mathbf{s} = (x, y)^T$ must be spherically symmetric with respect to the origin [48]. In other words, circularly symmetric PDF can be written as:

$$p_s(s) = g_s(|s|^2) \tag{II.1}$$

with g being a density generator, one dimensional representation of probabilities of absolute values of a complex number [49].

Circular random vector would be the one having real and imaginary parts independent. When extending the concept of circularity to complex random vectors, we ought to rely on the second order properties [50]. Therefore, we introduce the complex extended target vector:

$$\gimel = [\mathbf{k}^T, \mathbf{k}^H]^T = \begin{bmatrix} x_1 + iy_1 & x_2 + iy_2 & x_3 + iy_3 & x_1 - iy_1 & x_2 - iy_2 & x_3 - iy_3 \end{bmatrix}^T. \qquad \text{(II.2)}$$

Starting from $\gimel$, the second-order statistical properties of the complex target vector $\mathbf{k} = \mathbf{x} + i\mathbf{y}$ can be analysed using the extended covariance matrix:

$$\mathbf{R} = \mathbb{E}[\gimel\gimel^H] = \begin{bmatrix} \mathbf{C} & \mathbf{P} \\ \mathbf{P}^* & \mathbf{C}^* \end{bmatrix}, \qquad \text{(II.3)}$$

where $\mathbf{C} = \mathbb{E}[\mathbf{k}\mathbf{k}^H]$ is already defined covariance matrix and $\mathbf{P} = \mathbb{E}[\mathbf{k}\mathbf{k}^T]$ is the complex symmetric pseudo-covariance matrix of the target vector $\mathbf{k}$ [51]. The former is also known as "relation matrix" or "complementary covariance matrix".

In [52], Schreier et al. proposed the circularity Generalized Likelihood Ratio Test (GLRT) by employing the previously defined extended covariance matrix. The considered hypotheses are:

$$\begin{cases} H_0 : P = 0, & \mathbf{k} \text{ is circular,} \\ H_1 : P \neq 0, & \mathbf{k} \text{ is not circular} \end{cases}. \qquad \text{(II.4)}$$

This circularity test is checking for the block-diagonality of the extended covariance matrix with respect to the covariance and pseudo-covariance matrix. We will firstly introduce this test for the Gaussian multivariate process and further on, its extension to SIRV.

Before proceeding, we ought to mention that the term covariance matrix and coherence matrix are to be considered as synonyms in this Chapter, given that the presented statistical assessment appears to be invariant with respect to the target vector representation (lexicographic or Pauli).

II.2.1.1 Gaussian multivariate processes

The PDF of a zero-mean complex circular Gaussian target vector $\mathbf{k}$ (Eq. I.42) can be generalized with respect to its associated extended target vector $\gimel$ as [53, 50]:

$$\mathcal{N}(\mathbf{k}|\mathbf{R}) = \pi^{-m}(\det\mathbf{R})^{-\frac{1}{2}} \mathrm{e}^{-\frac{\gimel^H \mathbf{R}^{-1} \gimel}{2}}. \qquad \text{(II.5)}$$

The maximum-likelihood (ML) estimator of the extended covariance matrix is the Sample Extended Covariance Matrix (SECM) obtained by replacing the statistical mean from Eq. II.3 with the spatial average:

$$\widehat{\mathbf{R}}_{SECM} = \frac{1}{N}\sum_{i=1}^{N} \gimel_i \gimel_i^H = \begin{bmatrix} \widehat{\mathbf{C}}_{SCM} & \widehat{\mathbf{P}}_{SPM} \\ \widehat{\mathbf{P}}^*_{SPM} & \widehat{\mathbf{C}}^*_{SCM} \end{bmatrix}, \tag{II.6}$$

where N is the number of samples, $\gimel_i$ is the complex extended target vector of the i^{th} sample, $\mathbf{C}_{SCM}$ and $\mathbf{P}_{SPM}$ are the Sample Covariance Matrix (SCM) (Eq. I.46) and the Sample Pseudo-covariance Matrix (SPM) estimators, respectively. Under the constraint $\mathbf{P} = [\mathbf{0}]_3$ imposed by H_0, the ML estimator is [52]:

$$\widehat{\mathbf{R}}_{SECM_0} = \begin{bmatrix} \widehat{\mathbf{C}}_{SCM} & \mathbf{0}_m \\ \mathbf{0}^*_m & \widehat{\mathbf{C}}^*_{SCM} \end{bmatrix}. \tag{II.7}$$

By introducing Eqs. II.6 and II.7 into the Likelihood Ratio Test (LRT) associated to Eq. II.4, Schreier et al. derived the GLRT for N independent and identically distributed observed samples [52]:

$$\Lambda(\mathbf{k}_1, ...\mathbf{k}_N) = \frac{\det(\widehat{\mathbf{R}}_{SECM})}{(\det(\widehat{\mathbf{C}}_{SCM}))^2} \underset{H_1}{\overset{H_0}{\gtrless}} \lambda. \tag{II.8}$$

As it is demonstrated in the *Theorem 2* in [54], the asymptotic distribution of the decision statistics under the null hypothesis is chi-squared ($H_0 : -N \ln\Lambda \to \chi^2_{m(m+1)}$). Schreier et al. also demonstrated that the GLRT from Eq. II.8 is invariant with respect to invertible linear transforms.

II.2.1.2 Spherically Invariant Random Vectors

The GLRT makes use of the Gaussian assumption when inserting $\mathbf{C}_{SCM}$ and $\mathbf{P}_{SPM}$ estimators in the LRT. Therefore, it ought to be modified before being applied on SIRV data.

By directly applying Tyler's *Corollary 1* from [55], Ollila and Koivunen demonstrated in [54] that the GLRT for SIRV can be derived by dividing the logarithm of the GLRT statistics, given in Eq. II.8, with the correction factor γ, estimated as:

$$\gamma = \sum_{i=1}^{m} \frac{\frac{\mathbb{E}[|k_i|^4]}{\mathbb{E}[|k_i|^2]^2}}{r_i(k_i)^2 + 2}. \tag{II.9}$$

with respect to the circularity coefficients, representing the "amount of circularity" or target vector's elements:

$$r_i(k_i) = \frac{|\mathbb{E}[k_i^2]|}{\mathbb{E}[|k_i|^2]} \tag{II.10}$$

Following the same procedure as Ollila and Koivunen, N is replaced by $(N-m)$ from the Box approximation of the GLRT [56]. Finally, according to Tyler's *Corollary 1*, the decision statistic under the null hypothesis is also chi-squared ($H_0 : -(N-m)\frac{\ln\Lambda}{\hat{\gamma}} \to \chi^2_{m(m+1)}$).

II.2.2 Sphericity

The sphericity test presented here complements the previously introduced circularity test: the test for circularity checks that there is no correlation between the real and the imaginary part of the complex random vector, while the sphericity test checks for equal independence between the target vector components (independence and homoscedasticity). Hence, circularity is a requirement before testing for sphericity, as $\mathbf{k}$ and $\mathbf{k}^*$ cannot be independent otherwise.

The sphericity GLRT was introduced by Mauchly for real-valued m-dimensional Gaussian random processes [57]. If and only if the random process is circular, it can be directly extended to complex-valued random processes also. The hypotheses are:

$$\begin{cases} H_0 : \mathbf{C} = \varsigma \mathbf{I}_m, & \mathbf{k} \text{ is spherical,} \\ H_1 : \mathbf{C} \neq \varsigma \mathbf{I}_m, & \mathbf{k} \text{ is not spherical} \end{cases}, \tag{II.11}$$

where ς is an unknown variable.

For the sake of simplicity and without loss of generality, the test is build such that the normalized covariance matrix, defined in Eq. I.49, $\mathbf{M} = \mathbf{I}_m$. As a consequence, the derived sphericity test must be invariant to linear transforms, also.

Given a set of N independent and identically distributed observed target vectors, the Mauchly's sphericity LRT is:

$$\Lambda_s(\mathbf{k}_1, ...\mathbf{k}_N) = m\frac{(\det \mathbf{M})^{\frac{1}{m}}}{\operatorname{tr} \mathbf{M}} \underset{H_0}{\overset{H_1}{\gtrless}} \lambda_s. \tag{II.12}$$

In [58], Λ_s is reported to be invariant with respect to scale and invertible linear transforms (see Chapter 10.7 on page 431):

$$\Lambda_s(\mathbf{k}_1, ...\mathbf{k}_N) = \Lambda_s(\mathbf{V}\mathbf{k}_1, ...\mathbf{V}\mathbf{k}_N), \tag{II.13}$$

with $\mathbf{V}\mathbf{M}\mathbf{V}^H = \mathbf{I}_m$, where $\mathbf{V}$ does not necessarily represent the whitening transform introduced in Eq. I.56.

A SIRV exhibiting sphericity is a particular case of a SIRV with equal variances of the differences between all combinations of target vector components.

The sphericity property appears to be particularly important in case of conventional multi-pass SAR interferometry.

II.2.2.1 Gaussian random processes

When replacing the covariance matrix by the SCM (ML estimate under Gaussian assumption), the GLRT is obtained as:

$$\Lambda_s(\mathbf{k}_1, ...\mathbf{k}_N) = m\frac{(\det \widehat{\mathbf{M}}_{SCM})^{\frac{1}{m}}}{\operatorname{tr} \widehat{\mathbf{M}}_{SCM}} \underset{H_0}{\overset{H_1}{\gtrless}} \lambda_s. \tag{II.14}$$

Asymptotically, $H_0\ : -N \ln \Lambda_s \rightarrow \chi^2_{(m+2)(m-1)}$ [57, 59].

II.2.2.2 Spherically Invariant Random Vectors

Following Muirhead and Waternaux original studies on the robustness of the GLRT from Eq. II.12 when sampling from a SIRV [59], Tyler proposed two different robust approximated GLRTs for sphericity [60, 55].

The first method (*Corollary 1* from [55]) is derived using the same reasoning as in the case of circularity. However, this approximated GLRT appeared to be inefficient for moderate departures from Gaussianity.

In this chapter, we adopt the second method for constructing the approximated GLRT for sphericity (*Corollary 4* from [55]):

$$_{a}\Lambda_s(\mathbf{k}_1, ...\mathbf{k}_N) = (\det \widehat{\mathbf{M}}_{FP})^{\frac{1}{m}} \underset{H_0}{<} \lambda_s, \tag{II.15}$$

where $\widehat{\mathbf{M}}_{FP}$ is the iterative Fixed-Point covariance matrix estimator (already employed with multivariate SAR data in [30]):

$$\widehat{\mathbf{M}}_{FP} = \frac{m}{N}\sum_{i=1}^{N} \frac{\mathbf{k}_i\mathbf{k}_i^H}{\mathbf{k}_i^H \widehat{\mathbf{M}}_{FP}^{-1}\mathbf{k}_i}. \tag{II.16}$$

When originally introducing this estimator, Tyler showed in [61] that $\mathbf{M}_{FP}$ is an affine-invariant covariance matrix M-estimator [62]. It has been demonstrated by Tyler that the Fixed-Point estimator is an Approximate Maximum Likelihood (AML) estimator for SIRVs

[63]. Hence, all conditions required to apply *Corollary 4* from [55] are now fulfilled and H_0 : $-N\frac{m}{m+1}\ln {}_a\Lambda_s \to \chi^2_{(m+2)(m-1)}$ is the distribution. Due to the *Theorem V.4* in [64], N is replaced by $N\frac{m}{m+1}$.

II.3 Spherical symmetry

The concept of spherical symmetry, being an essential part of this section, is used as a mean for assessing the suitability of SIRV model in multivariate SAR data modelling [65].

Before introducing this concept, we ought to define a real derivative of the complex target vector $\mathbf{k}$. Let us presume that $\boldsymbol{\zeta} = [\mathbf{x}^T, \mathbf{y}^T]^T$ is that augmented $m \times 1$ real random vector, where $\mathbf{x}$ and $\mathbf{y}$ are its real and imaginary parts of $\mathbf{k}$, respectively.

In order not to alter too much from the formalism introduced in circularity analysis, we define the augmented real target vector as a function of the complex extended random vector ($\gimel$) using the following transform [53, 50]:

$$\boldsymbol{\zeta} = \frac{1}{2}\begin{bmatrix} \mathbf{I}_m & \mathbf{I}_m \\ -j\mathbf{I}_m & j\mathbf{I}_m \end{bmatrix} \gimel = \begin{bmatrix} x_1 & x_2 & x_3 & y_1 & y_2 & y_3 \end{bmatrix}^T . \tag{II.17}$$

According to Vershik's definition [66], complex vector $\mathbf{z}$ is spherically invariant if and only if the characteristic function of the augmented random vector $\boldsymbol{\zeta}$ can be written as $\Phi\left(\frac{\boldsymbol{\zeta}^T\mathbf{Z}\boldsymbol{\zeta}}{2}\right)$, with $\Phi(v)$ being a characteristic generator function:

$$\Phi(v) = \int_0^\infty e^{-\tau v} p_\tau(\tau) d\tau, \tag{II.18}$$

where matrix $\mathbf{Z}$ is a positive definite characteristic matrix, and $p_\tau(\tau)$ a PDF on $[0, \infty)$. More intuitively, by applying $\boldsymbol{\zeta}' = \mathbf{Z}^{-1/2}\boldsymbol{\zeta}$ linear transform on the augmented random vector, the density generator function $\Phi(v)$ takes the form:

$$\Phi(\boldsymbol{\zeta}'^T\boldsymbol{\zeta}'/2) = f(||\boldsymbol{\zeta}'||^2), \tag{II.19}$$

where $||.||$ is the Euclidian norm. This implies that the SIRV $\boldsymbol{\zeta}$ is reduced to a new SIRV $\boldsymbol{\zeta}'$ with its new covariance matrix equal to $\mathbf{I}_m$ (identity matrix of order m). In this case, $\boldsymbol{\zeta}'$ clearly exhibits spherical invariance.

The PDF of a SIRV vector whose characteristic function poses these properties, can be expressed in terms of normalized covariance matrix $\mathbf{M}$ and a texture PDF $p_\tau(\tau)$ as:

$$p_{\mathbf{k}}(\mathbf{k}) = \frac{1}{\pi^m \det \mathbf{M}} h_m\left(\mathbf{k}^\dagger \mathbf{M}^{-1}\mathbf{k}\right), \tag{II.20}$$

with $h_m(q) = \int_0^\infty \tau^{-m} \exp\left(-\frac{q}{\tau}\right) p_\tau(\tau) d\tau$ and det $\mathbf{M}$ denoting the determinant of the covariance matrix $\mathbf{M}$. Yao (*Lemma 4.1* in [67]) also demonstrated SIRV closure under invertible linear transform (e.g. as suggested for Eq. II.19). All target vectors $\mathbf{k}$ satisfying these conditions accept a product model stochastic representation [68].

Further on, we ought to note that a random target vector $\mathbf{k}_E$ has an elliptically symmetric distribution [69] if it is affinely equivalent in distribution to a spherically symmetric target vector $\mathbf{k}_S$:

$$\mathbf{k}_E = \mathbf{A}\mathbf{k}_S + \mathbf{b}. \tag{II.21}$$

Therefore, spherical symmetry represents a particular case of elliptical symmetry when $\mathbf{A} = \mathbf{I}_m$ and $\mathbf{b} = [0]_{m\times 1}$. In our case, by identifying in the SIRV whitening transform from Eq. II.19, it yields $\mathbf{A} = \mathbf{C}^{-1/2}$ and $\mathbf{b} = [0]_{m\times 1}$ (due to the zero mean).

Hence, on one side, a spherically symmetric white SIRV vector, being characterized with unity covariance matrix, is necessarily spherical. On the other side, the previously introduced sphericity test is no longer valid in the absence of the elliptical symmetry, making the last property a mandatory constraint in testing the sphericity.

The spherical symmetry property in multivariate statistics is defined with respect to a SIRV with covariance matrix $\mathbf{I}_m$ (white SIRV). The general SIRV case, with unknown covariance matrix, was studied under the "elliptical symmetry" property. Since the family of spherical symmetric distributions (SSD) can be considered as the standardized form of the family of elliptically contoured distributions (ECD) (by employing the whitening transform from Eq. II.19), we adopt in this chapter the original Yao's notation by considering zero mean elliptically contoured distributions as SIRVs. Hence, we use the term "spherical symmetry" for both SSD and ECD goodness-of-fit testing. An exhaustive presentation on SSD and ECD can be found in [70].

Spherical symmetry testing was firstly introduced by Kariya and Eaton [71], using an alternative form of the Lehmann and Stein lemma [72] with known covariance matrix. In the common situation where the covariance matrix is estimated from data, several strategies for robust spherical symmetry testing have been proposed by Beran [73], King [74], Baringhaus [75], Fang et al. [76], Manzotti et al. [77] and Huffer et al. [78] among the most recent publications. Li et al. proposed in [79] a graphical method for spherical symmetry testing: the Q-Q probability plots. This method has been applied in [80] to hyperspectral image analysis.

According to [78], one of the most powerful spherical symmetry tests was proposed in [81] for real random vectors. In this section, we have adapted the Schott test for multidimensional complex SAR data analysis.

II.3.1 The Schott test for circular complex random vectors

Assuming the existence of the forth order moment (or quadricovariance) matrix:

$$\mathbf{M}_4 = \mathbf{k}_i\mathbf{k}_i^H \otimes \mathbf{k}_i\mathbf{k}_i^H, \tag{II.22}$$

Schott proposed the Wald test [82] for verifying if the structure of $\mathbf{M}_4$ corresponds to a SIRV (as originally given by Tyler in [55]). This structure holds for circular complex random vectors, also [69].

With complex random vectors, the first modification is the sample quadricovariance estimator. According to [83], the sample complex quadricovariance estimator can be expressed in terms of the Kronecker product $\otimes$ as:

$$\widehat{\mathbf{M}}_4 = \frac{1}{N}\sum_{i=1}^{N} \mathbf{k}_i\mathbf{k}_i^H \otimes \mathbf{k}_i\mathbf{k}_i^H, \tag{II.23}$$

where the transposed operator T is replaced by the conjugate and transpose operator H. Its corresponding standardized form is:

$$\widehat{\mathbf{M}}_{4*} = \left(\widehat{\mathbf{M}}^{-\frac{1}{2}^H} \otimes \widehat{\mathbf{M}}^{-\frac{1}{2}^H}\right) \widehat{\mathbf{M}}_4 \left(\widehat{\mathbf{M}}^{-\frac{1}{2}} \otimes \widehat{\mathbf{M}}^{-\frac{1}{2}}\right). \tag{II.24}$$

According to the Schott's theorem, the Wald test statistic for spherical symmetry can be expressed as:

$$\begin{aligned} T_{Schott} &= N\{\beta_1 \mathrm{tr}\left(\widehat{\mathbf{M}}_{4*}^2\right) + \beta_2 \mathrm{vec}\left(\widehat{I}_m\right)^H \widehat{\mathbf{M}}_{4*}^2 \mathrm{vec}\left(\widehat{I}_m\right) \\ &- [3\beta_1 + (m+2)\beta_2]\, m(m+2)(1+\widehat{\kappa})^2\}, \end{aligned} \tag{II.25}$$

where:

$$\beta_1 = (1+\widehat{\theta})^{-1}/24, \tag{II.26}$$

$$\beta_2 = -3a[24(1+\widehat{\theta})^2 + 12(m+4)a(1+\widehat{\theta})]^{-1}, \tag{II.27}$$

$$a = (1+\widehat{\theta}) + (1+\widehat{\kappa})^3 - 2(1+\widehat{\kappa})(1+\widehat{\eta}), \tag{II.28}$$

with the Mardia's kurtosis $\widehat{\text{kurt}}_m$ and the generalized higher order scalar moments $\widehat{\theta}$, $\widehat{\eta}$ given by:

$$(1+\widehat{\text{kurt}}_m) = \frac{1}{m(m+2)N}\sum_{i=1}^{N}\left[\mathbf{k}_i^H\widehat{\mathbf{M}}^{-1}\mathbf{k}_i\right]^2, \tag{II.29}$$

$$(1+\widehat{\theta}) = \frac{1}{m(m+2)(m+4)N}\sum_{i=1}^{N}\left[\mathbf{k}_i^H\widehat{\mathbf{M}}^{-1}\mathbf{k}_i\right]^3, \tag{II.30}$$

$$(1+\widehat{\eta}) = \frac{1}{m(m+2)(m+4)(m+6)N}\sum_{i=1}^{N}\left[\mathbf{k}_i^H\widehat{\mathbf{M}}^{-1}\mathbf{k}_i\right]^4. \tag{II.31}$$

Asymptotically, $T_{Schott} \rightarrow \chi^2_{v_{m_{complex}}}$ with $v_{m_{complex}} = \frac{m^2(m+1)(m+5)}{12} - 1$. This represents the second modification with respect to the Wald test from [81]. According to Schott, the degrees of freedom is set according to the number of unknowns of the quadricovariance matrix:

$$v_{m_{complex}} = 2(v_{m_{real}}+1) - \left[\frac{m(m-1)}{2} + m\right] - 1, \tag{II.32}$$

with $v_{m_{real}} = m^2 + \frac{m(m-1)(m^2+7m-6)}{24} - 1$, being as in [81]. The second term in Eq. II.32 comes from the number of real elements of $\widehat{\mathbf{M}}_4$: $\frac{m(m-1)}{2}$ elements of the form $x_i^2x_j^2$ and m elements of the form x_i^4. It has been proven in [84] that the Wald test and the LRT are asymptotically equivalent.

II.4 Results and discussions

To illustrate the proposed tests, we applied them on two different POLSAR datasets: the synthetic dataset and very high-resolution ONERA RAMSES POLSAR dataset [85]. In order to reinforce derived conclusions, we include also the application on high-resolution TerraSAR-X multi-pass InSAR dataset. All of these datasets are shown in Fig. II.1.

This section is dedicated to the analysis of the three data sets in terms of circularity, sphericity and spherical symmetry. Since the mean equal to zero is a requirement for all the derived tests, the zero-mean test is firstly applied on the augmented real random vector $\boldsymbol{\zeta}$. This test is valid for both Gaussian and SIRV stochastic models, and its results for real datasets are illustrated along with the results of the proposed tests.

Under circularity, the zero-mean testing can be performed by using the T^2-statistic. When testing the hypothesis H_0 that a mean vector $\bar{\mathbf{k}}$ is equal to zero, the generalized likelihood ratio criterion for the circular multivariate Gaussian model is:

(a) (b) (c)

Figure II.1: Data sets: (a) Synthetic POLSAR data, intensity color composition of the target vector elements k_1-k_3-k_2 in Pauli basis, (b) Toulouse, RAMSES POLSAR data, intensity color composition of the target vector elements k_1-k_3-k_2 in Pauli basis, (c) TerraSAR-X 3-pass InSAR data, amplitude color composition of the complex random vector elements k_1-k_2-k_3.

$$T^2 = N\bar{\mathbf{k}}^H \widehat{\mathbf{M}}_{SCM}^{-1} \bar{\mathbf{k}}, \tag{II.33}$$

with $T^2 \to \chi^2_m$ under H_0 (see Theorem 5.2.3 from [58]). In case circularity is not assumed, this test can be directly applied on the augmented real random vector $\boldsymbol{\zeta}$. This results holds asymptotically for the SIRV models according to Theorem 5.7.1 from [58]. More details are provided in [86, 87, 88].

The GLRT from Eq. II.33 is not scale invariant like the ones from Sections II.2.1.2 and II.2.2.2. Thus, Tyler's Corollaries 1 and 4 from [55] cannot be applied directly.

The discussions associated to the results presented in this section, concern only these high-resolution multivariate SAR data sets. The estimation neighbourhood is the 13 × 13 boxcar and the false alarm probability threshold is $p_{fa} = 0.01$.

II.4.1 Synthetic data

The synthetic dataset is composed out of nine different regions (Fig. II.2a). Six of them are characterized with the SIRV PolSAR clutter, while for the remaining three the clutter is Gaussian (clutter covariance matrix for each of the regions is provided in Fig. II.2a). In four regions the additive thermal noise (circular or non-circular) is present. As well, we introduce a coherent scattering through the simulated elementary reflectors (two trihedrals, dihedral and dipole).

In the dataset derivation, we relied on the ML deterministic texture estimator:

Table II.1: Toulouse, RAMSES POLSAR data, X-band: detection results. A - the percentage of pixels exhibiting both the row and the column defined property, B - the percentage of pixels exhibiting both the row and the column defined property with respect to all the pixels exhibiting the row defined property. Margin of error is calculated for the percentage in A as 1.96 × standard error of a percentage, determining thus, 95% confidence interval.

	Non zero mean (45249 pixels)		Non circular (230104 pixels)		Spherical (1283 pixels)		Non spherically sym. (373983 pixels)	
	A	B	A	B	A	B	A	B
Non zero mean	4.52%	100%	0.91%	20.13%	0%	0%	2.3%	51%
Margin of error	±0.041%		±0.019%		±0%		±0.029%	
Non circular	0.91%	4%	23.01%	100%	0.02%	0%	7.18%	31%
Margin of error	±0.019%		±0.083%		±0%		±0.051%	
Spherical	0%	0%	0.02%	0%	0.13%	100%	0%	0%
Margin of error	±0%		±0%		±0.007%		±0%	
Non spherically sym.	2.3%	6.1%	7.18%	19.2%	0%	0%	37.4%	100%
Margin of error	±0.029%		±0.051%		±0%		±0.095%	

$$\widehat{\tau}_{FP} = \frac{\mathbf{k}^H \widehat{\mathbf{M}}_{FP}^{-1} \mathbf{k}}{m}. \tag{II.34}$$

Aside from the assumed detection of the coherent scattering sub-regions (elementary reflectors), circularity test rejects successfully the regions corrupted with additive non-circular thermal noise. The heterogeneity (borders between different regions) does not appear to influence this test significantly.

Sphericity test detects properly the Gaussian clutter with additive circular thermal noise as well as the Gaussian clutter without noise. As it is the case with the circularity test, the influence of non-stationarity is negligible.

However, the spherical symmetry test does not seem to be immune to the heterogeneity, but still quite successfully rejects the coherent scattering (deterministic target).

II.4.2 Very high resolution POLSAR data

Illustrated in Fig. II.1b, this data set was acquired over Toulouse, France with a mean incidence angle of 50^0. It represents a fully polarimetric (monostatic mode) X-band acquisition with a spatial resolution of approximately $0.5m$ in range and azimuth.

The background image from Fig. II.3a, II.3b, II.3c and II.3d is the estimated span of polarimetric target vectors, equivalent to the fixed point Polarimetric Whitening Filter (PWF) [30]. We have used here the same representation and the same color coding as in the previous

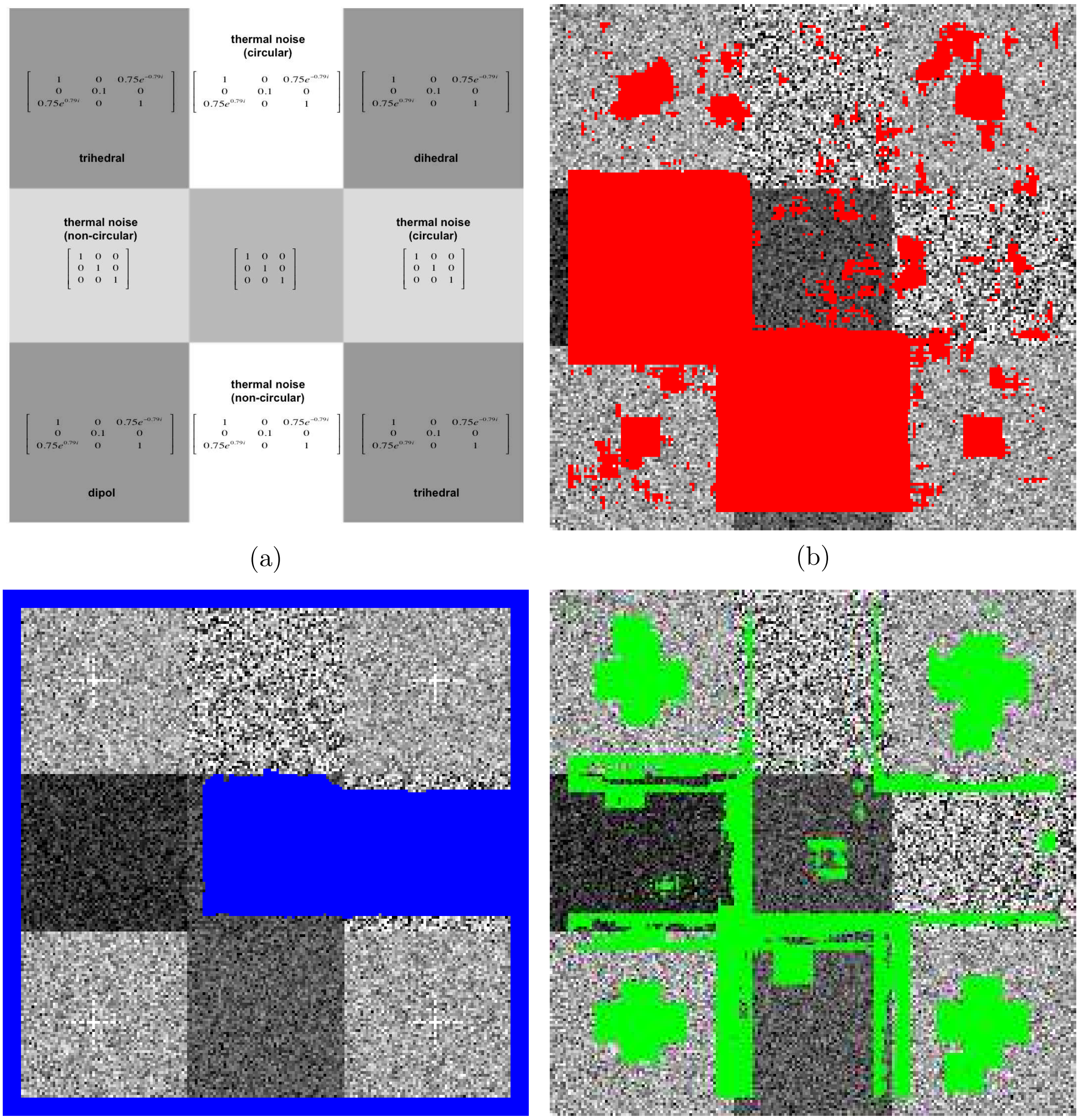

(a) (b)

(c) (d)

Figure II.2: Synthetic data set, 200x200 pixels: (a) description of the regions, (b) circularity rejection map superposed on the span, (c) sphericity map superposed on the span, (d) spherical symmetry rejection map superposed on the span.

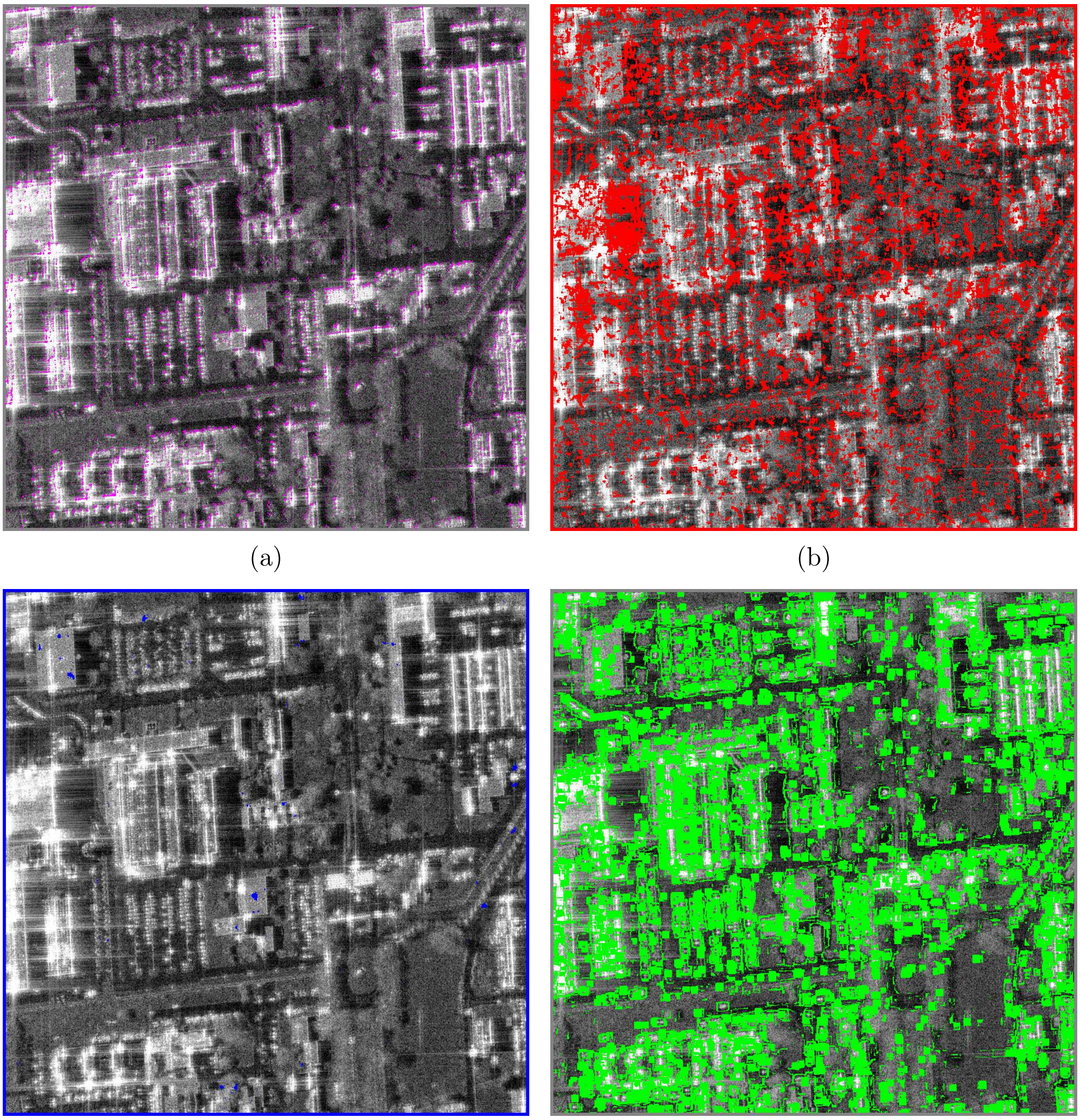

(a) (b)

(c) (d)

Figure II.3: Toulouse, RAMSES POLSAR data, X-band, 1000 × 1000 pixels: (a) zero-mean rejection map superposed on the PWF span in Db, (b) circularity rejection map superposed on the PWF span in Db, (c) sphericity map superposed on the PWF span in Db, (d) spherical symmetry rejection map superposed on the PWF span in Db.

section, while Table II.1 sums up the POLSAR results. It can be observed that this dataset is globally zero-mean and not spherical: the corresponding percentages are less than the imposed significance level. The SIRV model (spherical symmetry) holds in about two thirds of all realizations, while the non-sphericity confirms that multivariate statistical modelling is correctly employed since the clutter is not spherical.

In other words, Fig. II.3d indicated that the spherical symmetry is rejected over the urban areas exhibiting strong deterministic scattering. Quantitatively, one can deduce in Table II.1 that the Schott test for spherical symmetric circular complex random vectors rejects non circular pixels in about 31% of all cases, only (7.18% rejected, out of 23.01%). Hence, circularity testing is mandatory prior to testing the SIRV model conformity.

Finally, both Fig. II.3c and Table II.1 indicate a relatively high percentage of noncircular pixels in this POLSAR dataset. These pixels are mainly located in the weak backscattering image areas (shadowing). Since the data are zero-mean, this effect is not induced by any non-centered thermal noise additive component. However, it may be introduced by the specific calibration of this airborne very high resolution POLSAR data: the motion compensation module tracks and rectifies the signature of specific calibrated point targets on the ground.

II.4.3 High-resolution multi-pass InSAR data

The 3-pass interferometric stripmap HH images were acquired in 2009, at 11-day interval, over the Argentière village, France with a mean incidence angle of 5^0, an azimuth-resolution of $3.3m$ and a slant-range resolution of $1.8m$. This data set has been used for SAR tomography over this area as it exhibits a high coherence level over the main buildings from Fig. II.1c [89]. The background image from Fig. II.4a, b, c, d is the estimated span, equivalent to the fixed point Interferometric Whitening Filter (IWF).

The pixels illustrated in magenta on Fig.II.4a indicate where the zero-mean test is rejected. It can be observed from Table II.2 that this dataset is zero-mean: the percentage of rejected pixels is much less than the significance level a priori set (1% in all cases).

Fig. II.4b shows in red the pixels where the adjusted circularity test is rejected. These pixels should be processed as $2m$ real random vectors. The percentage of rejected non circular pixels (cf. Table II.2) is, although larger than the significance level, still small enough (3.14%) for us to conclude that this dataset is circular.

Fig. II.4c and Fig.II.4d illustrate in blue the pixels where the sphericity test from Eq. II.15 is accepted, and in green the pixels where the spherical symmetry test from Eq. II.26 is rejected. The quantitative results summed up in Table II.2 indicate that both sphericity and spherical symmetry properties are significant for this dataset. Qualitatively, it can be observed that:

- localized mainly in regions with high density of strong scatterers, the nonspherical pixels should be treated as a fully multivariate process inside the local neighborhood when

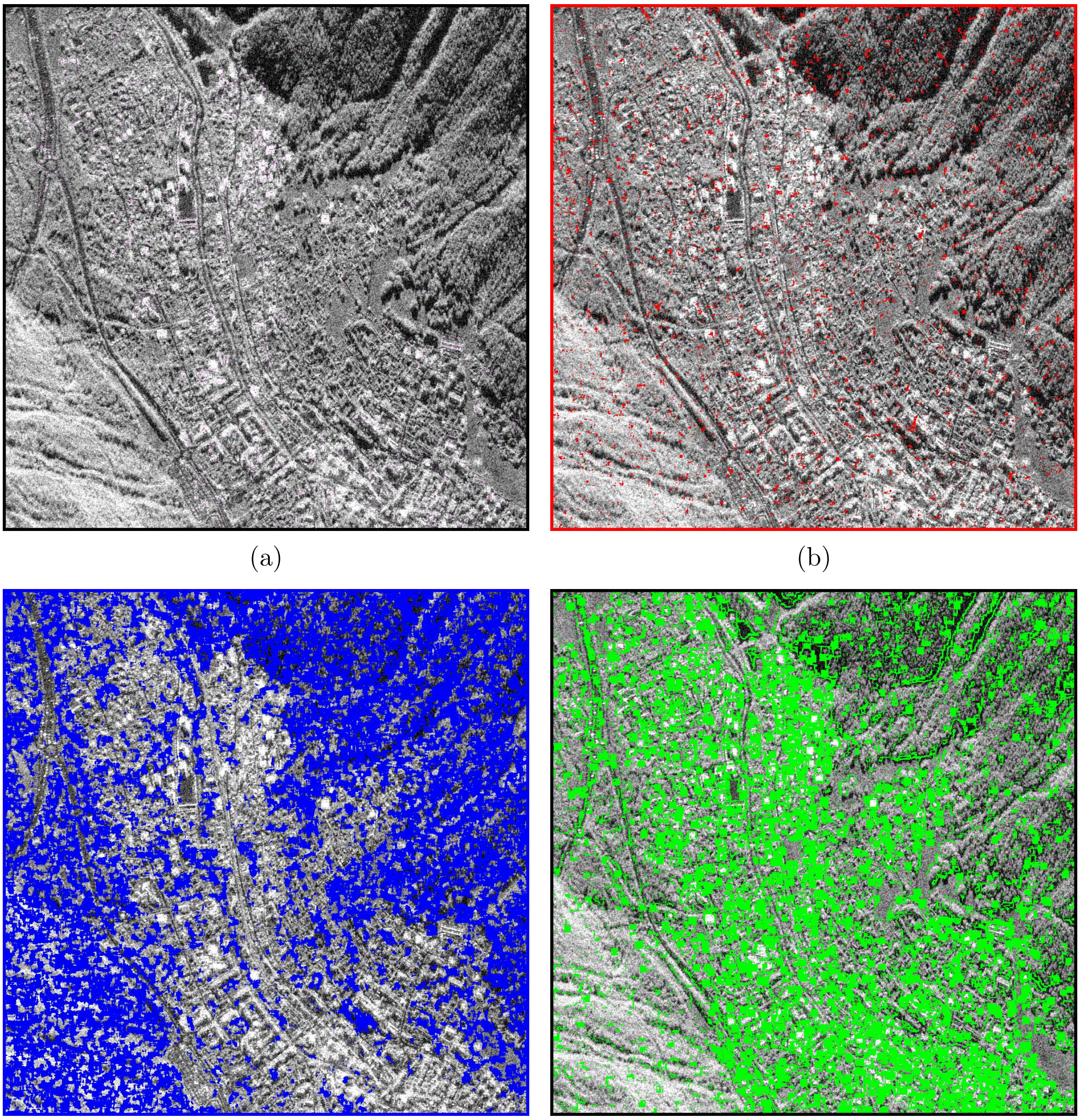
(a) (b)

(c) (d)

Figure II.4: Argèntiere, TerraSAR-X 3-pass InSAR data, X-band, 1024 × 1024 pixels: (a) zero-mean rejection map superposed on the IWF span in Db, (b) circularity rejection map superposed on the IWF span in Db, (c) sphericity map superposed on the IWF span in Db, (d) spherical symmetry rejection map superposed on the IWF-FP span in Db.

Table II.2: Argèntiere, TerraSAR-X 3-pass InSAR data, X-band: detection results. A - the percentage of pixels exhibiting both the row and the column defined property, B - the percentage of pixels exhibiting both the row and the column defined property with respect to all the pixels exhibiting the row defined property. Margin of error is calculated for the percentage in A as 1.96 × standard error of a percentage, determining thus, 95% confidence interval.

	Non zero mean (3751 pixels)		Non circular (32882 pixels)		Spherical (424856 pixels)		Non spherically sym. (328125 pixels)	
	A	B	A	B	A	B	A	B
Non zero mean	0.36%	100%	0.01%	2.8%	0.02%	5.6%	0.18%	50%
Margin of error	±0.012%		±0%		±0%		±0.008%	
Non circular	0.01%	0%	3.14%	100%	1.27%	40%	0.55%	17.6%
Margin of error	±0%		±0.033%		±0.02%		±0.014%	
Spherical	0.02%	0%	1.23%	3%	40.52%	100%	3.14%	7.8%
Margin of error	±0%		±0.021%		±0.094%		±0.033%	
Non spherically sym.	0.18%	0%	0.6%	2%	3.14%	10%	31.3%	100%
Margin of error	±0.008%		±0.015%		±0.033%		±0.089%	

estimating the InSAR coherence and phase parameters;

- mostly located in the same areas of the image, the nonspherically symmetric pixels indicate where the SIRV (and consequently the compound Gaussian) model fails to properly describe the multivariate clutter.

This specific behavior may be linked with the presence of strong deterministic scattering in urban areas: the analyzed target is not distributed but deterministic. Nevertheless, the proposed tests build a methodological framework to study this effect with respect to the SIRV model.

Spherical symmetry is a prerequisite for sphericity. For quantitatively validating the obtained results, the percentage pixels detected as spherical and rejected for spherical symmetry was computed in Table II.2: the value is quite small considering the significance level. This condition is met for non circular and non-zero mean pixels, also.

Additionally, about 18% of non circular pixels are rejected by the Schott test for spherical symmetric circular complex random vectors. This reinforces the previously established conslusion that circularity should be tested before testing for spherical symmetry.

II.5 Analysis

When dealing with multivariate high-resolution SAR data, it is crucial to decide if a specific stochastic model is properly fitting the experimental dataset inside the estimation neighborhood. The accepted stochastic process with the smallest number of parameters should be selected. In other words, if both the SIRV model and the Gaussian model are fitting the data, the latter will have better estimation performances with a finite number of samples. Based on the results presented in this chapter, we provide the methodological framework to asses multivariate SAR data conformity, based on the following tests:

1. Zero-mean test,
2. Circularity test,
3. Sphericity test,
4. Spherical symmetry test,
5. non-Gaussianity test.

The algorithmic representation of proposed methodological framework is provided in Fig. II.5.

By successively performing the proposed tests for a specific multivariate SAR dataset, it is possible to asymptotically evaluate the pertinence of various model-based statistical processing schemes (filtering, segmentation or detection).

In terms of theoretical performance analysis, the adjusted generalized LRT is asymptotically uniformly most powerful according to the Neyman-Pearson lemma. This "optimality" holds provided the estimators plugged into the LRT (or the Wald test) are consistent and unbiased, which is the case for our study.

Special care must be taken when applying the tests with multivariate SAR data. In theory, the proposed conformity testing holds as long as the observed number of samples (estimation neighborhood) is large enough with respect to the dimension of the target vector, especially for the spherical symmetry test (based on the specific structure of the quadricovariance).

Finally, it is important to stress that no predefined analytical form was imposed on the texture probability function when establishing the conformity tests. Therefore, they can be directly applied for a wide class of stochastic processes currently used for describing multivariate high-resolution SAR data.

II.6 Conclusions

In this chapter we have presented a new methodological framework to asymptotically asses the conformity of multivariate high-resolution SAR data. The proposed approach consist of applying successively three statistical hypotheses tests for verifying three important statistical properties: circularity, sphericity and spherical symmetry, briefly summarized in Fig. II.6. The latter is asymptotically equivalent, under certain hypotheses, to the conformity of the

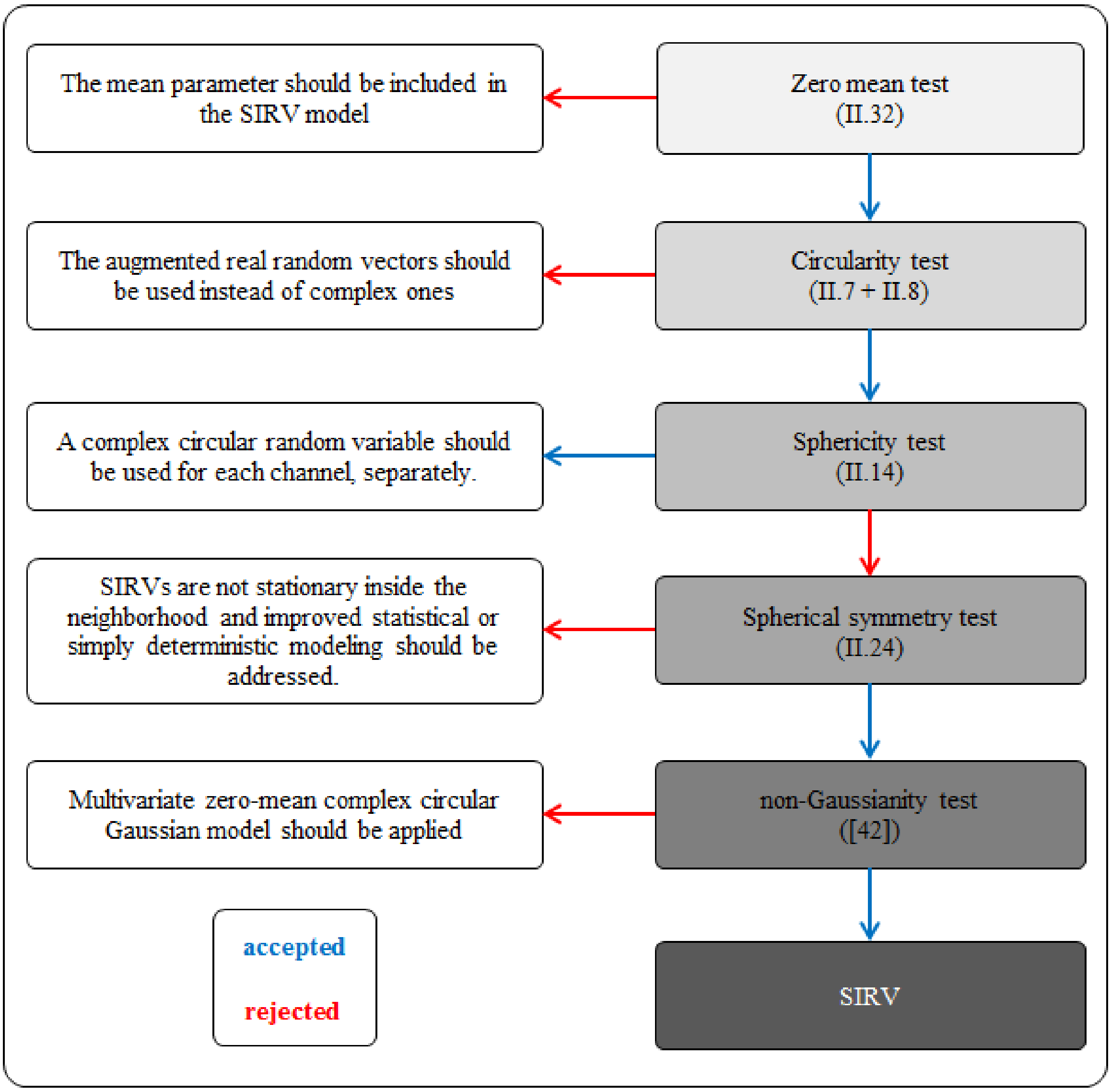

Figure II.5: Methodological framework

experimental data with respect to the SIRV product model. In addition, the zero-mean and the non-Gausiannity [44] tests can be used to decide which model is better suited to asymptotically fit the experimental data.

The proposed framework, aside from the fact that it is gathering the most notable advances in the field of signal processing, is introducing the extension of both the sphericity and the spherical symmetry tests with zero-mean complex circular SIRV assumption.

The effectiveness of the proposed detection schemes was illustrated by synthetic and very high resolution ONERA RAMSES POLSAR data. Additionally, the analysis has been strengthened by high-resolution TerraSAR-X multi-pass InSAR. The conclusions driven from the analysis of the obtained results are important with respect to the two tested real datasets: circularity is important for very-high resolution POLSAR data, while non-sphericity can be an important issue for high-resolution multi-pass InSAR.

It has been illustrated that in strong heterogeneous clutter, such as the urban environment, the SIRV model can fail. The bottom line is that characterization of urban regions is much more complex (and difficult) - since a more complex model, with more parameters, may be required. In the light of the results shown in this chapter, SIRV models may be less appropriate for urban areas characterization. However, alternative explanations are possible. As an example, the root of this inappropriateness might as well be the assumed ergodicity / stationarity (in spatial sense) for the backscattered signal and, also, even in the hypothesis of randomness: targets exhibit a deterministic behavior.

First, the very use of a sliding analysis window for estimating the stochastic parameters of the scattered signal may be questioned, as it implicitly assume that the considered signal is ergodic / stationary in spatial sense (homogeneous). While this hypothesis holds for distributed and uniform targets, where the physical parameters (and, thus, the electromagnetic scattering behavior) differs very little from one resolution cell to another, in urban areas the physical structure (and, as such, its electromagnetic behavior) may change considerably from one resolution cell to the next. This makes the hypothesis of ergodicity / stationarity less applicable.

Second, one should note that even the randomness of the radar echo is not given, but assumed. This is mainly a way to deal with the inherent complexity of the signal. Anyway, for identical measuring conditions, the recorded radar data is perfectly identical. Even if small differences in measuring conditions lead to strong discrepancies in the recorded data, this is not an evidence for randomness, as such behaviour can be fully explain under a deterministic paradigm - the chaotic models. Various parameters, such as meteorological conditions and, even more important, the changes that the target suffers in time (between two succeeding acquisitions, for example), account for the observed randomness of the recorded data. However, these changes of the target are more significant for green targets (such as forests and agricultural fields), where humidity and wind modify both their physical structure and their electromagnetic behavior. On the other hand, those changes are less significant for urban targets and, as such, randomness is less likely for the latter.

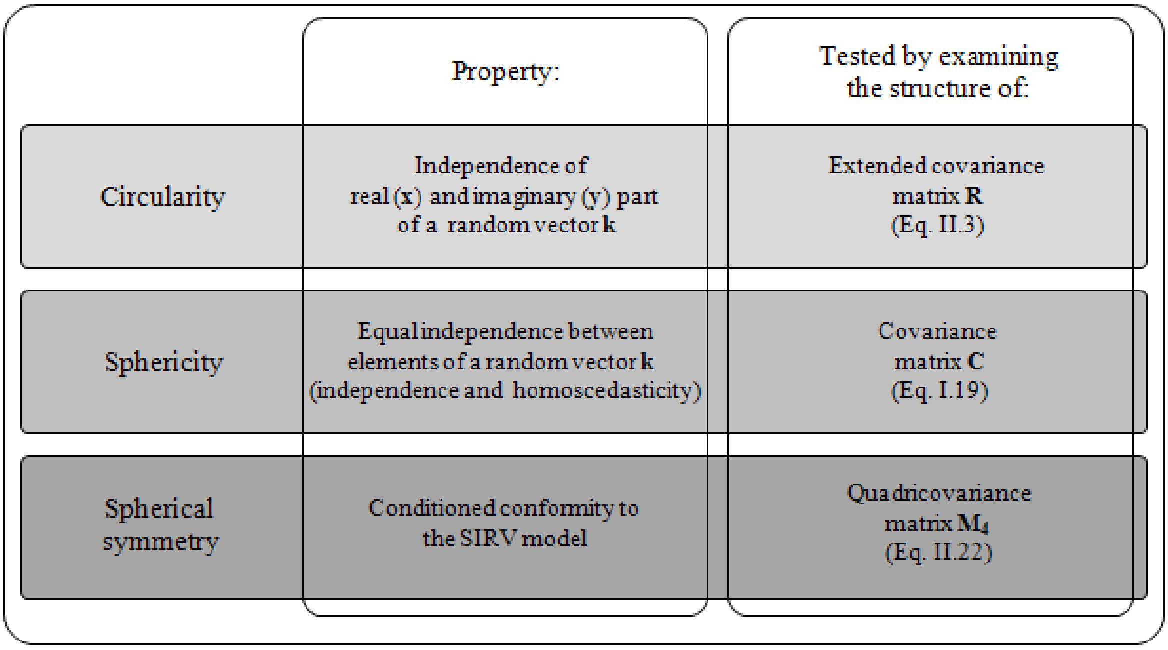

	Property:	Tested by examining the structure of:
Circularity	Independence of real (**x**) and imaginary (**y**) part of a random vector **k**	Extended covariance matrix **R** (Eq. II.3)
Sphericity	Equal independence between elements of a random vector **k** (independence and homoscedasticity)	Covariance matrix **C** (Eq. I.19)
Spherical symmetry	Conditioned conformity to the SIRV model	Quadricovariance matrix $\mathbf{M}_4$ (Eq. II.22)

Figure II.6: Brief summary of the analysed statistical properties.

In perspective, applying chaotic (or pseudo-chaotic) [90, 91, 92] models to POLSAR / InSAR data from urban areas can be a possible solution. These models should be able to take into account the deterministic features of those areas (presence of dihedral angles, straight edges, cavities, etc.), while still leaving room for some unpredictability (orientation of those elements). Using chaotic models in POLSAR and multi-pass InSAR data will make the object of our future work.

This work has many interesting perspectives. We believe that it contributes toward the description and the analysis of heterogeneous clutter over scenes exhibiting complex polarimetric signatures. Firstly, the exact texture normalization condition for the PWF-SCM estimator has been derived under the SIRV clutter hypothesis. A novel estimation / detection strategy has been proposed which can be used with conventional boxcar neighborhoods directly. Finally, the proposed estimation scheme can be extended to other multidimensional SAR techniques using the covariance matrix descriptor, such as the following: repeat-pass interferometry, polarimetric interferometry, or multifrequency polarimetry.

CHAPTER III

Polarimetric decomposition by means of BSS

This chapter represents the focal point of the thesis. Here, we generalize Incoherent Target Decomposition concept to the level of BSS, by replacing conventional eigenvector decomposition with ICA algorithm. The proposed decomposition exploits the higher order statistical information, emerging from POLSAR clutter heterogeneity [1]. The result is a set of mutually independent, non-orthogonal target vectors, characterizing dominant scatterers over a stationary set of observed target vectors. The most dominant component appears to be quite similar to the ones obtained by means of conventional methods, but the second ones carries a new information.

Firstly, relying on Section I.3, we discuss the role of BSS in ICTD. The description of the method, comprising the elaborated comparison of applied ICA algorithms, is provided thereafter. The roll-invariance properties are as well discussed at this point. Finally, we present the application of the decomposition on two real data-sets, followed by corresponding discussion. The last contains an application on a synthetic data set as well, used to demonstrate the capability of retrieving non-orthogonal mechanisms. The polarization basis invariance analysis is demonstrated using one of the real data sets.

III.1 Introduction

As already stated in Section I.3, under certain constraints, the eigenvector decomposition of the scattering coherence matrix, provides the same results as the Principal Component Analysis (PCA) of the corresponding representative target vector [93]. Thus, the conventional approach in POLSAR images incoherent target decomposition, elaborated in Section I.1.2.2, results in deriving uncorrelated components. This is adequate if we consider the conventional statistical model assuming Gaussian homogeneous clutter [94]. However, as being elaborated in the previous two chapters, the high and very high POLSAR data can be characterised by Non-Gaussian heterogeneous clutter [30]. In this case decorrelation cannot be considered as the most meticulous way for separating the scattering sources present in the scene. It appears that more advantageous solutions, capable of deriving independent components, are needed. Applying the Independent Component Analysis (ICA) seems to be one of such solutions.

The research presented in this chapter would be our effort to answer the second question posed in the preface of this thesis. Namely, by accepting the altered statistical models we are accessing in a different manner to the target decompositions, trying to exploit the information contained in the higher statistical orders. This information allows different characterization of POLSAR data, which could prove to be advantageous with respect to the conventional one.

The ICA methods have been already successfully employed on SAR data: in speckle reduction, feature extraction and data fusion [95, 96]. The application on polarimetric data was, however, either restricted to the analysis of two-components polarimetric target vector [97], either rather related to the POL-InSAR data analysis [98].

The main idea of this chapter is to propose a generalization of the polarimetric decompositions to the level of blind source separation techniques by introducing the ICA method instead of the eigenvector decomposition. Essentially, our motivation is the possibility to exploit higher order statistics of the non-Gaussian target vector in order to recover a set of independent dominant scatterers. The recovered linearly independent scattering target vectors are not necessarily mutually orthogonal, which is demonstrated using a synthetic data set. At first, we apply the statistical classification algorithm (for example [43]) in order to obtain stationary sets of polarimetric observations - scattering matrices projected onto the Pauli basis. Then, the target vectors of the single scatterers are estimated by applying comparatively the representative ICA algorithms, introduced in Section I.3.2, on each of the sets derived in the previous step. They are parametrised using the TSVM, allowing the adapted Poincaré sphere representation with direct physical interpretation [99]. The share of the component in the total backscattering is computed by the squared ℓ^2 norm of the single scatterer target vector.

The proposed method, based on the particular version of the FastICA algorithm [100] is invariant both under the rotation of the line of sight and under the change of polarization basis. The latter is demonstrated using the projection of the observations onto the circular basis, coupled with the Circular Polarization Scattering Vector (CPSV) model [101] and furthermore, by additionally employing $\alpha - \beta - \gamma - \delta$ model in Pauli basis [15].

The method particularities with respect to the conventional approach are demonstrated using RAMSES X-band and ALOS L-band data sets. Comparative analysis points out strong similarity when dealing with the first most dominant components. However, there is a remarkable difference in the behaviour of the second components. It appears that on the expense of a negligible increase in entropy, the second most dominant component contains some valuable information. In the first data set, acquired over urban area, while analysing the class which corresponds to the elementary trihedral placed in the scene, we detect the diffraction scattering by identifying dipole as the second most dominant component. On the other side, when dealing with the distributed targets (mountainous region), we are able to rely on the symmetry of the second most dominant component in discriminating between different types of snow cover and the bare ground. In terms of the second component, we as well, demonstrate and discuss the advantage of the "global" (classification) over the "local" approach (sliding window) in selecting observation datasets.

III.2 PCA and ICA

Relaying on Section I.3, where we have elaborated the concept of BSS by emphasizing PCA and ICA, we are reinforcing here the link between these two, in order to better position the proposed decomposition with respect to the conventional ones.

If we introduce the spatially averaged covariance matrix of the observation vector $\mathbf{x}$ as $\mathbf{C}_x$, the mixing matrices, $\mathbf{A}'$ and $\mathbf{A}''$, corresponding respectively to PCA ($'$) and ICA ($''$), can be represented as factorizations of the covariance matrix [93]:

$$\mathbf{C}_x = \mathbf{A}'\mathbf{A}'^H = \mathbf{A}''\mathbf{A}''^H, \tag{III.1}$$

and they are mutually related by an unitary matrix $\mathbf{P}$:

$$\mathbf{A}'' = \mathbf{A}'\mathbf{P}. \tag{III.2}$$

Choosing the columns of $\mathbf{A}'$ to be denormalized eigenvectors of $\mathbf{C}_x$, ensures decorrelation between the elements of $\mathbf{s}'$. The denormalization assumes multiplying by the square root of eigenvalue and it is emphasized since it is the denormalized eigenvector which forms a coherence matrix of a single scatterer in a conventional approach. Even though multiplication of $\mathbf{A}'$ with an arbitrary unitary matrix (rotation) preserves decorrelation, maximum energies for the components of $\mathbf{s}'$ are achieved with the matrix of eigenvectors. For this reason, we are identifying the first step of the conventional approach in ICTD (eigenvector decomposition) with the PCA [93].

On the other side, the matrix $\mathbf{A}''$ cannot be retrieved using only second-order statistics, unless we treat Gaussian observations, only. Even though it is intrinsically linked to the matrix $\mathbf{C}_x$, the mixing matrix of independent sources cannot be estimated using this matrix only. Namely, considering the equation III.2, it appears that the estimation of the unitary "floating" matrix **P** requires knowledge of the higher order statistics.

Therefore, it is necessary to apply a method capable of exploiting higher order statistical moments - ICA. The ICDT method, proposed thereafter, has been molded by comparatively testing both the fixed-point iterative algorithm (FastICA) [34, 100], and the most representative tensorial methods [40, 41, 42].

III.3 Method

The proposed incoherent polarimetric decomposition method consists in three main steps:

1. Data selection - the observation data sets are selected using statistical classification of the POLSAR image (named "global approach"). This choice, rather than a sliding window (named "local approach") is discussed in the following section, dealing with the performance analysis.
2. Estimation of the independent components - the most appropriate among analyzed ICA algorithms is applied on each of the formerly derived data sets in order to estimate the most dominant single scatterers.
3. Parametrization - derived target vectors are parametrized using the Touzi's Target Scattering Vector Model (TSVM) [16].

After the first step, we can assume having defined stationary sets of observed target vectors. The novelty with respect to both the Cloude and Pottier [15] and the Touzi [16] decompositions is introduced mostly in the second stage.

III.3.1 Estimation of the independent components

The core of the novel ICA based polarimetric decomposition is the estimation of the mixing matrix $\mathbf{A}^c$, for each of the derived classes (c). In the first chapter we introduced several criteria for determining the elements of $\mathbf{A}^c$ in order to ensure the mutual independence of the sources in $\mathbf{s}^c$. The common factor for all of them is the assumption of high-resolution polarimetric SAR images [102] - at most one of the sources is Gaussian and thus their mixture or the observation data prove to be Non-Gaussian [34]:

$$\mathbf{k}^c(i,j) = \begin{bmatrix} A_{11}^c & A_{12}^c & A_{13}^c \\ A_{21}^c & A_{22}^c & A_{23}^c \\ A_{31}^c & A_{32}^c & A_{33}^c \end{bmatrix} \cdot \begin{bmatrix} s_1^c(i,j) \\ s_2^c(i,j) \\ s_3^c(i,j) \end{bmatrix} = \mathbf{A}^c \mathbf{s}^c(i,j). \tag{III.3}$$

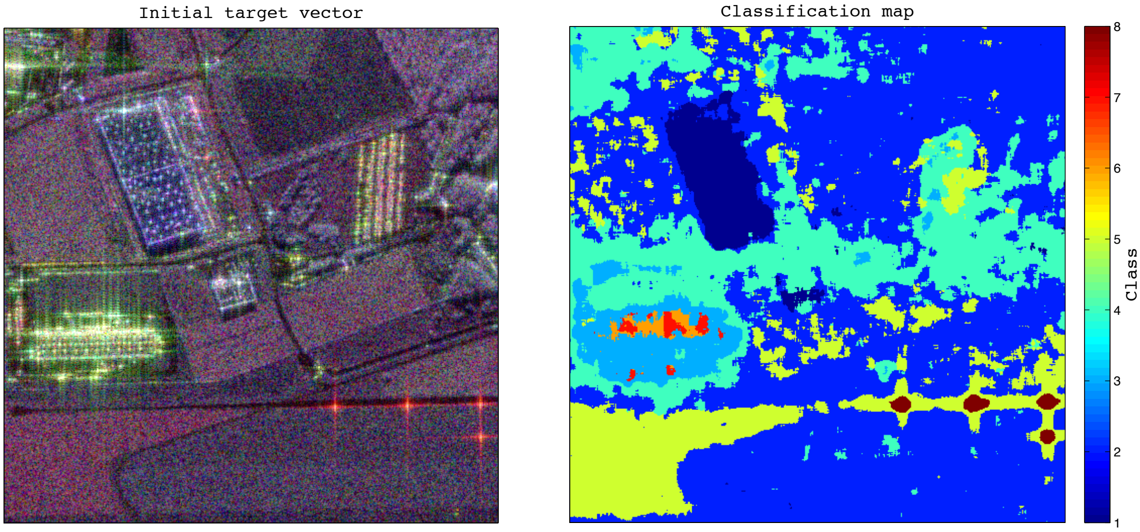

(a) (b)

Figure III.1: RAMSES POLSAR X-band, Brétigny, France: (a) Pauli RGB coded image; (b) Statistical classification performed in the first step.

In our case, the observation data are the Pauli target vectors corresponding to the *a priori* defined class ($\mathbf{k}_c \in \mathbf{K}_c$), meaning that we finally obtain one mixing matrix $\mathbf{A}^c$ for each of the classes c. In the particular case of ICDT, we are facing the complex nature of the observation data.

By applying different criteria in the Complex FastICA algorithm, followed by the most representative tensorial methods, we compare, in the framework of ICTD, the performances of several strategies used in the estimation of the complex independent components [103]. The constraint we introduce at this point would be that the selected approach has to be adapted to the scenario where sources may eventually exhibit non-circular distributions i.e. non-circularity. Given the potential for circularity rejection demonstrated in the second chapter, it appears reasonable to stay restrained to the ICA methods with this particular property.

The observed target vectors are centered and whitened. The later is the orthogonalization transform $\mathbf{V}$ (Eq. I.56) applied on a set of vectors $\mathbf{k}^c$ and therefore on the mixing matrix $\mathbf{A}^c$ as well:

$$\tilde{\mathbf{k}} = \mathbf{V}\mathbf{k}^c = \mathbf{V}\mathbf{A}^c\mathbf{s}^c = \tilde{\mathbf{A}}\mathbf{s}^c, \tag{III.4}$$

However, at this stage, the components are not scrupulously decorrelated, which can be deduced from non-diagonalized pseudo-covariance matrix $\mathbb{E}\{\tilde{\mathbf{k}}\tilde{\mathbf{k}}^T\}$ [100].

The first among tested ICA algorithms would be the version of the FastICA, introduced in Section I.3, but adapted to the complex nature of the observation data and thus, the mixing matrix. Rather than relying on one of the four introduced conventional measures of non-

Gaussianity, we use as a measure a set of non-linear functions $f_{ng}(s)$. As well, the contrast function given in Eq. I.63, is slightly modified by inserting a squared module operator:

$$\max_{\mathbf{w}} J'_{ng}(\mathbf{w}) = \max_{\mathbf{w}} \mathbb{E}\left[f_{ng}(|\mathbf{w}^H\tilde{\mathbf{k}}|^2)\right], \tag{III.5}$$

with $\mathbf{w}$ being a whitened mixing matrix column, converging toward a column of $\tilde{\mathbf{A}}$, as in Section I.3.2.1.

The performances of the algorithm strongly depend on the choice of the specific nonlinear function $f_{ng}(s)$, which is supposed to be suited to the particular application. Therefore, we use here three different functions, leading to different criteria (C) in deriving the independent target vectors:

- *kurtosis* (*C1*):
$$f_{ng1}(s) = \frac{1}{2}s^2; \tag{III.6}$$
- *logarithm* (*C2*):
$$f_{ng2}(s) = \log(0.05 + s); \tag{III.7}$$
- *square root* (*C3*):
$$f_{ng3}(s) = \sqrt{0.05 + s}; \tag{III.8}$$

In the first case, the contrast functions approximately matches one of the criteria introduced in Section I.3.2.1, becoming essentially a measure of the fourth statistical moment of the source, e.g. a non-normalized kurtosis. As its value in case of the Gaussian variable equals $\mathbb{E}\{s^4\} = 3\left(\mathbb{E}\{s^2\}\right)^2 = 3$, by maximizing the kurtosis of each of the sources, we ensure their independence. Being slowly growing non-linear functions (Fig. III.2), $f_{ng2}(s)$ and $f_{ng3}(s)$ allow more robust estimation with respect to the presence of outliers. However, in case of all three functions, super-Gaussian (leptokurtic) distributions are favoured.

In this version of FastICA, by including the pseudo-covariance matrix of the observation target vectors in maximizing the contrast function (Eq. III.5), the applied algorithm is generalized to the case of complex sources having a non-circular distribution [100]. This way, despite the modulus in equation III.5, the phase information is preserved.

The other means for mixing matrix estimation, satisfying our constraint, are the introduced tensorial decompositions: FOBI, JADE and SOBI. As indicated in Section I.3.2.2, the only necessary adaptation with respect to the already introduced methodology, would be changing the operation transpose with conjugate-transpose [104].

Finally, the estimated mixing matrix is de-whitened using the inverse orthogonalisation transform $\mathbf{V}^{-1}$:

$$\mathbf{A}^c = \mathbf{V}^{-1}\mathbf{W}. \tag{III.9}$$

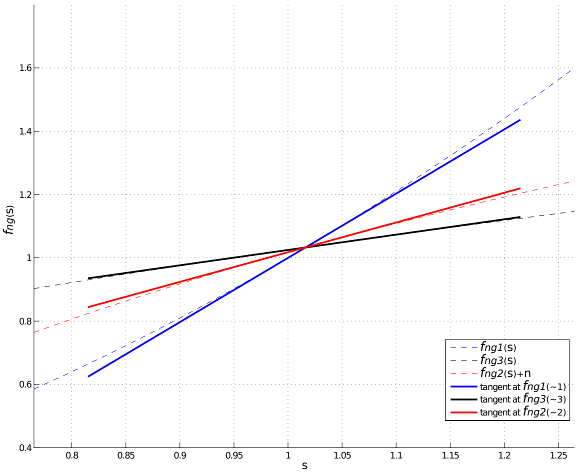

Figure III.2: Nonlinear functions used in the Complex Non-Circular FastICA algorithm, along with the tangents in the point 1, indicating the difference in the monotony. Function f_{ng2} is translated for value n for the purpose of monotony comparison.

The result of the incoherent target decomposition is the set of target vectors representing elementary scatterers and a set of scalars, providing their proportion in the total scattering. In our case, the target vectors of the independent scatterers are the columns of the estimated de-whitened mixing matrix $\mathbf{A}^c$.

The contributions to the total backscattering are computed as the squared ℓ^2 complex norms of the mixing matrix columns - the energies of the single scatterers [105]:

$$||\mathbf{A_i}||_2^2 = |A_{1i}|^2 + |A_{2i}|^2 + |A_{3i}|^2. \tag{III.10}$$

In the framework of the formalism introduced in section III.2, the contributions summed up in equation III.10 could be defined as diagonal elements of the matrix $\mathbf{A}''^{\dagger}\mathbf{A}''$. In the same way, eigenvalues are diagonal elements of $\mathbf{A}'^{\dagger}\mathbf{A}'$. Even though the matrix $\mathbf{A}''$ is not orthogonal and therefore some information contained in the non-diagonal elements of $\mathbf{A}''^{\dagger}\mathbf{A}''$ is lost, the entropy estimated in these two cases is significantly similar. In the earlier attempt of introducing the ICA into the POLSAR data analysis [98], the contributions were estimated by rather relying on the derived sources ($P_i = \frac{1}{3}\mathbf{s}(i)\mathbf{s}^H(i)$), which doesn't appear to be an appropriate choice, given the variances of the estimated sources being set to the unit value.

Finally, we parametrise the estimated target vectors by applying Target Scattering Vector Model, introduced in the Section I.1.2.2.

III.3.2 Roll-Invariance

One of the major conveniences of the conventional approach is the roll-invariance of the coherence matrix constructed from a linear combination of the eigenvectors [106]. Even though

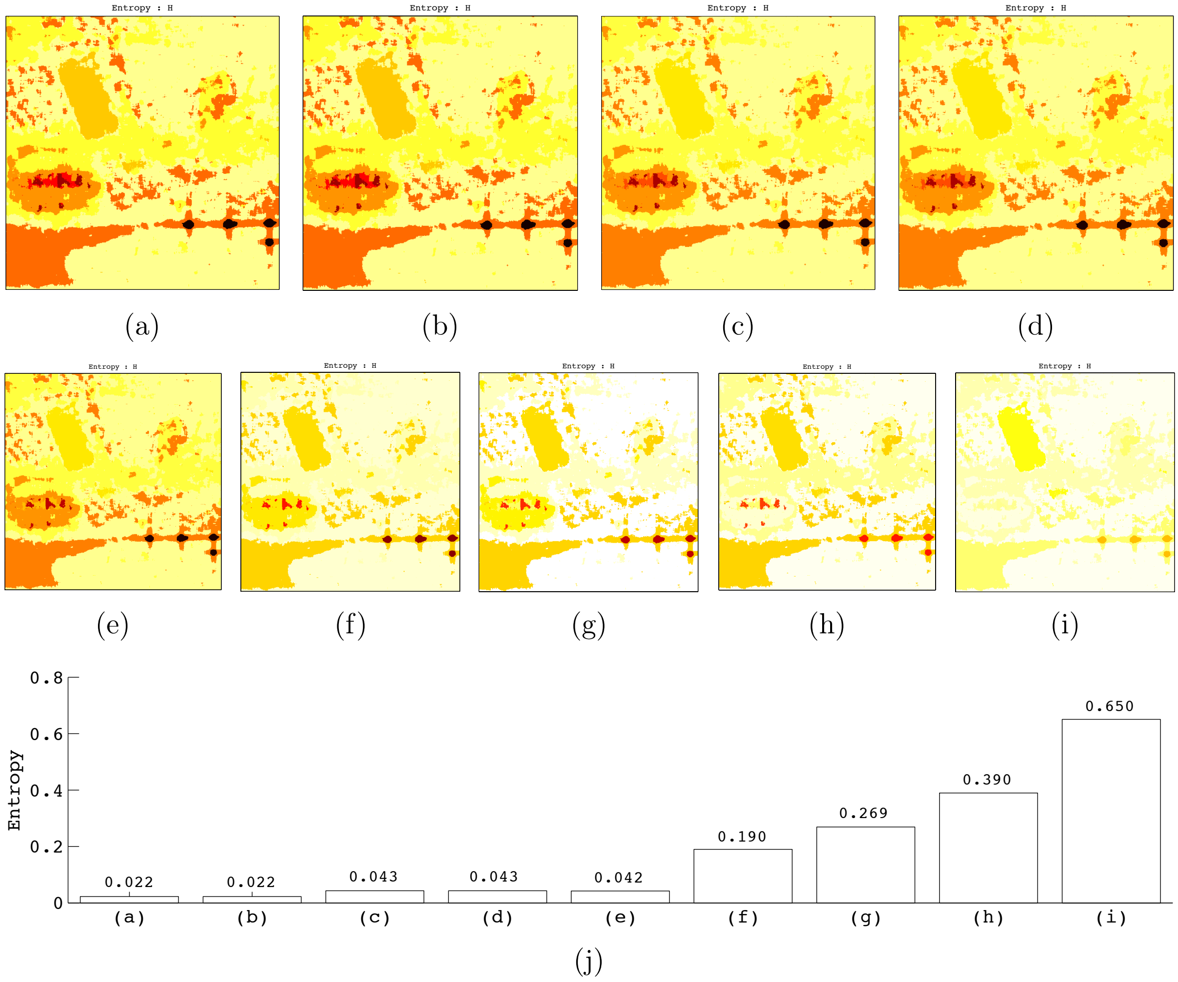

(a) (b) (c) (d)

(e) (f) (g) (h) (i)

(j)

Figure III.3: RAMSES POLSAR X-band, Brétigny, France: entropy estimation using (a) PCA - Pauli basis, (b) PCA - circular basis, (c) ICA - Pauli basis (C2 criterion), (d) ICA - circular basis (C2 criterion), (e) ICA - Pauli basis (C3 criterion), (f) ICA - Pauli basis (FOBI), (f) ICA - Pauli basis (JADE), (h) ICA - Pauli basis (C1 criterion), (i) ICA - Pauli basis (SOBI), (g) Entropy estimated for the trihedral class (Class 8).

the proposed method does not directly conserve the roll-invariance through the reconstruction from a linear combination of the eigenvectors, it appears as well to be invariant to the rotation $\mathbf{R}(\theta)$ of the observed target vectors (Table III.2):

$$\mathbf{k}^{c\theta} = \mathbf{R}(\theta)\mathbf{k}^{c} = \begin{bmatrix} 1 & 0 & 0 \\ 0 & \cos(2\theta) & -\sin(2\theta) \\ 0 & \sin(2\theta) & \cos(2\theta) \end{bmatrix} \mathbf{k}^{c}. \qquad \text{(III.11)}$$

In order to prove and justify this, we ought to get back to the "geometrical" interpretation of the ICA, introduced in Section I.3.2, but now considered in the appropriate three dimensions. Let us presume having three uniformly distributed real sources $\mathbf{s}$ (Fig. III.4a).

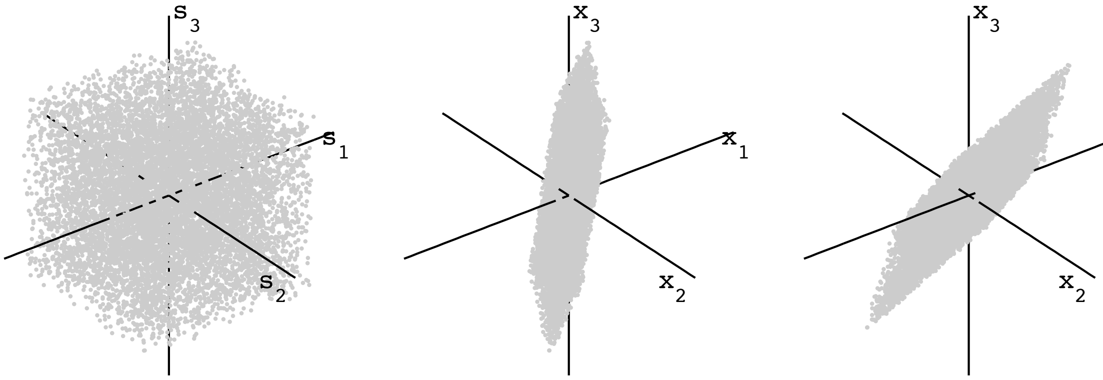

(a) (b) (a)

Figure III.4: The joint probability density functions of: (a) three uniformly distributed real sources, (b) the mixture, (c) the mixture rotated about the line of sight ($x1$ axis) for $\theta = 30°$.

By multiplying them by a non-orthogonal mixing matrix $\mathbf{A}$, we get the set of observations $\mathbf{x}$ (Fig. III.4b). Given that the whitening and de-whitening deal with the form (transforming data in Fig. III.4b into "the cube"), the estimated mixing matrix actually accounts for the orientation of "the cube", representing a 3D rotation, defined with three angles corresponding to three degrees of freedom.

Switching to the complex domain does not change the essence of the presented "geometrical" interpretation. In the context of our application ($\mathbf{x} = \mathbf{k}^c$), with implicitly assumed whitening and de-whitening, the rotation around the line of sight $\mathbf{R}(\theta)$ affects only one of the angles defining $\mathbf{A}(\phi, \xi, \chi)$:

$$\mathbf{k}_r^c = \mathbf{R}(\theta)\mathbf{k}^{\mathbf{c}} = \mathbf{R}(\theta)\mathbf{A}(\psi, \xi, \chi)\mathbf{s} = \mathbf{A}_r(\psi + \theta, \xi, \chi)\mathbf{s}. \tag{III.12}$$

The other rotation angles (ξ and χ) remain the same, which does not change with the performed inversions and they provide us the roll-invariant parameters in the estimated mixing matrix $\underline{\mathbf{A}_r}$:

$$\mathbf{B} = \mathbf{A}_r^{-1} = (\mathbf{R}\mathbf{A})^{-1} = \mathbf{A}^{-1}\mathbf{R}^{-1}, \tag{III.13}$$

$$\mathbf{A}_r = \mathbf{B}^{-1} = \mathbf{R}\mathbf{A}. \tag{III.14}$$

The columns of the estimated mixing matrix $\mathbf{A}_r$ are the estimated backscattering components and, as the derived TVSM parameters are invariant with respect to change of the ψ of the component, they are equally invariant with respect to the change introduced by the rotation applied on the observation target vectors $\psi + \theta$. Therefore, even though the FastICA algorithm itself is not invariant under the rotations of the observation data ($\mathbf{A}_r \neq \mathbf{A}$), the TSVM parameters derived in our case are indeed invariant.

For the purpose of comparison, in this case we have neglected the identity in Eq. I.31, which however, does not by any means compromise the validity of the derived conclusions.

III.4 Performance analysis

After discussing the data selection criteria, we demonstrate the particularities of the proposed method through the application on two real POLSAR data sets: RAMSES X-band image acquired over Brétigny, France and ALOS L-band images acquired over Chamonix, Mont Blanc, France. Aside from that, using a synthetically generated data set, we emphasise the difference with respect to the conventional approach (PCA).

III.4.1 Data selection

The principal drawback of the proposed method is the size of the observation dataset, which has to be somewhat larger than the size of the sliding window used in the well established methods. The inevitable consequence is the bigger number of the independent components out of which not more that the most dominant three can be estimated [98]. In view of this, rather than using a very large sliding window, we rather rely on a classification algorithm in the data selection. The influence of the size of the window is demonstrated and discussed at the end of the chapter.

The first step is the classification of the POLSAR image. At this stage of research, we choose to classify the input image using the statistical classifier developed for highly textured POLSAR data [43]. Unlike the classical $H/\alpha/A$ unsupervised classification [106], assuming Gaussian homogeneous clutter and therefore relying on the Sample Covariance Matrix (SCM) estimate, classical mean and Wishart distance [107, 108], the Non-Gaussian heterogeneous clutter is taken into account.

Under the Spherically Invariant Random Vector (SIRV) model assumption of the POLSAR clutter [67, 30], the initialization is performed through the H/α unsupervised classification based on the Fixed Point (FP) Covariance Matrix estimator [109]. The barycenters of the initialized classes are calculated iteratively using the Riemannian metric corresponding to the geometric mean [43]. At the end, pixels are assigned using the Wishart criterion.

In this phase, we obtain the set of representative target vectors for each of the classes. These vector sets represent the observation data for the BSS, while the selection method assures relevance in the case of incoherent targets.

III.4.2 Synthetic data set

In this section, we demonstrate the capability of retrieving orthogonal mechanisms using synthetic POLSAR data [93]. The observation data set is created using the non-orthogonal complex mixing matrix:

$$\mathbf{A} = \begin{bmatrix} -0.4840 - 0.4105i & 0.0505 + 0.2020i & 0.1556 - 0.2645i \\ 0.0545 - 0.3043i & -0.0155 + 0.2180i & 0.0546 - 0.3471i \\ 0.0051 + 0.0015i & 0.6174 - 0.1503i & 0.4683 + 0.2601i \end{bmatrix}, \tag{III.15}$$

and three independent sources characterized by the Gamma distribution, each of them having different parameters k and θ:

$$\mathcal{G}(s|k,\theta) = \frac{1}{\theta^k \Gamma(k)} s^{k-1} e^{-\frac{s}{\theta}}. \tag{III.16}$$

The components retrieved in case of applying the ICA algorithm (Eq. III.17) correspond approximately to the components in Eq. III.15. On the other side, because the mixing matrix **A** is not orthogonal, the PCA (Eq. III.18) is not capable of retrieving the original matrix:

$$\mathbf{A}^{ICA} = \begin{bmatrix} -0.4458 - 0.4016i & -0.0181 + 0.1954i & -0.1720 - 0.2288i \\ 0.0592 - 0.2847i & -0.0919 + 0.1947i & -0.2751 - 0.1703i \\ 0.0070 + 0.0223i & 0.5987 + 0.1189i & 0.3953 - 0.3058i \end{bmatrix}, \tag{III.17}$$

$$\mathbf{A}^{PCA} = \begin{bmatrix} -0.4625 + 0.2230i & 0.5624 + 0.5072i & -0.2665 - 0.3030i \\ 0.8393 + 0.1568i & 0.0443 + 0.4372i & -0.1068 - 0.2577i \\ 0.0854 & 0.4831 & 0.8714 \end{bmatrix}. \tag{III.18}$$

This is confirmed through the analysis of their 2D cross-correlations [110] illustrated in Fig. III.5:

$$\mathbf{C}_{\mathbf{M_1},\mathbf{M_2}}(k,l) = \sum_{m=0}^{M-1} \sum_{n=0}^{N-1} \mathbf{M_1}(m,n) \mathbf{M_2}^{\dagger}(m-k, n-l). \tag{III.19}$$

This section demonstrated that the ICA, aside from being able to assure the independence of the components, identifies the second component without any constrain of orthogonality.

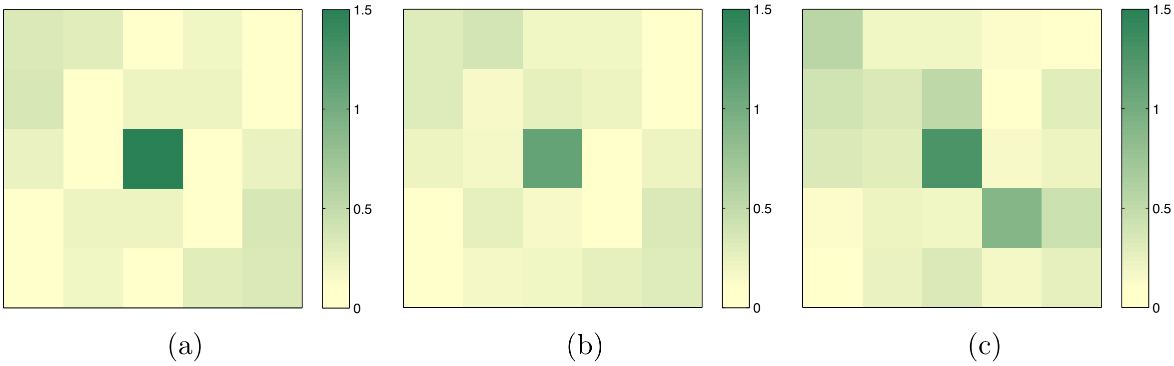

Figure III.5: Synthetic data set analysis: (a) matrix $\mathbf{A}$ autocorrelation; (b) cross-correlation of $\mathbf{A}$ and $\mathbf{A}^{ICA}$; (c) cross-correlation of $\mathbf{A}$ and $\mathbf{A}^{PCA}$.

III.4.3 Data set I: Urban area

The results presented in this section are obtained by applying the proposed ICTD on the RAMSES POLSAR X-band image acquired over Brétigny, France. Fig. III.1 illustrates the Pauli RGB coded image and shows the classification map used to define the observation data sets for the ICA algorithm.

III.4.3.1 The criterion selection

In the first place, the goal is to compare the ICA methods and choose the appropriate in the context of ICDT.

The first point of comparison between the proposed methods in complex independent components derivation is the possibility of identifying the class of trihedral reflectors present in the scene (Class 8 in Fig. III.1). The mask derived from the classification map allowed us to select the observation data set containing only target vectors from the regions in the image where the reflectors were placed. Further, one mixing matrix is estimated using each of the three criteria. In each case, the first and the second dominant components are presented on the symmetric scattering target adapted Poincaré sphere (Fig. III.6) [16]. The third component parameters are provided in the Table V.1 but, due to the values of helicity and symmetric scattering type phase, the illustration using a sphere is not possible for each of the applied methods.

All the methods are able to identify the class corresponding to the trihedral reflectors placed in the scene. A curious fact is that the second dominant component in each case appears to be symmetric as well. Concerning the FastICA, *kurtosis* criterion results however in both first and second components almost matching trihedral. This indicates apparent "splitting" of the trihedral on the two dominant components, which cannot be granted as a good estimation. On the other side, in case of the *logarithm* and the *square root* criteria, the second component, although symmetric, rather represents weaker dipole backscattering. In

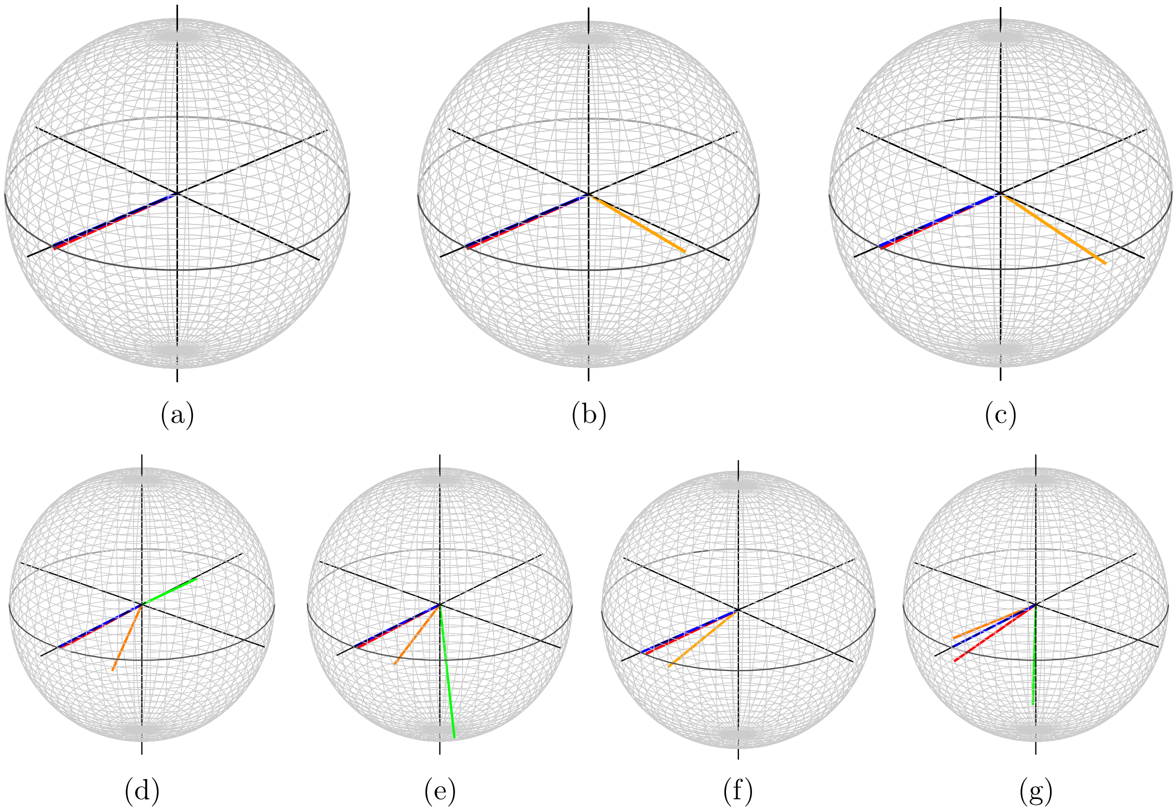

Figure III.6: RAMSES POLSAR X-band, Brétigny, France: Adapted Poincaré sphere representation of the trihedral class (Class 8) single scatteres (first component, second component, third component, trihedral) using (a) PCA, (b) ICA - C2 criterion, (c) ICA - C3 criterion, (d) ICA - FOBI, (e) ICA - JADE, (f) ICA - C1 criterion, (g) ICA - SOBI.

Table III.1: RAMSES X-band POLSAR data over Brétigny, France: roll-invariant parameters of the single scatterers in the trihedral class (Class 8). Trihedral expected values are: $\tau_m = 0°, \alpha_s = 0°, \Phi_{\alpha_s} = [-90, +90]$.

	Comp.	PCA	ICA-C2	ICA-C3	FOBI	JADE	ICA-C1	SOBI
$\tau_m[°]$	1st	-0.23	-0.28	-0.28	-0.32	-0.33	-0.33	0.32
	2nd	-37.15	-0.24	-0.36	0.50	0.43	-0.42	-1.18
	3rd	36.15	19.84	5.77	-1.80	-1.67	7.11	1.45
$\alpha_s[°]$	1st	0.50	0.53	0.53	0.90	1.14	1.49	3.09
	2nd	89.21	39.91	41.20	13.54	10.25	7.34	2.23
	3rd	87.90	58.49	54.97	36.19	34.43	24.82	21.84
$\Phi_{\alpha_s}[°]$	1st	-51.25	-27.42	-27.70	5.93	7.01	7.54	-77.67
	2nd	-18.64	2.56	-3.33	12.49	11.09	-9.60	-80.66
	3rd	68.86	77.92	-68.60	34.38	60.93	-83.22	-34.70

case of tensorial methods the third component appears to be symmetric, as well. However, with respect to established criterion, FOBI and JADE are placed behind the FastICA *logarithm* and *square root* criteria, although the trihedral "splitting" appears to be less conspicuous than in the case of *kurtosis*. SOBI completely fails to separate two dominant components.

The second point of comparison is the entropy estimation [106] (Fig. III.3). Having PCA based classic decomposition as a reference, we have compared the overall estimation of entropy (all classes), paying particular attention to the trihedral class. The entropy estimation scheme appears to be by far the best with the criteria (*C2* and *C3*). Actually, the gradation of methods corresponds exactly to the one obtained at the first point of comparison. This is however, not surprising, given that the inability to concentrate the energy of trihedral in the first component implies the "splitting" of the same and thus the inevitable increase of entropy.

The overall performance of the analysed ICA criteria in the frame of ICTD, seems to depend directly on the growth rate of the employed nonlinear function. The ICA based on slowly growing nonlinear functions (*logarithm* and *square root*) are more efficient in both identifying trihedral as the most dominant backscattering mechanism and, although it is an implication, in estimating entropy. The poor performances of selected tensorial decompositions rise from the fact elaborated in section I.3.2 - they depend too much on the particularities of the data 2nd and 4rd order structures. On the other side, FastICA is far more adaptive.

After choosing the second criterion (C2) of the NC FastICA as the most appropriate one, we have compared the ICA based ICDT with the PCA classic counterpart. The estimated first dominant component is nearly equivalent in both cases (Fig. III.8). It was this fact which inclined us toward the comparison of the estimated entropy as one of the criteria for selecting the appropriate non-linearity.

The second component, however, appears to be significantly different (Fig. III.8). This is both due to the constraint of mutual orthogonality present in the conventional approach and due to the useful information contained in the higher order statistical moments. The same class used in comparing the different criteria (Class 8) happens to be favourable for demonstrating the utility of the second dominant component. Namely, dipole as the second strongest single scatterer indicates the capability of recognizing the trihedral's edge diffraction, eventually.

III.4.3.2 Polarisation basis invariance

The same dataset was used to demonstrate the invariance with respect to more complex uniform transform - the change of the polarization basis. The observed scattering matrices are projected on the circular polarization basis and the obtained components parametrized using Circular Polarization Scattering Vector (CPSV) [111, 112]:

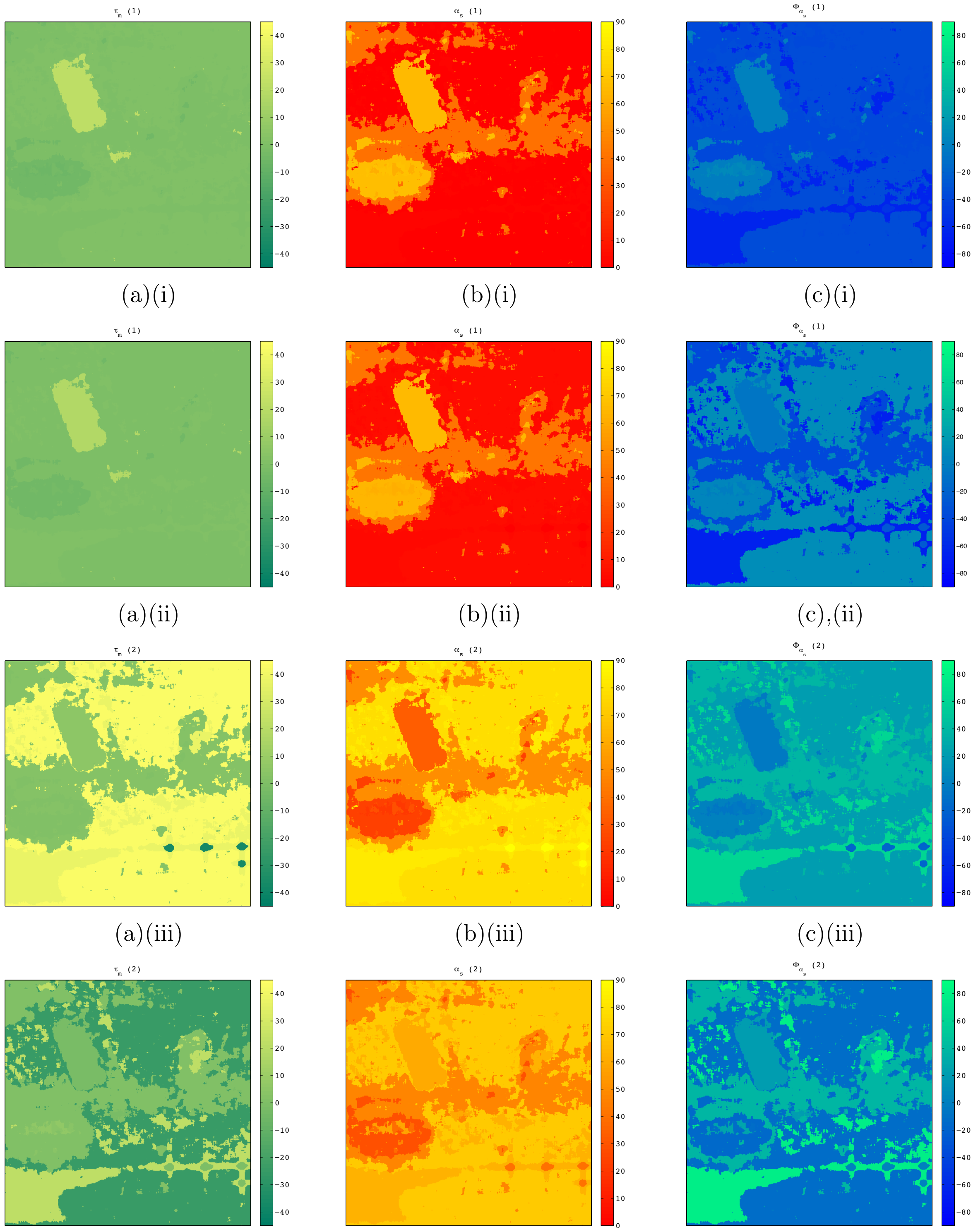

(a)(i) (b)(i) (c)(i)

(a)(ii) (b)(ii) (c),(ii)

(a)(iii) (b)(iii) (c)(iii)

(a)(iv) (b)(iv) (c)(iv)

Figure III.7: RAMSES POLSAR X-band, Brétigny, France: comparison between the TSVM parameters obtained by means of PCA (first most dominant component (i) and second most dominant component (iii) and by means of ICA (first most dominant component (ii) and second most dominant component (iv)): (a) τ_m, (b) α_s, (c) Φ_{α_s}.

$$\mathbf{k}_c = \sqrt{\mathrm{SPAN}} \exp j\Phi \begin{bmatrix} \sin\alpha_c \cos\beta_c \exp j(-\frac{4}{3}\Upsilon_c - 2\psi) \\ \cos\alpha_c \exp j\frac{8}{3}\Upsilon \\ -\sin\alpha_c \sin\beta_c \exp j(-\frac{4}{3}\Upsilon_c + 2\psi) \end{bmatrix}. \tag{III.20}$$

Among four parameters invariant to the rotation around the LOS (ψ) and to the target absolute phase (Φ): energy (SPAN), angle Υ_c, angle α_c and helicity defined as $\mathrm{Hel}_c = \sin^2\alpha_c\left[\cos^2\beta_c - \sin^2\beta_c\right]$, we have compared the last three with their counterparts derived from TSVM parametrisation in the Pauli basis. The angles Υ_c and α_c, if the target is symmetric ($\tau_m = 0$), correspond, respectively, to $\Upsilon_{\mathrm{TVSM}} = (\pi/2 - \Phi_{\alpha_s})/4$ and α_s. Helicity $\mathrm{Hel}_{\mathrm{TVSM}}$ is defined as a function of τ_m and the Huynen con-eigenvalues polarizability γ_H [7, 10]:

$$\mathrm{Hel}_{\mathrm{TVSM}} = \frac{\cos 2\gamma_H \sin 2\tau_m}{\cos^4\gamma_H \left(1 + tan^4\gamma_H\right)}. \tag{III.21}$$

On one side, as it is demonstrated in Fig. III.8 and in Table III.3, we obtain the perfect matching in terms of Hel (if we do not apply Eq. I.31). On the other side, even for the symmetric classes ($\tau_m \approx 0$), we don't have a perfect matching of Υ, which is justified by the values of α_c, which converge either to 0 or $\pi/2$, when this parameters becomes meaningless [101]. The angle α_c agrees perfectly with α_s in case of symmetric target. However, in order to reinforce this robustness proof, we have as well implicated $\alpha - \beta - \gamma - \delta$ parametrization, given in Eq. I.26 [15].

As it can be seen in Table III.3 and Fig. III.9, the derived α_p parameter, as expected, matches perfectly α_c, regardless of symmetry. Aside from this we compared the $\alpha - \beta - \gamma - \delta$ parameters derived conventionally (using PCA) with the ones obtained using our approach. It is the angle α_c (or α_p) which fortifies the conclusion arising from the TSVM parameters - the first dominant components are quite similar, but the second (non-orthogonal in our case) contains undoubtedly different information. This difference is certainly related to the removal of orthogonality constraint, which imposes conventionally $\alpha_{p1} + \alpha_{p2} \approx \pi/2$.

III.4.4 Data set II: Mountainous region

In order to analyse the performances in case of a distributed target, the proposed ICDT is applied on POLSAR images acquired over mountainous regions. Two ALOS L-band images of Chamonix, Mont Blanc in France, are used for this purpose. Their classification is given in Fig. III.10.

Based on *a priori* known ground truth provided by the *Électricité de France (EDF)*, we have labelled the classes (Table III.4) in two images with one of the four labels (dry snow, wet snow, bare ground and foldover) [99]. Using both the PCA based method (the first and the second component) and the first component of the ICA based method, we didn't manage to characterize the labelled classes with any of the derived roll-invariant parameters from Eq.

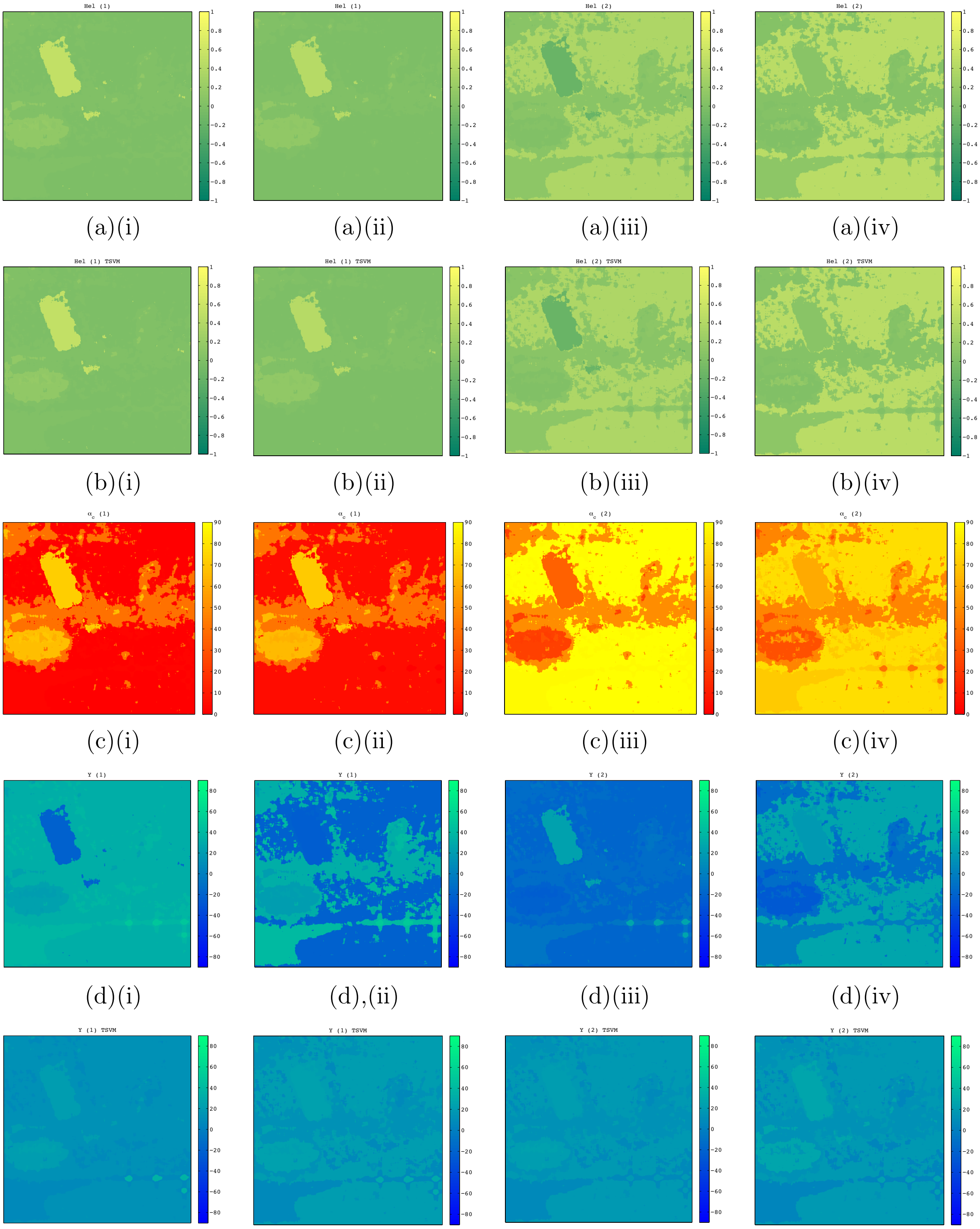

(a)(i) (a)(ii) (a)(iii) (a)(iv)

(b)(i) (b)(ii) (b)(iii) (b)(iv)

(c)(i) (c)(ii) (c)(iii) (c)(iv)

(d)(i) (d),(ii) (d)(iii) (d)(iv)

(e)(i) (e),(ii) (e)(iii) (e)(iv)

Figure III.8: RAMSES POLSAR X-band, Brétigny, France: comparison between the CPSV parameters obtained by means of PCA (first most dominant component (i) and second most dominant component (iii)) and by means of ICA (first most dominant component (ii) and second most dominant component (iv)): (a) Hel_c, (b) $\mathrm{Hel}_{\mathrm{TSVM}}$, (c) α_c, (d) Υ_c, (e) Υ_{TSVM}.

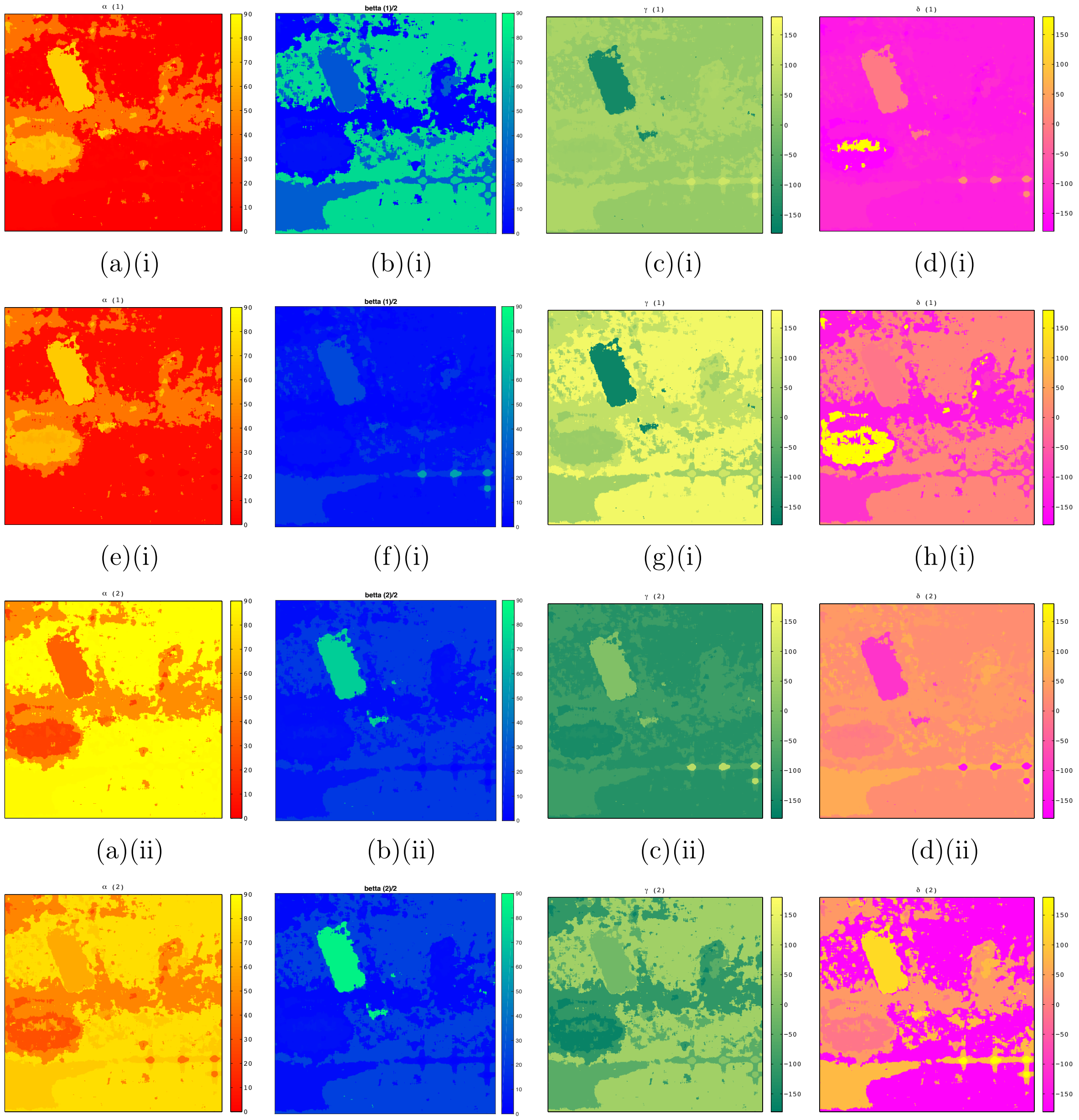

(a)(i) (b)(i) (c)(i) (d)(i)

(e)(i) (f)(i) (g)(i) (h)(i)

(a)(ii) (b)(ii) (c)(ii) (d)(ii)

(e)(ii) (f)(ii) (g)(ii) (h)(ii)

Figure III.9: RAMSES POLSAR X-band, Brétigny, France: comparison between the first (i) and the second (ii) most dominant components in terms of $\alpha-\beta-\gamma-\delta$ parameters: (a) α (PCA), (b) β mod $\pi/2$ (PCA), (c) γ (PCA), (d) δ (PCA), (e) α (ICA), (f) β mod $\pi/2$ (ICA), (g) γ (ICA), (h) δ (ICA);

Table III.2: RAMSES X-band POLSAR data over Brétigny, France: comparison of the derived TSVM parameters for three different rotations around the line of sight of the observation target vectors.

Parameter (rotation)	Method	Class II			Class IV			Class VI			Class VIII		
		1st	2nd	3rd	1st	2nd	3rd	1st	2nd	3rd	1st	2nd	3rd
$\tau_m[°](-20°)$	PCA	0.04	43.25	42.21	-0.22	2.71	-42.84	-6.71	1.7	-42.87	-0.23	-37.15	36.15
	ICA	-0.15	-25.12	42.73	-0.64	1.27	2.92	-4.71	6.15	-29.42	-0.28	-0.24	19.84
$\tau_m[°](0°)$	PCA	0.04	43.25	42.21	-0.22	2.71	-42.84	-6.71	1.7	-42.87	-0.23	-37.15	36.15
	ICA	-0.15	-25.12	42.73	-0.64	1.27	2.92	-4.71	6.15	-29.42	-0.28	-0.24	19.84
$\tau_m[°](20°)$	PCA	0.04	43.25	42.21	-0.22	2.71	-42.84	-6.71	1.7	-42.87	-0.23	-37.15	36.15
	ICA	-0.15	-25.12	42.73	-0.64	1.27	2.92	-4.71	6.15	-29.42	-0.28	-0.24	19.84
$\Phi_{\alpha_s}[°](-20°)$	PCA	-34	20.19	-24.89	-38.39	38.36	-84.16	6.02	-5.72	69.01	-51.25	-18.64	68.86
	ICA	9.6	-11.65	-34.12	-38.92	39.32	-34.23	-1.83	26.25	-74.18	-27.42	2.56	77.92
$\Phi_{\alpha_s}[°](0°)$	PCA	-34	20.19	-24.89	-38.39	38.36	-84.16	6.02	-5.72	69.01	-51.25	-18.64	68.86
	ICA	9.6	-11.65	-34.12	-38.92	39.32	-34.23	-1.83	26.25	-74.18	-27.42	2.56	77.92
$\Phi_{\alpha_s}[°](20°)$	PCA	-34	20.19	-24.89	-38.39	38.36	-84.16	6.02	-5.72	69.01	-51.25	-18.64	68.86
	ICA	9.6	-11.65	-34.12	-38.92	39.32	-34.23	-1.83	26.25	-74.18	-27.42	2.56	77.92
$\alpha_s[°](-20°)$	PCA	1.35	78.48	78.02	39.9	49.95	64.49	68.3	20.85	73.19	0.5	89.21	87.9
	ICA	5.03	71.48	18.74	41.7	47.1	84.59	62.19	58.22	33.23	0.53	39.91	58.49
$\alpha_s[°](0°)$	PCA	1.35	78.48	78.02	39.9	49.95	64.49	68.3	20.85	73.19	0.5	89.21	87.9
	ICA	5.03	71.48	18.74	41.7	47.1	84.59	62.19	58.22	33.23	0.53	39.91	58.49
$\alpha_s[°](20°)$	PCA	1.35	78.48	78.02	39.9	49.95	64.49	68.3	20.85	73.19	0.5	89.21	87.9
	ICA	5.03	71.48	18.74	41.7	47.1	84.59	62.19	58.22	33.23	0.53	39.91	58.49

Table III.3: RAMSES X-band POLSAR data over Brétigny, France: comparison of the derived TSVM, Cloude-Pottier and CPSV parameters.

Parameter	Method	Class II			Class IV			Class VI			Class VIII		
		1st	2nd	3rd	1st	2nd	3rd	1st	2nd	3rd	1st	2nd	3rd
$\tau_m[^\circ]$	PCA	0.04	43.25	42.21	-0.22	2.71	-42.84	-6.71	1.7	-42.87	-0.23	-37.15	36.15
	ICA	-0.15	-25.12	42.73	-0.64	1.27	2.92	-4.71	6.15	-29.42	-0.28	-0.24	19.84
$\Phi_{\alpha_s}[^\circ]$	PCA	-34	20.19	-24.89	-38.39	38.36	-84.16	6.02	-5.72	69.01	-51.25	-18.64	68.86
	ICA	9.6	-11.65	-34.12	-38.92	39.32	-34.23	-1.83	26.25	-74.18	-27.42	2.56	77.92
$\alpha_s[^\circ]$	PCA	1.35	78.48	78.02	39.9	49.95	64.49	68.3	20.85	73.19	0.5	89.21	87.9
	ICA	5.03	71.48	18.74	41.7	47.1	84.59	62.19	58.22	33.23	0.53	39.91	58.49
$\Upsilon_{\mathrm{TSVM}}[^\circ]$	PCA	14	17.45	16.28	12.9	12.91	43.54	24.01	23.93	5.25	35.31	17.84	39.71
	ICA	20.1	19.59	13.97	12.77	12.67	31.06	22.04	15.94	3.96	29.35	23.14	3.02
$\mathrm{Hel}_{\mathrm{TSVM}}$	PCA	0	0.37	-0.37	0.01	0.07	-0.08	0.16	0.04	-0.2	0	0.03	-0.03
	ICA	0	0.45	-0.5	0.02	0.03	0.02	0.14	0.17	0.21	0	0.01	0.12
$\Upsilon_c[^\circ]$	PCA	31.02	-17.25	-61.03	32.1	-12.87	1.19	20.98	-23.97	-4.84	50.37	27.16	-39.72
	ICA	-20.09	25.61	-45.8	32.23	-12.66	-31.06	22.96	-15.84	43.55	52.13	21.86	-47.63
Hel_c	PCA	0	0.37	-0.37	0.01	0.07	-0.08	0.16	0.04	-0.2	0	0.03	-0.03
	ICA	0	0.45	-0.5	0.02	0.03	0.02	0.14	0.17	0.21	0	0.01	0.12
$\alpha_c[^\circ]$	PCA	1.35	89.3	88.84	39.9	50.16	88.14	68.93	21.11	88.77	0.67	89.78	89.36
	ICA	5.04	78.28	85.69	41.72	47.15	84.62	62.6	59.03	64.36	0.77	39.91	66.28
$\alpha_p[^\circ]$	PCA	1.35	89.3	88.84	39.9	50.16	88.14	68.93	21.11	88.77	0.67	89.78	89.36
	ICA	5.04	78.28	85.69	41.72	47.15	84.62	62.6	59.03	64.36	0.77	39.91	66.28
$\beta_p[^\circ]$	PCA	76.06	20.19	69.8	1.12	4.74	86.79	7.66	10.88	81.95	70.71	0.81	89.19
	ICA	6.61	22.51	66.92	1.41	3.58	88.91	7.25	8.99	53.49	57.56	2.4	76.58
$\gamma_p[^\circ]$	PCA	33.4	-127.96	-150.67	59.79	-92.94	94.85	36.97	-132.16	71.22	111.26	81.9	-68.88
	ICA	158.49	49.66	-88.08	91.17	-109.95	-34.24	44.57	-105.09	89.8	111.33	11.32	-101.44
$\delta_p[^\circ]$	PCA	-134.2	17.55	174.86	-141.61	38.34	49.92	173.41	-6.87	25.73	19.77	-161.36	-132.05
	ICA	9.98	-172.32	-132.54	-141.08	39.27	-9.49	-178.62	25.94	-106.17	9.6	177.42	-83.09

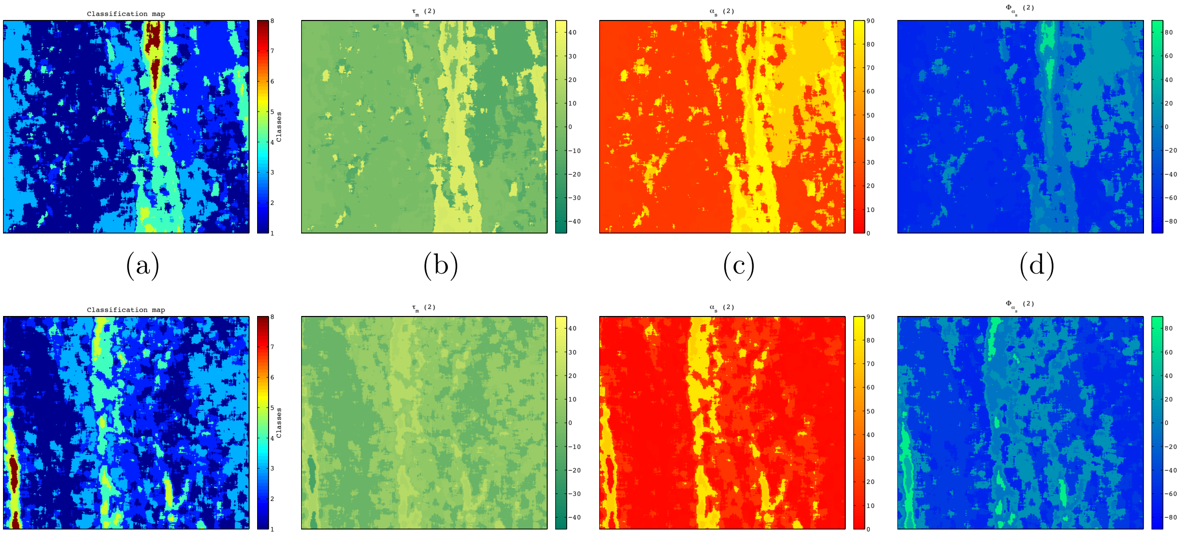

(a) (b) (c) (d)

(e) (f) (g) (h)

Figure III.10: ALOS L-band image acquired over Chamonix, Mont Blanc, France: (a) classification of image I; (b) $\tau_m(2)$ (ICA-C2, image I); (c) $\alpha_s(2)$ (ICA-C2, image I); (d) $\Phi_{\alpha_s}(2)$ (ICA-C2, image I); (e) classification of image II; (f) $\tau_m(2)$ (ICA-C2, image II); (g) $\alpha_s(2)$ (ICA-C2, image II); (h) $\Phi_{\alpha_s}(2)$ (ICA-C2, image II).

I.30. However, the second most dominant component of the ICA based ICDT proves to be useful. As it is demonstrated in Table III.4, the bare ground can be characterized with helicity parameter close to zero (symmetric target), the dry snow appears to have positive helicity, while the negative values can be associated to the wet snow.

The same data set serves to demonstrate the advantage of the "global approach" (observation data selected using classification) with respect to the "local" one (sliding window based selection). As it can be seen in Figure III.11, the local approach cannot be used to discriminate between the labelled classes. The reason is the insufficient size of the observation dataset, selected by a sliding window. On the other side, as it is demonstrated in Fig. III.12, augmenting the size of the same window causes the blurring effect. However, it improves the overall estimation of entropy, the remark emerging from the comparison with PCA counterpart.

III.5 Conclusion

In this chapter we presented a novel method for Polarimetric Incoherent Target Decomposition, based on the Independent Component Analysis [113]. Motivated by the Non-Gaussian nature of the clutter in high resolution POLSAR images, we aimed to exploit higher order statistical moments in retrieving single scatterers present in a scene. Given the stated equivalence between the Principal Component Analysis and the eigenvector decomposition (conventional approach), we generalized ICTD to the level of Blind Source Separation techniques (which

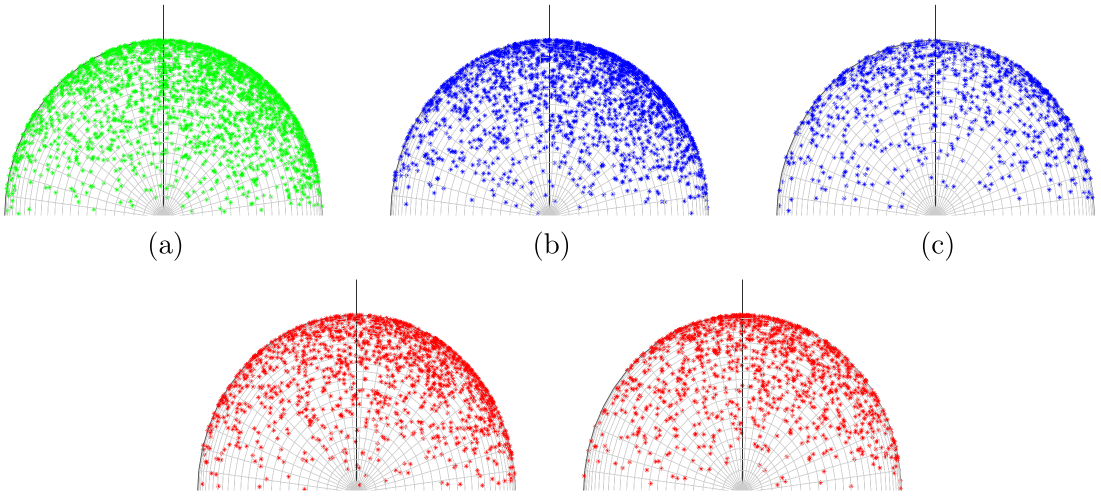
(a) (b) (c)
(d) (e)

Figure III.11: ALOS L-band image acquired over Chamonix, Mont Blanc, France: Adapted Poincaré sphere representation of the "locally" derived 2nd dominant components: (a) bare ground class (I/1); (b) wet snow class (I/2); (c) wet snow class (II/1); (d) dry snow class (II/2); (e) dry snow class (II/3).

Table III.4: ALOS L-band POLSAR data over Chamonix, Mont Blanc, France: comparison of TSVM parameters of the 2nd dominant component, obtained either by means of PCA or ICA, for the labelled classes.

Image/Class	Class description	$\tau_m[°]$		$\alpha_s[°]$		$\Phi_{\alpha_s}[°]$	
		PCA	ICA	PCA	ICA	PCA	ICA
I/1	bare ground	6.41	**-2.42**	12.64	20.33	18.45	-58.20
I/2	wet snow	-5.83	**-14.83**	68.77	72.50	-22.73	8.87
II/1	wet snow	5.84	**-7.72**	5.55	3.45	25.96	-48.09
II/2	dry snow	-6.96	**6.59**	20.22	18.49	-32.46	12.17
II/3	dry snow	-6.47	**9.30**	10.27	5.50	-85.02	-62.80

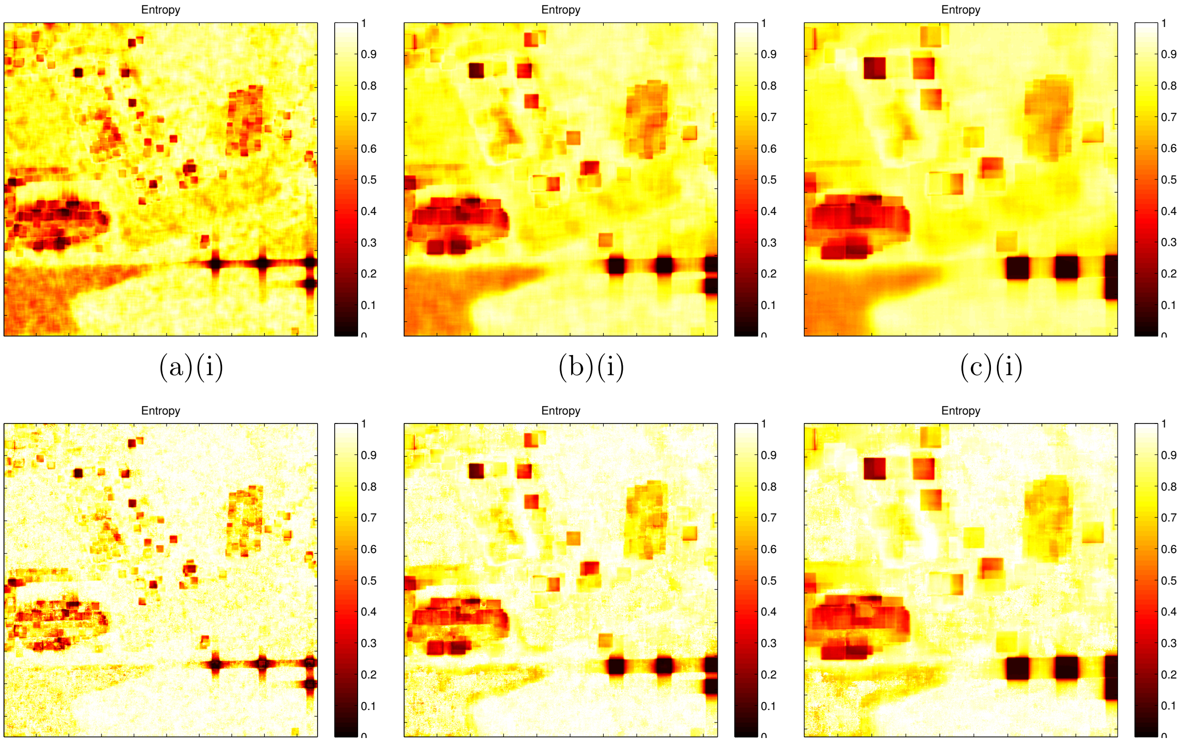

(a)(i) (b)(i) (c)(i)

(a)(ii) (b)(ii) (c)(ii)

Figure III.12: The entropy estimated using sliding window (local approach): (i) PCA based method, (ii) ICA based method. Sliding window size: (a) 11×11, (b) 21×21, (c) 31×31;

comprise both PCA and ICA). After comparing several criteria, the Non-Circular FastICA algorithm [100] based on maximizing the logarithmic non-linear function in order to achieve mutual independence of sources, proved to be the best approach in the framework of ICTD.

The proposed method is able to retrieve non-orthogonal single scatterers, which was illustrated using a synthetic POLSAR data set. It is invariant both under rotations of the observed target vectors and to the change of the polarization basis.

The results obtained by applying the proposed method on airborne POLSAR data over Brétigny anticipate the potential of the additional information provided by the second dominant component. This was possible by properly taking advantage of both the non-orthogonality property and the higher order statistical moments.

Finally, when dealing with distributed targets, the second dominant component appears to be of great interest, also. This was illustrated using Touzi's roll-invariant parameters, by achieving a better discrimination between the *a priori* labelled classes in mountainous regions.

Future work concerning this part of the thesis will enrol in two main directions. Firstly, we will try to explore as much as possible all the benefits of the new information contained in the second dominant component. Secondly, we will continue with applying and comparing different ICA methods in order to achieve the optimal decomposition with respect to the class of stochastic processes under study. The approach which seems to be particularly interesting is to achieve BSS using Maximum Likelihood Estimation.

Methodology: Conclusions

The methodological context of this thesis is devoted to the analysis of high and very high resolution SAR multichannel data, with a particular emphasis on polarimetric data. In one part, it concerns the assessment of statistical properties, which are in some way altered with respect to the conventional assumptions, the latter being founded on the hypothesis of Gaussianity. However, the focal point of this part, and the entire thesis, would be the accordingly proposed approach in polarimetric target decomposition, motivated by contemporary statistical hypotheses.

As indicated in the preface, the research presented in Chapters II and III, represents genuinely our efforts to answer two questions, which appear to be, at the moment, quite intriguing for a SAR community:

- Are the newly proposed statistical models truly appropriate for modelling POLSAR and other multi-dimensional SAR data sets?
- In terms of interpretation, what are we exactly gaining by acknowledging the departure from the Gaussianity assumption?

In Chapter I we have presented a brief but systematic review of most representative polarimetric target decompositions as well as the overview of statistical models, conventionally characterizing POLSAR datasets. The latter was reinforced by introducing the SIRV statistical model, named above as contemporary statistical hypothesis. This was done by generalizing a model related to the highly textured SAR image, occurring in case of heterogeneous SAR clutter. Finally, we introduced the family of selected BSS techniques, whose implication in the processing of POLSAR images, would represent the major contribution of this thesis.

The opinion on the first posed question constitutes Chapter II. Namely, here we introduced the test of spherical symmetry, which can be, under certain defined constraints, considered as a measure of fitness of the SIRV statistical model in the multi-dimensional POLSAR data characterization. At the same time, the circularity and the sphericity tests, originally defined for Gaussian multi-variate data, were extended to the SIRV model. The results and consequently, conclusions, obtained for a three-dimensional POLSAR dataset, were reinforced by applying the derived tests on a three-dimensional InSAR dataset.

It appears that the circularity property, often assumed in case of homogeneous clutter, can not be taken as granted in a SIRV case. The remarked circularity rejection can point out the defects in the calibration. At the same time, the circularity would be one of the defined constraints for a spherical symmetry test to be used for the SIRV conformity assessment. However, given that the latter does not necessarily reject non-circular pixels, the circularity test must be employed before. The sphericity property is analysed in order to grant legitimacy to the spherical symmetry test, given that the spherical pixels do not require multivariate modelling. Finally, with all the constrained respected, the spherical symmetry i.e. the SIRV model conformity test, leaded us to the conclusion that SIRV model fits rather well, except in case of urban area, where the deterministic scattering occurs dominantly.

The second question motivated us to propose a novel method for incoherent polarimetric target decomposition, which is founded on the previously stated non-Gaussianity hypothesis. Namely, by replacing the eigenvector decomposition, an equivalent to PCA, comprised in the conventional algebraic ICTD, with ICA method, in a certain manner, we generalize ICTD to the level of BSS. The new method provides mutually non-orthogonal and independent, rather than decorrelated, target vectors, parametrised by means of Touzi's TSVM. Given that they have been derived by exploiting higher-order statistical information, non-existent in case of Gaussian clutter, we consider this decomposition to be a contribution in the discussion related to the second posed question.

The first most dominant component appears to be equal as in the case of conventional approach, as well as the entropy estimation. However, the second most dominant components contains different information which, as we anticipate, can be useful in interpreting polarimetric datasets. To justify this anticipation we provide two examples. Firstly, in the case of application on urban target, when applied on pixels corresponding to the elementary trihedral, the second estimated component appears to be dipole, which can be associated to the trihedral edge diffraction. Secondly, in the case of distributed target i.e. snow in the mountainous region, using parametrised second component, we manage to distinguish bare ground, dry snow and wet snow.

Part B

APPLIED CONTEXT

Chapter IV

Remote sensing of snow

This chapter serves as an introduction to the applied context of the thesis. Namely, as stated in the preface, remote sensing is an applied scientific discipline, often intrinsically linked to Earth's sciences. Therefore, aside from the contributions, presented in Part A, which could be designed as rather methodological, we present in this part more concrete environmental problem, approached by means of SAR remote sensing, with the important incorporation of optical imagery.

Firstly we briefly introduce the snow cover properties, particularly emphasizing the parameter of special interest - Snow Water Equivalent (SWE). Then, the interaction of the snow cover with EM waves is discussed i.e. the employed simulator and the consequently assumed snow cover backscattering mechanism are presented. Finally, we discuss the aspect of spatial hydrological modelling, complementing remote sensing techniques in the context of particular problematic - SWE spatial estimation.

IV.1 Snow pack properties

Snow pack represents a mixture of ice crystals, liquid water and air. The proportion of these materials is a function of many factors, the most dominant one being the temperature. For temperatures below 0°, the proportion of liquid water is negligible so we consider that type of snow to be the dry snow. Above this temperature, certain quantity of liquid water can be present, in which case snow is characterized as the wet one [114]. As it will be elaborated in this chapter, the backscattering properties and therefore the methods employed in snow parameters extraction, differ significantly for these two types of snow.

IV.1.1 Basic physical properties

The most basic physical parameter of a snow pack is the snow density $\rho_s(kg/m^3)$:

$$\rho_s = \frac{m_i + m_w}{V_s} = \rho_i f_i + \rho_w f_w, \tag{IV.1}$$

with m_i and m_w being the mass of ice and water respectively, and V_s the volume of snow. Further, ρ_i is the density of ice ($\approx 917kg/m^3$), ρ_w is the density of water ($\approx 1000kg/m^3$), and f_i and f_w their volumetric fractions.

In the mountainous regions, snow pack represents a significant water resource, used in agriculture, power production, as a drinking water supply etc. The exact amount of liquid water contained in the snow pack is given through the physical quantity - Snow Water Equivalent (SWE). It would be a function of two independent snow physical properties [115]: snow density (Eq. IV.1), and the second basic snow cover property - the depth of a snow pack (d):

$$\text{SWE} = \frac{1}{\rho_w} \int_0^d \rho_s dz \tag{IV.2}$$

In other words, SWE is defined as the depth of the layer of liquid water that would be produced if all the ice in the snow pack were melted [114]. Due to numerous difficulties in performing *in situ* measurements (high altitudes, global coverage), the estimation of this quantity turns out to be suitable for remote sensing application. The advantages evoked in the preface, as significant snow pack penetration, along with the high spatial resolution and the clouds penetration capability, candidate SAR remote sensing for this kind of application [116, 117].

Estimating SWE by means of remote sensing implies estimating independently density and depth, where knowing density, in fact means, knowing ice volumetric fraction - dry snow density (ρ_{ds}) and the water volumetric fraction, or the third basic snow property - wetness $w(\%)$. However, either the target vector in the POLSAR image, or the intensity pixel in the single channel SAR image, depend on many more, both sensor and snow cover parameters [115].

On one side, we can consider sensor parameters i.e. local incident angle (LIA), frequency and polarization, as known. On the other side, snow pack parameters which influence radar response, as the three introduced snow parameters, along with the snow and the underlying ground dielectric permeabilities and the surface roughness properties, are generally not *a priori* known.

IV.1.2 Dielectric and surface roughness properties

Snow dielectric permittivity depends upon the type of snow. Namely, in the context of their dielectric properties, above defined dry and wet snow behave like two different materials. Dry snow cover is characterized by a dielectric constant, which is a function of dry snow density only (ρ_{ds}) [114, 118]:

$$\varepsilon'_{ds} = 1 + 1.9\rho_{ds} = 1 + 1.9\rho_{ice} f_{ice}, \tag{IV.3}$$

where ρ_{ds} depends on ice volume fraction (f_{ice}), with ρ_{ice} having a value $917 kg/m^3$. In this case, the dielectric constant is purely real, indicating the absence of medium dielectric losses.

On the other side, wet snow dielectric constant is a complex quantity, function of wetness and of frequency (f), as well. For the frequency range of $3GHz - 15GHz$ it is [114, 119]:

$$\varepsilon_{ws} = 1 + 1.83\rho_{ds} + 0.02w^{1.105} + \frac{0.073w^{1.31}}{1 + (\frac{f}{9.07})^2} + j\frac{0.073\frac{f}{9.07}w^{1.31}}{1 + (\frac{f}{9.07})^2}, \tag{IV.4}$$

Unlike the dry snow one, wet snow dielectric constant, being a complex quantity, has its imaginary part, indicating the presence of the medium absorption losses.

Finally, surface roughness is described using surface root mean square (RMS) height deviation and surface correlation length.

The root mean square height deviation σ_{RMS} is given by:

$$\sigma_{RMS}^2 = \langle (h(x,y) - \langle h(x,y) \rangle)^2 \rangle = \langle h^2(x,y) \rangle - \langle h(x,y) \rangle^2 \tag{IV.5}$$

where $h(x,y)$ represents a surface height at given coordinates x, y.

Surface correlation length l_c is defined using the autocorrelation function for one dimension (x), which shows how the surface profile is similar to itself when it is displaced for ξ in x or any other direction in general:

$$\rho(\xi) = \frac{\langle (h(x+\xi) - \langle h(x) \rangle)(h(x) - \langle h(x) \rangle) \rangle}{\sigma^2} \tag{IV.6}$$

with l_c being a value of ξ for which function drops to $\rho(0)/e$. If we assume the autocorrelation function to be the same for each direction, we have isotropic surface roughness.

In case of natural surfaces the exponential autocorrelation function is adopted [114]. Therefore, for snow pack surface, but also for the underlying ground, the most commonly employed function would be the isotropic exponential correlation function:

$$\rho(\xi) = \exp\left(-\frac{|\xi|}{l_c}\right) \tag{IV.7}$$

At the end, it would be important to mention the liquid water distribution, which can be very important for the wet snow characterization, although estimating it appears to be quite difficult [120].

Therefore, one can deduce that the estimation of the snow basic properties represents an underdetermined problem, which at first, requires a sophisticated electromagnetic modelling i.e. an appropriate backscattering model. At this point, we ought to remark that any effort toward inverting that model and estimating these parameters, appears to be conditioned by the proper identification of a snow type. Following this remark, in Chapter V we propose a method for wet snow detection, and here we turn to introducing a snow microwave backscattering mechanism. The latter represents a base for both the mentioned detection method and all our efforts undertaken in estimating the snow cover basic physical parameters constituting SWE by means of SAR remote sensing.

IV.2 Snow backscattering mechanism

In [120], we have implemented a simulator which was, in its refurbished version, used in deriving hypotheses about the snow backscattering mechanism, employed in Chapters V and VI. Furthermore, the calibrated version of this simulator is an integral component of the method forming Chapter V.

Here, we present the concept of the simulator, which is based on the fundamental scattering theories: Integral Equation Model (IEM-B) and Dense Media Radiative Transfer (DMRT). At the end, we provide the most important conclusions deduced from the snow cover backscattering simulations [121, 122], granted as above voiced hypotheses.

The intensity value of a single channel SAR image represents the appropriate measure of backscattering coefficient. For the purpose of simplification, the snow cover backscattering mechanism and the employed simulator in this section will be presented in the context of this parameter, although an extension to the Mueller matrix is provided in the Appendix A.

Therefore, particularly used for distributed target characterization, the backscattering coefficient (σ^0) is a dimensionless variable, representing a ratio between the backscattering cross-section to physical area (A) in the monostatic radar equation:

$$P_r = \frac{\lambda^2 G^2 P_t}{(4\pi)^3 \eta R^4} \sigma^0 A \tag{IV.8}$$

where P_r and P_t represent, respectively, received and transmitted power, G is antenna gain, η - efficiency, λ - wavelength, and R would be a distance between antenna and the target.

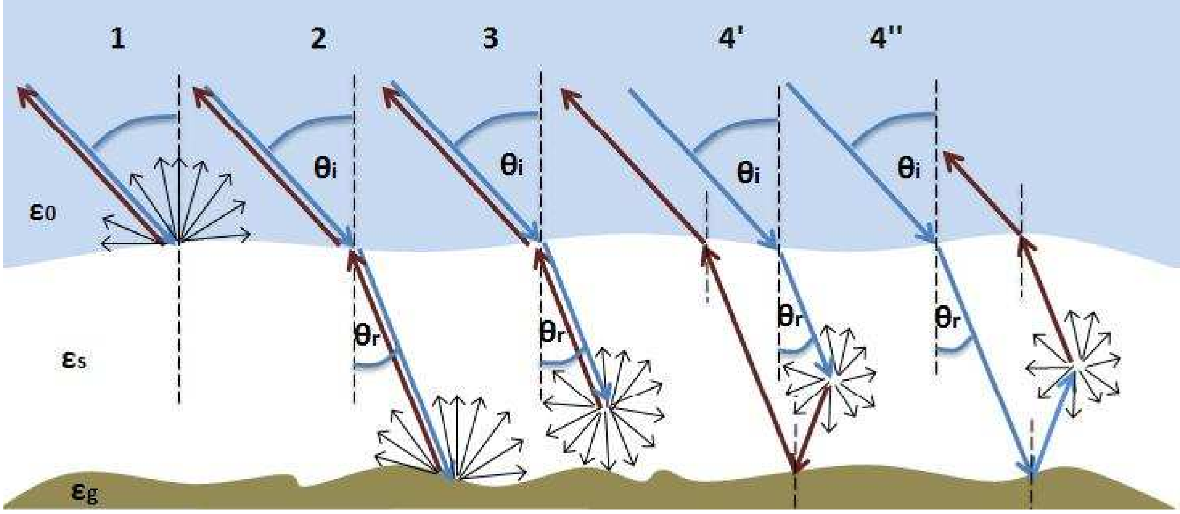

Figure IV.1: Single-layer snow cover backscattering sub-components.

IV.2.1 Single-layer backscattering simulator

Total backscattering (σ_0) of the single-layer snow pack can be decomposed as the sum of the four components [123],[124] (Fig. IV.1):

1. Snow pack surface component (σ_s),
2. Underlying ground surface component(σ_{gr}),
3. Snow volume component (σ_v),
4. Ground-volume interaction component(σ_{gv}).

$$\sigma_0 = \sigma_s + \sigma_{gr} + \sigma_v + \sigma_{gv} \tag{IV.9}$$

The backscattering components for co-polarized channels ($pp = hh \vee vv$), are given as [123]:

$$\sigma_s = \sigma(\varepsilon_0, \theta_i, \theta_i, \phi_s - \phi, \frac{\varepsilon_s}{\varepsilon_0}, \sigma^s_{RMS}, l^s_c), \tag{IV.10}$$

$$\sigma_{gr} = \frac{\mu_i}{\mu_r} T^2_{pp}(\theta_r, \theta_i) e^{(\frac{-2\kappa_e d}{\mu_r})} \sigma(\varepsilon_s, \theta_r, \theta_r, \phi_s - \phi, \frac{\varepsilon_g}{\varepsilon_s}, \sigma^g_{RMS}, l^g_c), \tag{IV.11}$$

$$\sigma_v = a\frac{\mu_i}{2} T^2_{pp}(\theta_r, \theta_i)[1 - e^{(\frac{-2\kappa_e d}{\mu_r})}] P_{pp}(\mu_r, -\mu_r, \phi_s - \phi), \tag{IV.12}$$

$$\begin{aligned} \sigma'_{gv} &= \mu_i a R_{pp}(\theta_r,\theta_i,\varepsilon_g)\frac{\kappa_e d}{\mu_r} e^{(\frac{-2\kappa_e d}{\mu_r})-4k^2\sigma^s_{RMS}\mu_r^2} \\ &\cdot \; T^2_{pp}(\theta_r,\theta_i)P_{pp}(-\mu_r,-\mu_r,\phi_s-\phi), \end{aligned} \tag{IV.13}$$

$$\begin{aligned} \sigma''_{gv} &= \mu_i a R_{pp}(\theta_r,\theta_i,\varepsilon_g)\frac{\kappa_e d}{\mu_r} e^{(\frac{-2\kappa_e d}{\mu_r})-4k^2\sigma^s_{RMS}\mu_r^2} \\ &\cdot \; T^2_{pp}(\theta_r,\theta_i)P_{pp}(\mu_r,\mu_r,\phi_s-\phi). \end{aligned} \tag{IV.14}$$

Snow pack surface backscattering coefficient (Eq.IV.10) is calculated using IEM-B) [123], as a function of local incidence elevation angle (θ_i), azimuth angle (ϕ_s), snow dielectric constant, surface root mean square hight (σ^s_{RMS}) and its correlation length (l^s_c).

For better comprehension of the underlying ground backscattering component (Eq. IV.11), three different impacts on backscattering coefficient can be distinguished:

- Air-snow interface direct impact, represented through the incident and refracted angle (θ_r), cosines ratio ($\frac{\mu_i}{\mu_r}$) and squared Fresnel transmission coefficient ($T^2_{pp}(\theta_r,\theta_i)$),
- Snow medium propagation impact, meaning the extinction impact ($e^{(\frac{-2\kappa_e d}{\mu_r})}$),
- Ground surface backscattering in the presence of snow, derived by applying the same model as in the case of snow surface. The presence of snow, through the snow dielectric constant, defines the refracted angle (behaving as an incidence one at the ground surface), refracted wave wavelength and ground-snow dielectric contrast ($\frac{\varepsilon_g}{\varepsilon_s}$).

Figuring in the last three sub-components and being the most important volume scattering parameter, the extinction coefficient κ_e is defined through the radiative transfer equation:

$$\frac{dI(\mathbf{r},\mathbf{s})}{ds} = -\kappa_e I(\mathbf{r},\mathbf{s}) + \int_{4\pi} P(\mathbf{r},\mathbf{s}')I(\mathbf{r},\mathbf{s}')\,\mathrm{d}\Omega', \tag{IV.15}$$

which models electromagnetic waves propagation through a particular medium. It is computed by employing the Dense Media Radiative Theory (DMRT) [125].

In case of the dry snow, an ensemble of spherical ice particles with radius r_{ice} and dielectric permittivity ε_{ice}, placed in the air as a host medium, has been assumed. Appropriately, the Quasi Crystalline Approximation (QCA) was employed [126], implying that the influence of the scattered waves on other particles' scattering was not neglected. The extinction is estimated by means of effective permittivity ($\varepsilon^{eff'}$ and $\varepsilon^{eff''}$), by neglecting the electromagnetic absorption (real ice dielectric constant):

$$\begin{aligned}
\kappa_e &= 2k\Im\left\{\sqrt{\varepsilon^{eff'} + j\varepsilon^{eff''}}\right\}, \\
\varepsilon^{eff'} &= 1 + \frac{3f_{ice}(\varepsilon_{ice}-1)}{3+(1-f_{ice})(\varepsilon_{ice}-1)}, \\
\varepsilon^{eff"} &= \frac{2(kr_{ice})^3 f_{ice}(\varepsilon_{ice}-1)^2(1-f_{ice})^4}{[3+(1-fice)(\varepsilon_{ice}-1)]^2(1+f_{ice})^2}.
\end{aligned} \tag{IV.16}$$

On the other side, wet snow rather required Quasi Crystalline Approximation with Coherent Potentials (QCA-CP) [126], capable of accounting for larger variations in dielectric permittivity between the particles and the host media. The former one appeared as suitable given that the water inclusions were modelled through the mixed ice-water spherical particles:

$$r_{part} = r_{ice}(1 + \frac{f_{part} - f_{ice}}{f_{ice}})^{\frac{1}{3}}, \tag{IV.17}$$

$$\frac{\varepsilon_{part}-1}{\varepsilon_{part}+1} = \frac{(\varepsilon_{lw}-1)(\varepsilon_{ice}+2\varepsilon_l w) + \left(\frac{r_{ice}}{r_{part}}\right)^3(\varepsilon_{ice}-\varepsilon_{lw})(1+2\varepsilon_{lw})}{(\varepsilon_{lw}+2)(\varepsilon_{ice}+2\varepsilon_{lw}) + 2\left(\frac{r_{ice}}{r_{part}}\right)^3(\varepsilon_{ice}-\varepsilon_{lw})(\varepsilon_{lw}-1)}.$$

In this case, the effective permittivity has slightly different form:

$$\begin{aligned}
\varepsilon^{eff'} &= 1 + \frac{3f_{part}(\varepsilon_{part}-1)\varepsilon^{eff0}}{3\varepsilon^{eff0}+(1-f_{part})(\varepsilon_{part}-1)}, \\
\varepsilon^{eff"} &= \frac{2(k_{part}r\sqrt{\varepsilon^{eff0}})^3 3f_{part}(\varepsilon_{part}-1)^2(1-f_{part})^4\varepsilon^{eff0}}{[3\varepsilon^{eff0}+(1-fpart)(\varepsilon_{part}-1)]^2(1+f_{part})^2},
\end{aligned} \tag{IV.18}$$

The wet snow electromagnetic absorption is not negligible and therefore it is necessary to introduce the albedo coefficient a as the ratio of the scattering and the extinction coefficient [125]:

$$a = \frac{\kappa_s}{\kappa_e} = \frac{2r_{part}^3 f_{part}\left|\frac{k^2(\varepsilon_{part}-1)\varepsilon^{eff0}}{3\varepsilon^{eff0}+(1-fpart)(\varepsilon_{part}-1)}\right|^2\frac{(1-f_{part})^4}{(1+f_{part})^2}}{\kappa_e}. \tag{IV.19}$$

At this point we ought to mention the most important deficiency of this simulator, which would be non-sensitivity to the shape of water distribution.

The volume backscattering component (Eq. IV.12) is as well affected by air-snow boundary transmission, but importantly, it is the consequence of the extinction phenomena. It is a function of normalized (relative to the scattering coefficient) Rayleigh phase coefficient ($P_{pp}(\mu_r, -\mu_r, \phi_s - \phi)$) [124], giving the amount of energy scattered in the backward direction.

Component named ground-volume interaction is related to the waves directed by the volume and then specularly reflected toward the antenna (Eq. IV.14) and the waves specularly reflected of the ground and then redirected toward the direction of interest by the volume (Eq. IV.14). Specular reflection is introduced through Fresnel reflection power coefficient $R_{pp}(\theta_r, \theta_i, \varepsilon_g)$ corrected with a factor $4k^2\sigma^s_{RMS}\mu_r^2$, which brings the terrain roughness into the account. The change of the waves direction caused by volume is modelled via the normalized Rayleigh phase matrix.

IV.2.2 Multi-layer backscattering simulator

The developed multi-layer simulator assumes three out of four presented subcomponents. The fourth one, the ground-volume interaction component has been neglected for simplification, given its minor contribution to the total backscattering.

The first backscattering component in this case accounts not only for the snow pack surface ($j = 0$), but as well for the interfaces between different layers. Therefore it is defined for a n-layer snow cover as:

$$\sigma_s = \sum_{j=0}^{n-1} \frac{\mu_i}{\mu_{r_j}} \mathrm{Att}_{\mathrm{down}}(j)\sigma(\varepsilon_{s_j}, \theta_{r_j}, \theta_{r_j}, \phi_s - \phi, \frac{\varepsilon_{s_{j+1}}}{\varepsilon_{s_j}}, \sigma_{RMS}^{s_{j+1}}, l_c^{s_{j+1}})\mathrm{Att}_{\mathrm{upp}}(j), \qquad \text{(IV.20)}$$

with $\mathrm{Att}_{\mathrm{down}}(j)$ and $\mathrm{Att}_{\mathrm{upp}}(j)$ being the downwards and upwards attenuations, respectively:

$$\begin{aligned} \mathrm{Att}_{\mathrm{down}}(j) &= \prod_{i=1}^{j} \exp(-2\kappa_{e_i} d_i/\mu_{r_i}) T_{i-1,i}, \qquad \text{(IV.21)} \\ \mathrm{Att}_{\mathrm{upp}}(j) &= \prod_{i=1}^{j} T_{i,i-1} \exp(-2\kappa_{e_i} d_i/\mu_{r_i}). \end{aligned}$$

The parameters indexed with i correspond to the parameters provided in the previous section, but here characterizing the ith layer of snow, $T_{i,i-1}$ would be the Fresnel transmission between ith and $(i-1)$th layer. In case of $j = 0$, $\mu_{r_0}, \varepsilon_{s_0}, \theta_{r_0}$, correspond respectively to $\mu_i, \varepsilon_0, \theta_i$.

The underlying ground component would be an addend of Eq. IV.20 for $j = n$ [127], in which case $\varepsilon_{s_{n+1}}, \sigma_{RMS}^{s_{n+1}}, l_c^{s_{n+1}}$, correspond respectively to $\varepsilon_g, \sigma_{RMS}^g, l_c^g$.

Volume scattering components is modelled as:

$$
\begin{aligned}
\sigma_v &= 4\pi\mu_i \sum_{i=1}^{n} \mathrm{Att}_{\mathrm{down}}(i-1) T_{i-1,i} \frac{1-\exp(-2\kappa_{e_i} d_i/\mu_{r_i})}{2\kappa_{e_i}} \\
&\cdot \quad \mathbf{P}_{pp}(\mu_{r_i}, \mu_{r_i}, \phi_s - \phi) T_{i,i-1} \mathrm{Att}_{\mathrm{upp}}(i-1)
\end{aligned} \tag{IV.22}
$$

After simulating snow cover in [121] and [122], the most important conclusions, taken as the founding hypotheses for the method presented in the following chapter, would be the dominance of underlying ground component in case of the dry snow and the dominance of the snow pack surface components for the wet snow. As well, the sensitivity studies performed with respect to the change of density and depth, indicated far more encouraging results when the density estimation is concerned.

IV.3 SWE hydrological modelling

Given the underdetermination of the SWE estimation problem using single channel SAR image, we have complemented the remote sensing techniques with the hydrological model developed by EDF for our study area. This way, we have rather managed to integrate the remote sensing into the SWE estimation.

Therefore, as an introductory to the approach presented in Chapter VI, here we present the SWE sub-model of the internally developed hydrological model *MOdèle à Réservoirs de Détermination Objective du Ruissellement* (MORDOR) [128], used by EDF, for the estimation of the contribution of the melted snow to their water accumulations.

The MORDOR model principally covers five hydrological processes [129]: evapotranspiration, surface runoff, infiltration, dewatering and snow accumulation and melting. Basically, it assumes five different reservoirs and models their mutual exchange. They represent: snowpack, surface supply (absorption), stock of water which transforms to vapour, intermediary supply and deep supply (rivers).

Our particular interest is the sub-model dealing with the snow accumulation and melting.

Two versions of this snow sub-model exist:

- The historical version, which is lumped and represents the snowpack with only a single reservoir, impossible to compare with Moderate-Resolution Imaging Spectroradiometer (MODIS) data or local *in situ* measurements,
- The distributed version, named SWEEP (Snow Water Equivalent Estimation at the Pixel scale), where comparison with distributed and *in situ* measurements are able.

SWEEP is a distributed degree-day model, taking into account snowpack temperature, liquid water content and ground melt. For each pixel, daily air temperature $(T_{\min}(i), T_{\mathrm{mean}}(i), T_{\max}(i))$ and precipitation $P(i)$ are available.

The phase of the precipitation, a S-shape function, allows to discriminate between rain and snow:

$$\Phi_{\mathrm{P}}(i) = 1 - \frac{1}{1 + \exp\frac{10*(T_{\mathrm{mean}}(i) - T_{50})}{\Delta}}, \tag{IV.23}$$

with Δ=4 and T_{50}=1. Rain $R(i)$ and snow $S(i)$ are further derived as:

$$R(i) = P(i)\Phi_{\mathrm{P}}(i), \tag{IV.24}$$

$$S(i) = c_{\mathrm{p}}P(i)(1 - \Phi_{\mathrm{P}}(i)). \tag{IV.25}$$

with c_{p} being the snow accumulation coefficient.

The temperature of the snow pack evolves with minimal temperature $T_{\mathrm{min}}(i)$ as:

$$T_{\mathrm{S}}(i) = T_{\mathrm{S0}}T_{\mathrm{min}}(i) + (1 - T_{\mathrm{S0}})T_{\mathrm{S}}(i), \tag{IV.26}$$

with $T_{\mathrm{S0}} = 0.04$, and constraint $T_{\mathrm{S}} \leq 0$.

The snowmelt process is modeled with a degree-day factor:

$$M(i) = k_{\mathrm{f}} * (T_{\mathrm{mean}}(i) + T_{\mathrm{S}}(i)) \tag{IV.27}$$

where k_{f} is the degree-day factor, defined as the snow melting coefficient.

The snow water equivalent evolves respect with the snow accumulation and the snow melt:

$$\mathrm{SWE}(i) = \mathrm{SWE}(i-1) + S(i) - M(i) - \mathrm{gm}, \tag{IV.28}$$

with $\mathrm{gm} = 0.6\,mm/day$ being the ground melting.The snowpack is able to store liquid water until liquid water content of 10%. After the liquid water flows.

Namely, based on the precipitation and the air temperature measurements, this sub-model estimates the quantity of water contained in the snowpack (one of the assumed reservoirs). Aside from these meteorological parameters, the two coefficients characterizing the accumulation and the melting processes c_{p} and k_{f}), define the SWE as well.

The accumulation during one day is estimated rather commonly, using both precipitation and air temperature, where the later one defines the ice fraction in the former. However, the melting estimation, being more sophisticated, is performed by simultaneously assessing the superficial melting, melting due to the rain and the one caused by the geothermal flux. The first of them is modelled using a degree day model which relies on both the air temperature and the temperature of the snow. Only this summand is corrected by the coefficient k_{f}.

Unlike the precipitation and the air temperature, which can be measured [130] at the distributed meteorological ground stations and then interpolated [131], the coefficients c_{p} and k_{f} have to be either assumed or determined based on some reliable measurements. The later is the point where we integrate remote sensing techniques and the topic of Chapter VI - proposing a method which exploits remote sensing measurements in order to derive the snow accumulation and melting correction coefficients.

Chapter V

Stochastic snow mapping using high-resolution SAR data

As we stated in Chapter IV any effort in inverting snow backscattering model in order to estimate snow pack parameters, appears to be conditioned by the formerly performed discrimination between the dry snow and the wet one. Therefore, using the introduced single-layer and multi-layer backscattering simulator and above all, using the asserted conclusions, we developed a change detection method carrying out this indispensable step in remote sensing of snow [2, 132]. Furthermore, relaying on the single SAR image statistics, elaborated in Chapter I, the method presented in this chapter, estimates wet snow probability by accounting for the local speckle statistics, which makes it stochastic.

The chapter is organized as follows. Section II briefly introduced the required input data. The analysis of the wet/dry backscattering ratio relying on the backscattering simulator, along with its calibration, are given in Section III. The stochastic approach is introduced in the following section. In Section V, we present the results obtained with two TerraSAR-X dual-pol stripmap images acquired in the French Alps. This section provides the performance analyses, and therefore serves as the overture to the conclusion of this chapter.

V.1 Introduction

As indicated in the preceding chapter the dry and the wet snow behave like two completely different materials with respect to their dielectric properties: the wet snow contains liquid water with a dielectric constant differing significantly from the one of the ice. This fact is pointing out to a difference in backscattering mechanisms [133], and consequently that different feature extraction methods should be applied. Therefore, the estimation of any snow pack parameter by means of SAR remote sensing, requires firstly the proper identification of the snow cover type [134].

Although studies on snow mapping by polarimetric SAR existed already [135], it was not before the ERS-1 started providing repeat pass images that the idea of snow mapping based on SAR multitemporal data appeared [136]. Further refinement on the initial change detection method leaded eventually to the compact algorithm based on the ratio of two C band SAR images introduced in [137]. The Nagler and Rott method requires as inputs the SAR wet snow image and the reference SAR image of the dry snow (or the snow free terrain). After corregistration, either mutilooking or speckle filtering is applied on the two SAR intensities before constructing the backscattering ratio image. This ratio image is then georeferenced and an unique threshold of -3 dB is used to discriminate the wet snow from other surfaces. The expected difference in backscattering is justified by the increased electromagnetic absorption of the wet snow. The resulting maps are successfully validated by using snow terrain optical images. Subsequently, constraints concerning both sensor and target parameters with respect to the validity of the defined threshold have been introduced [138].

We propose in this chapter an alternative change detection method with X-band SAR data for wet snow detection. The goal is to introduce an algorithm which is eventually more suited to the presence of the speckle noise and is based on, to some degree modified hypothesis on wet/dry snow backscattering ratio behaviour. The first novelty is related the choice of the reference image. It is supposed to be the image acquired in the accumulation (winter) season, when the dry snow assumption is valid.

The *state of the art* backscattering measurements [139] indicate the complex relationship in terms of backscattering between the two types of snow, which cannot be simplified by assuming increased absorption and therefore lower backscattering of the wet snow, for all values of LIA. In order to account for this fact, we employ simultaneously the single-layer and the multi-layer snow backscattering simulator, introduced in the precedent chapter. The simulators are calibrated with the scatterometer measurements in C band, before being used to analyse a wet/dry snow backscattering ratio as a function of LIA, in X band. Thereupon, we determine the range of ratio values, pointing to the presence of the wet snow. The derived range slightly differs with respect to the conventional assumption used in the C band.

Further, the speckle noise statistics is introduced through the local estimation of the intensity ratio probability. This allows additional enhancement of the discrimination accuracy, which is illustrated through the matching of the independently obtained HH and VV maps. Finally, we analyse the performances by comparing snow maps obtained using TerraSAR-X

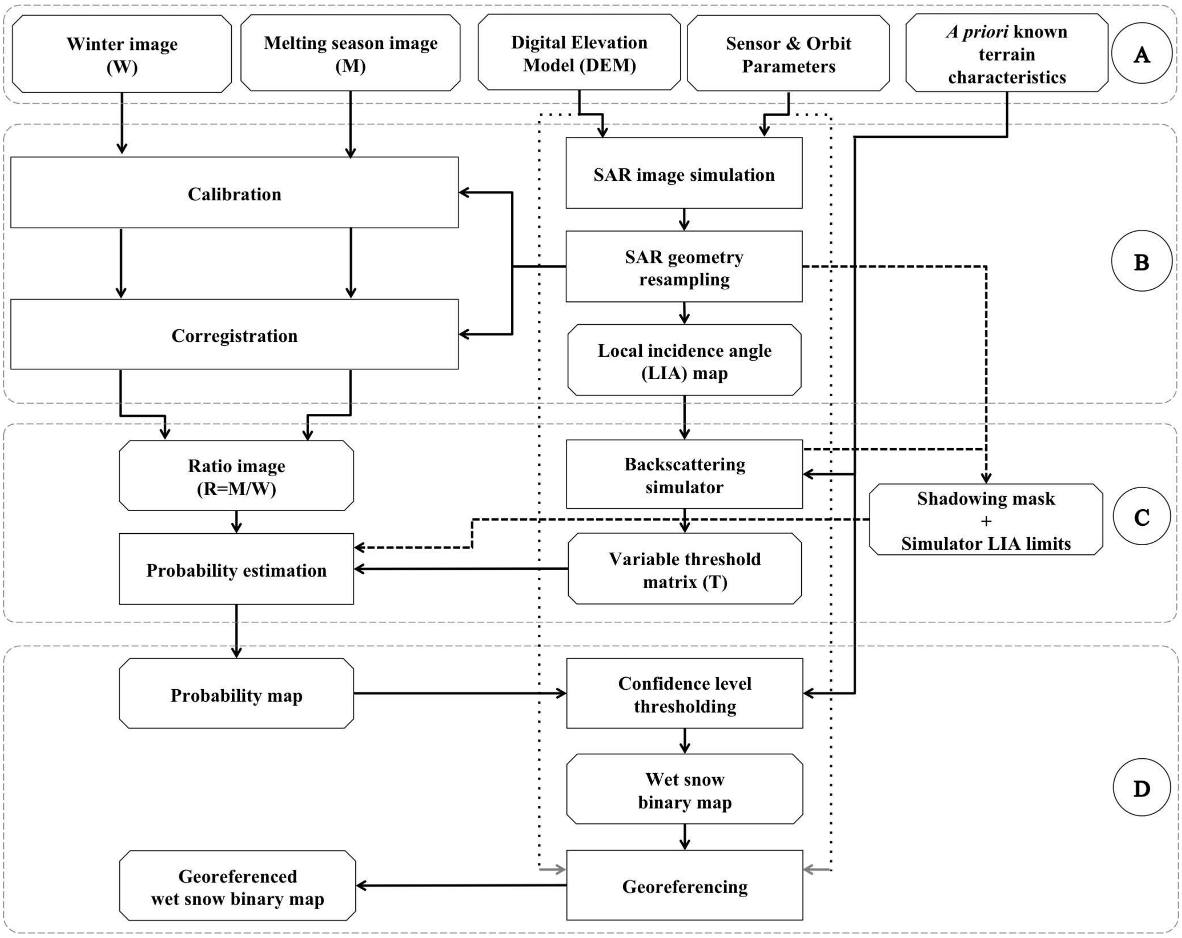

Figure V.1: Algorithmic representation of the wet snow detection method

data with interpolated temperature map.

V.2 The preamble of the detection algorithm

As illustrated in Fig. V.1, the wet snow detection algorithm consist of four principal parts, among which the first two assume the selection of data and the appropriate pre-processing.

V.2.1 Input data

The approximate equivalence between the bare ground and the dry snow backscattering, perceived in the C band, does not appear to be true for higher frequencies [140]. Therefore, in order to assure applicability in a wider range of frequencies, we compare directly the dry snow cover image with the mixed dry/wet snow cover one.

The following data are required as input:

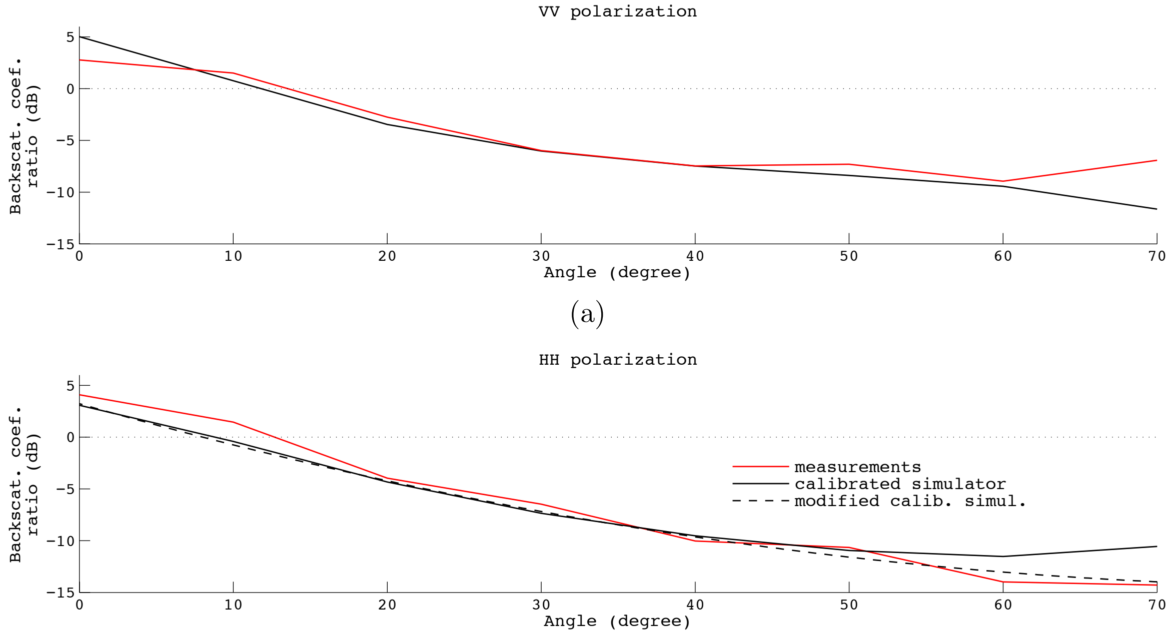

(a)

(b)

Figure V.2: Calibration of the backscattering simulator using scatterometer measurements in C band [139]: (a) VV, (b) HH.

- Winter SAR image, slant range geometry - image acquired during the winter season, when the dry snow assumption is fairly valid due to the air temperature at ground level;
- Melting season SAR image, slant range geometry - image acquired at the end of the winter season, when the increase in the air temperature causes melting to occur;
- Digital Elevation Model (DEM) and Sensor & Orbit parameters (georeferencing and derivation of LIA map);
- Approximate information about the snow cover in the region (verifying the appropriateness of the proposed method);

V.2.2 SAR image processing

In this part, the input images are calibrated and corregistrated using the resampled SAR geometry intensity simulation. The slant range LIA is also derived.

V.3 Wet/Dry snow backscattering ratio

Given the fundamental role of both the snow surface and the underlying layer in snow backscattering, the local incidence angle (LIA) appears to be the most appropriate choice of the independent variable for the analysis of the wet/dry snow backscattering ratio - ratio of backscattering coefficients (Eq. IV.8). In order to both qualitatively and quantitatively analyse the backscattering ratio, we rely on the backscattering simulator introduced in Section IV.2.

In the region of particular interest - the French Alps, the large multilayer snow cover occurs both in the accumulation and in the melting season, containing, in the former case, inevitably present ice crust.

The analysis performed using the derived simulator pointed out that the most significant portion of the backscattered energy, in case of an ice crust present in a dry snow pack, comes from the ice crust, not from the "real" underlying ground. Namely, refreezing, by forming a snow crust, leads to a very strong volume scattering (big grains representing strong scatterers) [140]. However, if the ice crust (a continuous layer of ice) is formed, it should rather be associated with a strong surface scattering. That is why we have decided to rather ignore the contribution of the underlying layer in deriving the backscattering difference. The support for this conclusion was found as well in the literature dealing with the passive microwave sensing of a snow cover. Namely, the formation of the crust significantly decreases the measured emissivity, by decreasing the influence of the underlying layers, causing the latter to be ignored in the modelling [141].

Therefore, we assumed the dominance of this underlying ice crust backscattering component in case of the dry snow [121]. Consequently, the layers above the ice crust are considered to be the effective snow cover. We adopt the parameters of these layers as the multi-layer (ML) simulator input data.

In case of the wet snow, the surface layer is considered as the most contributory [122]. Thus, the wet snow backscattering is simulated using a single-layer (SL) approach, by adopting the parameters of the surface layer.

V.3.1 Simulator calibration

The derived backscattering simulator is calibrated in C band (5.3 GHz) using the scatterometer measurements from [140] (Fig. V.2). The applied calibration is essentially the optimization with respect to both the underlying ice crust and the snow surface parameters.

We have selected two sets of measurements performed in the C band, by Strozzi and Matzler in Weissfluhjoch (Davos, Switzerland) [139]: first one ($M1$) corresponding to the dry snow (27 January 1994) and the second one ($M2$) to the wet snow (24 March 1995). The latter have been specifically chosen because of the wetness value characterizing the upper layer (0.73%).

The calibration we apply is basically the optimization with respect to the both ice crust (ic) and snow surface (ss) parameters. After introducing the input parameters measured *in situ* ($\mathbf{p} = \rho, d, \varepsilon, w$), we derive the surface parameters by applying the optimization algorithm [142] based on minimizing the MSE between the simulator output in the C band and the

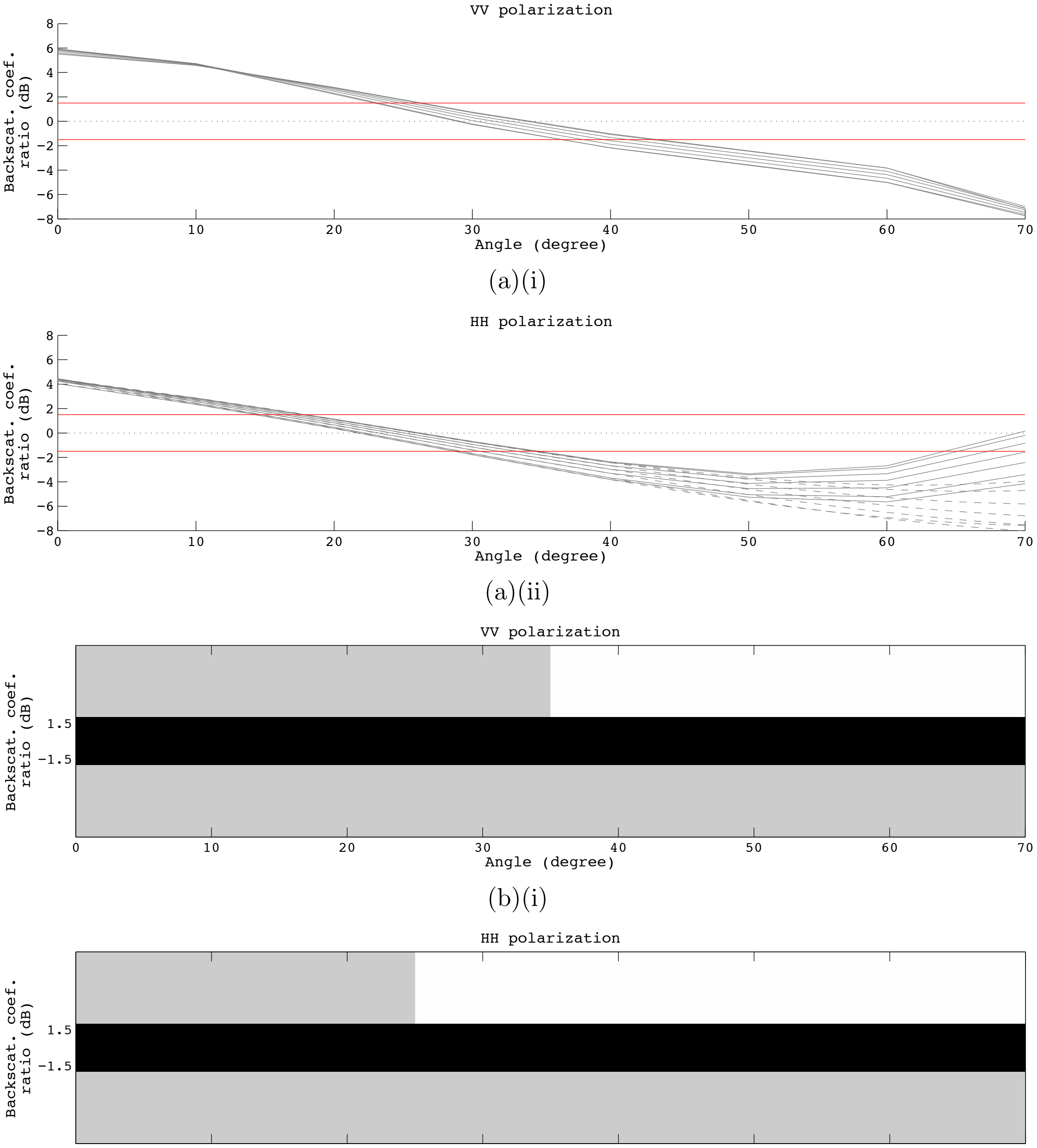

(a)(i)

(a)(ii)

(b)(i)

(b)(ii)

Figure V.3: Wet/dry snow backscattering ratio for input parameters in Table I (a) and backscattering ratio values indicating wet snow (grey) and dry snow (black) (b): (i) VV, (ii) HH. Grey lines are backscattering curves for different roughness parameters (Table V.1), red lines represent defined thresholds (Table V.2). Dashed grey lines are extrapolated backscattering curves, correcting the observed anomaly of the IEM-B (HH) for high incidence angle, occurred due to the dielectric permittivity value (modified calibrated simulator in Fig. V.2).

measurements (for the range of Local Incidence Angle $\theta \in \{0°, 70°\}$).

$$\begin{aligned}[\sigma^{ic}_{RMS}, l^{ic}_c] = f_{opt}(\quad & \text{MSE} \quad \{\sigma^0_{hh}(\sigma^{ic}_{RMS}, l^{ic}_c, \theta, \mathbf{p}), \sigma^0_{hh_{M1}}\} + \\ + \quad & \text{MSE} \quad \{\sigma^0_{vv}(\sigma^{ic}_{RMS}, l^{ic}_c, \theta, \mathbf{p}), \sigma^0_{vv_{M1}}\}, [\sigma^{ic}_{RMS_0}, l^{ic}_{c0}]),\end{aligned} \tag{V.1}$$

$$\begin{aligned}[\sigma^{ss}_{RMS}, l^{ss}_c] = f_{opt}(\quad & \text{MSE} \quad \{\sigma^0_{hh_s}(\sigma^{ss}_{RMS}, l^{ss}_c, \theta, \mathbf{p}), \sigma^0_{hh_{M2}}\} + \\ + \quad & \text{MSE} \quad \{\sigma^0_{vv_s}(\sigma^{ss}_{RMS}, l^{ss}_c, \theta, \mathbf{p}), \sigma^0_{vv_{M2}}\}, [\sigma^{ss}_{RMS_0}, l^{ss}_{c0}]).\end{aligned} \tag{V.2}$$

The details concerning the Nelder-Mead simplex optimization algorithm (f_{opt}) are provided in Appendix B.

The HH simulation results have been modified by extrapolating the backscattering curves after $LIA = 50°$. This is due to the observed anomaly of the IEM-B, related to the low values of dielectric permittivity, causing quite a radical increase of the surface backscattering for higher incidence angles, which is not fully consistent neither with the ground truth data, nor with the theoretical expectations.

V.3.2 Variable threshold derivation

The simulator is then applied in the X band (10 GHz), using the extended set of parameters, reinforced by the derived surface parameters (Table I). By slightly varying the surface roughness parameters (RMS height and correlation length) we obtain the wet/dry snow backscattering ratio (Fig. V.3a), allowing us foremost the following qualitative interpretation: the wet snow backscattering is not necessarily inferior in the X band, neither.

Using the derived wet/dry snow backscattering ratio, we identify the ranges of values which should point to the wet snow presence in the ratio image - variable threshold (Fig. V.3b). Given that the dry snow image is used as the reference, regions around 0 dB indicate dry snow presence (no change). Further, assuming this result not to be a "universal case" (the low value of the wetness - 0.73%), we have additionally employed the standard hypothesis of higher wet snow absorption for big wetness values and thus associated the negative regions (below -1.5 dB) to the wet snow presence. However, believing that the positive backscattering difference for lower local incidence angles should as well indicate the wet snow, sooner than the dry one, we assign wet snow as well to the positive regions corresponding to the lower LIA.

The latest is justified by the fact that the melting process which occurs in the upper layer gives rise to the snow pack surface backscattering, which augments total snow backscattering at lower LIA. Of course, this assumption is conditioned by the choice of input data (winter and melting season images). The support for this claim was found in the remarks of Strozzi and

Matzler [140], which say that liquid water presence in the upper layer leads to the domination of surface backscattering, and that, which appears as logical, wet snow backscattering can be characterized by decreased backscattering at high incidence angles. Even though originally derived using measurements at higher frequencies, these conclusion should stay valid also in the X band [122].

Table V.1: Input parameters for the snow backscattering simulation, used in thresholds derivation. different shades of grey represent different dry snow layers.

Input parameter	Dry snow (ML)			Wet snow (SL)
Snow density	$144\ kg/m^3$	$185\ kg/m^3$	$333\ kg/m^3$	$315\ kg/m^3$
Wetness	0 %	0 %	0 %	0.73 %
Snow depth	$0.24\ m$	$0.12\ m$	$0.24\ m$	$1.77\ m$
Frequency	$5.3\,GHz$ (C), $10\,GHz$ (X)			
Particles effective radius	$(\circ\ \circ)$, $r_{eff} = 225\ \mu m$			
Water dielectric constant	$55 + j40$ (C), $38 + j40$ (X)			
Snow layers RMS height	4.5 - 6.5 mm			
Snow layers correlation length	42 - 82 mm			
Ice crust dielectric constant	3.2			
Ice crust RMS height	8.4 mm			
Ice crust correlation length	24 mm			

V.4 Stochastic approach

As already indicated in Section I.2, assuming the gaussianity of the SAR clutter, the intensity over homogeneous regions can be modelled by Gamma probability density function (PDF), according to the fully developed speckle model [19]:

$$\mathcal{G}(\tau|\nu,\mu) = \frac{1}{\Gamma(\nu)}\left(\frac{\nu}{\mu}\right)^{\nu}\tau^{\nu-1}e^{-\frac{\nu\tau}{\mu}}, \qquad \text{(V.3)}$$

with μ being the texture intensity mean, ν - shape factor providing deviation with respect to the corresponding Gaussian distribution and Γ - the Gamma function. If the intensity is expressed as $\frac{\mu}{2\nu}X$, the random variable X follows chi-squared distribution $\chi^2(2\nu)$ with 2ν degrees of freedom. The ratio of two chi-squared random variables, normalized with respect to the degrees of freedom, follows the Fisher-Snedecor distribution $\mathcal{F}(\nu_1,\nu_2)$ [29]. This implies that the ratio of two Gamma random variables, having different shape factors but the same mean value is modelled using the Fisher-Snedecor distribution:

$$\mathcal{F}(r|k,\nu_1,\nu_2) = \frac{\Gamma(\nu_1+\nu_2)}{\Gamma(\nu_1)\Gamma(\nu_2)} \frac{\nu_1}{k\nu_2} \frac{(\frac{\nu_1 r}{k\nu_2})^{\nu_1-1}}{(1+\frac{\nu_1 r}{k\nu_2})^{\nu_1+\nu_2}}. \tag{V.4}$$

The proposed stochastic approach is exactly based on the probability estimation relaying on the previously elaborated assumption. The algorithm uses the boxcar neighbourhood, coupled with approximate maximum likelihood estimator (MLE), in order to obtain local statistics for each of the areas in the image. Due to the poor performances of the Fisher-Snedecor MLE, the estimation is performed rather on the normalized ratio intensity (ξ) than the ratio intensity itself ($r = \mu\xi$). If the ratio intensity (r) follows the Fisher-Snedecor distribution, the normalized ratio intensity (ξ) is modelled by the Beta prime distribution:

$$\mathcal{B}'(\xi|\nu_1,\nu_2) = \frac{\Gamma(\nu_1+\nu_2)}{\Gamma(\nu_1)\Gamma(\nu_2)} \frac{\xi^{\nu_1-1}}{(1+\xi)^{\nu_1+\nu_2}}. \tag{V.5}$$

For each local neighbourhood, we derive the mean value (μ), normalize the texture locally and estimate ν_1 and ν_2 parameters. This way, we define the probability density function ($\mathcal{B}'_{(i,j)}$) for every region in the image. By integrating the obtained PDF with respect to the normalized texture, we are getting the cumulative distribution function ($B'_{(i,j)}$) for the normalized threshold of the central pixel:

$$\begin{aligned} i_{out}(i,j) &= B'_{(i,j)}\left(\frac{T_2(i,j)}{\mu(i,j)}\right) - B'_{(i,j)}\left(\frac{T_1(i,j)}{\mu(i,j)}\right) = \\ &= \int_{\frac{T_1(i,j)}{\mu(i,j)}}^{\frac{T_2(i,j)}{\mu(i,j)}} \mathcal{B}'_{(i,j)}(\xi)d\xi. \end{aligned} \tag{V.6}$$

This value is the probability that the ratio fits the predefined range of values or exactly the wet snow probability.

Table V.2: Thresholds determining the range of values pointing to: wet snow (white), dry snow (gray).

	HH		VV	
Angle (°)	0-25	26+	0-35	36+
T2 (dB)	1.5	-1.5	1.5	-1.5
T1 (dB)	-1.5	-∞	1.5	-∞

The thresholds T_1 and T_2, given in the Table V.2, are functions of the local incidence angle (Fig. V.3). The grey coloured fields in Table V.2 indicate dry snow, in which case we compute the wet snow probability as the complement to one (i.e. for LIA = 10°, wet snow probability equals to $1 - i_{out}(i,j)$).

V.4.1 Confidence level

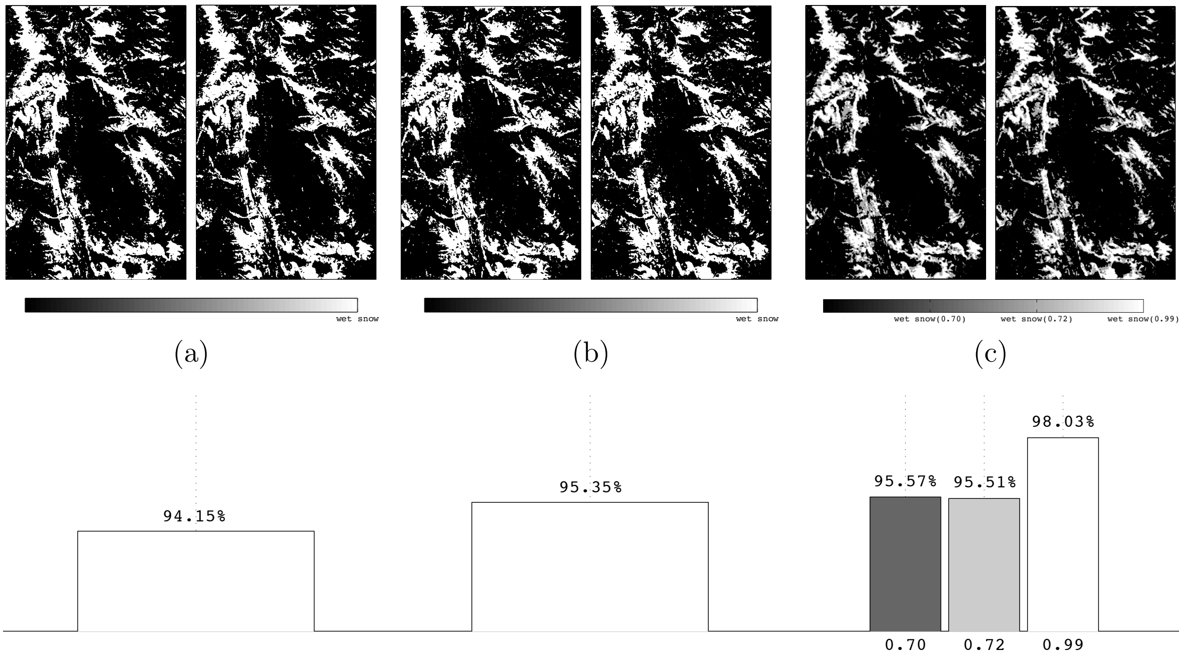

(a) (b) (c)

(d)

Figure V.4: The comparison between HH (left) and VV (right) polarization maps obtained after: (a) filtering the thresholded ratio of input images, (b) thresholding the ratio of speckle filtered input images, (c) thresholding the probability map with 70%, 72% and 99% confidence level. (d) HH-VV matching.

The obtained wet snow probability map is transformed into the wet snow binary map by applying the confidence level C, which reflects the level of certainty that the derived map indeed represents wet snow regions:

$$I_{out}(i,j) = \begin{cases} 1 & \text{if } i_{out}(i,j) \geq C, \\ 0 & \text{if } i_{out}(i,j) < C. \end{cases} \tag{V.7}$$

V.5 Performance analyses

The proposed algorithm is illustrated by the results obtained using two X-band TerraSAR-X stripmap images acquired over the Grandes Rousses massif near Grenoble, France: the winter image, acquired on the 8th of February 2009, holding for the dry snow assumption (according to the local meteorological data and the DEM - 88% of the area is at the altitude $> 1500m$; and the melting season image, acquired on the 2nd of March 2009, in the presence of wet snow, according to the same source. The local incidence angle map is computed using the DEM (Datum: WGS-84, UL Geo: $5°57'3.64''E, 45°24'15.21''N$).

For comparison, we provide in Fig. V.4 three pairs of binary maps (HH and VV) derived using different change detection methods. Firstly, we present the results obtained by using the criteria illustrated in Fig. V.3b on the filtered ratio of original input images (Fig. V.4a). Further, the same criteria is applied on the ratio of formerly speckle filtered (7×7 mean filter) input images (Fig. V.4b). Finally, we include the proposed stochastic approach, and therefore present the results obtained with the proposed method, using very high confidence level - 99% (Fig. V.4c).

The quantitative correspondence between the independently obtained HH and VV maps (Fig. V.4) significantly augments in case of the proposed stochastic approach. By applying an unconstrained optimization technique (Appendix B), we estimate that the maps in Fig. V.4a and Fig. V.4b approximately correspond to the probability maps thresholded with (70%) and (72%) confidence level, respectively. Increase of confidence level decreases the fraction of wet snow, but augments the certainty.

The verification of the obtained results is performed using the local temperature measurements at the ground level. The measurements data, provided by the EDF, are related to the area of interest (Grandes Rousses massif) at the same date (03 March 2009), meaning that comparison with the available SAR images was possible.

The temperature used in the validation is the air temperature measured at the ground level. The single point measurements are acquired at 36 stations in the wider region. Among them, there are seven measurement stations in the region which corresponds to the acquired TerraSAR-X images:

- Five belonging to Eléctricité de France (EDF): Agnelin, Lac Noir, Montfroid, Chancel and Rif Puy Vacher.
- Two belonging to Centre d'Etudes de la Neige (CEN): Col du Lac Blanc and Lac Carrelet.

The acquired single point measurements are spatially interpolated using the kriging method.

The procedure is based on the stated fact that wet snow presence is characteristic for the local ground temperature above 0°C, while dry snow can be found below 0°C. The temperature measurements are compared to the obtained wet snow probability map (Fig. V.5). Quantitative evaluation of the comparison is done by calculating a spatial cross-correlation, using sliding window (Fig. V.5d). The approximate matching between the high temperature regions and the high probability regions, two information sources which could be considered as independent, is pointing to the validity of the obtained results.

In the absence of the appropriate optical remote sensing data, we cannot be entirely sure that the whole region is snow covered. However, we can rely on the DEM (Fig. V.5c) in deducing some conclusions. Namely, according to the consulted meteorological reports, we can reasonably assume that the "snow line" in this region of the French Alps, at the beginning of the month of March, varies between $1000m$ and $1500m$. Therefore, in Figures V.5e and

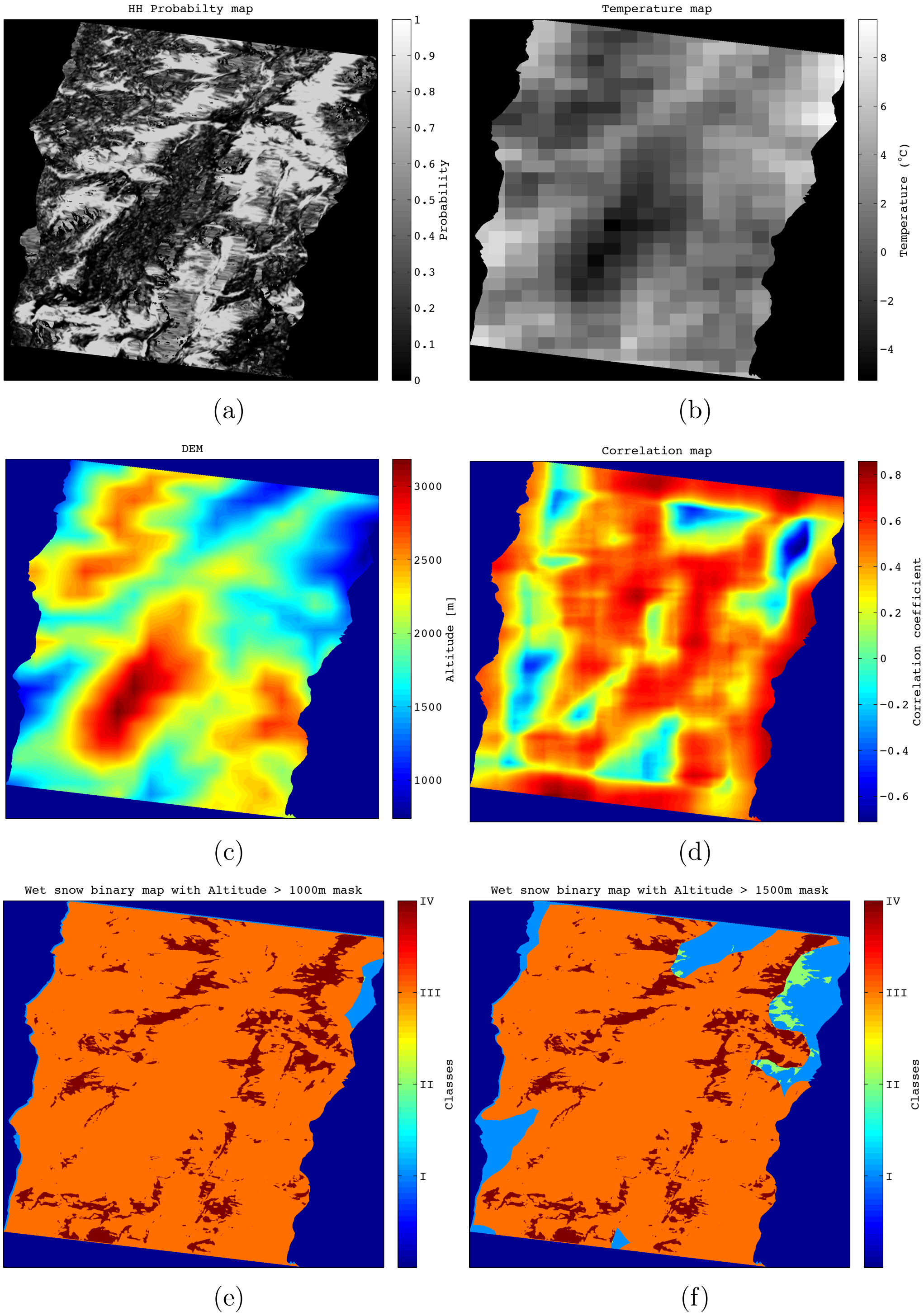

(a) (b)

(c) (d)

(e) (f)

Figure V.5: Georeferenced maps: (a) HH wet snow probability map; (b) interpolated ground level temperature map, (c) DEM, (d) Coefficient of correlation between the HH wet snow probability map and the ground level temperature map. Wet snow binary maps (confidence level set at 99%) superposed with the altitude masks: (e) Altitude $> 1000m$, (f) Altitude $> 1500m$. Class 1 - no wet snow below the defined altitude, Class II - wet snow below the defined altitude, Class III - no wet snow above the defined altitude, Class IV - wet snow above the defined altitude.

V.5f we superpose the derived wet snow binary maps (for confidence level of 99%) with two altitude masks derived using the DEM: Altitude $> 1000m$ and Altitude $> 1500m$. In the first case percentage of the estimated wet snow falling out of $> 1000m$ region is negligible (0.05%). In the second case as well, only 10.7% of the detected wet snows risks to be misestimated by being confounded with a potential bare ground.

V.6 Conclusions

Snow backscattering simulations, reinforced by the state of art measurements, resulted in the conclusion that the difference in backscattering of wet and dry snow occurs to be significantly dependent on the local incidence angle and on the operating frequency. Consequently, we have proposed an alternative version of the conventionally used wet snow detection method, by analysing a wet/dry snow backscattering ratio in X band and moderately modifying the range of values in the ratio image pointing to the presence of wet snow. As well, we chose preferably the winter image as the reference, avoiding constraints related to the frequency dependent relation between dry snow and bare ground backscattering and therefore allowing application in wider frequency range. Finally, instead of directly thresholding the ratio of multitemporal images, by considering the spatial correlation, we rather estimated the probability of the wet snow occurrence, making the approach stochastic.

The plausibly modified assumption of the wet/dry snow backscattering ratio, the implicitly introduced spatial correlation between the wet snow areas, and the possibility to vary the level of confidence of the wet snow binary maps by thresholding the obtained probability map, are altogether the supplements brought by the introduced stochastic approach to the ensemble of change detection techniques in snow mapping.

Further refinements of the proposed detection method are going in two main directions. In the first, the quantitative interpretation of the wet/dry snow backscattering ratio will be improved, which should allow more accurate discrimination between different regions in Figure V.3b, in terms of LIA. Concerning the second direction, further work will mostly consist in adjusting the proposed method to polarimetric SAR input data [143]. The idea is to exploit the dual-pol images in the probability derivation.

Chapter VI

SWE spatial modelling using remote sensing data

As specified in Chapter IV, the derivation of snow pack parameters by means of single channel SAR image, represents an under-determined problem. However, in the preceding chapter we have developed a snow classification method based on multitemporal single channel SAR images. In this chapter, in order to derive spatial distribution of SWE, we turn toward the optical remote sensing accompanied the hydrological model, introduced in Section IV.3 [3]. As well, we briefly present the ongoing efforts in employing POLSAR methods, reinforced by a BSS technique (PCA), in monitoring the snow pack parameters forming SWE [144].

We commence by briefly introducing the ongoing study on the potential of POLSAR methods backed by PCA in spatial SWE modelling. Further on, as we pass on the major topic of this chapter, the comparative calibration of MORDOR hydrological model using three different optimization methods, based on the *in situ* measurements, is presented. In Section IV we describe the highlight of this chapter - calibration strategy based on the optical remote sensing dataset. Section V contains the results and the corresponding discussions, a preamble to the conclusion of this chapter.

VI.1 Introduction

The estimation of SWE in mountainous regions appears to be very important for the hydroelectric power supply, since it allows anticipating the water resources available during the snow melting season [145]. Using thirty-six meteorological stations distributed around the accumulation reservoir of the Serre-Ponçon dam, the MORDOR forecasting hydrological model, introduced in Section IV.3, currently provides, among other parameters, the SWE used to evaluate the potential intakes to this reservoir and to optimize the operation of the corresponding power plant. The sub-model, providing the SWE, uses the available precipitation and air temperature measurements as input parameters. Aside from those, each station is supposed to be characterized with the appropriate accumulation (c_p) and melting (k_f) correction coefficients.

Ongoing efforts in bypassing hydrologicals model and directly using POLSAR data are based on applying a conventional ICTD on C band RADARSAT-2 images, and applying PCA, the most widespread BSS technique, for performing one sort of de-noising of the derived polarimetric descriptors. A promising inverse correlation between de-noised entropy and the depth of the snow above the ice crust, was observed in case of the dry snow. For the wet snow, a weak link between the wetness and the second Yamaguchi component, is remarked. This study could eventually come up with a mean for spatial monitoring of snow pack parameters constituting SWE, but at the time being the possibilities for the autonomous estimation of this parameter appear to be quite limited.

Therefore, the topic of this chapter would be rather a novel calibration strategy of the SWE sub-model of MORDOR based on a multi-temporal set of fractional snow cover maps [146]. In fact, we are deriving a mean to properly establish the spatially varying accumulation and melting correction coefficients, required by the MORDOR model. These parameters represent a mean to account for the strong influence of the topology and mountain winds on the hydrological model [147, 148]. The MODIS data (providing fractional snow cover maps) were already, despite the ever-present issue with the cloud coverage, successfully used in calibrating and validating hydrological models [149, 150]. Here we propose a suitable calibration procedure, reduced to the estimation of the spatially varying correction coefficients and, by comparing it with the one performed using *in situ* measurements, we demonstrate the utility of the remote sensing data in the context of the calibration of distributed hydrological models.

As a case study for the derivation and the demonstration of the proposed method, we use the formerly introduced Serre-Ponçon dam. Out of the existing thirty-six stations, local *in situ* measurements are available for four of them. These data sets are initially used for comparative optimization aiming both to derive representative coefficients (c_p,k_f) at these four locations and to select the most appropriate optimization method. Still being restricted to these four stations, we employ the formerly selected method in defining the parameters of the continuous activation function. Further, we derive the spatially varying coefficients characterizing the entire region, including the remaining stations, by rather relying on the MODIS multi-temporal set of snow cover maps. This is done through the optimization of the continuously thresholded (by means of the continuous activation function) SWE model, using the available remote sensing data acquired over the entire region. The final comparison with the *in situ* measurements indicates significantly increased accuracy with respect to the initial case, where the c_p and the k_f are considered as fixed for the entire region. Moreover, the proposed method based on the MODIS data, eventually appears to be superior with respect to the calibration using *in situ* measurements.

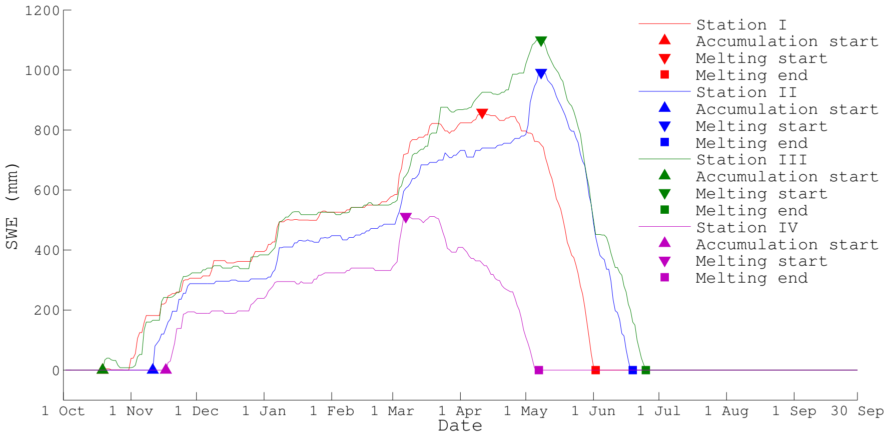

Figure VI.1: SWE measurements, acquired *in situ* at four different stations, during the season 2001-2002.

VI.2 POLSAR potential in SWE monitoring

The study is based on the RADARSAT-2 dataset acquired over the region of Northern French Alps between 2009 and 2011. The *in situ* snow measurements were simultaneously performed at 15 different sites in the covered area.

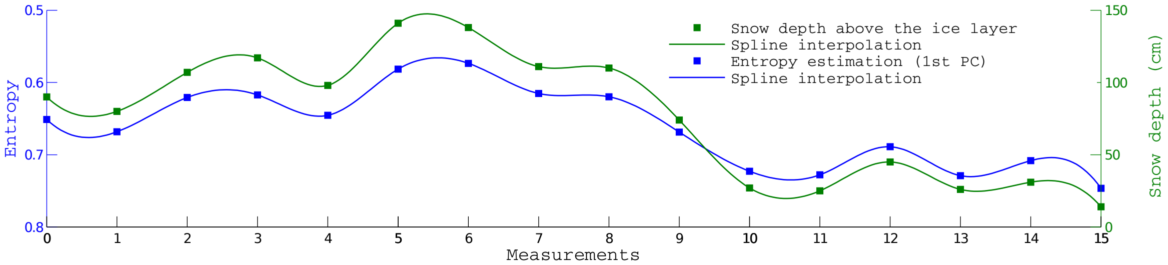

Figure VI.2: Entropy vs. depth of the snow above the first ice crust: temporal correlation.

After applying conventional Cloude and Pottier ICTD (Section I.1.2.2), the derived standard polarimetric descriptors: α_{p1} (Eq. I.26), $\overline{\alpha}_p$ (Eq. I.27) and H (Eq. I.28), are georeferenced and assigned to the measurements sites. They are reinforced by two new descriptors [151]:

- Single bounce Eigenvalue Relative Difference (SERD):

$$SERD = \begin{cases} \frac{\lambda_1-\lambda_3}{\lambda_1+\lambda_3} & \text{for} \quad \alpha_{p1} \leq \pi/4, \\ \frac{\lambda_2-\lambda_3}{\lambda_2+\lambda_3} & \text{for} \quad \alpha_{p1} \geq \pi/4, \end{cases} \tag{VI.1}$$

with λ being the eigenvalue defined in Eq. C.1, and,

- Double bounce Eigenvalue Relative Difference (DERD), obtained when the conditions related to α_{p1} in Eq. VI.1 switch places.

The de-noising by means of PCA is performed by calculating principal components of n-dimensional dataset $\mathbf{X}$, containing values of five polarimetric descriptors for d different dates ($N = 5d$ in total - each descriptor estimated at d dates), with n being the number of measurements sites.

If we rely on the formalism introduced in Section I.3.1, de-noised polarimetric descriptors for different dates $\mathbf{X}_d$ could be represented as:

$$\mathbf{X}_d = \mathbf{E}'\mathbf{Y}' = \mathbf{E}'\mathbf{E}'^T\mathbf{X}, \tag{VI.2}$$

with the apostrophe signifying that not the entire eigenvector matrix was taken, but rather just the first eigenvector (the first column of $\mathbf{E}$ in Eq. I.51). Given that all the descriptors together constitute the observation dataset for one dimension, the de-noising is performed on account of the information "exchanged" between them.

The de-noised or let us say "enriched" entropy parameter, compared with the depth of the dry snow above the first formed ice crust, indicate the inverse correlation (Fig. VI.2), with a coefficient of determination for a deduced linear regression $R^2 = 0.8439$ (Fig. VI.3a).

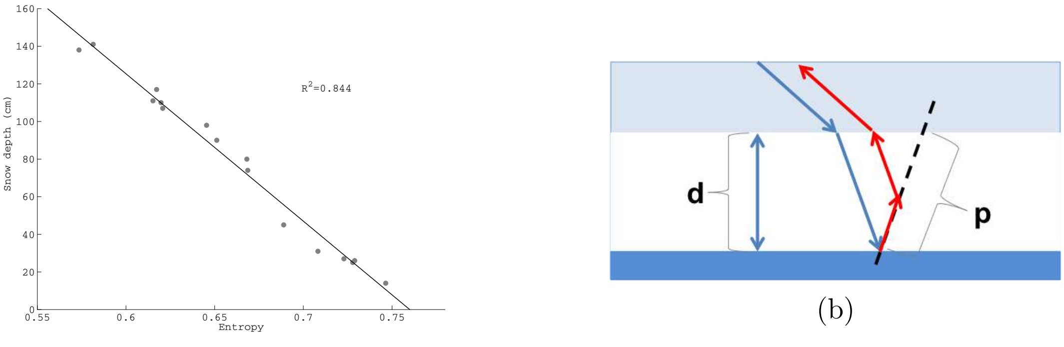

(a)

(b)

Figure VI.3: Entropy vs. depth of the snow above the first ice crust: (a) scatter plot (b) physical hypothesis.

We propose the following hypothesis as a physical justification [144]. At the considered frequency (C band), given the unavoidable presence of ice crust inside the snow pack due to the metamorphism of the snow during the winter season, the reflection of the layer of ice under a pack of dry fresh snow will dominate over the underlying ground backscattering.

The reasoning here is quite similar to the one applied in Section V.3 [140, 141], with an important difference brought by the change of frequency. Namely, at C band EM waves are much more probable to penetrate the ice crust than at X band. However, if we recall the dominance of the surface scattering (or reflection), stated in case of a wet snow (Section IV.2), and consider an inevitable liquid water presence in the underlying snow layer (the last being as rough as the ice crust), the hypothesis still stands.

The inferior roughness of the ice crust surface should rather cause specular reflection of the incident electromagnetic waves than their scattering. This fact, along with the insignificance of the snow surface and volume backscattering components in case of the dry snow, indicates the dominance of the ground (ice crust)-volume interaction component.

As it is seen in Fig. VI.3b, bigger depth of a snow layer (d) means bigger propagation distance (p) of the reflected electromagnetic wave, which is to be rescattered by the volume. This implies bigger probability of interaction with snow particles, therefore bigger probability of recovering the most dominant mechanism.

Concerning the wet snow, given the very small number of points, the correlation between the wetness and the second component of Yamaguchi ICTD does not deserve any detailed elaboration at this point.

Waiting for some more promising results in terms of autonomous SWE estimation by means of POLSAR backed by BSS, we have to turn to the trade-off obtained by using the external input - distributed hydrological model.

VI.3 Calibration of MORDOR using *in situ* measurements

The *in situ* measurements are acquired at some ground meteorological stations by cosmic-ray snow gauges. Conventionally used in the characterization of the soil moisture [152], this technique proved to be an efficient method for the SWE estimation, as well [153].

These, available *in situ* measurements, were used both to determine the representative optimal coefficients at the corresponding sites and to select the most appropriate optimization method. Firstly, we are identifying the characteristic periods (accumulation and melting) over one year. Later, we perform the comparative analyses by applying simultaneously three different optimization algorithms.

In order to identify the accumulation and the melting periods, we have to determine three dates: accumulation start date, melting start and melting end dates.

This is done using the smoothed gradient operator: positive gradient values correspond to snow accumulation, while negative indicate melting. Therefore, the radical change in gradient value points to the melting start. The other two dates are related to the first and the last non-zero values during the year of study (1 October 2000 to 30 September 2001).

We use the MSE as optimization criterion. The goal is to find the values of the accumulation (c_p) and the melting (k_f) coefficients which lead to the smallest difference between the model output (given the local meteorological data) and the measurements. Actually, it is the minimum of the MSE function we are searching for:

$$[c_p, k_f] = f_{opt}\left(\mathrm{MSE}\{g(c_p, k_f, t), m(t)\}, [c_p^0, k_f^0]\right). \tag{VI.3}$$

with f_{opt} signifying the function of optimization, g being the model output as a function of time (t) and m representing the acquired *in situ* measurements. c_p^0 and k_f^0 are the fixed values of the coefficients used in the original model, derived statistically using several meteorological stations.

Three unconstrained non-linear optimization algorithms [154] are compared using the available measurements:

- M1 - fmin search: the Nelder-Mead simplex function minimization. The algorithm creates a simplex around the initial guesses (c_p^0 and k_f^0) which is further modified in the iterative process [142, 155] (Appendix B).
- M2 - pattern search: the generalized pattern search (GPS). It relies on positive spanning directions by assuming the treated function (model output) is continuously differentiable [156].
- M3 - genetic algorithm: natural selection process that mimics biological evolution. The only of the three used algorithms that doesn't require any initial guess, but rather creates random solutions, which are evolving toward the optimal ones [157].

By relying on previously derived characteristic periods, the optimization procedure was performed using the values acquired during:

- the whole year (all),
- the accumulation (A) and melting (M) period (winter+spring),
- the accumulation period (winter),
- the melting period (spring).

At the end of this section, we have both the most suitable optimization method and the representative optimal coefficients, which were due to be considered as the reference in analysing the performances of the proposed method.

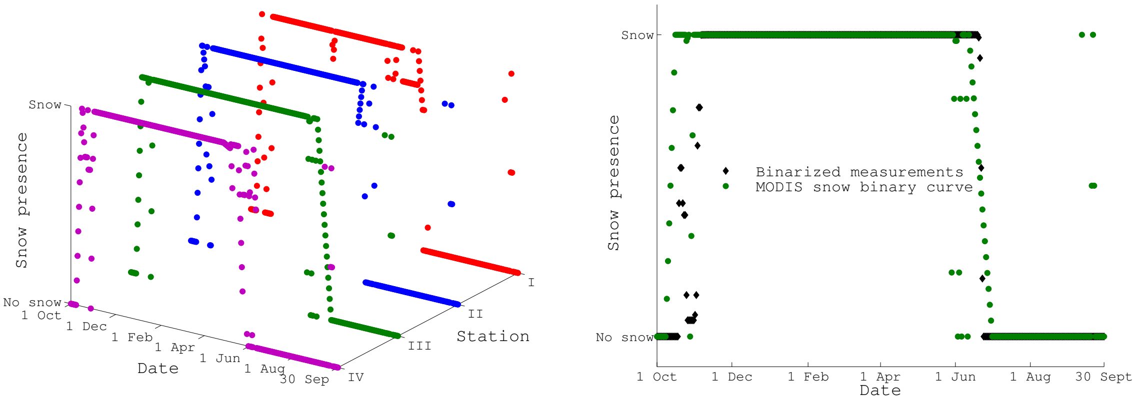

(a) (b)

Figure VI.4: The MODIS fractional snow maps: (a) interpolated "SWE binary" curves (four stations with *in situ* measurements); (b) comparison with the optimally binarized *in situ* measurements (station III).

VI.4 Calibration of MORDOR using MODIS remote sensing data

Due to its accuracy and daily availability, MODIS remote sensing data represent a valuable tool in snow cover monitoring [158]. Despite the necessity to perform spatial and temporal filtering in order to decrease cloud obscuration, the overall accuracy of the derived snow cover maps stays above 90% [149].

Therefore, MODIS snow cover maps happen to be particularly useful in calibrating and validating semi-distributed hydrological models [159]. The standard procedure assumes comparing the SWE output of the hydrological model with the observed maps.

Obviously, the previously introduced calibration relying on the *in situ* measurements cannot be applied to the entire region of interest, unless the measurements are spatially interpolated. Even though both the air temperature and the precipitation are interpolated by means of kriging (Gaussian random regression), the same type of spatial continuity cannot be expected in case of correction coefficients. Therefore, in order to account for their strong spatial variability, we have developed a new strategy for exploiting the MODIS fractional snow maps, instead. This method allows the calibration of the distributed hydrological model.

The proposed method consists in the following three steps.

VI.4.1 MODIS data preprocessing

Moderate-resolution Imaging Spectroradiometer (MODIS) instrument, being in the orbit since 1999, has sensors in 36 wavelength bands, ranging from $620\,nm$ to $14.385\,\mu m$. The set of multitemporal fractional snow maps is derived out of geo-referenced MODIS images, acquired in 2000/2001. Their resolution has been decreased to $1 \times 1\,km$ in order to fit the resolution of spatially interpolated temperature and precipitation maps.

The temporal curves derived for each pixel were then linearly interpolated in order to compensate for the eventual lack of the data during the year. Among them, four correspond to the meteorological stations characterized with *in situ* measurements (Fig. VI.4(a)).

VI.4.2 Continuous thresholding of the SWE sub-model

The conventional "hard" thresholding with respect to the predefined threshold T (values less than T labelled by "0" and greater than T by "1"), did not appear to be appropriate, given that a non-continuous function does not suit any of the formerly introduced optimization methods (Fig. VI.5). Therefore, we turned toward a continuous thresholding strategy, based on the continuous activation function:

$$x_b = \frac{\tanh\left(\frac{x-h}{\sigma}\right) + 1}{2}, \tag{VI.4}$$

where σ reflects the uncertainty in the SWE sub-model, while h depends on the value order of SWE, here called x. The later value was selected *ad hoc*, while the derivation of the σ value assumed the optimization (algorithm M1) of the binarized *in situ* measurements $(m_b(\sigma, h, t))$ with respect to the corresponding MODIS temporal binary curve $(M(t))$ (Fig. VI.4 (b)):

$$[\sigma] = f_{opt}\left(\mathrm{MSE}\{m_b(\sigma, h, t), M(t)\}, [\sigma^0]\right), \tag{VI.5}$$

with σ^0 being the initial, assumed value of σ.

The completely defined linear binarization function was further to be applied on the SWE sub-model. Binarized this way, the SWE sub-model is ready for the comparison with the MODIS snow temporal curves i.e. "SWE binary" curves.

VI.4.3 The derivation of the correction coefficients

Finally, we derive the correction coefficients (c_p and k_f) by minimizing MSE between: (1) the product of the binarized SWE sub-model output (g_b) with the model itself (g), and (2) the product of the smooth MODIS binary curves M with the SWE sub-model.

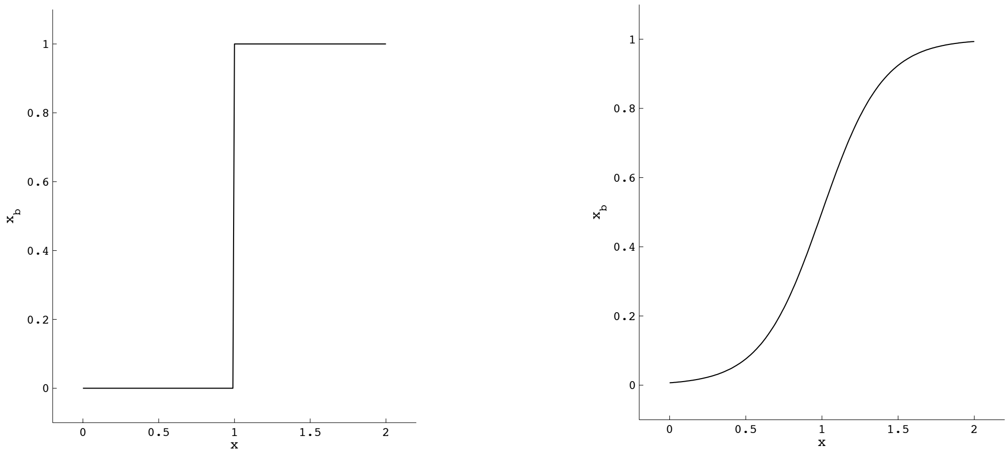

(a) (b)

Figure VI.5: Thresholding: (a) discontinuous ("hard"), (b) continuous.

Empirically, we established that the optimization at the ground stations characterized by large SWE values, should be performed using the *a priori* assumed SWE sub-model (based on the initially assumed coefficients) paired with the MODIS measurements. Namely, in these cases, the SWE sub-model multiplying the smooth MODIS binary curves, is not the subject of the optimization:

$$[c_p, k_f] = f_{opt}\left(\text{MSE}\{g_b(c_p, k_f, t)g(c_p, k_f, t), M(t)g(c_p^0, k_f^0, t)\}, [c_p^0, k_f^0]\right). \tag{VI.6}$$

However, in other cases, where SWE values are not perceived as large (station IV), the optimization is to be performed by considering all the (c_p and k_f) coefficients as optimizable variables:

$$[c_p, k_f] = f_{opt}\left(\text{MSE}\{g_b(c_p, k_f, t)g(c_p, k_f, t), M(t)g(c_p, k_f, t)\}, [c_p^0, k_{\mathrm{f}}^0]\right). \tag{VI.7}$$

VI.5 Results

Firstly, we present the optimization results obtained using the *in situ* measurements. The comparison between three optimization algorithms indicates the best overall performances of the *M1* method. This method, elaborated in Appendix B, is therefore adopted as the standard optimization procedure in this chapter. Concerning the characteristic periods, it appears that the most suitable one is "accumulation+melting (A+M)" period (Fig. VI.6).

As expected, the SWE sub-model, optimized this way, exhibits significantly increased accuracy with respect to the *in situ* ground measurements. This can be noticed in Table VI.1.

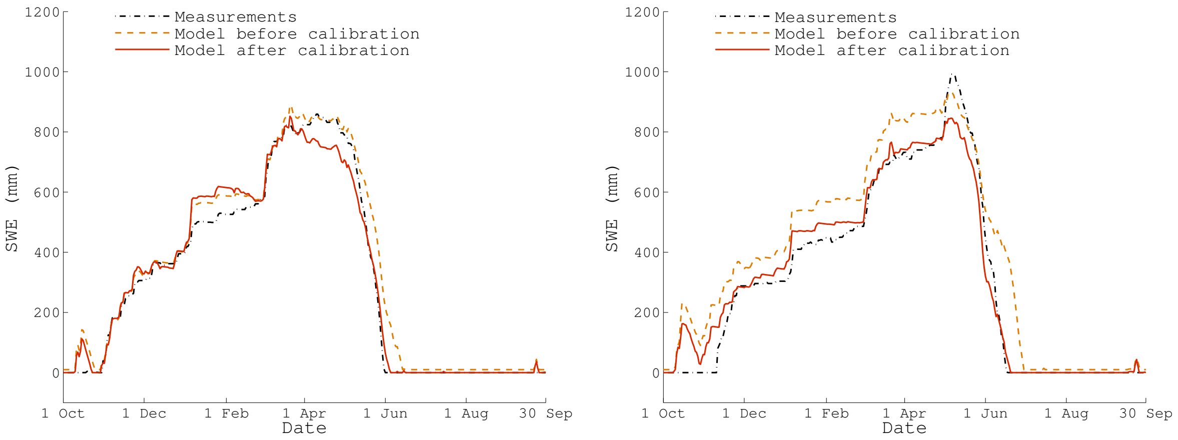

OI OM	all	A+M	A	M
M0	3.141			
M1	2.056	2.034	16.53	7.030
M2	2.056	2.034	15.93	7.030
M3	2.036	2.496	18.38	7.406

(a)

OI OM	all	A+M	A	M
M0	13.49			
M1	3.228	3.205	4.964	7.525
M2	3.228	3.205	4.972	7.526
M3	3.230	3.230	151.4	8.390

(b)

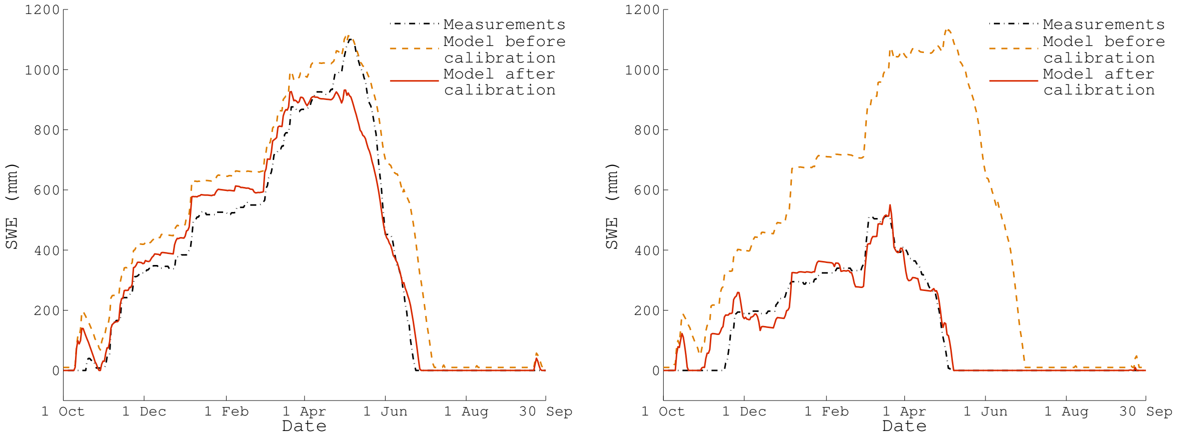

OI OM	all	A+M	A	M
M0	16.95			
M1	4.528	4.528	8.081	23.88
M2	4.528	4.506	4.789	23.88
M3	4.510	4.484	17.29	26.00

(c)

OI OM	all	A+M	A	M
M0	201.2			
M1	1.870	1.888	15.25	2.118
M2	1.870	1.887	15.32	2.101
M3	1.870	3.079	18.08	1.887

(d)

Figure VI.6: Qualitative and quantitive (in terms of MSE $\times 10^{-3}$) comparison of SWE model calibrated using *in situ* measurements, with the measurements from: (a) station I, (b) station II, (c) station III, (d) station IV. OM - optimization method, OI - optimization interval, M0 - non-calibrated model (based on the initial values of the correction coefficients), A - the accumulation period, M - the melting period, all - the whole year.

Table VI.1: Calibration results using both the *in situ* measurements and the MODIS snow cover binary maps: $\text{MSE}_c/\text{MSE}_0$ - ratio between (1) the mean square error (MSE) of the calibrated model and the measurements, and (2) the MSE of the model before calibration and the measurements.

Calibration method	Station	$\text{MSE}_c/\text{MSE}_0$	Time (s)	c_p	k_f
Calibration using *in situ* measurements	Station I	0.6476	18.678	1.4077	2.5994
	Station II	0.2375	34.640	0.9581	6.0304
	Station III	0.2672	17.873	1.1898	2.3090
	Station IV	0.0094	26.655	1.4345	8.0675
	Average	**0.2904**	**24.462**		
Calibration using MODIS data	Station I	0.3578	52.116	1.3406	4.1960
	Station II	0.9946	65.782	1.5492	6.2212
	Station III	0.4071	48.683	1.3692	3.9532
	Station IV	0.0067	123.87	0.7738	10.4578
	Average	**0.4415**	**72.613**		

Further, we present the optimization results obtained using the MODIS binary snow maps (Fig. VI.7) for the four stations with the *in situ* measurements. Even though this optimization appears to be slightly more time consuming, the overall results (Table VI.1) indicate far better performances with respect to the original ones. Curiously, in case of two stations (I and IV) the obtained results are even better than the ones achieved using *in situ* measurements, which are considered as representative optimal solutions. This can be considered both as the validation of the proposed calibration procedure and the demonstration of the utility of remote sensing data in terms of calibration.

As anticipated, the proposed optimization in temporal domain results in spatially optimized maps. It can be seen in Figure VI.8 that the newly obtained SWE maps match far better the MODIS snow maps in terms of the presence/absence of snow. This is particularly true for the melting season, where the proposed optimization exhibits better performances, which can be analogously deduced from the comparison with the ground measurements (Fig. VI.7). The matching was calculated as:

$$m = \frac{\sum_{i=1}^{d_1 d_2} \neg(M_{\text{MODIS}} \oplus M_{\text{MODEL}})}{d_1 d_2} \times 100\% \tag{VI.8}$$

with M_{MODIS} being the snow map (column (i) in Fig. VI.8), and M_{MODEL} the map obtained by thresholding the model (> 0) either before (column (ii) Fig. VI.8) or after the calibration (column (iii) in Fig. VI.8). Finally, d_1 and d_2 are the dimensions of the maps.

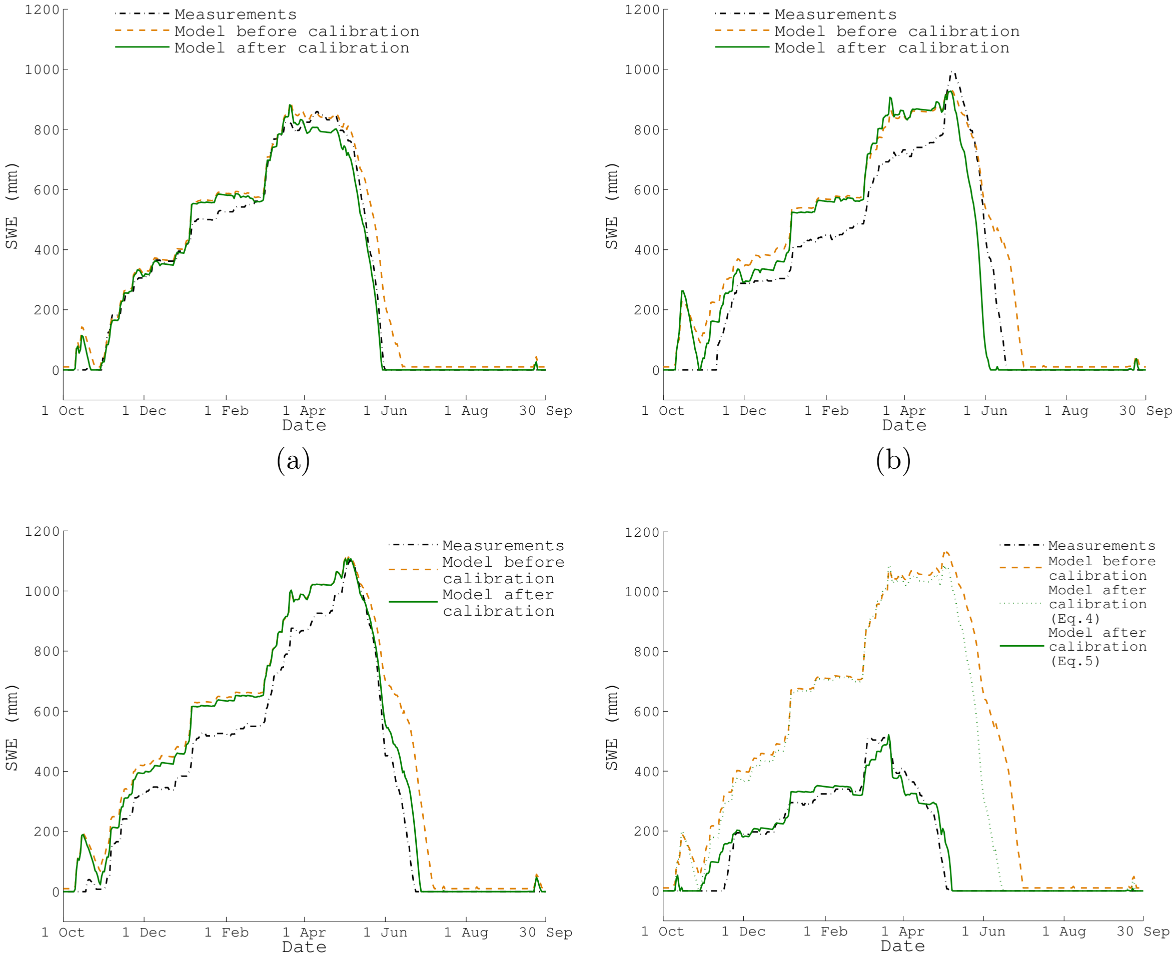

(a) (b) (c) (d)

Figure VI.7: Qualitative comparison with *in situ* ground measurements of the SWE model calibration scheme based on MODIS data: (a) Station I, (b) Station II, (c) Station III, (d) Station IV.

VI.6 Conclusion

Before passing on the highlight of this chapter, we have introduced the ongoing study on potential of POLSAR backed by BSS, in monitoring the snow pack parameters constituting SWE. The first results can be taken as promising, but are still far from the results obtained by relying on the external input - distributed hydrological model, making the most of this chapter.

Namely, due to their role in introducing the influences of topology and mountain winds, the SWE sub-model of the MORDOR hydrological model appears to be quite sensitive with respect to the accumulation and melting correction coefficients. Because of the spatial discontinuity of these coefficients, interpolating locally estimated values, like it is the case with the air

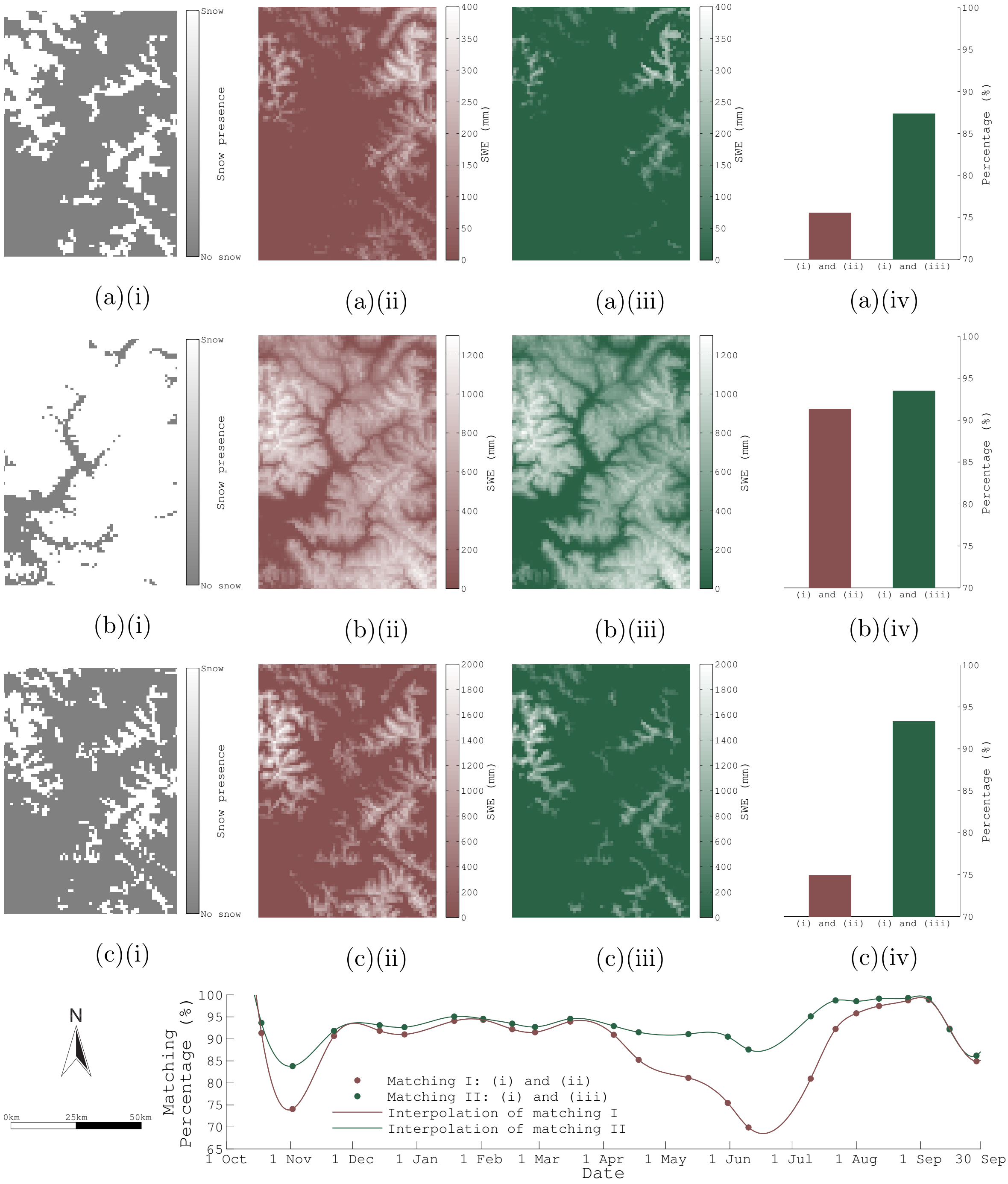

(a)(i) (a)(ii) (a)(iii) (a)(iv)

(b)(i) (b)(ii) (b)(iii) (b)(iv)

(c)(i) (c)(ii) (c)(iii) (c)(iv)

(d)

Figure VI.8: Matching of the obtained SWE maps for: (a) the 26 October 2000, (b) the 4 February 2001, (c) the 1 June 2001. Part (i) shows the MODIS map, part (ii) the SWE map before calibration, part (iii) the SWE map after calibration and part (iv) the matching percentages. (d) The (spline) interpolated matching curves covering the one year period (2000-2001). Geographical coordinates of the provided maps are 44°16'N, 06°13'E (bottom-left corner).

temperature or the precipitation, doesn't appear as a proper solution. Therefore, we proposed a new strategy for their derivation using multi-temporal MODIS binary snow cover maps and *in situ* ground measurements. Firstly, we compared several optimization methods in deducing the representative optimal coefficients for each of the four stations with *in situ* measurements. Further on, using the method which proved as the most appropriate, we presented the strategy for deriving the accumulation and melting coefficients using the MODIS binary snow maps. This method allows covering the entire region of interest, by characterizing each spatial cell (pixel of the MODIS image) with a pair of coefficients. In the same time, it assures better accuracy with respect to the original SWE sub-model, which assumes global values for these two coefficients. Using only MODIS data, the obtained optimized results are comparable to the representative optimal coefficients, derived by the *in situ* data based optimization.

Finally, the spatial SWE estimation is achieved, by with the help of distributed hydrological model and the interpolated temperature and precipitation measurements, which is however still far from our long-term aim in the context of this problem - to autonomously estimate SWE by means of remote sensing data.

Future work aims to investigate the potential role of spaceborne multi-temporal Synthetic Aperture Radar data in improving the accuracy of the SWE sub-model of the MORDOR.

Application: Conclusions

The applied context of this thesis is dedicated to the remote sensing of snow pack. In the preceding three chapters we have elaborated this particular problem (Chapter IV) and offered our contributions in resolving some aspects of it (Chapters V and VI).

Firstly, in Chapter IV we set forth, although obvious, difficulties in estimating snow pack parameters by means of single-polarization SAR remote sensing data. The reasons could be summed up in the ill-posedness we are facing when trying to invert a snow backscattering model. Although numerous empirical and semi-empirical (e.g. [115, 124]) were proposed in resolving this issue, we have rather chosen pursuing and investigating the alternative possibilities, anticipated in Chapter VI. We introduced the backscattering simulator of a single-layer snow pack, expanded to a multi-layer case and stated derived elementary hypotheses about the snow backscattering mechanism. Finally, an external hydrological model, being an integral part of above mentioned alternative possibilities was presented.

The fact arising from these elementary hypotheses about the snow backscattering, affirmed in Chapter IV, is that the dry and the wet snow, in the context of microwaves, represent two distinct materials. Consequently, the choice of the techniques which are to employed in extracting snow parameters, should be conditioned by the identification of the snow type. Therefore, in Chapter V we proposed a mean to achieve this first step, based on exploiting single channel SAR remote sensing datasets, which was the first contribution in the applied context of this thesis. The proposed change detection method compares winter and melting season image and makes a decision, by relying on *a priori* defined ranges of backscattering difference pointing to the wet snow presence. These ranges, named "variable threshold", are derived by the appropriate calibration of the single-layer and multi-layer backscattering simulator from Chapter IV, through the process which was as well founded on the qualitative conclusions constituting above voiced hypothesis. Additionally, the local speckle statistic is considered not before nor after, but directly in the decision process. The last made this approach a stochastic method, which yields at the output a wet snow probability map.

The benefits of the novelty which assumes introducing speckle statistics directly in the change detection, were illustrated by comparing the correspondence between wet snow maps derived using two co-polarized channels (HH and VV). The comparison was performed with respect to the scenario where speckle filtering is applied before the ratio and the one which assumes speckle filtering of the ratio image. Aside from higher matching in case of proposed approach, we established that the other two wet snow binary maps correspond to the wet snow probability map threshold with a confidence level 70% and 72%, respectively. The overall validity of the approach is demonstrated by computing a quite good spatial correlation with the interpolated temperature map.

The above cited alternative possibilities presented in the last chapter firstly assume alluding to our ongoing efforts to promote POLSAR, backed by BSS techniques, in anticipating spatial distribution of snow parameters constituting SWE, the parameter of general interest.

However, the highlight of this chapter is not the autonomous remote sensing method, but rather the integration of multitemporal remote sensing datasets in the external hydrological model. Namely, in Chapter VI we present an calibration method for distributed SWE hydrological model, based on optical remote sensing data.

The (inverse) correlations between polarimetric descriptors, processed by means of PCA, and snow pack parameters, seem to be promising, but however cannot still be considered as decisive in resolving snow parameters derivation issue. On the other side, the role of remote sensing in the existing spatial models can be crucial, as demonstrated in this chapter. Namely, the comparison pointed out that the SWE model calibrated by means of optical remote sensing data, at some of the measurement stations, even outperforms its counterpart calibrated using local *in situ* measurements. Given the obvious advantage of remote sensing data in terms of spatial coverage, this approach, although not autonomous, has an interesting potential.

Overall remarks and perspectives

This thesis was contemplated to reflect in a credible way everything we have done in the frame of remote sensing during the last three years, and which could be granted as contributory to the remote sensing scientific community. The idea was to try facing some of the open questions in the POLSAR community, but as well to try providing the less abstract solutions to some of the "palpable" environmental problems, which should be, in fact, the very purpose of remote sensing. Given our affinity and tendency in our working environment, the former one is tightly related to the implantation of very efficient statistical signal processing tools into the POLSAR data analysis and interpretation. The latter, rather due to the geographic position of this working environment, concerns estimation of an important derived snow pack parameter - Snow Water Equivalent.

As the detailed conclusions were already provided at the end of, both methodological and applied context of this thesis, here we tried to briefly, but very concisely, get together and illustrate its four major contributions:

- The statistical tests for assessing the circularity and the sphericity in case of the alternative statistical modelling of highly textured POLSAR data, followed by a method founded on the spherical symmetry test, used for the evaluation of the suitability of the Spherically Invariant Random Vector, being the above voiced contemporary model [160].
- The incoherent polarimetric target decomposition, based on the Independent Component Analysis, rather than the eigenvector decomposition of the observed polarimetric data, providing non-orthogonal and mutually independent target vectors, on account of the information stored in higher statistical orders [1].
- The stochastic approach for wet snow mapping, based on a change detection method, with a decision being a function of the local incidence angle through the variable threshold, and local speckle statistics introduced implicitly in the decision making [2].
- The method for SWE model calibration, based on multitemporal optical remote sensing datasets, allowing non-autonomous but still very effective implication of remote sensing in SWE spatial derivation [3].

Fortunately, at this point we can not see any insurmountable obstacle, but rather an open horizon for further development and exploitation of these contributions. The most evident perspectives of the presented work would be the following:

- Adapting the interpretation of highly textured POLSAR and InSAR data to the asserted statistical properties. Proposing new alternative models for statistical modelling of targets which do not fit neither multivariate Gaussian nor SIRV model.

- Applying the developed ICTD in case of different targets and exploiting the information contained in the second most dominant component, unconstrained by the imposed orthogonality and influenced by higher order statistical information. Instead of relying on the iterative and adaptive FastICA algorithm, proposing a particular ICA method, eventually based on Maximum Likelihood Estimation, suited to the particular structure of the observed polarimetric data.

- Extending the single channel based method to its polarimetric variant and deriving a variable threshold which appears to be more adaptable to the spatial diversity of snow pack parameters.

- Exploiting the possibilities of SWE monitoring by means of either conventional or contemporary POLSAR decomposition methods, with the implication of PCA in terms of de-noising. Using SAR data i.e. derived wet snow probability maps, in a sort of a fusion with optical datasets, to ameliorate the calibration of SWE spatial models, and to ultimately demonstrate the indispensability of remote sensing in monitoring distributed natural targets.

Appendix A

The polarimetric model of snow backscattering

Snow backscattering can be represented in terms of polarimetric descriptors using Mueller matrix [124].

Mueller matrix ($\mathbf{M}$), evoked in Section I.1 is the 4×4 matrix relating the Stokes vector of the incident $\mathbf{i}_i$ and the scattered $\mathbf{i}_s$ partly polarized EM wave:

$$\mathbf{i}_s = \mathbf{M}\mathbf{i}_i, \tag{A.1}$$

where Stokes vector is the 4×1 vector given in Eq. I.6, completely describing the polarization state of the partly polarized wave [6].

Mueller matrix correspond to FSA hypothesis, and its counterpart for BSA hypothesis would be Kennaugh matrix.

Snow cover backscattering components, illustrated in Fig. IV.1, using the polarimetric counterpart to the backscattering coefficient can be represented as [124]:

- snow pack surface component ($\mathbf{M}_s$):

  $$\mathbf{M}_s = \mathbf{S}_s(\mu_i, -\mu_i, \phi_s - \phi), \tag{A.2}$$

  with $\mathbf{S}_s$ being the snow surface backscattering matrix (formed of co-polarized and cross-polarized backscattering coefficients).

- underlying ground component ($\mathbf{M}_{gr}$):

  $$\mathbf{M}_{gr} = \mathbf{T}(\theta_r, \theta_i)\mathbf{S}_g(\mu_r, -\mu_r, \phi_s - \phi)\mathbf{T}(\theta_i, \theta_r) \exp \frac{-2\kappa_e d}{\mu_r}, \tag{A.3}$$

  with $\mathbf{S}_g$ being the ground surface backscattering matrix and $\mathbf{T}$ the Fresnel transmission coefficients 4×4 matrix.

- volume component ($\mathbf{M}_v$):

$$\mathbf{M}_v = \mathbf{T}(\theta_r, \theta_i)\frac{\mathbf{P}(\mu_r, -\mu_r, \phi_s - \phi)}{2\kappa_e}\mu_r \left(1 - \frac{-2\kappa_e d}{\mu_r}\right)\mathbf{T}(\theta_i, \theta_r), \tag{A.4}$$

where $\mathbf{P}$ if the Rayleigh 4×4 matrix.

- ground-volume interaction component ($\mathbf{M}_{gv}$):

$$\begin{aligned} \mathbf{M}_{gv}^{'} &= \frac{1}{\mu_i}\mathbf{T}(\theta_r, \theta_i)\mathbf{T}(\theta_i, \theta_r) \exp\frac{-2\kappa_e d}{\mu_r}\mathbf{R}(\theta_r, \theta_r) \\ &\cdot \mathbf{P}(-\mu_r, -\mu_r, \phi_s - \phi)\frac{1 - \exp -2k'd}{k'}, \\ \mathbf{M}_{gv}^{''} &= \frac{1}{\mu_i}\mathbf{T}(\theta_r, \theta_i)\mathbf{T}(\theta_i, \theta_r) \exp\frac{-2\kappa_e d}{\mu_r}\mathbf{R}(\theta_r, \theta_r) \\ &\cdot \mathbf{P}(\mu_r, \mu_r, \phi_s - \phi)\frac{\exp -2k'd - 1}{k'} \end{aligned} \tag{A.5}$$

where $\mathbf{R}$ is the Fresnel reflection coefficients 4×4 matrix, and $k' = \kappa_e\left(\frac{1}{\mu'} - \frac{1}{\mu''}\right)$, μ' and μ'' being cosines of volume indicent and scattered angle.

Appendix B

The Nelder-Mead simplex optimization method

The Nelder-Mead simplex optimization method can be considered as one of the most popular non-linear unconstrained optimization algorithm [155]. It minimizes the scalar function value by relying only on the function values, without taking into the account the derivative information.

The algorithm is defined with four characteristic coefficients:

- reflection (ρ)
- expansion (χ)
- contraction (γ)
- shrinkage (σ)

whose standard values would be $\rho = 1, \chi = 2, \gamma = \sigma = \frac{1}{2}$.

We define the optimization problem as the minimization of $f(x)$ for $x \in R^n$, where n would be the dimension of the simplex. Point x_1 is "the best" vertex, while point x_{n+1} would be "the worst" one of the simplex, meaning that $f(x_1)$ is the minimal value we have and $f(x_{n+1})$ the maximal one. After each iteration we get a new simplex, defined with a set of vertices $x_1, x_2, \dots x_{n+1}$. The aim would be to find the best among "the best" vertices, which gives "the global minimum" for $f(x)$.

The algorithm steps during one iteration would be the following [142, 155]:

1. Ordering the vertices of the n-dimensional simplex so that:

$$f(x_1) \leq f(x_2) \leq \cdots \leq f(x_{n+1}). \tag{B.1}$$

2. Computing the reflection point (Fig. B.1a):

$$x_r = (1+\rho)\overline{x} - \rho x_{n+1}, \tag{B.2}$$

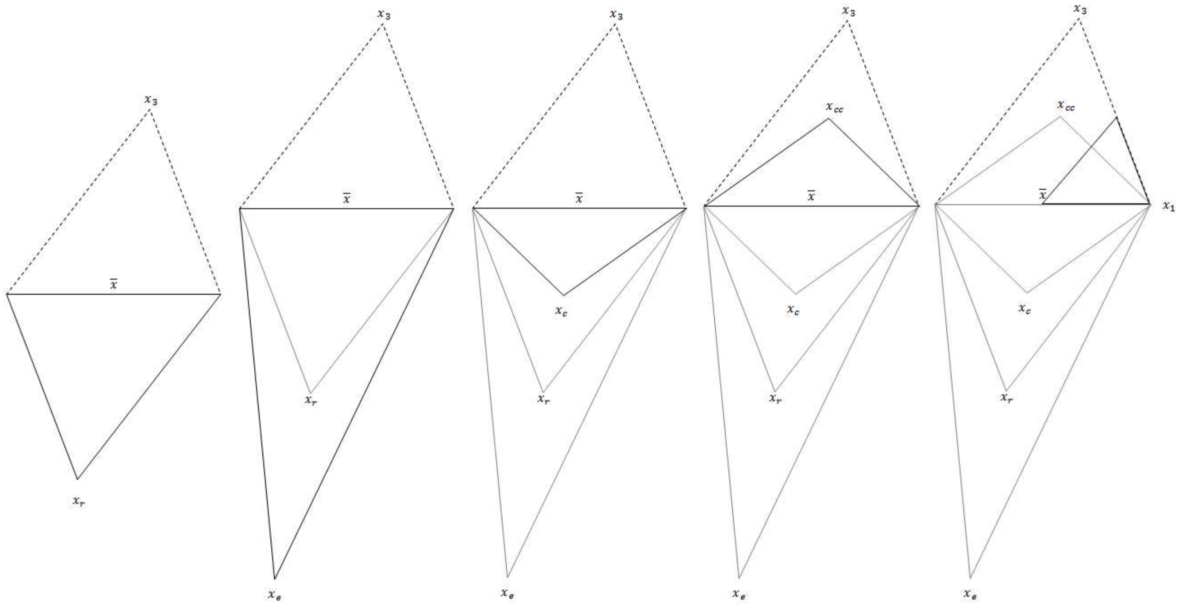

(a) (b) (c) (d) (e)

Figure B.1: Two dimensional simplex (triangle) through different steps of the algorithm, for standard value of the characteristic coefficients.

with $\overline{x} = \sum_{i=1}^{n} x_i/n$. At this point, if $f(x_1) \leq f(x_r) < f(x_n)$, the iteration is terminated by accepting x_r.

3. If $f(x_r) < f(x_1)$, the expansion point x_e is derived as (Fig. B.1b):

$$x_e = \overline{x} + \chi(x_r - \overline{x}). \tag{B.3}$$

If $f(x_e) < f(x_r)$, the iteration is terminated by accepting x_e, if not x_r is accepted.

4. However, if $f(x_r) \geq f(x_n)$, contraction is needed:

   - if $f(x_n) \leq f(x_r) < f(x_{n+1})$, it is the outside contraction (Fig. B.1c):

   $$x_c = \overline{x} + \gamma(x_r - \overline{x}). \tag{B.4}$$

   If $f(x_c) \leq f(x_r)$, accept x_c. If not, go to step 5.

   - on the other side, if $f(x_r) \geq f(x_{n+1})$, it would be the inside contraction (Fig. B.1d):

   $$x_{cc} = \overline{x} - \gamma(\overline{x} - x_{n+1}). \tag{B.5}$$

   If $f(x_cc) < f(x_{n+1})$, accept x_{cc}. If not, go to step 5.

5. The last step is shrinking (Fig. B.1e). The function value is computed for n points $v_i = x_i + \sigma(x_i - x_1)$, and the vertices of the simplex at the next iteration are $x_1, v_2, \ldots v_{n+1}$.

APPENDIX C

Résumé étendu (fr)

Séparation aveugle des sources polarimétriques en télédétection RSO satellitaire à très haute résolution spatiale

Introduction

La télédétection désigne la science de l'acquisition d'information sur la surface de la Terre, sans le contact avec cette dernière, ce qui veut dire la détection de l'énergie électromagnétique diffusée, réfléchie ou émise puis le traitement, l'interprétation et l'application de cette information. Nous pouvons la définir comme une discipline scientifique appliquée, qui comprenne et compte sur les domaines plus fondamentaux, comme le traitement du signal et d'image, l'électromagnétisme et pratiquement toutes les sciences de la Terre. Aujourd'hui, il paraît impossible d'envisager les dernières privées de large couverture spatiale de, soit les objets existants sur notre planète, soit les processus et phénomènes ayant lieu partout sur sa surface. Cela fait de la télédétection un outil indispensable dans la surveillance de la Terre.

L'importance de cette science et la nécessité de son développement supplémentaire sont soulignés par certains des plus grands défis que l'humanité rencontre dans l'ère moderne : les changements climatiques observés, la croissance rapide de la population mondiale, le développement durable etc.

L'impact significatif du réchauffement global sur l'environnement, indiqué principalement par la fonte des glaces dans les pôles et dans les régions montagnardes, impose la surveillance de la cryosphère comme une de nos priorités principales. En dehors de cela, glaciers et manteau neigeux représentent les sources importantes de l'eau potable ainsi que industrielle, dont le quantité peut être estimée précisément seulement au moyen de large évaluation spatiale. La végétation, particulièrement les forêts, étant les poumons de notre planète, ne peuvent être préservées que par l'évaluation attentive et régulière de leur état. Le besoin pour la recrudescence de production de nourriture, reconnu il y a longtemps, qui devrait être faite en optimisant les régions agricoles actuelles, demande leur inspection constante et précise. La surveillance de surface des océans, qui couvrent presque 70% de la Terre, ne peut être effectuée qu'au moyen de la télédétection.

Cela, ce n'est que quelques des nombreux exemples, est un effort pour démontrer l'essentialité de l'information acquise à distance dans l'observation de la Terre. Dire, en généralisant, que tout ce qui ne peut pas être mesuré *in situ*, au moyen de l'échantillonnage spatial, dépend de la télédétection, ne devrait pas être une exagération.

Selon la fréquence des ondes électromagnétiques qui portent l'information, nous pouvons distinguer entre différents types de capteurs actifs et passifs, qui peuvent être soit satellitaires, soit aéroportés. Par conséquent, il y a plusieurs disciplines de télédétection, dont, en prenant en compte l'infrastructure actuelle, la télédétection optique passive et la télédétection Radar à Synthèse d'Ouverture (RSO) active, sont considérées comme prééminantes.

La télédétection optique fonctionne dans les régions visibles et infrarouges du spectre électromagnétique. Selon la résolution spectrale c'est à dire, combien de différentes fréquences peut-on utiliser simultanément, nous pouvons discriminer entre des images optiques monospectrales (panchromatiques), multispectrales et hyperspectrales. Malgré le fait qu'elle ne peuvent être acquises que pendant la journée et malgré les contraintes qui concernent la présence de nuages, une image optique, étant essentiellement une photographie "renforcée", représente une pièce vitale d'information.

La télédétection RSO, qui fonctionne plutôt dans la partie microondes du spectre électromagnétique, continue d'être particulièrement attractive grâce à ses performances de détection "toute la journée" et "toutes les conditionnes météorologique". En dehors de cela, l'avantage de RSO serait la pénétration plus profonde de microondes par rapport à la lumière visible, qui nous permet de déduire non seulement les propriétés de surface, mais aussi de volume. Le principal désavantages concerne l'interprétation de données. Autrement dit, contrairement au cas de l'imagerie optique, en raison de la géométrie différente et de l'interaction particulière avec la cible, nous ne pouvons pas entièrement compter sur notre intuition.

De façon analogue à la télédétection optique, où nous utilisons simultanément plusieurs fréquences pour approfondir la connaissance de la cible, dans le cas de la télédétection RSO nous utilisons plutôt plusieurs polarisations des ondes électromagnétiques, à l'émission et à la réception. On appelle cette sous-discipline la polarimétrie RSO et il en résulte une image RSO avec plusieurs canaux, dont chacun correspond à une combinaison de différentes polarisations.

Dans cette thèse nous proposons principalement des contributions à l'analyse et l'interprétation des images RSO. Cependant, nous ne négligeons pas l'imagerie optique multispectrale, mais nous l'utilisons plutôt, en démontrant son utilité.

Les contributions présentées sont divisées en deux parties principales. La première partie traite des avancements théoriques et en tant que tel, elle est liée à l'interprétation des données polarimétriques RSO. Plus précisément, elle concerne l'implication des techniques de séparation aveugle des sources, ayant comme l'objectif une amélioration de la qualité de l'interprétation, en considérant les caractéristiques particulières des données acquises récemment. Comme un prélude, le cadre méthodologique de l'évaluation statistique de ces particularités est inclus. La seconde partie, traitant plutôt une application - la télédétection du manteau neigeux, concerne le rôle de la télédétection RSO dans la cartographie de la neige et finalement, la modélisation spatiale de l'équivalent en eau de la neige (EEN). La dernière est faite en intégrant les données optiques dans un modèle hydrologique, mais aussi considérée dans le contexte du RSO polarimétrique.

Les particularités des nouvelles données concernent principalement l'amélioration importante de la résolution spatiale, notamment la taille de l'objet le plus petit au sol, qui peut être distingué. Ce progrès influence significativement la statistique des images RSO. Notamment, l'hypothèse conventionnelle pour le modèle statistique de l'image RSO polarimétrique multi-canaux serait la distribution Gaussienne multidimensionnelle. Pourtant, l'amélioration de la résolution spatiale compromet cette hypothèse, causant plutôt un clutter hétérogène, caractérisé par le statistique non-Gaussienne.

Les dilemmes importants dans la communauté à propos de ce sujet, peuvent être résumées en deux questions :

- Est-ce que ces nouveaux modèles statistiques proposés sont vraiment appropriés pour la modélisation de données RSO polarimétriques, ainsi que les autres types de données RSO multidimensionnelles ?
- Qu'est-ce que nous gagnons exactement en admettant le départ de l'hypothèse Gaussienne, dans le cadre de l'interprétation ?

Ces deux questions furent une force motrice pour la recherche constituant le contexte méthodologique de cette thèse.

Après avoir introduit les bases sur la statistique d'image RSO dans le premier chapitre, dans le chapitre II nous proposons une analyse statistique élaborée, dans le but de déterminer quantitativement la nécessité et les bénéfices de l'hypothèse statistique altérée. C'est-à-dire que nous répondons à la première question.

Une interprétation de l'image RSO polarimétrique assume principalement l'application de décompositions polarimétriques, dans le but d'exprimer la diffusion totale comme la somme (soit cohérente ou incohérente) de composants de la diffusion plus élémentaire. Parmi différentes décompositions, introduites dans le premier chapitre avec le concept de la polarimétrie RSO, les algébriques, arrivent à être les plus utilisées dans la communauté aujourd'hui. Étant basées sur l'analyse des valeurs propres, elles sont intrinsèquement liées à l'hypothèse de Gaussianité du clutter RSO polarimétrique. Comme on le dit dans l'introduction de la partie méthodologique, le décalage par rapport à cette hypothèse a comme conséquence que les vecteurs propres dérivés ne sont pas indépendants statistiquement, mais plutôt seulement décorrélés. Donc, en employant de préférence la technique la plus proéminente de séparation aveugle des sources - analyse en composantes indépendantes (ACI), introduite dans le premier chapitre, nous proposons une nouvelle approche pour la décomposition de données polarimétriques dans le Chapitre III. Cette décomposition serait notre réponse à la deuxième question.

Après avoir introduit les bases de la télédétection de manteau neigeux dans le Chapitre IV, dans le chapitre suivent nous proposons une nouvelle méthode stochastique pour la cartographie de la neige. Bien que l'application de la décomposition développée sûr les images RSO polarimétrique des régions neigeux, aboutit à quelques conclusions empiriques intéressantes, nous avons inclus les propriétés électromagnétiques de la neige dans le contexte d'une image RSO mono-canal. Notamment, les propriétés diélectriques de la neige dépendent significativement de la quantité d'eau présente dans le manteau. Par conséquent, les techniques de télédétection employées dans l'extraction des paramètres de la neige, ce qui serait le but ultime de la télédétection de la neige, varient selon le type de neige : si elle est séchée ou humide. Donc, au début, il faut identifier le type du manteau neigeux. Dans l'approche présentée, à part avoir proposé une décision stochastique pour discriminer entre deux types de neige, nous dérivons aussi un nouveau seuil variable de rétrodiffusion, qui est basé sur le simulateur de rétrodiffusion ainsi que le mécanisme de rétrodiffusion déduit depuis le dernier, les deux introduits dans le Chapitre IV.

Finalement, nous nous concentrons sur la dérivation spatiale de l'équivalent en eau de la neige. Vu que l'inversion du modèle de rétrodiffusion représente un problème mal posé, qui cause que l'image RSO mono-canal ne soit pas très utile dans ce contexte, nous nous tournons vers la conjonction du modèle hydrologique avec les données de télédétection. Aussi, nous présentons brièvement les recherches en cours, qui concerne le potentiel de modélisation de l'EEN au moyen de données RSO polarimétriques, renforcées en impliquant les techniques de séparation des sources (analyse en composantes principales) dans l'analyse des paramètres dérivés. Cependant, le point culminant de ce chapitre serait la méthode de calibration du modèle hydrologique de l'EEN, basée plutôt sur les données optiques. Le modèle réfèrent, qui nécessita la calibration spatiale, est introduit dans la section IV.2. Le chapitre VI décrit l'algorithme proposé, et même plus, sert comme un type de démonstration de la suprématie éventuelle de la télédétection par rapport aux mesures *in situ*.

C.1 Image RSO polarimétrique et séparation aveugle des sources

Ce chapitre sert comme un introduction aux méthodes de l'état de l'art qui nous ont inspirés pour effectuer la recherche présentée dans la partie méthodologique de la thèse. Ce chapitre en constitue une revue, brève mais systématique. La fusion d'une partie de ces méthodes forme les bases des contributions théoriques présentées.

C.1.1 Polarimétrie RSO

La polarimétrie RSO représente l'émission en alternance des ondes polarisées horizontalement (H) et verticalement (V), et la réception des ondes rétrodiffusées de la cible et captées par les antennes horizontales et verticales (Fig. C.1). Cela nous permet d'avoir une information complexe, c'est-à-dire le rapport du champ électrique incident et rétroduffusé, pour quatre combinaisons de polarisations. Dans le cas de cibles cohérentes, qui ne montrent pas de

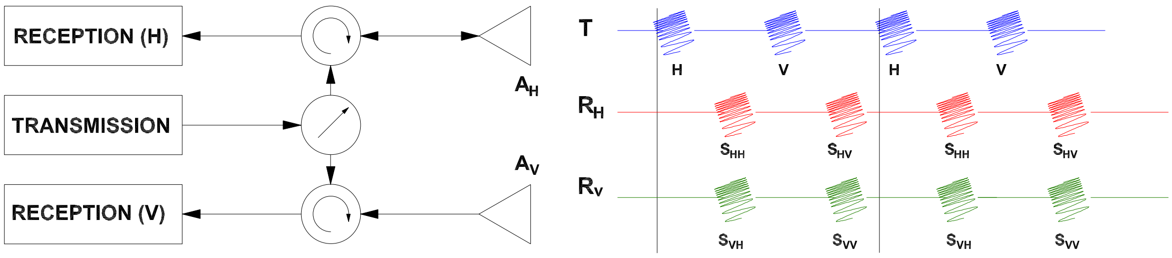

(a) (b)

Figure C.1: Principe de la polarimétrie : (a) schéma de l'instrument, (b) les pulses à la transmission (T) et à la réception (R).

$$\mathbf{S} = \begin{bmatrix} S_{hh} & S_{hv} \\ S_{vh} & S_{vv} \end{bmatrix} \qquad \mathbf{k} = \frac{1}{\sqrt{2}} \begin{bmatrix} S_{hh} + S_{vv} \\ S_{hh} - S_{vv} \\ 2S_{hv} \end{bmatrix} \qquad \mathbf{k}_c = \begin{bmatrix} S_{hh} \\ \sqrt{2}S_{hv} \\ S_{vv} \end{bmatrix}$$

matrice de rétrodiffusion | *vecteur cible Pauli* | *vecteur cible lexicographique*

fluctuations ni spatiales ni temporelles, cette information peut être représentée soit dans la forme de la matrice de rétrodiffusion (**S**), soit dans la forme du vecteur cible (**k**) :

Cependant, la plupart de cibles naturelles que nous rencontrons fluctuent soit dans l'espace ou dans le temps, ce qui veut dire qu'elles ont un caractère incohérent. Dans ce cas là, la représentation appropriée de l'information acquise serait plutôt la covariance du vecteur cible ($\mathbf{T} = \mathbf{k}\mathbf{k}^H$), estimée sur l'ensemble de pixels. En conséquence, à cause de cet effet de l'interférence spatiale aléatoire que nous appelons *speckle*, la formation d'une image RSO et par conséquent d'une image RSO polarimétrique représente un processus stochastique. Si nous présumons l'homogénéité du clutter, l'hypothèse conventionnelle dit que le vecteur cible est supposé être un vecteur aléatoire complexe Gaussien circulaire à moyenne nulle et sa matrice de covariance distribuée selon la distribution de Wishart. Par contre, l'amélioration de la résolution spatiale, c'est-à-dire la réduction de la cellule spatiale qui correspond à un pixel, engendre un clutter hétérogène, ce qui nécessite l'implication de la texture (τ). Donc, pour décrire un pixel dans l'image polarimétrique texturée il nous faudrait un modèle multiplicatif $\mathbf{k} = \sqrt{\tau}\mathbf{z}$, où $\mathbf{z}$ représente le vecteur cible normalisé. Le modèle qui correspond à cette description et qui est proposé pour caractériser les images RSO polarimétriques texturées est les vecteurs aléatoires sphériquement invariants (SIRV).

Le but principal de la polarimétrie radar, et finalement de toutes les autres disciplines de la télédétection, est de mieux comprendre les cible observées sur la Terre. Le moyen d'y parvenir serait de représenter l'information acquise et représentée dans la forme du **S**, **k** ou **T** comme la mélange des diffuseurs élémentaires qui paraissent être plus compréhensibles, c'est-à-dire de décomposer la cible. Les décompositions polarimétriques, en dehors du fait d'être cohérentes ou incohérentes, peuvent être soit basées sur les modèles (nous cherchons dans le mélange les modèles à priori définis), soit algébriques (nous affirmons les composantes du mélange et puis nous essayons de les caractériser). La décomposition incohérente algébrique proéminente est la décomposition proposé par Cloude et Pottier, où nous représentons la matrice de covariance **T** comme la somme pondérée des covariances de ses vecteurs propres :

$$\mathbf{T} = \lambda_1 \mathbf{k}_1 \mathbf{k}_1^H + \lambda_2 \mathbf{k}_2 \mathbf{k}_2^H + \lambda_3 \mathbf{k}_3 \mathbf{k}_3^H, \tag{C.1}$$

où les valeurs propres (λ_i) sont associées aux contributions de composantes. Chacune de ces composantes est en suite paramétrée en utilisant le modèle $\alpha - \beta - \gamma - \delta$ ou le modèle TSVM dans le cas de décomposition de Touzi, tandis que les contributions forment les paramètres de l'entropie (H) et l'anisotropie (A).

C.1.2 Séparation aveugle des sources

La séparation aveugle des sources représente l'ensemble des techniques qui ont pour but la récupération des signaux de sources (**s**) depuis leur mélange (**x**), sans avoir à priori la connaissance du processus de mélange (**A**) :

$$\mathbf{x}(t) = \begin{bmatrix} x_1(t) \\ x_2(t) \\ \vdots \\ x_n(t) \end{bmatrix} = \mathbf{A}\mathbf{s}(t) = \begin{bmatrix} A_{11} & A_{12} & \cdots & A_{1n} \\ A_{21} & A_{22} & \cdots & A_{2n} \\ \vdots & \vdots & \ddots & \vdots \\ A_{n1} & A_{n2} & \cdots & A_{nn} \end{bmatrix} \begin{bmatrix} s_1(t) \\ s_2(t) \\ \vdots \\ s_n(t) \end{bmatrix}, \tag{C.2}$$

D'un coté, la technique la plus classique qui correspond à cette description est l'Analyse en Composantes Principales (ACP), où les sources **s** sont mutuellement décorrélées et la matrice de mélange **A** doit être orthogonale. De l'autre coté, la technique proéminente qui assure l'indépendance des sources et qui n'impose pas l'orthogonalité de la matrice de mélange est l'Analyse en Composantes Indépendantes (ACI).

Les méthodes de l'ACI utilisées dans cette thèse peuvent être divisées en méthodes itératives et tensorielles. Finalement, la méthode qui correspond le mieux dans notre contexte de la polarimétrie RSO, est une méthode itérative - FastICA. Dans ce cas, le critère pour l'indépendance des sources est leur non-gaussianité, le concept qui découle du théorème centrale limite. En général, nous assurons l'indépendance en maximisant un des critères de non-gaussianité comme le kurtosis ou la néguentropie, en minimisant l'information mutuelle ou en utilisant l'Estimation de Vraisemblance Maximum. Si nous traitons les signaux complexes, comme si c'est le cas dans la polarimétrie RSO, l'indépendance est assurée en maximisant la fonction non-linéaire de contraste, qui peut être quadratique, logarithmique ou racine carrée.

C.2 Évaluation statistique des images RSO polarimétriques à haute résolution spatiale

Dans ce chapitre, nous proposons un cadre méthodologique pour l'évaluation statistique des particularités des données RSO multidimensionnelles et à haute résolution spatiale. Celui surtout représente l'analyse des trois importants paramètres statistiques : circularité, sphericité et symétrie sphérique. Tous les trois sont considérés dans le contexte de modèle statistique SIRV. Les conclusions dérivées après avoir appliqué ce cadre sur les données RSO polarimétriques, sont renforcées en impliquant également les données RSO interférométriques.

C.2.1 Paramètres statistique

Le but principal est d'examiner la conformité des données RSO multidimensionnelles hautement texturées par rapport à l'hypothèse statistique contemporaine - vecteur aléatoire sphériquement invariant (SIRV). Nous démontrons que cela peut être fait en analysant la symétrie sphérique du vecteur cible, après avoir vérifié des propriétés de circularité et de sphéricité.

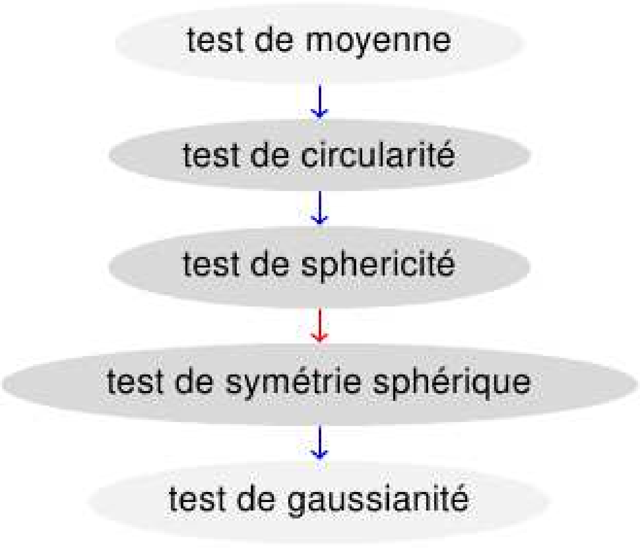

Figure C.2: Cadre méthodologique pour l'évaluation statistique de données RSO multidimensionnelles.

La circularité concerne l'indépendance entre la partie réelle ($\mathbf{x}$) et la partie imaginaire ($\mathbf{y}$) d'un vecteur aléatoire ($\mathbf{k} = \mathbf{x} + i\mathbf{y}$). Dans le contexte de polarimétrie, nous la vérifions en considérant le vecteur de cible augmenté $\beth = [\mathbf{k}^T, \mathbf{k}^H]^T$, qui forme la matrice de covariance augmentée :

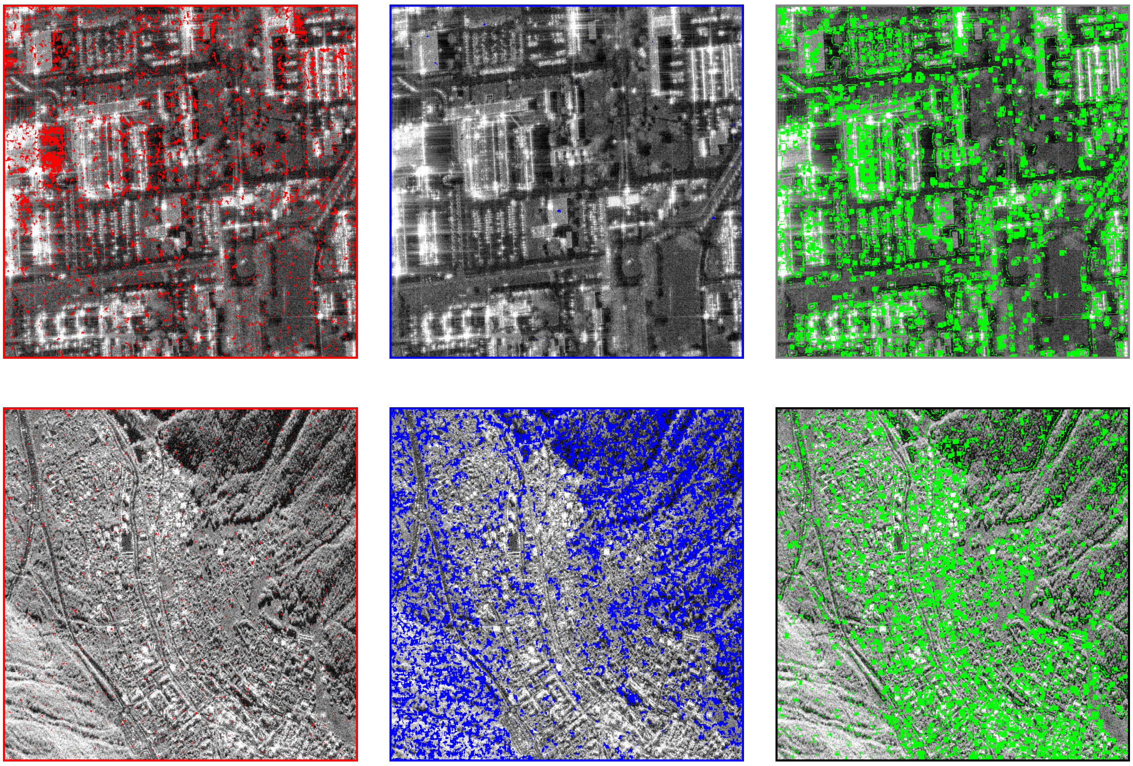

Figure C.3: Image RSO polarimétrique de Toulouse, acquise par RAMSES en bande X (en haut); Image RSO interférométrique de Chamonix, acquise par TerraSAR-X en bande X (en bas) : pixels non-circulaires, pixels sphériques, pixels sphériquement non-symétriques.

$$\mathbf{R} = \mathbb{E}[\gimel\gimel^H] = \begin{bmatrix} \mathbf{C} & \mathbf{P} \\ \mathbf{P}^* & \mathbf{C}^* \end{bmatrix} \tag{C.3}$$

Le test concerne la structure de matrice de pseudo-covariance ($\mathbf{P}$) (Table C.1). Des vecteurs non-circulaires devraient être traités comme les vecteurs réels augmentés.

$\begin{cases} H_0 : P = 0, \\ H_1 : P \neq 0 \end{cases}$	Gaussien	SIRV
	$\Lambda(\mathbf{k}_1, ...\mathbf{k}_N) = \frac{\det(\widehat{\mathbf{R}}_{SECM})}{(\det(\widehat{\mathbf{C}}_{SCM}))^2} \gtrless^{H_0}_{H_1} \lambda$	$\ln \Lambda(\mathbf{k}_1, ...\mathbf{k}_N) / \sum_{i=1}^{m} \frac{\frac{\mathbb{E}[\lvert k_i \rvert^4]}{\mathbb{E}[\lvert k_i \rvert^2]^2}}{r_i(k_i)^2+2}$

Table C.1: Circularité : test ratio de vraisemblance généralisé pour vecteur cible gaussien et pour SIRV.

La sphéricité concerne plutôt l'indépendance égale entre les éléments d'un vecteur aléatoire. Elle est testée en vérifiant la structure de matrice de covariance (Table C.2). Les vecteurs sphériques ne devraient pas être traités au moyen de l'analyse multivariée.

$\begin{cases} H_0 : \mathbf{C} = \varsigma \mathbf{I}_m \\ H_1 : \mathbf{C} \neq \varsigma \mathbf{I}_m \end{cases}$	Gaussien	SIRV
	$\Lambda_s(\mathbf{k}_1, ..\mathbf{k}_N) = m \frac{(\det \widehat{\mathbf{M}}_{SCM})^{\frac{1}{m}}}{\mathrm{tr}\, \widehat{\mathbf{M}}_{SCM}} \gtrless_{H_0}^{H_1} \lambda_s$	${}_a\Lambda_s(\mathbf{k}_1, ..\mathbf{k}_N) = (\det \widehat{\mathbf{M}}_{FP})^{\frac{1}{m}} <_{H_0} \lambda_s$

Table C.2: Sphéricité : test généralisé du ratio de vraisemblances pour vecteur cible gaussien et pour SIRV.

Enfin, la symétrie sphérique pour des vecteurs circulaires et non-sphériques présume une conformité par rapport à la famille de distributions elliptiquement profilées. Cette propriété est testée en vérifiant la structure de la matrice de quadri-covariance $\widehat{\mathbf{M}}_4 = \frac{1}{N} \sum_{i=1}^{N} \mathbf{k}_i \mathbf{k}_i^H \otimes \mathbf{k}_i \mathbf{k}_i^H$.

C.2.2 Résultats

L'application des tests réalisés sur une image polarimétrique et une image interférométrique (Fig. C.3) nous permettent les conclusions suivantes :

- la circularité, ne découlant pas de bruit thermique, ne devrait pas être à priori présumée,
- la sphéricité devrait être testée, pour éventuellement éviter l'analyse multivariée,
- le modèle SIRV répond bien sauf dans les régions caractérisées plutôt par une forte rétrodiffusion cohérente.

C.3 Décomposition polarimétrique par séparation aveugle des sources

Ce chapitre représente le point central de la thèse. Ici, en remplaçant la décomposition conventionnelle en valeurs propres par un algorithme de l'ACI, nous généralisons le concept de décomposition incohérente de la cible au niveau de séparation aveugle des sources. La décomposition proposée exploite l'information statistique des ordres supérieurs, émergeant de l'hétérogénéité du clutter RSO polarimétrique. Le résultat est l'ensemble de vecteurs de cible, mutuellement indépendants et non-orthogonaux. La composante la plus dominante est très similaire à celle obtenue au moyen des méthodes conventionnelles, mais la deuxième, par contre, porte une nouvelle information.

La première étape serait de sélectionner des ensembles de données d'observation, c'est-à-dire des vecteurs de cible. À priori, il y a deux façons pour faire cela :

- une approche globale qui présume une classification statistique donnant à la sortie des ensembles de données stationnaires.
- une approche locale qui est basée sur une fenêtre glissante.

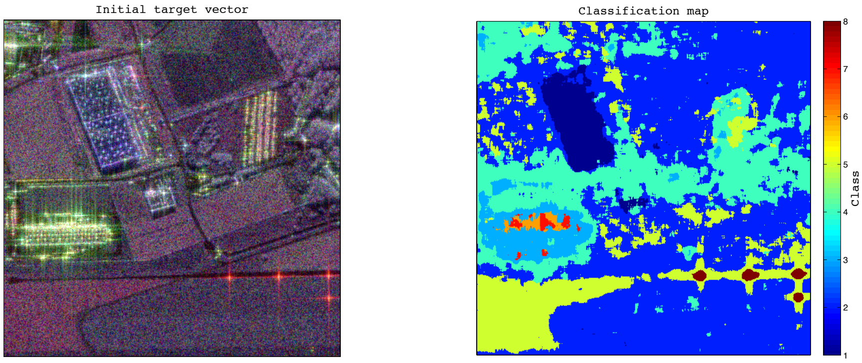

(a) (b)

Figure C.4: Image de Brétigny, acquise par RAMSES en bande X : (a) vecteur cible Pauli, (b) classification.

Vu la taille de fenêtre requise en cas de l'ACI, nous sommes plutôt concentrés sur l'approche globale.

Ensuite, sur tous les sous-ensembles de l'image RSO (classes), nous appliquons l'algorithme de l'ACI, ce qui nous permet de caractériser chacun parmi eux avec une matrice de mélange et des sources appropriées (Eq. C.2, $n = 3$). Chaque colonne de matrice $\mathbf{A}$ est liée à une des sources dans le vecteur $\mathbf{s}$, chacune étant mutuellement indépendante. En conséquence, les colonnes de la matrice de mélange sont également indépendantes et vu qu'elles représentent physiquement des vecteur cibles, nous les considérons comme les mécanismes indépendants de rétrodiffusions (Fig. C.5). Leur indépendance est assurée en maximisant la fonction logarithmique comme la mesure de contraste, tandis que leurs contributions à la rétrodiffusion totale (homologue de valeurs propres) sont estimées au moyen de ℓ_2^2 norme au carré.

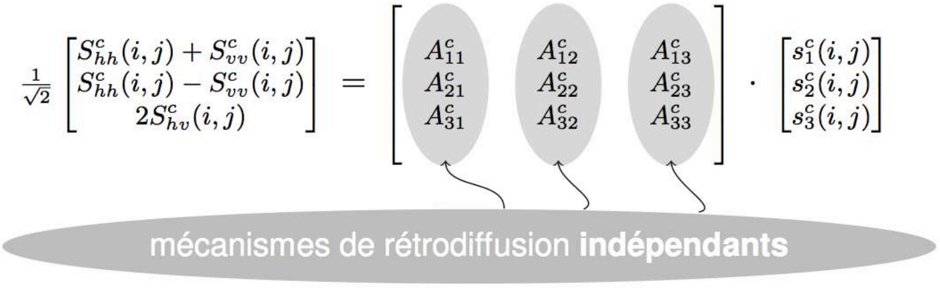

Figure C.5: Le concept d'implication de l'ACI dans le contexte de polarimétrie.

Le vecteur cible de chacun de mécanismes indépendants est ensuite paramétré en utilisant le modèle de vecteur de rétrodiffusion de la cible (TSVM) de Touzi. Cela nous permet de caractérise les trois mécanismes les plus dominants en fonction de paramètres invariants par rapport à la rotation, ainsi que de les illustrer avec une sphère de Poincaré (Fig. C.6).

Le choix de l'algorithme de l'ACI (Complex FastICA logarithmique) est fait en appliquant la décomposition sur une image de la région urbaine (Fig. C.6) qui contient des trièdres placés

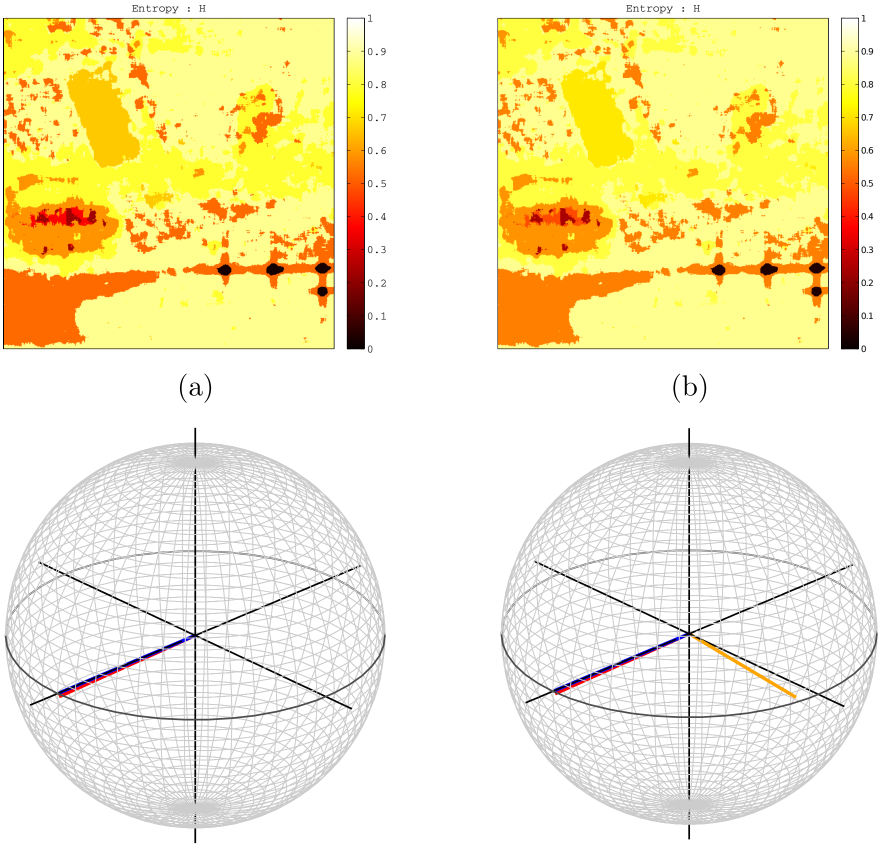

(a) (b)

(c) (d)

Figure C.6: Image de Brétigny, acquise par RAMSES en bande X : (a) entropie (ACP), (b) entropie (ACI - log), (c) composantes (1ère, trièdre) de classe VIII (ACP), (d) composantes (1ère, 2éme, trièdre) de classe VIII (ACI-log).

en fin de calibration, par rapport à deux critères :

- l'estimation d'entropie : l'hypothèse de départ fut que les composantes estimées devraient avoir des contributions similaires à celles obtenues au moyen de la décomposition conventionnelle (Fig. C.6a et b).
- l'identification des trièdres : l'algorithme choisi devrait être capable d'estimer aussi précisément le trièdre tant que la première composante comme la décomposition conventionnelle (Fig. C.6c et d).

De la même manière comme pour la classe de "trièdres", la première composante est très similaire à celle estimée par l'ACP pour toutes les autres classes. Par contre, la deuxième composante est différente. Notamment, elle est maintenant non seulement décorrélée mais indépendante par rapport à la première et en plus, elle n'est plus contrainte par orthogonalité. L'information portée par cette deuxième composante représente l'apport principal de la nouvelle décomposition proposée.

C.4 Télédétection de la neige

Ce chapitre sert comme une introduction au contexte appliqué de cette thèse. Notamment, comme il est indiqué dans l'introduction, la télédétection représente une discipline scientifique appliquée, souvent intrinsèquement liée aux sciences de la Terre. Donc, en dehors de contributions présentées dans la première partie, qui peuvent être désignées comme plutôt méthodologiques, nous présentons dans cette partie un problème environnemental plus concret, approché au moyen de la télédétection radar, avec avec l'apport important de l'imagerie optique.

Le problème considéré est l'estimation spatiale de l'équivalent en eau de la neige (EEN), il étant une fonction de la densité (ρ) et du profondeur de la neige (d) :

$$\text{EEN} = \frac{1}{\rho_w} \int_0^d \rho_s dz \tag{C.4}$$

Les travaux présenté, effectues en collaboration avec *Électricité de France (EDF)*, sont liés au cas d'études qui concerne la région autour du barrage Serre-Ponçon, en France.

Le but principal fut de :

- soit estimer EEN de manière indépendante, en utilisant que des données de télédétection.
- soit intégrer des données de télédétection dans l'infrastructure existante - le modèle hydrologique.

Pour faire cela, nous avons disposé de l'ensemble de mesure *in situ*, l'ensemble des images RSO et l'ensemble des cartes de la neige délivrées à partir des données MODIS multitemporelles. Évidement, les premiers efforts sont dirigés vers une approche autonome.

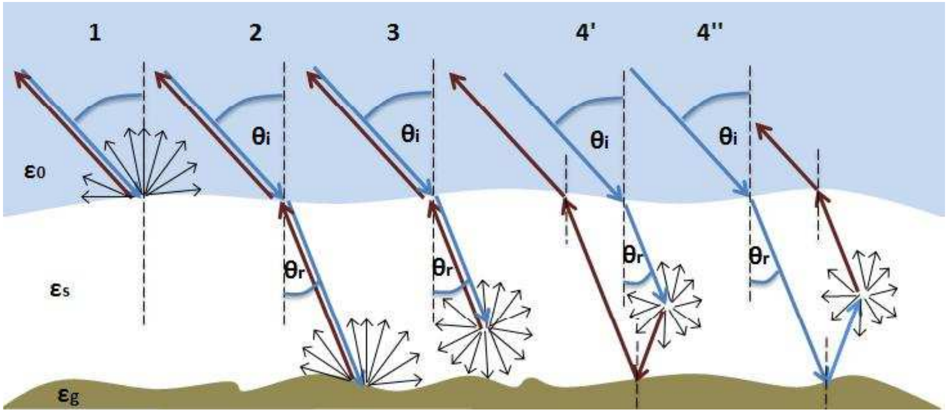

Figure C.7: Le rétrodiffusion de manteau neigeux.

D'abord, nous dérivons un simulateur de la rétrodiffusion de la neige sèche et humide, qui prend en compte le manteau neigeux mono-couche et multi-couche. Les simulations effectuées nous permettent d'arriver jusqu'aux conclusions concernant la physique de la rétrodiffusion de la neige, ainsi que de former les bases d'une méthode de cartographie, présentée dans le chapitre suivant.

La rétrodiffusion de la neige est décomposé en quatre composantes (Fig. C.7) :

1. rétrodiffusion de la surface de la neige,
2. rétrodiffusion du sol au-dessous de la neige,
3. rétrodiffusion de la volume de la neige.
4. interaction entre le sol au-dessous et la volume de la neige.

Tous les types de rétrodiffusion sont simulés en appliquant les théories fondamentales. Pour la rétrodiffusion de la surface cela fut *Integral Equation Model (IEM-B)*, tandis que pour celle du volume nous utilisâmes comparativement le modèle de Rayleigh (la diffusion indépendante) et Transfert Radiatif de Milieux Denses (DMRT). Le dernier est basé sur l'approximation quasi-cristalline (QCA) dans le case de la neige sèche et l'approximation quasi-cristalline avec potentiels cohérents pour la neige humide.

Après avoir fait des analyses dans trois bandes de fréquences (L, C et X) pour les paramètres représentatifs du manteau neigeux, nous avons obtenus les conclusions suivantes par rapport à deux paramètres formant l'EEN :

- neige sèche : la composante la plus dominante est la deuxième - le rétrodiffusion du sol au-dessous de la neige. La sensibilité au changement de profondeur est très faible, bien qu'elle augmente avec la fréquence. Par contre, la sensibilité au changement de densité est assez forte et la façon dans laquelle la densité influence la rétrodiffusion dépend significativement de la fréquence.
- neige humide : la composante la plus dominante est le première - le rétrodiffusion de la surface de la neige. La sensibilité au changement de profondeur est presque négligeable. Dans ce cas là, la sensibilité au changement de densité est aussi forte, mais il y a qu'un moyen de l'influence - le changement de permittivité diélectrique.

C.5 Cartographie de la neige humide par les données RSO à haute résolution spatiale

Comme il était indiqué dans le chapitre précèdent, tous les efforts pour inverser le modèle de rétrodiffusion de la neige pour estimer les paramètres de manteau neigeux, parait être conditionné par la discrimination appropriée entre la neige sèche et la neige humide. Donc, en

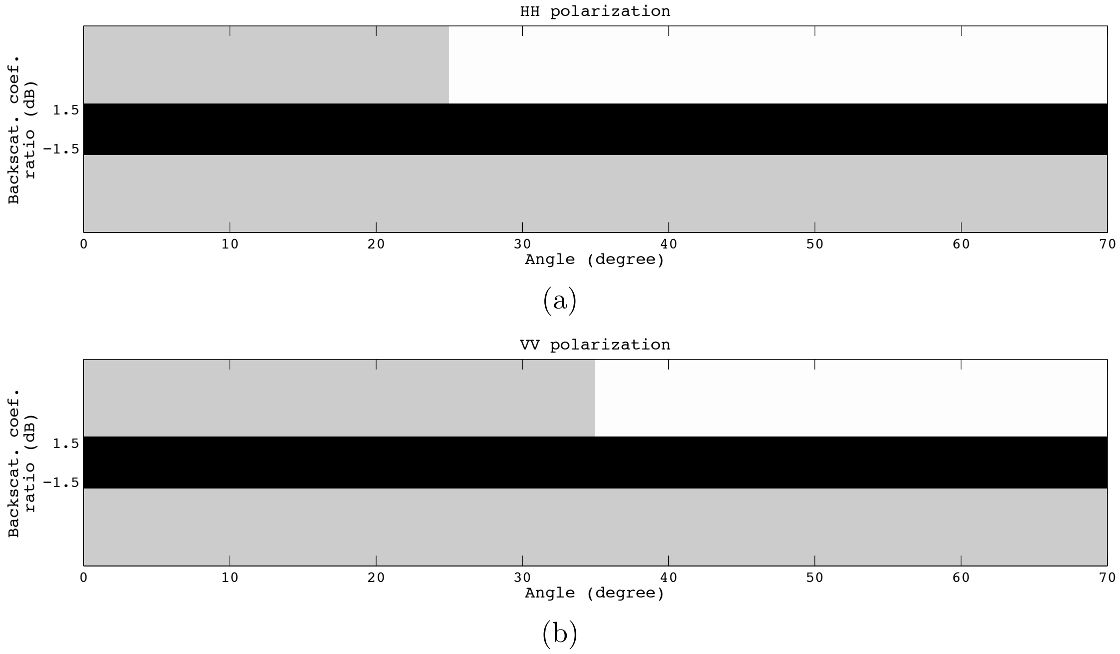

Figure C.8: Le seuil variable : (a) polarisation HH, (b) polarisation VV. Les régions noires indiquent la neige sèche, tandis que les régions grises sont associées à la présence de la neige humide.

utilisant le simulateur de rétrodiffusion de la neige mono-couche et multi-couche, et surtout, en utilisant les conclusions affirmées, nous développons une méthode de détection de changements de la neige. Par ailleurs, en s'appuyant sur la statistique de l'image RSO, élaborée en premier chapitre, la méthode présentée dans ce chapitre, estime la probabilité de la neige humide en tenant compte de la statistique locale de speckle, ce qui en fait une méthode stochastique.

L'approche classique de cartographie de la neige est une méthode de détection de changements basée sur la ratio de deux images RSO acquises en bande C, une pendant l'hiver et l'autre dans l'été. En présument que la rétrodiffusion de la neige sèche peut être considérée comme assez proche à celle du sol nu, et que la rétrodiffusion de la neige humide doit être caractérisé par les fortes pertes électromagnétique, la ratio inférieur au $-3dB$ devrait montrer la présence de la neige humide.

Pourtant, les résultats que nous obtînmes par le simulateur introduit dans le chapitre précèdent ainsi que les mesure de l'état de l'art (Alpes Suisses, 1994/95) indiquent que ces hypothèses classique peuvent être appropriement modifiées. En conséquence, la méthode proposée dans ce chapitre est caractérisée par les points suivants :

- vu que la présence de la neige sèche influence la rétrodiffusion du sol, nous proposons plutôt la ratio des images acquises en bande X, une pendant la saison de fonte et l'autre pendant l'hiver.
- en considérant l'importance du rôle de la rétrodiffusion des surfaces, nous dérivons un

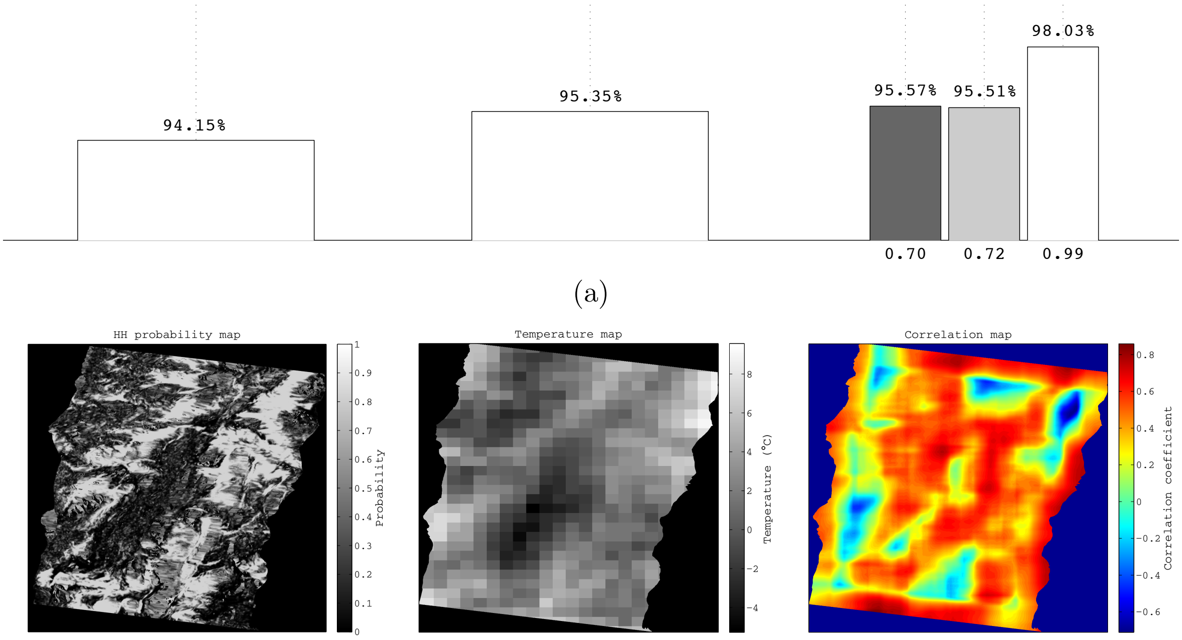

(a)

(b) (c) (d)

Figure C.9: La validation de méthode proposée : (a) correspondance entre les cartes HH et VV dans trois cas - filtrage de speckle avant le rapport, filtrage de speckle après le rapport et notre approche, respectivement, (b) la carte de probabilité georéférencée, (c) la carte de température interpolée, (d) la corrélation spatiale de deux cartes précédentes.

seuil variable, il étant la fonction de l'angle local d'incidence.

- pour mieux refléter la nature des images RSO, nous impliquant la statistique locale de speckle dans la prise de la décision.

Le simulateur de la rétrodiffusion est d'abord calibré en bande C, en utilisant les mesures de l'état de l'art, citées ci-dessus. Cette calibration est, au fond, une optimisation du ratio de rétrodiffusion de la neige humide et de la neige sèche, elle étant une fonction de l'angle local d'incidence, par rapport à la rugosité de surface.

Une fois nous avons les paramètres optimaux, nous refaisons les simulations en bande X. Les conclusions sont ensuite généralisées, en variant ces paramètres. Le paramètre qui ne varie pas est l'humidité de la neige humide. Notamment, dans nos analyses, elle est très base ($w = 0.73\%$), ce qui est supposé de refléter le cas où la variation de la ratio par rapport à l'angle d'incidence devient importante. Autrement, pour les valeurs d'humidité augmentées, l'hypothèse physique qui associe l'absorption au comportement électromagnétique de la neige humide est incontestable.

Enfin, grâce à ces simulations en bande X, nous formons des zones associées à la présence de la neige sèche et la neige humide (Fig. C.8).

Au lieu de tout simplement calculer la ratio de deux images filtrées et puis associer chacun des pixels soit à la classe de neige sèche, soit à celle de neige humide, nous dérivons plutôt la probabilité de la neige humide. Notamment, en présument que la ratio normalisée d'intensité est distribuée selon la loi Bêta prime, nous estimons les paramètres de la densité de probabilité ($\mathcal{B}'$) pour chaque région (fenêtre glissante). Ensuite, la probabilité de la neige humide est estimée au moyen de la fonction de répartition (B') :

$$\begin{aligned} i_{out}(i,j) &= B'_{(i,j)}\left(\frac{T_2(i,j)}{\mu(i,j)}\right) - B'_{(i,j)}\left(\frac{T_1(i,j)}{\mu(i,j)}\right) = \\ &= \int_{\frac{T_1(i,j)}{\mu(i,j)}}^{\frac{T_2(i,j)}{\mu(i,j)}} \mathcal{B}'_{(i,j)}(\xi)d\xi. \end{aligned} \tag{C.5}$$

où μ représente la moyenne utilisée pour la normalisation, tandis que T_1 et T_2 sont les seuils définis dans l'étape précédente (Fig. C.8).

La méthode est validée :

- quantitativement : pour démontrer l'utilité du caractère stochastique, nous avons analysé la correspondance entre deux cartes de probabilité estimées séparément (HH et VV). La comparaison de notre approche (les cartes binaires) avec celle où nous calculons le ratio de deux images filtrée et celle où le ratio est filtrée, montre le supériorité de l'implication de statistique dans la prise de décision (Fig. C.9a).
- qualitativement : nous comparons la carte de probabilité geo-référencée avec la carte de température de l'air au niveau de sol, en obtenant une bonne corrélation spatiale (Fig. C.9b, c et d).

C.6 Modélisation spatiale de l'EEN par les données de télédétection

Comme il était spécifié dans le chapitre IV, la dérivation de paramètres de la neige au moyen de l'image RSO, représente un problème sous-déterminé. Pourtant, dans le chapitre précèdent nous développions une méthode pour la classification de neige, basée sur les images RSO multi-temporelles. Dans ce chapitre, pour dériver la distribution spatiale de l'EEN, nous nous tournons vers la télédétection optique, accompagnée par le modèle hydrologique introduit dans le chapitre IV. Également, nous présentons brièvement les efforts en cours pour faire travailler les méthodes RSO polarimétriques, renforcées par une technique de séparation aveugle des sources (ACP), dans la surveillance de paramètres de la neige qui forment EEN.

Le sub-modèle du MORDOR qui concerne l'équivalent en eau de la neige (EEN) prend à l'entrée :

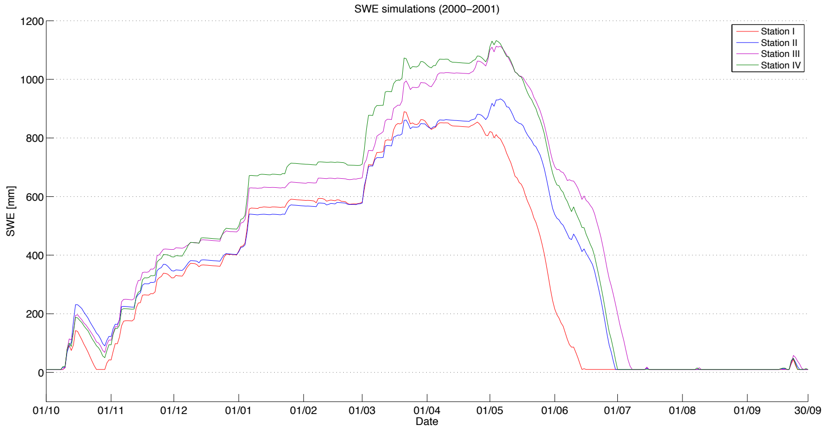

Figure C.10: Une des sorties du modèle MORDOR : Équivalent en eau de la neige.

- la température spatialisée,
- la précipitation spatialisée,
- le coefficient de l'accumulation (c_p),
- le coefficient de la fonte (k_f),

et il donne à la sortie l'EEN comme une fonction spatiale et temporelle (Fig. C.10). L'implication des données optiques, c'est-à-dire la calibration du modèle est liée à l'estimation de deux coefficients spatiales (c_p et k_f) qui ne peuvent pas être mesurés autrement.

La calibration peut être divisée en trois étapes :

- sélection de la méthode d'optimisation,
- paramétrisation de la fonction de binarisation,
- dérivation des coefficients c_p et k_f.

D'abord, nous choisissons la méthode d'optimisation en calibrant le modèle par rapport aux mesures *in situ* de l'EEN pour quatre différentes stations dans la région d'intérêt. Le critère pour l'optimisation est l'erreur quadratique moyenne.

Ensuite, pour utiliser les carte de la neige multi-temporelles, dérivées des images MODIS (données optiques), ou bien les courbes quasi-binaires temporelles, délivrées à partir de ces cartes, nous fûmes obligé de binariser la sortie du modèle. Les paramètres de la fonction de binarisation sont calculés en optimisant les mesures *in situ* par rapport aux courbes MODIS qui correspondent à quatre stations.

Finalement, en optimisant la sortie binarisée du modèle par rapport aux courbes MODIS nous calibrons le modèle, c'est-à-dire nous dérivons les coefficients de l'accumulation et de la fonte dans toute la région couverte par les images optiques.

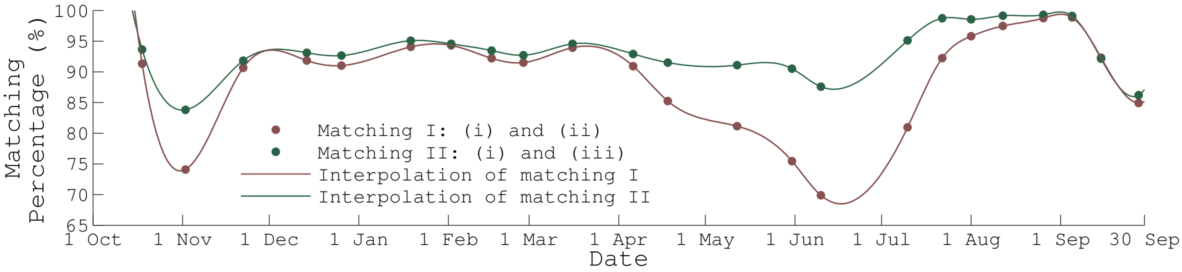

Figure C.11: Correspondance entre les cartes de la neige dérivées depuis le modèle non-calibré (ii) et celui calibré (iii) avec les cartes MODIS (i).

Les résultats obtenus et affichés dans la Fig. C.11 montrent que le modèle calibré spatialement correspond beaucoup mieux aux cartes de la neige délivrées des données MODIS, pendant toute l'année. Pour deux sur quatre stations où nous avons disposé des mesures, la calibration avec des données optiques est supérieur par rapport à celle effectuée avec des mesures *in situ*. Cela peut servir comme une démonstration de la nécessité d'impliquer la télédétection dans les problématiques environnemental avec un caractère spatial.

C.6.1 Le rôle potentiel de RSO polarimétrique

Dans la partie qui concerne la spatialisation de l'équivalent en eau de la neige, nos efforts actuel sont dirigés vers l'analyse du rôle de RSO polarimétrique dans la spatialisation des paramètres qui forment EEN.

Cette piste de recherche est basée sur la corrélation observée ($R^2 = 0.8439$) entre l'entropie "enrichie" et le profondeur de la neige (Fig. C.12). Entropie "enrichie" ou bien entropie débruitée est obtenue en appliquant l'ACP sur l'ensemble de cinq descripteurs polarimétriques.

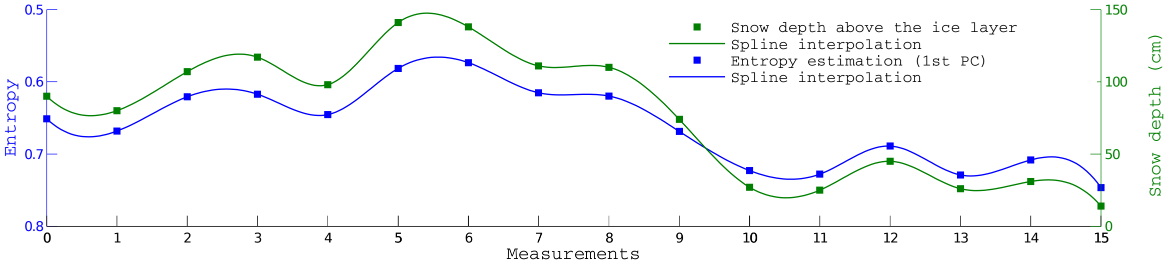

Figure C.12: Entropie vs. profondeur de la neige au-dessus de la première croute de glace : corrélation temporelle.

C.7 Conclusions

Cette thèse fut envisagée de refléter d'une manière crédible tous ce que nous avons fait dans le cadre de la télédétection pendant les trois dernières années, et ce qui peut être considéré en tant que contribution à la communauté scientifique de télédétection. L'idée fut d'essayer de confronter des questions ouvertes dans la communauté RSO polarimétrique, ainsi que d'essayer de proposer des solutions moins abstraites pour des problèmes environnementaux "palpables". Vu notre affinité et les tendances actuelles dans notre environnement professionnel, la première est liée à l'implantation des outils très efficaces de traitement statistique du signal dans l'analyse et l'interprétation des données polarimétriques. La dernière, plutôt grâce à la position géographique de notre environnement professionnel, concerne l'estimation d'un paramètre dérivé du manteau neigeux - l'équivalent en eau de la neige.

Alors que les conclusions un peu plus détaillés sont déjà fournis pour chacun des chapitres, ici nous essayons d'illustrer brièvement, mais concisément, les quatre contributions principaux :

- Les tests statistiques pour l'évaluation de la circularité et de la sphericité dans le cas de la modélisation statistique alternative des données RSO polarimétriques hautement texturées. Ceux-ci sont suivis par une méthode basée sur le test de symétrie sphérique, utilisé pour l'évaluation de la pertinence de vecteurs aléatoires sphériquement invariants (SIRV).
- La décomposition incohérente polarimétrique, basée sur l'analyse en composantes indépendantes des données polarimétriques observées, plutôt que sur leur décomposition en valeurs propres. Elle fournit les vecteurs de cible qui sont mutuellement indépendants et non-orthogonaux, en exploitant l'information contenue dans les ordres statistiques supérieurs.
- L'approche stochastique pour la cartographie de la neige humide, basée sur la méthode de la détection de changements, où la décision est la fonction de l'angle d'incidence local via le seuil variable, et la statistique locale de *speckle* est introduite implicitement dans la prise de décision.
- La méthode de calibration d'un modèle EEN, basée sur les données optiques multi-temporelles, qui permet l'implication non-autonome mais toujours très efficace de la télédétection dans la dérivation spatiale de l'EEN.

Heureusement, en ce moment nous ne percevons pas d'obstacles insurmontable, mais plutôt un horizon ouvert pour le développement supplémentaire et l'exploitation de ces contributions. Les perspectives les plus évidentes du travail présenté seraient les suivantes :

- Adapter l'interprétation des données RSO polarimétriques et interférométriques hautement texturées aux propriétés statistiques affirmées. Proposer de nouveaux modèles alternatifs pour la modélisation statistique de cibles qui ne répondent ni au modèle Gaussien multivarié ni au modèle SIRV.

- Appliquer la décomposition développée et exploiter l'information contenue dans la deuxième composante, qui n'est pas contrainte pas l'orthogonalité. Au lieu de compter sur l'algorithme itérative (FastICA), proposer une méthode de l'ACI particulière, basée éventuellement sur l'Estimation de Vraisemblance Maximale, et adaptée à la structure particulière des données polarimétriques observées.
- Étendre la méthode basée sur un seul canal à sa version polarimétrique et dériver un seuil variable qui semble être mieux adapté à la diversité spatiale des paramètres de manteau neigeux.
- Exploiter la possibilité de surveillance de l'EEN au moyen de décompositions RSO polarimétriques (conventionnelles ou contemporaines) avec l'implication de l'ACP dans le contexte de débruitage. Utiliser les données RSO, c'est-à-dire, des cartes de probabilité de la neige humide dérivées, pour améliorer la calibration des modèles spatiaux de l'EEN, et pour finalement démontrer la nécessité de la télédétection dans la surveillance de cibles naturelles distribuées.

Appendix D

Rezime (me)

Karakterizacija polarimetrijskih SAR slika velike rezolucije tehnikama slijepog razdvajanja izvora

---

Ova teza podrazumijeva dva pravca istraživanja. Prvi, metodološki, predstavlja naše napore da odgovorimo na neka od otvorenih pitanja u POLSAR zajednici, dok je drugi vezan za specifičnu aplikaciju - teledetekciju sniježnog pokrivača.

Uzevši u obzir alternativno statističko modelovanje multivarijantnih SAR slika visoke rezolucije koristeći SIRV model, mi predlažemo odgovarajuću estimaciju, uostalom pretpostavljenih parametara cirkularnosti i sfernosti. Integrišući posljednju u test sferne simetrije, formiran je metod za evaluaciju prikladnosti statističkog modela SIRV u kontekstu POLSAR slika visoke rezolucije. Posmatrajući stopu odbacivanja, sumnja u opravdanost pretpostavke cirkularnosti i sfernosti se čini opravdanom, dok pogodnost SIRV modela mora biti preispitana u regionima koje karakteriše jako determinističko elektromagnetno rasijanje. U nastavku, kao primarni doprinos ove teze, predlažemo polarimetrijsku nekoherentnu dekompoziciju mete, koja je bazirana na ICA metodu i zasnovana na hipotezi o otklonu od Gausove prirode POLSAR *clutter*-a. Eksploatišući informaciju sadržanu u višim statističkim redovima, predložena dekompozicija daje na izlazu set međusobno nezavisnih (prije nego samo nekorelisanih), neortogonalnih vektora mete. Za razliku od prve dominante komponente, koja je skoro identična komponenti estimiranoj koristeći konvencionalnu ICTD metodu, druga dominanta komponenta se značajno razlikuje, što predstavlja dodatan potencijal u interpretaciji POLSAR slika.

Prvi prezentovani doprinos u primijenjenom kontekstu bio bi stohastički metod za mapiranje sniježnog pokrivača baziran na multitemporalnom setu SAR slika. Najznačajniji prilozi prezentovane metode grupi tehnika "detekcije promjene" u mapiranju sniježnog pokrivača su opravdano promijenjena pretpostavka o količniku povratnog rasijanja djelimično otopljenog i suvog snijega, kao i implicitno uvedeno prostorna korelacija između regiona djelimično otopljenog snijega, postignuta direktnim uvođenjem lokalne statistike *speckle* šuma u proces odlučivanja. Konačno, predlažemo neautonomni metod za prostornu estimaciju SWE parametra, zasnovan na optičkim slikama. Uspješno inflitrirajući teledetekciju u kalibraciju eksternog SWE modela, imamo za cilj demonstrirati njenu korisnost i neophodnost u monitoringu sniježnog pokrivača.

Publications

Journal papers:

[1] N. Besic, G. Vasile, J. Chanussot, and S. Stankovic. “Polarimetric Incoherent Target Decomposition by Means of Independent Component Analysis”. In: *IEEE Trans. Geosci. Remote Sens.* 53.3 (2015) (cit. on pp. 3, 53, 123).

[2] N. Besic, G. Vasile, J. P. Dedieu, J. Chanussot, and S. Stankovic. “Stochastic Approach in Wet Snow Detection using Multitemporal SAR Data”. In: *IEEE Geosci. Remote Sens. Lett.* 12.2 (2015) (cit. on pp. 3, 93, 123).

[3] N. Besic, G. Vasile, F. Gottardi, J. Gailhard, A. Girard, and G. d’Urso. “Calibration of a distributed SWE model using MODIS snow cover maps and in situ measurements”. In: *Remote Sensing Letters* 5.3 (2014), pp. 230–239 (cit. on pp. 3, 107, 123).

Journal papers outside of scope of the thesis:

[161] N. Besic, G. Vasile, A. Anghel, T. Petrut, C. Ioana, S. Stankovic, A. Girard, and G. d’Urso. “Zernike Ultrasonic Tomography for Fluid Velocity Imaging based on Pipeline Intrusive Time-of-Flight Measurements”. In: *IEEE Trans. Ultrason., Ferroelectr., Freq. Control* 61.11 (2014).

Journal papers undergoing review:

[160] N. Besic, G. Vasile, and A. Anghel. “Circularity and Sphericity of Complex Stochastic Models in Multivariate High-Resolution SAR Images”. In: *IEEE J. Sel. Topics Appl. Earth Observ.* (2014). submitted May 2014 (cit. on p. 123).

Conference papers:

[65] G. Vasile, N. Besic, A. Anghel, C. Ioana, and J. Chanussot. “Sphericity of complex stochastic models in multivariate SAR images”. In: *Proc. IGARSS*. Melbourne, Australia, 2013, pp. 2994–2997 (cit. on p. 38).

[99] N. Besic, G. Vasile, J. Chanussot, and S. Stankovic. “Poincare sphere representation of independent scattering sources: application on distributed targets”. In: *ESA SP-713 - POLinSAR 2013*. Frascati, IT, 2013 (cit. on pp. 54, 68).

[103] N. Besic, G. Vasile, J. Chanussot, S. Stankovic, D. Boldo, and G. d’Urso. “Independent Component Analysis within Polarimetric Incoherent Target Decomposition”. In: *Proc. IGARSS*. Melbourne, AUS, 2013, pp. 4158–4161 (cit. on p. 57).

[104] N. Besic, G. Vasile, J. Chanussot, S. Stankovic, A. Girard, and G. d'Urso. "Analysis of supplementary information emerging from the ICA based ICTD". In: *Proc. IGARSS*. Quebec, Canada, 2014 (cit. on p. 58).

[121] N. Besic, G. Vasile, J. Chanussot, S. Stankovic, J.-P. Dedieu, G. d'Urso, D. Boldo, and J.-P. Ovarlez. "Dry Snow Backscattering Sensitivity on Density Change for SWE Estimation". In: *Proc. IGARSS*. Munich, Germany, 2012, pp. 4418–4421 (cit. on pp. 84, 89, 97).

[122] N. Besic, G. Vasile, J. Chanussot, S. Stankovic, D. Boldo, and G. d'Urso. "Wet Snow Backscattering Sensitivity on Density Change for SWE Estimation". In: *Proc. IGARSS*. Melbourne, Australia, 2013 (cit. on pp. 84, 89, 97, 100).

[132] N. Besic, G. Vasile, J. Chanussot, S. Stankovic, J.-P. Ovarlez, G. d'Urso, D. Boldo, and J.-P. Dedieu. "Stochastically Based Wet Snow Mapping with SAR Data". In: *Proc. IGARSS*. Munich, Germany, 2012, pp. 4859–4862 (cit. on p. 93).

[144] J. P. Dedieu, N. Besic, G. Vasile, J. Mathieu, Y. Durand, and F. Gottardi. "Dry snow analysis in Alpine regions using RADARSAT-2 full polarimetry data. Comparison with in situ measurements." In: *Proc. IGARSS*. Quebec, Canada, 2014 (cit. on pp. 107, 110).

Bibliography

[4] G. Stokes. “On the composition and resolution of streams of polarized light from different sources”. In: *Proceedings of the Cambridge Philosophical Society* 1 (1852), pp. 140–147 (cit. on p. 7).

[5] H. Poincaré. *Théorie mathématique de la lumiere*. Paris, FR: George Carré, 1852 (cit. on p. 7).

[6] D. Massonet and J.-C. Souyris. *Imaging with Synthetic Aperture Radar*. Boca Raton, FL, USA: CRC Press, Taylor and Francis Group, 2008 (cit. on pp. 7, 8, 12, 16, 125).

[7] E. M. Kennaugh. *Polarization properties of radar reflectors*. Columbus, OH, US, 1952 (cit. on pp. 8, 17, 68).

[8] C. D. Graves. “Radar polarization power scattering matrix”. In: *Proc. IRE* 44.2 (1956), pp. 248–252 (cit. on p. 8).

[9] J. R. Huynen. “Phenomenological theory of radar targets”. PhD thesis. Delft, The Netherlands: Technical University, 1970 (cit. on pp. 8, 11, 14).

[10] J. R. Huynen. “Measurement of the target scattering matrix”. In: *Proc. IEEE* 53.8 (1965), pp. 936–946 (cit. on pp. 11, 17, 68).

[11] E. Krogager. “New decomposition of the radar target scattering matrix”. In: *Electronic letters* 26.18 (1990), pp. 1525–1527 (cit. on p. 12).

[12] W. L. Cameron, N. Youssef, and L. K. Leung. “Simulated polarimetric signatures of primitive geometrical shapes”. In: *IEEE Trans. Geosci. Remote Sens.* 34.E (1996), pp. 793–803 (cit. on p. 12).

[13] A. Freeman and S. L. Durden. “A three-component scattering model for polarimetric SAR data”. In: *IEEE Trans. Geosci. Remote Sens.* 36.3 (1998), pp. 963–973 (cit. on p. 14).

[14] Y. Yamaguchi, T. Moriyama, M. Ishido, and H. Yamada. “Four-Component Scattering Model for Polarimetric SAR Image Decomposition”. In: *IEEE Trans. Geosci. Remote Sens.* 43.8 (2005), pp. 1699–1706 (cit. on p. 14).

[15] S. R. Cloude and E. Pottier. “An entropy based classification scheme for land applications of polarimetric SAR”. In: *IEEE Trans. Geosci. Remote Sens.* 35.1 (1997), pp. 68–78 (cit. on pp. 15, 54, 56, 68).

[16] R. Touzi. “Target scattering decomposition in terms of roll-invariant target properties”. In: *IEEE Trans. Geosci. Remote Sens.* 45.1 (2007), pp. 73–84 (cit. on pp. 15–17, 56, 64).

[17] R. Touzi and F. Charbonneau. “Characterization of target symmetric scattering using polarimetric SARs”. In: *IEEE Trans. Geosci. Remote Sens.* 40.11 (2002), pp. 2507–2516 (cit. on p. 17).

[18] S. R. Cloude. “The characterization of polarization effect in EM scattering”. PhD thesis. Birmingham, UK: University of Birmingham, 1986 (cit. on p. 17).

[19] J. W. Goodman. “Some fundamental properties of speckle”. In: *J. Opt. Soc. Amer.* 53.11 (1976), pp. 1145–1149 (cit. on pp. 18, 100).

[20] J. S. Lee, I. Jurkevich, P. Dewaele, P. Wambacq, and A. Costerlinck. “Speckle filtering of synthetic aperture radar images: A review”. In: *Remote Sens. Rev.* 8 (1994), pp. 311–340 (cit. on p. 19).

[21] Jong-Sen Lee and Eric Pottier. *Polarimetric radar imaging: from basics to applications.* CRC Press, Taylor and Francis, 2009 (cit. on pp. 19, 20).

[22] F. T. Ulaby, F. Kouyate, B. Brisco, and T. H. L. Williams. “Textural information in SAR images”. In: *IEEE Trans. Geosci. Remote Sens.* GE-24.2 (1986), pp. 235–245 (cit. on p. 20).

[23] N. R. Goodman. “Statistical analysis based on a certain multivariate complex gaussian distribution (an introduction)”. In: *Annals of Mathematical Statistics* 34.1 (1963), pp. 152–177 (cit. on p. 20).

[24] K. Sarabandi. “Derivations of phase statistics from the Mueller matrix”. In: *Radio Science* 27.5 (1992), pp. 553–560 (cit. on p. 20).

[25] J. S. Lee, D. L. Schuler, R. H. Lang, and K. J. Ranson. “K-distribution for multilook processed polarimetric SAR imagery”. In: *Proceedings of the IEEE International Geoscience and Remote Sensing Symposium, Pasadena, SUA*. Vol. 4. 1994, pp. 2179–2182 (cit. on p. 20).

[26] B. Picinbono. “Spherically invariant and compound Gaussian stochastic processes”. In: *IEEE Transactions on Information Theory* 16.1 (1970), pp. 77–79 (cit. on p. 21).

[27] L. M. Novak and M. C. Burl. “Optimal speckle reduction in polarimetric SAR imagery”. In: *IEEE Transactions on Aerospace and Electronic Systems* 26.2 (1990), pp. 293–305 (cit. on p. 21).

[28] A.D.C. Nascimento, R.J. Cintra, and A.C. Frery. “Hypothesis Testing in Speckled Data With Stochastic Distances”. In: *IEEE Trans. Geosci. Remote Sens.* 48.1 (2010), pp. 373–385 (cit. on p. 21).

[29] L. Bombrun, G. Vasile, M. Gay, and F.C. Totir. “Hierarchical segmentation of polarimetric SAR images using heterogeneous clutter models”. In: *IEEE Trans. Geosci. Remote Sens.* 49.2 (2011), pp. 726–737 (cit. on pp. 21, 32, 100).

[30] G. Vasile, J. P. Ovarlez, F. Pascal, and C. Tison. “Coherency matrix estimation of heterogeneous clutter in high-resolution polarimetric SAR images”. In: *IEEE Trans. Geosci. Remote Sens.* 48.4 (2010), pp. 1809–1826 (cit. on pp. 21, 32, 37, 43, 54, 62).

[31] G. Vasile, J.-P. Ovarlez, F. Pascal, M. Gay, G. d’Urso, and D. Boldo. “Stable scatterers detection and tracking in heterogeneous clutter by repeat-pass SAR interferometry”. In: *Asilomar Conference on Signals, Systems, and Computers, Pacific Grove, California, USA*. 2010, pp. 1343–1347 (cit. on pp. 22, 32).

[32] P. Comon and C. Jutten. *Handbook of blind source separation, independent component analysis and applications.* Oxford, UK: Academic Press, 2010 (cit. on p. 22).

[33] I. T. Jolliffe. *Principal Component Analysis*. 2nd. Springer Series in Statistics, 2002 (cit. on p. 23).

[34] A. Hyvarinen and E. Oja. “Independent Component Analysis: Algorithms and Applications”. In: *Neural Networks* 13.4-5 (2000), pp. 411–430 (cit. on pp. 25, 27, 56).

[35] A. Hyvarinen, J. Karhunen, and E. Oja. *Independent Component Analysis*. New York, NY, USA: John Wiley & Sons, 2001 (cit. on p. 26).

[36] A. Hyvarinen. “Fast and robust fixed-point algorithms for independent component analysis”. In: *IEEE Trans. on Neural Netw.* 10.3 (1999) (cit. on p. 27).

[37] A. Hyvarinen. “New approximations of differential entropy for independent component analysis and projection pursuit”. In: *Advances in Neural Information Processing Systems* 10 (1998), pp. 273–279 (cit. on p. 27).

[38] A. Hyvarinen. “The fixed-point algorithm and maximum likelihood estimation for independent component analysis”. In: *Advances in Neural Information Processing Systems* 10.1 (1999), pp. 1–5 (cit. on p. 28).

[39] Pham D.T. Garrat P and Jutten C. “Separation of a mixture of independent sources through a maximum likelihood approach”. In: *Proceedings of 6th European Signal Processing Conference*. Brussels, Belgium, 1992, pp. 771–774 (cit. on p. 28).

[40] Jean-François Cardoso. “Source Separation Using Higher-order Moments”. In: *Proc. ICASSP*. Glasgow, May 1989, pp. 2109–2112 (cit. on pp. 28, 56).

[41] Jean-François Cardoso and Antoine Souloumiac. “Blind beamforming for non Gaussian signals”. In: *IEE Proceedings-F* 140.6 (Dec. 1993), pp. 362–370 (cit. on pp. 29, 56).

[42] A. Belouchrani, K. Abed Meraim, J.-F. Cardoso, and E. Moulines. “A blind source separation technique based on second order statistics”. In: *IEEE Trans. on Signal Processing* 45.2 (1997), pp. 434–444 (cit. on pp. 29, 56).

[43] P. Formont, F. Pascal, G. Vasile, J.-P. Ovarlez, and L. Ferro-Famil. “Statistical Classification for Heterogeneous Polarimetric SAR Images”. In: *IEEE J. Sel. Topics Signal Process.* 5.3 (2011), pp. 398–407 (cit. on pp. 32, 54, 62).

[44] G. Vasile, F. Pascal, J.-P. Ovarlez, P. Formont, and M. Gay. “Optimal Parameter Estimation in Heterogeneous Clutter for High Resolution Polarimetric SAR Data”. In: *IEEE Geoscience and Remote Sensing Letters* 8.6 (2011), pp. 1046–1050 (cit. on pp. 32, 51).

[45] G. Vasile, D. Boldo, R. Boudon, and G. d’Urso. “Multidimensional Very High Resolution SAR Interferometry for Monitoring Energetic Structures”. In: *Proceedings of IEEE International Geoscience and Remote Sensing Symposium, Munchen, Germany*. 2012, pp. 3943–3946 (cit. on p. 32).

[46] G. Vasile, A. Anghel, D. Boldo, R. Boudon, G. d’Urso, and R. Muja. “Potential of Multi-Pass High-Resolution SAR Interferometry for Dam Monitoring”. In: *MTA Review (ISSN 1843-3391), special issue of the COMM’12 conference, Romanian Military Technical Academy Publishing House* 22.4 (2012), pp. 235–246 (cit. on p. 32).

[47] D. Massonnet and T. Rabaute. “Radar interferometry, limits and potential”. In: *IEEE Trans. Geosci. Remote Sens.* 31.2 (1993), pp. 455–464 (cit. on p. 33).

[48] B. Picinbono. “On circularity”. In: *IEEE Transactions on Signal Processing* 42.12 (1994), pp. 3473–3482 (cit. on p. 33).

[49] E. Ollila, J. Eriksson, and V. Koivunen. “Complex elliptically symmetric random variables - generation, characterization, and circularity tests”. In: *IEEE Transactions on Signal Processing* 59.1 (2011), pp. 58–69 (cit. on p. 34).

[50] B. Picinbono. “Second-order complex random vectors and normal distributions”. In: *IEEE Transactions on Signal Processing* 44.10 (1996), pp. 2637–2640 (cit. on pp. 34, 38).

[51] F.D. Neeser and J.L. Massey. “Proper complex random processes with applications to information theory”. In: *IEEE Transactions on Information Theory* 39.4 (1993), pp. 1293–1302 (cit. on p. 34).

[52] P.J. Schreier, L.L. Scharf, and A. Hanssen. “A Generalized Likelihood Ratio Test for Impropriety of Complex Signals”. In: *IEEE Signal Processing Letters* 13.7 (2006), pp. 433–436 (cit. on pp. 34, 35).

[53] A. van den Bos. “The multivariate complex normal distribution - A generalization”. In: *IEEE Transactions on Information Theory* 41.2 (1995), pp. 537–539 (cit. on pp. 34, 38).

[54] E. Ollila and V. Koivunen. “Adjusting the generalized likelihood ratio test of circularity robust to non-normality”. In: *IEEE Workshop on Signal Processing Advances in Wireless Communications, Perugia, Italy.* 2009, pp. 558–562 (cit. on p. 35).

[55] D.E. Tyler. “Robustness and efficiency properties of scatter matrices”. In: *Biometrika* 70.2 (1983), pp. 411–420 (cit. on pp. 35, 37, 38, 40, 42).

[56] A.T. Walden and P. Rubin-Delanchy. “On testing for impropriety of complex-valued gaussian vectors”. In: *IEEE Transactions on Signal Processing* 57.3 (2009), pp. 835–842 (cit. on p. 36).

[57] J.W. Mauchly. “Significance test for sphericity of a normal n-variate distribution”. In: *Annals of Mathematical Statistics* 11.2 (1940), pp. 204–209 (cit. on pp. 36, 37).

[58] T. W. Anderson. *An Introduction to Multivariate Statistical Analysis.* 3rd Ed. New York: Wiley-Interscience, 2003 (cit. on pp. 36, 42).

[59] R.J. Muirhead and C.M. Waternaux. “Asymptotic distributions in canonical correlation analysis and other multivariate procedures for nonnormal populations”. In: *Biometrika* 67.1 (1980), pp. 31–43 (cit. on p. 37).

[60] D.E. Tyler. “Radial estimates and the test for sphericity”. In: *Biometrika* 69.2 (1982), pp. 429–436 (cit. on p. 37).

[61] D.E. Tyler. “A distribution-free M-estimator of multivariate scatter”. In: *Annals of Statistics* 15.1 (1987), pp. 234–251 (cit. on p. 37).

[62] R.A. Maronna. “Robust M-Estimators of Multivariate Location and Scatter”. In: *Annals of Statistics* 4.1 (1976), pp. 51–67 (cit. on p. 37).

[63] D.E. Tyler. “Statistical analysis for the angular central Gaussian distribution”. In: *Biometrika* 74.3 (1987), pp. 579–589 (cit. on p. 38).

[64] F. Pascal, P. Forster, J.-P. Ovarlez, and P. Larzabal. “Performance analysis of covariance matrix estimates in impulsive noise”. In: *IEEE Transactions on Signal Processing* 56.6 (2008), pp. 2206–2216 (cit. on p. 38).

[66] A.M. Vershik. “Some characteristic properties of Gaussian stochastic processes”. In: *Theory of Probability and its Applications* 9.2 (1964), pp. 353–356 (cit. on p. 38).

[67] K. Yao. “A representation theorem and its applications to spherically-invariant random processes”. In: *IEEE Transactions on Information Theory* 19.5 (1973), pp. 600–608 (cit. on pp. 39, 62).

[68] K.T. Fang, S. Kotz, and K.W. Ng. *Symmetric Multivariate and Related Distributions.* Vol. 36. Distributions, ser. Monographs on Statistics and Probability. London, U.K.: Chapman & Hall, 1990 (cit. on p. 39).

[69] E. Ollila, D.E. Tyler, V. Koivunen, and H.V. Poor. “Complex elliptically symmetric distributions: survey, new results and applications”. In: *IEEE Transactions on Signal Processing* 60.11 (2012), pp. 5597–5625 (cit. on pp. 39, 40).

[70] K.T. Fang and J. Liang. “Encyclopedia of Statistical Sciences”. In: ed. by S. Kotz, C.B. Read, and D.L. Banks. Vol. 3. John Wiley & Sons, New York, 1999. Chap. Testing spherical and elliptical symmetry, pp. 686–691 (cit. on p. 39).

[71] T. Kariya and M.L. Eaton. “Robust Tests for Spherical Symmetry”. In: *Annals of Statistics* 5.1 (1977), pp. 206–215 (cit. on p. 39).

[72] E.L. Lehmann and C. Stein. “On the Theory of Some Non-Parametric Hypotheses”. In: *Annals of Mathematical Statistics* 20.1 (1949), pp. 28–45 (cit. on p. 39).

[73] R. Beran. “Testing for Ellipsoidal Symmetry of a Multivariate Density”. In: *Annals of Statistics* 7.1 (1979), pp. 150–162 (cit. on p. 39).

[74] M. L. King. “Robust Tests for Spherical Symmetry and Their Application to Least Squares Regression”. In: *Annals of Statistics* 8.6 (1980), pp. 1265–1271 (cit. on p. 39).

[75] L. Baringhaus. “Testing for Spherical Symmetry of a Multivariate Distribution”. In: *Annals of Statistics* 19.2 (1991), pp. 899–917 (cit. on p. 39).

[76] K.T. Fang, L.-X. Zhu, and P.M. Bentler. “A necessary test of goodness of fit for sphericity”. In: *Journal of Multivariate Analysis* 45 (1993), pp. 34–55 (cit. on p. 39).

[77] A. Manzotti, F.J. Perez, and A.J. Quiroz. “A Statistic for Testing the Null Hypothesis of Elliptical Symmetry”. In: *Journal of Multivariate Analysis* 81.2 (2002), pp. 274–285 (cit. on p. 39).

[78] F.W. Huffer and C. Park. “A test for elliptical symmetry”. In: *Journal of Multivariate Analysis* 98.2 (2007), pp. 256–281 (cit. on p. 39).

[79] R.Z. Li, K.T. Fang, and L.X. Zhu. “Some Q-Q probability plots to test spherical and elliptical symmetry”. In: *Journal of Computational and Graphical Statistics* 6.4 (1997), pp. 435–450 (cit. on p. 39).

[80] S. Niu, V.K. Ingle, D.G. Manolakis, and T.W. Cooley. “Tests for the elliptical symmetry of hyperspectral imaging data”. In: *Proceedings of SPIE.* Vol. 7812. 2010, pp. 78120D1–78120D10 (cit. on p. 39).

[81] J. R. Schott. “Testing for elliptical symmetry in covariance-matrix-based analyses”. In: *Statistics & Probability Letters* 60.4 (1993), pp. 395–404 (cit. on pp. 39, 41).

[82] D.S. Moore. “Generalized Inverses, Wald’s Method, and the Construction of Chi-Squared Tests of Fit”. In: *Journal of the American Statistical Association* 72.357 (1977), pp. 131–137 (cit. on p. 40).

[83] A. Ferrari and G. Alengrin. “Estimation of the frequencies of a complex sinusoidal noisy signal using fourth order statistics”. In: *IEEE International Conference on Acoustics, Speech, and Signal Processing, Toronto, Ontario, Canada.* Vol. 5. 1991, pp. 3457–3460 (cit. on p. 40).

[84] R.F. Engle. *Wald, Likelihood Ratio, and Lagrange Multiplier Tests in Econometrics.* Vol. 2. eds. Z. Griliches M.D. Intriligator, Handbook of Econometrics, Elsevier, 1984, pp. 775–826 (cit. on p. 41).

[85] P. Dreuillet, H. Cantalloube, E. Colin, P. Dubois-Fernandez, X. Dupuis, P. Fromage, F. Garestier, D. Heuze, H. Oriot, J. L. Peron, J. Peyret, G. Bonin, O. R. duPlessis, J. F. Nouvel, and B. Vaizan. “The ONERA RAMSES SAR: latest significant results and future developments”. In: *Proceedings of the IEEE International Radar Conference, Verona, USA*. 2006 (cit. on p. 41).

[86] T. W. Anderson and K. T. Fang. *On the theory of multivariate elliptically contoured distributions and their applications.* Tech. rep. 54. Stanford, California, USA: Department of Statistics, Stanford University, 1982 (cit. on p. 42).

[87] T. W. Anderson and K. T. Fang. *Maximum likelihood estimators and likelihood ratio criteria for multivariate elliptically contoured distributions.* Tech. rep. 1. Stanford, California, USA: Department of Statistics, Stanford University, 1982 (cit. on p. 42).

[88] T. W. Anderson, K. T. Fang, and H. Hsu. “Maximum-Likelihood Estimates and Likelihood-Ratio Criteria for Multivariate Elliptically Contoured Distributions”. In: *Canadian Journal of Statistics* 14.1 (1986), pp. 55–59 (cit. on p. 42).

[89] G.A. Ilie, G. Vasile, G. d’Urso, and D. Boldo. *Spaceborne SAR Tomography: application in Urban Environment.* Tech. rep. GIPSA-lab - EDF, Grenoble, France, 2011 (cit. on p. 46).

[90] J. Gao and Z. Zheng. “Direct dynamical test for deterministic chaos and optimal embedding of a chaotic time series”. In: *Physical Review E (Statistical Physics, Plasmas, Fluids, and Related Interdisciplinary Topics)* 49.5 (1994), pp. 3807–3814 (cit. on p. 52).

[91] J. Gao, W.W. Tung, Y.H. Cao, J. Hu, and Y. Qi. “Power-law sensitivity to initial conditions in a time series with applications to epileptic seizure detection”. In: *Physica A* 353 (2005), pp. 613–624 (cit. on p. 52).

[92] S.S. Haykin and S. Puthusserypady. *Chaotic dynamics of sea clutter.* John Wiley & Sons, New York (NY) USA, 1999 (cit. on p. 52).

[93] F. Totir, G. Vasile, L. Bombrun, and M. Gay. “PolSAR images characterization through blind source separation techniques”. In: *Proc. IGARSS.* Hawaii, USA, 2010, pp. 4039–4042 (cit. on pp. 54, 55, 63).

[94] C. Lopez-Martinez and X. Fabregas. “Polarimetric SAR speckle noise model”. In: *IEEE Trans. Geosci. Remote Sens.* 41.10 (2003), pp. 2232–2242 (cit. on p. 54).

[95] S. Fiori. “Overview of Independent Component Analysis Technique with an Application to Synthetic Aperture Radar (SAR) Imagery Processing”. In: *Neural Networks* 16.3-4 (2003), pp. 453–467 (cit. on p. 54).

[96] C. H. Chen and X. Zhan. “On the roles of independent component analysis in remote sensing”. In: *Proc. of Progress in Electromagnetics Research Symposium.* Cambridge, MA, USA, 2000 (cit. on p. 54).

[97] O. Tannous and D. Kasilingam. “Independent Component Analysis of polarimetric SAR data for separating ground and vegetation components”. In: *Proc. IGARSS.* Vol. IV. Cape Town, ZA, 2009, pp. 93–96 (cit. on p. 54).

[98] H. Yamada, R. Takizawa, Y. Yamaguchi, and R. Sato. “POLSAR/POL-InSAR Data Analysis by Using ICA”. In: *EUSAR 2010.* Aachen, DE, 2010 (cit. on pp. 54, 59, 62).

[100] M. Novey and T. Adali. “On Extending the complex FastICA algorithm to noncircular sources”. In: *IEEE Trans. Signal Processing* 56.5 (2008), pp. 2148–2154 (cit. on pp. 54, 56–58, 75).

[101] R. Paladini, L. Ferro-Famil, E. Pottier, M. Mortorella, F. Berizzi, and E. Dalle Mese. “Lossless and sufficient orientation invariant decomposition of random reciprocal target”. In: *IEEE Trans. Geosci. Remote Sens.* 50.9 (2012), pp. 3487–3501 (cit. on pp. 54, 68).

[102] M. S. Greco and F. Gini. “Statistical analysis of high-resolution SAR ground clutter data”. In: *IEEE Trans. Geosci. Remote Sens.* 45.3 (2007), pp. 566–575 (cit. on p. 56).

[105] R. A. Horn and C. R. Johnson. “Matrix Analysis”. In: ed. by F. D. Carsey. Oxford, UK: Cambridge University Press, 1990. Chap. Norms for Vectors and Matrices (cit. on p. 59).

[106] S. R. Cloude and E. Pottier. “A review of target decomposition theorems in radar polarimetry”. In: *IEEE Trans. Geosci. Remote Sens.* 34.2 (1996), pp. 498–518 (cit. on pp. 59, 62, 66).

[107] J. S. Lee, M. R. Grunes, T. L. Ainsworth, D. Li-Jen, D. L. Schuler, and S. R. Cloude. “Unsupervised Classification Using Polarimetric Decomposition and the Complex Wishart Classifier”. In: *IEEE Trans. Geosci. Remote Sens.* 37.5 (1999), pp. 2249–2258 (cit. on p. 62).

[108] J. S. Lee, M. R. Grunes, E. Pottier, and L. Ferro-Famil. “Unsupervised Terrain Classification Preserving Polarimetric Scattering Characteristics”. In: *IEEE Trans. Geosci. Remote Sens.* 42.4 (2004), pp. 722–731 (cit. on p. 62).

[109] F. Pascal, Y. Chitour, J. P. Ovarlez, P. Forsterand, and P. Larzabal. “Covariance Structure Maximum Likelihood Estimates in Compound Gaussian Noise: Existence and Algorithm Analysis”. In: *IEEE Trans. Signal Process.* 56.1 (2008), pp. 34–38 (cit. on p. 62).

[110] R. C. Gonzales and R. E. Woods. *Digital Image Processing.* Reading, Massachusetts, USA: Addison-Wesley, 1993 (cit. on p. 63).

[111] R. Paladini, L. Ferro-Famil, E. Pottier, M. Mortorella, F. Berizzi, and E. Dalle Mese. “Point Target Classification via Fast Lossless and Sufficient $\Omega-\Psi-\Phi$ Invariant Decomposition of High-Resolution and Fully Polarimetric SAR/ISAR Data”. In: *Proc. IEEE* 101.3 (2013), pp. 798–830 (cit. on p. 66).

[112] R. Paladini, L. Ferro-Famil, E. Pottier, M. Mortorella, and F. Berizzi. “Lossless and sufficient orientation invariant decomposition of random target”. In: *ESA SP-695 - POLinSAR 2013*. Frascati, IT, 2011 (cit. on p. 66).

[113] P. Comon. “Independent Component Analysis: A new concept?” In: *Signal Processing* 36 (1994), pp. 287–314 (cit. on p. 73).

[114] W. Gareth Rees. *Remote Sensing of Snow and Ice.* Boca Raton, FL, USA: CRC Press, Taylor and Francis Group, 2006 (cit. on pp. 81–83).

[115] Jiancheng Shi and Jeff Dozier. “Estimation of Snow Water Equivalence Using SIR-C/X-SAR, Part I: Inferring Snow Density and Subsurface Properties”. In: *IEEE Trans. Geosci. Remote Sens.* 38.6 (2000), pp. 2465–2474 (cit. on pp. 82, 121).

[116] Fawwaz T. Ulaby and W. Herschel Stiles. “Microwave response of snow”. In: *Advances in Space Research* 1.10 (1981), pp. 131 –149 (cit. on p. 82).

[117] H. Rott and C. Matzler. “Possibilities and Limits of Synthetic Aperture Radar for Snow and Glacier Surveying”. In: *Annals of Glaciology* 9 (1987), pp. 195–199 (cit. on p. 82).

[118] M.T. Hallikainen, F. Ulaby, and M. Abdelrazik. “Dielectric properties of snow in the 3 to 37 GHz range”. In: *Antennas and Propagation, IEEE Transactions on* 34.11 (1986), pp. 1329–1340 (cit. on p. 83).

[119] M. T. Hallikainen and D. P. Winebrenner. “Microwave Remote Sensing of Sea Ice”. In: ed. by F. D. Carsey. American Geophysical Union, 1992. Chap. The physical basis for sea ice remote sensing (cit. on p. 83).

[120] N. Besic. *Electromagnetic simulation of radar signals: application on studies of snow.* GIPSA-lab, Grenoble, FR, 2011 (cit. on p. 84).

[123] A. K. Fung, D. Schutzer, and K. S. Chen. *Microwave Scattering and Emission Models for Users.* Norwood, MA, USA: Artech House, 2010 (cit. on pp. 85, 86).

[124] Jiancheng Shi and Jeff Dozier. “Estimation of Snow Water Equivalence Using SIR-C/X-SAR, Part II: Inferring Snow Depth and Particle Size”. In: *IEEE Trans. Geosci. Remote Sens.* 38.6 (2000), pp. 2475–2488 (cit. on pp. 85, 87, 121, 125).

[125] Nicolas Longepe. “Snow Remote Sensing using Spaceborne SAR Imagery at L- and C-Bands”. PhD thesis. Rennes, FR: University of Rennes I, 2008 (cit. on pp. 86, 87).

[126] L. Tsang, J.A. Kong, K.H. Ding, and C.O. Ao. *Scattering of Electromagnetic Waves, Vol. 2: Numerical Simulations.* Wiley Interscience, 2001 (cit. on pp. 86, 87).

[127] Nicolas Longepe, Sophie Allain, Laurent Ferro-Famil, Eric Pottier, and Yves Durand. “Snowpack Characterization in Mountainous Regions Using C-Band SAR Data and a Meteorological Model”. In: *IEEE Trans. Geosci. Remote Sens.* 47.2 (2009), pp. 406–418 (cit. on p. 88).

[128] R. Garcon. “Operational forecast of supply from Durance to Serre-Poncon by means of MORDOR model. Balance for the year 1994-1995”. In: *La Houille Blanche International Water Journal* 5 (1996), pp. 71–76 (cit. on p. 89).

[129] E. Paquet. “A new version of the hydrological model MORDOR : snowpack model at different elevations”. In: *La Houille Blanche International Water Journal* 2 (2004), pp. 75–81 (cit. on p. 89).

[130] F. Gottardi and J. Gailhard. “Quantitative estimation of precipitation over the French mountainous areas using snow measurements and weather patterns approach”. In: *Geophysical Research Abstracts, EGU General Assembly* (2009) (cit. on p. 91).

[131] P. Goovaerts. “Geostatistical approaches for incorporating elevation into the spatial interpolation of rainfall”. In: *Journal of Hydrology* 228.1-2 (2000), pp. 113–129 (cit. on p. 91).

[133] Fawwaz T. Ulaby, W. Herschel Stiles, and Mohamed AbdelRazik. “Snowcover Influence on Backscattering from Terrain”. In: *IEEE Trans. Geosci. Remote Sens.* GE-22.2 (1984), pp. 126 –133 (cit. on p. 94).

[134] J. Shi, J. Dozier, and H. Rott. “Snow Mapping in Alpine Regions with Synthetic Aperture Radar”. In: *IEEE Trans. Geosci. Remote Sens.* 32.1 (1994), pp. 152 –158 (cit. on p. 94).

[135] Helmut Rott. “Thematic studies in Alpine areas by means of polarimetric SAR and optical imagery”. In: *Advances in Space Research* 14.3 (1994), pp. 217–226 (cit. on p. 94).

[136] Helmut Rott and Thomas Nagler. “Capabilities of ERS-1 SAR for snow and glacier monitoring in alpine areas”. In: *Proceedings of ERS-1 2nd symposium.* 1994, pp. 965–970 (cit. on p. 94).

[137] Thomas Nagler and Helmut Rott. “Retrieval of Wet Snow by Means of Multitemporal SAR Data”. In: *IEEE Trans. Geosci. Remote Sens.* 38.2 (2000), pp. 754–765 (cit. on p. 94).

[138] R. Magagi and M. Bernier. “Optimal conditions for wet snow detection using RADARSAT SAR data”. In: *Remote Sensing of Environment* 84.2 (2003), pp. 221 –233 (cit. on p. 94).

[139] T. Strozzi and C. Matzler. “Backscattering measurements of alpine snowcovers at 5.3 and 35 GHz”. In: *IEEE Trans. Geosci. Remote Sens.* 36.3 (1998), pp. 838–848 (cit. on pp. 94, 96, 97).

[140] Tazio Strozzi. “Backscattering Measurements of Snowcovers at 5.3 and 35 GHz”. PhD thesis. Bern, CH: University of Bern, 1996 (cit. on pp. 95, 97, 100, 111).

[141] C. Matzler and A. Wiesmann. “Extension of the Microwave Emission Model of Layered Snowpacks to Coarse-Grained Snow”. In: *Remote Sensing of Environment* 70.3 (1999), pp. 317 –325 (cit. on pp. 97, 111).

[142] J. A. Nelder and R. Mead. “A simplex method for function minimization”. In: *Computer Journal* 7 (1965), pp. 308–313 (cit. on pp. 97, 112, 127).

[143] A. Lessard-Fontaine, S. Allain-Bailhache, J.-P. Dedieu, and Y. Durand. "Multi-temporal dry and wet snow mapping in alpine context using polarimetric RADARSAT-2 time-series". In: *Proc. IGARSS*. Munich, Germany, 2012, pp. 1569–1571 (cit. on p. 105).

[145] P. Tourasse. "The telenivometry and the prevision of filling supply for EDF reservoirs". In: *La Houille Blanche International Water Journal* 5/6 (1995), pp. 92–97 (cit. on p. 108).

[146] G. Vasile, A. Tudoroiu, F. Gottardi, J. Gailhard, A. Girard, and G. d'Urso. "Unconstrained Nonlinear Optimization Of A Distributed SWE Model Using Modis And In Situ Measurements Over The French Alps". In: *IGARSS*. Melbourne, AUS, 2013, pp. 4859–4862 (cit. on p. 108).

[147] G. Bloschl, D. Gutknecht, and R. Kirnbauer. "Distributed snowmelt simulations in an Alpine catchment. 1. Model Evaluation on the Basis of Snow Cover Patterns." In: *Water Resources Research* 27.12 (1991), pp. 3171–3179 (cit. on p. 108).

[148] G. Bloschl, D. Gutknecht, and R. Kirnbauer. "Distributed snowmelt simulations in an Alpine catchment. 2. Parameter study and model predictions." In: *Water Resources Research* 27.12 (1991), pp. 3181–3188 (cit. on p. 108).

[149] J. Parajka and G. Bloschl. "The value of MODIS snow cover data in validating and calibrating conceptual hydrologic models". In: *Journal of Hydrology* 358.3-4 (2008), pp. 240–258 (cit. on pp. 108, 113).

[150] J. Parajka and G. Bloschl. "Multiscale Hydrologic Remote Sensing Perspectives and Applications". In: ed. by P. Laugier and G. Haiat. CRC Press, 2012. Chap. MODIS-based Snow Cover Products, Validation, and Hydrologic Applications, pp. 185–212 (cit. on p. 108).

[151] Allain S., C. Lopez, L. Ferro-Famil, and E. Pottier. "New eigenvalue-based parameters for natural media characterization". In: *Proc. IGARSS*. Seoul, South Korea, 2005 (cit. on p. 109).

[152] M. Zreda, W.J. Shuttleworth, X. Zeng, C. Zweck, D. Desilets, T. Franz, and R. Rosolem. "COSMOS: The COsmic-ray Soil Moisture Observing System". In: *Hydrology and Earth System Science* 16 (2012), pp. 4079–4099 (cit. on p. 111).

[153] E. Paquet and M.T. Laval. "Operation feedback and prospects of EDF cosmic-ray snow sensors". In: *La Houille Blanche International Water Journal* 2 (2006), pp. 113–119 (cit. on p. 111).

[154] John E. Dennis and Robert B. Schnabe. *Numerical Methods for Unconstrained Optimization and Nonlinear Equations*. SIAM, 1983 (cit. on p. 112).

[155] J.C. Lagarias, J. A. Reeds, M. H. Wright, and P. E. Wright. "Convergence Properties of the Nelder-Mead Simplex Method in Low Dimensions". In: *SIAM Journal on Optimization* 9.1 (1998), pp. 112–147 (cit. on pp. 112, 127).

[156] A. Charles and J.E. Dennis. "Analysis of generalized pattern searches". In: *SIAM Journal on Optimization* 13.3 (2003), pp. 889–903 (cit. on p. 112).

[157] Z. Michalewicz. “Genetic algorithms, numerical optimization and constraints”. In: *6th International Conference on Genetic Algorithms*. Pittsburgh, USA, 1995, pp. 151–158 (cit. on p. 112).

[158] A.G. Klein and J. Stroeve. “Development and validation of a snow albedo algorithm for the MODIS instrument”. In: *Annals of Glaciology* 34 (2002), pp. 45–52 (cit. on p. 113).

[159] J. Parajka and G. Bloschl. “Spatio-temporal combination of MODIS images - potential for snow cover mapping”. In: *Water Resources Research* 44.3 (1999) (cit. on p. 113).

Abstract: This thesis comprises two research axes. The first, being rather methodological, consists of our efforts to answer some of the open questions in the POLSAR community, while the latter is sooner related to the specific application - the remote sensing of snow. Following the alternative statistical modelling of highly textured multivariate SAR datasets by means of SIRV model, we propose the appropriate assessment of, otherwise assumed, circularity and sphericity parameters. The last is coupled with the spherical symmetry test, forming a method for the evaluation of SIRV statistical model suitability in the context of POLSAR data. Given the rejection rate, challenging circularity and sphericity appears to be justified, while SIRV model pertinence must be doubted in the regions characterized by strong deterministic scattering. Further on, as the highlight of this thesis, we propose a polarimetric incoherent target decomposition, based on ICA and founded on the hypothesis of non-Gaussianity of POLSAR clutter. By exploiting the information contained in the higher statistical orders, this decomposition provides at the output a set of mutually independent (rather than only decorrelated), non-orthogonal target vectors. Unlike the first dominant component, which is nearly identical to the one estimated by the conventional ICTD counterpart, the second dominant component differs significantly, which, as we anticipate, represents an additional potential for the POLSAR datasets interpretation. In the applied context, the first presented contribution would be a stochastic approach in snow mapping by means of multitemporal SAR datasets. The most notable supplements of the presented method to the ensemble of change detection techniques in snow mapping are the plausibly modified assumption of the wet/dry snow backscattering ratio and implicitly introduced spatial correlation between wet snow areas, achieved by directly implicating local speckle statistics in the decision process. Finally, we present the non-autonomous method for SWE spatial estimation, based on optical datasets. By successfully involving the remote sensing datasets in the calibration of the external SWE model, we seek to demonstrate the utility and the necessity of the former in the snow pack monitoring.

Résumé: Cette thèse est composée de deux axes de recherche. Le premièr, plutôt méthodologique, consiste de nos efforts pour répondre à des questions ouvertes dans la communauté de RSO polarimétrique, tandis que le second est plutôt lié à l'application spécifique - le télédétection du manteau neigeux. Suite à la modélisation statistique alternative des images RSO multivariées et hautement texturées, par le modèle SIRV, nous proposons d'abord une évaluation appropriée des paramètres de circularité et sphéricité, autrement à priori présumés. La dernière est accouplée avec le test de symétrie sphérique, ce qui forme une méthode pour l'évaluation de pertinence de modèle statistique SIRV dans le contexte de données RSO polarimétriques. Compte tenu du taux de réjection, cela parait justifié de mettre en question les hypothèses de circularité et sphéricité, alors que la pertinence de modèle SIRV doit être soupçonnée dans les régions caractérisées par la diffusion déterministe forte. En suite, comme le point culminant de cette thèse, nous proposons une décomposition incohérente de cible polarimétrique, basée sur l'ACI et fondée sur l'hypothèse de non-Gaussianité du *clutter* RSO polarimétrique. En exploitant l'information contenue dans les ordres statistiques supérieurs, cette décomposition donne à la sortie un ensemble de vecteurs de cible, qui sont mutuellement indépendants (plutôt que seulement décorrélés) et non-orthogonaux. Contrairement à la première composant dominante, qui parait presque identique à l'une estimée par le homologue conventionnel, la deuxième composante dominante diffère significativement, ce qui représente un potentiel additionnel pour l'interprétation des données RSO polarimétriques. Dans le contexte appliqué, la première contribution présentée serait une approche stochastique pour la cartographie du manteau neigeux au moyen de données RSO multi-temporelles. Les apports les plus notables de la méthode présentée à l'ensemble de techniques de la détection de changements dans la cartographie du manteau neigeux, sont l'hypothèse modifiée du ratio de rétrodiffusion entre la neige sèche et la neige humide, aussi que la corrélation spatiale entre les régions de la neige humide, introduite en impliquant la statistique locale de *speckle* dans le processus de décision. Finalement, nous présentons la méthode non-autonome pour l'estimation spatiale de l'équivalent en eau de la neige (EEN), basée sur des données optiques. En utilisant avec succès des données de télédétection dans la calibration du modèle EEN externe, on essaie de démontrer l'utilité et la nécessite du télédétection dans la surveillance du manteau neigeux.